

**DESIGN OF A ROBOT ASSISTED MINIMALLY
INVASIVE SURGICAL SYSTEM FOR PITUITARY
TUMOR SURGERY BASED ON SAFETY FEATURES**

**A Thesis Submitted to
the Graduate School of
İzmir Institute of Technology
in Partial Fulfillment of the Requirements for the Degree of
DOCTOR OF PHILOSOPHY
in Mechanical Engineering**

**by
Omar Waleed Najm MAAROOF**

**July 2020
İZMİR**

ACKNOWLEDGMENTS

I would like to express my gratitude to my advisor Assoc. Prof. Dr. Mehmet İsmet Can Dede for his priceless advice, guidance, support, and encouragement not only during my study. Without him, the NeuRoboScope project would not be true. My thanks and gratitude to his friendly family for their support and hospitality.

I would like to thank all my professors in IYTE for their help during my study and research. I thank all the professors and friends who participated and added valuable inputs in the NeuRoboScope project as well as all the surgeons who participated in the experimental analyses in this project. I am grateful for the help and support of all my dear friends in Robotics Laboratory, Human-robot Interaction Laboratory, Modeling and Prototyping Laboratory, and RAML laboratory.

Many thanks to my professor and friend Assoc. Prof. Dr. Saad Zaghlul Saeed, the head of the mechatronics engineering department at the University of Mosul, for his help in Chapter 8.

I would like to thank my wonderful wife Ruaa Almallah and my lovely daughter Melek for their great support and patience during my long hours of working. I am so grateful to my parents for their endless love and support during my life.

And finally, thanks to IYTE Library for providing the resources and off-campus facility during the COVID19 pandemic and quarantine.

This dissertation study is conducted as a part of the TUBITAK research project (The Scientific and Technological Research Council of Turkey) via grant number 115E726.

ABSTRACT

DESIGN OF A ROBOT ASSISTED MINIMALLY INVASIVE SURGICAL SYSTEM FOR PITUITARY TUMOR SURGERY BASED ON SAFETY FEATURES

The study is on the designing a robot assisted endonasal endoscopic surgical system; NeuRoboScope, the pituitary tumor resection surgery system. This system comprises of a passive and an active arm. The passive arm positions the active arm in the surgery zone while the active arm assists the surgeon by positioning the endoscope during the surgery. The focus of this dissertation is the mechanical and control safety features that can be implemented in the system. The safety enhancement methods of robot assisted minimally invasive surgery systems are investigated. Among the seventeen investigated robot assisted endoscope holders, sixteen of them have been implemented in pituitary tumor and sinus surgeries. Safety is the main criterion that advances the progress of these systems and places them in operation rooms. Accordingly, two optimization procedures have been applied during the design of the NeuRoboScope system that have a direct effect on the suggested safety features.

A novel optimization technique is proposed by employing a redundancy resolution method. The most suitable fixing point of the passive arm and its first link length is optimized to achieve the maximum manipulability with restrictions imposed by a modified condition number index and impedance of the passive arm.

The active arm's partial gravity compensation is studied. Three spiral springs are used as a compact and lightweight partial gravity compensation method. Particle swarm optimization method is employed for the optimization of the design parameters: spiral spring stiffness and initial angle values. Consequently, at least 66% of gravity related actuator loads are compensated.

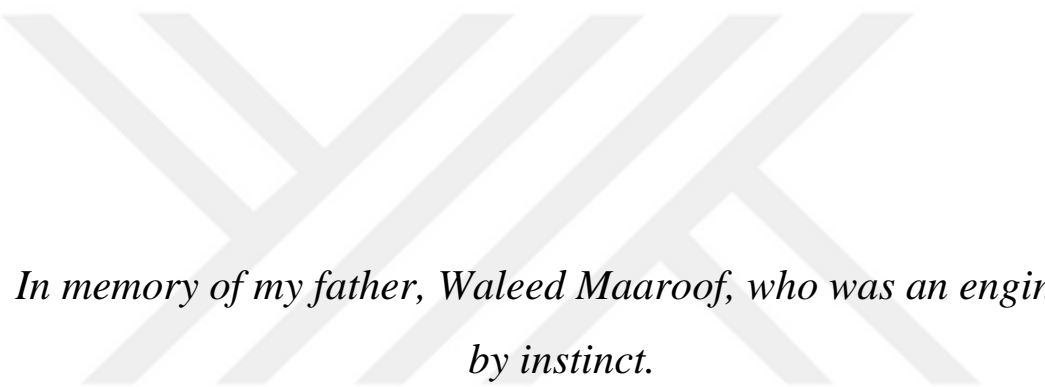
ÖZET

HİPOFİZ TÜMÖRÜ AMELİYATI İÇİN GÜVENLİK ÖZELLİKLERİ TEMEL ALINARAK ROBOT YARDIMLI BİR MİNİMAL İNVAZİV AMELİYAT SİSTEMİ TASARIMI

Bu çalışma bir yardımcı robotlu endonazal endoskopik ameliyat sistemi; NeuRoboScope, hipofiz bezi tümörü rezeksiyonu ameliyat sistemi, tasarımı hakkındadır. Bu sistem bir pasif kol ve bir aktif koldan oluşmaktadır. Pasif kol aktif kolu ameliyat bölgesinde konumlandırırken aktif kol endoskopu ameliyat sırasında yönlendirerek cerraha yardımcı olur. Bu tezde söz konusu sistemde kullanılacak mekanik ve kontrol alanlarındaki güvenlik özelliklerine odaklanılmıştır. Robot yardımcılı minimal invaziv ameliyat sistemlerinin güvenliği artırıcı yöntemleri araştırılmıştır. Mevcut onyediy robot yardımcılı endoskop tutucu arasından onaltısı hipofiz bezi tümörü ve sinüs ameliyatlarında kullanılmıştır. Bu sistemlerin ilerleyip ameliyat odalarında yer bulmasında güvenlik en önemli kriterdir. Bu doğrultuda, NeuRoboScope sistemi için önerilen güvenlik özelliklerine doğrudan etkisi olan iki eniyileme yöntemi tasarım sırasında uygulanmıştır.

Artıksıllık çözünümü yönetimini kullanan yeni bir eniyileme yöntemi önerildi. Pasif kolun bağlantı noktası konumu ve ilk uzvunun boyu en yüksek manipüle edilebilirliğe ulaşmak için, değiştirilmiş kondüsyon numarası ve pasif kolun empedans kısıtları gözetilerek, eniyilendi.

Aktif kolun kısmi yerçekimi telafisi çalışıldı. Az yer kaplayan ve hafif bir kısmi yerçekimi yöntemi olarak üç adet helezon yay dengeleme yayı olarak kullanıldı. Partikül sürü eniyilemesi yöntemi kullanılarak tasarım parametreleri olan spiral yayın direngenliği ve öngerilme açısı eniyilendi. Sonuç olarak yerçekimi kuvveti ile alakalı eyleyicilerin yüklerinin en az %66'sı telafi edildi.



*In memory of my father, Waleed Maarooof, who was an engineer
by instinct.*

TABLE OF CONTENTS

LIST OF FIGURES.....	x
LIST OF TABLES.....	xvi
CHAPTER 1. INTRODUCTION.....	17
1.1. Minimal Invasive Surgery.....	17
1.2. Pituitary Tumor Resection Surgery.....	18
1.3. Problem Definition.....	20
1.4. Aim of the Dissertation.....	23
1.5. Contributions.....	23
1.6. Outline of the Dissertation.....	24
CHAPTER 2. BACKGROUND ON SURGICAL ROBOTS	26
2.1. Surgical Robotic Systems.....	27
2.1.1 Supervisory-Controlled Systems.....	28
2.1.2 Telesurgical Systems.....	29
2.1.3 Shared-Control Systems.....	31
2.1.4 Cooperative Systems.....	33
2.2. Background on Robotic Endoscopic / Laparoscopic Surgery.....	34
2.3. Background and a Review on Robots Designed / Applicable for Endonasal Surgery.....	37
2.4. Discussions.....	55
2.4.1 Safety Features.....	56
2.4.2 Mechanical Structure.....	57
2.4.3 Dimensions.....	58
2.4.4 User-Robot Interfacing.....	58
2.5. Conclusion.....	59
CHAPTER 3. ANALYSIS OF DESIGN REQUIREMENTS.....	61
3.1. The Anatomy and Physiology of the Surgical Area.....	61
3.2. Measurement and Analysis of the Surgeon's Motion.....	64

3.2.1. Experimentation Setup for Measurements.....	66
3.2.2. Decomposition of a General Rotation into Two Elementary Rotations of Euler Angles.....	67
3.2.3. Acquisition and Analysis of the Data.....	70
3.3. Measuring the Impedance Characteristics of the Surgical Environment.....	75
3.3.1. Measurement Device Design.....	77
3.3.2. Gravity Cancellation for Higher Accuracy in Measurements.....	79
3.3.3. Experimental Tests of the Device.....	81
3.4. Conclusions.....	84

CHAPTER 4. DESCRIPTION AND DESIGN OF THE NEUROBOSCOPE

SYSTEM.....	86
4.1. General Description of the System.....	86
4.2. Design Requirements for the Robot Assisted Endoscope Holder System.....	87
4.3. Description of the Active Arm and its Analyses.....	89
4.3.1. A Conceptual Design of the Active Arm: RPRP Serial-Arm.....	90
4.3.1.1. Forward Kinematics Analysis of RPRP Serial-Arm.....	92
4.3.1.2. Inverse Kinematics Analysis of RPRP Serial-Arm.....	94
4.3.2. Mechanism of the Selected Spatial Parallel Manipulator.....	96
4.3.3. Kinematic Analysis of the Selected Spatial Parallel Manipulator.....	98
4.3.3.1. Inverse Kinematics Analysis of the Spatial Parallel Manipulator.....	98
4.3.3.2. Forward Kinematics Analysis of the Spatial Parallel Manipulator.....	103
4.3.4. Dynamic Analysis of the Selected Spatial Parallel Manipulator.....	107
4.3.4.1. Calculation of the Inertial Forces and Moments.....	109
4.3.4.2. The Virtual Displacements of Each Link.....	112
4.3.4.3. The Generalized Input Torques.....	113
4.4. Description of the Passive Arm and its Kinematic Analysis.....	116
4.4.1. Forward Kinematics Analysis of the Passive Arm.....	118

4.4.2. Description of the Parallelogram Loop for Gravity Compensation.....	119
CHAPTER 5. MECHANICAL SAFETY FEATURES FOR SURGICAL ROBOTS.....	122
5.1. Surgery Zone Definition.....	122
5.2. Positioning and Setting-up the System.....	128
5.3. Modification of the Passive-Arm's Kinematics.....	129
5.4. Reachability and Joint Limits.....	131
5.4.1. The Passive Arm Joint limits.....	132
5.4.2. The Active Arm Joint limits.....	132
5.5. Gravity Compensation.....	133
5.5.1. Gravity Compensation for the Passive Arm.....	135
5.5.2. Gravity Compensation for the Active-Arm.....	137
5.6. Mechanical Safety at Endoscope Holder.....	141
CHAPTER 6. CONTROL SAFETY FEATURES FOR SURGICAL ROBOTS.....	144
6.1. Systematic Design for Safety.....	144
6.2. Safety Standards of Robot Assisted Surgical Systems.....	146
6.3. Risk Assessment for Safety.....	149
6.4. Control Safety Features.....	150
6.5. Robot assisted Surgical Systems Control for Safety.....	152
6.6. Modeling and Analysis of Patients for Safety.....	153
6.7. Contact Force Information for Safety.....	154
6.8. Setup and Operation for Safety.....	155
6.9. Redundancy for Safety.....	156
6.10. Other Control Safety Features.....	158
6.11. Conclusions.....	158
CHAPTER 7. PASSIVE ARM'S DESIGN OPTIMIZATION.....	159
7.1. Optimization Methods.....	159
7.2. Redundancy Resolution Techniques.....	160
7.3. Applications on Redundancy Resolution.....	162
7.4. Description of the Case Scenario.....	163
7.5. Description of the New Design Optimization Method.....	164

7.6. Design Optimization Constraints.....	165
7.7. Optimization by Using Mechanical Redundancy.....	166
7.8. Implementation of the New Optimization Strategy.....	169
7.8.1. Manipulability Ellipse and (SVD) Singular Value Decomposition.....	171
7.8.2. The Modified Condition Number.....	172
7.8.3. Generalized Inertia Matrix.....	172
7.9. Test Setup and Simulation Results.....	174
7.9.1. Test 1: Two design Parameters.....	174
7.9.2. Test 2: One design Parameter.....	176
7.9.3. Test 3: With the Modified Condition Number as the Performance Index.....	178
7.10. Conclusions.....	183
CHAPTER 8. ACTIVE ARM'S GRAVITY COMPENSATION DESIGN OPTIMIZATION.....	184
8.1. Description of the Case Scenario.....	184
8.2. Particle Swarm Optimization Method.....	185
8.3. The Procedure Followed in PSO Method.....	187
8.4. Design Optimization Constraints.....	188
8.5. Optimization Test Results.....	189
8.5.1. Spring Utilizing Effect on the Partial Gravity Compensation.....	189
8.5.2. Optimization Study by Minimizing the Summation of Actuators' Torques.....	191
8.5.3. Optimization Study by Using the Minimum Upper Limit of Actuators' Torques.....	193
8.5.4. Discussion on the Design and Improvements.....	196
8.6. Conclusions.....	200
CHAPTER 9. CONCLUSIONS.....	202
REFERENCES	210

LIST OF FIGURES

<u>Figure</u>	<u>Page</u>
Figure 1.1. The minimally invasive surgery.....	18
Figure 1.2. Pituitary gland position on human.....	19
Figure 1.3. The pituitary gland tumor surgery.....	20
Figure 1.4. The pituitary tumor surgery problems.....	21
Figure 1.5. The passive arm solution Martin's Arm.	22
Figure 1.6. Operation Assisting Device iArmS [®]	22
Figure 2.1. Classifications of healthcare robots.....	27
Figure 2.2. The TSolution [®] One Surgical System.....	29
Figure 2.3. Da Vinci [®] surgical systems, a) Da Vinci x [®] , b) Da Vinci SP [®] , c) Da Vinci XI [®] , d) Surgeon console.....	30
Figure 2.4. Senhance [®] surgical system Telelap Alf-X.	30
Figure 2.5. The CMR surgical, Versius [®] surgical robotic system.....	30
Figure 2.6. The DLR MiroSurge [®] system.	31
Figure 2.7. Flex [®] Robotic System.	32
Figure 2.8. The MAZOR systems, a) MAZOR [®] X, b) Mazor [®] Robotics Renaissance	32
Figure 2.9. The ROSA systems, a) ROSA ONE [®] brain system, b) ROSA [®] knee system.....	32
Figure 2.10. MAKO [®] Robotic-Arm Assisted Surgery.	33
Figure 2.11. The Robotic Visualization System KINEVO 900 [®]	33
Figure 2.12. EMARO [®]	34
Figure 2.13. The AESOP [®] system.	34

<u>Figure</u>	<u>Page</u>
Figure 2.14. Classification results of characteristics of endoscope robots and manipulation: a) A460 CRS Plus, b) AESOP, c) LARS, d) EndoAssist (Endosista), e) Staubli Rx60, f) ERM, g) LapMan, h) RES, i) Naviot, j) PASEO, k) HISAR, l) ViKY (LER), m) 5-DOFs Laparoscopic Assistant Robot (KaLAR), n) FIPS, o) Imag Trac, p) Wide-Angle View Endoscope, q) Dual- View Endoscopic System, r) Automatic Tracking And Zooming System, s) COVER, t) P-arm, u) FreeHand, v) Robolens, w) Swarup Robotic Arm (SWARM), x) MST Laparoscope Manipulator, y) ROBOX, z) FELIX, aa) Paramis.	37
Figure 2.15. EVOLUTION 1.....	42
Figure 2.16. The A73 system.....	43
Figure 2.17. The robot arm PA10–6c with Strauß et al.’s designed holder mechanism	44
Figure 2.18. The Tx-40 for robot assisted endoscopy system	45
Figure 2.19. The Endoscope Manipulator System EMS with a different setup, a) beside the operation table, b) behind the operation table.....	46
Figure 2.20. The HYBRID system, a) test scenario, b) the passive gamble holder	47
Figure 2.21. a) Stewart platform with the endoscope, b) Insertion of the endoscope to the artificial model	47
Figure 2.22. The FREE Endoscopic holder.	48
Figure 2.23. The BEAR system.	49
Figure 2.24. Insertion and visualization of the endoscope by EndoscopeRobot® by Medineering	50
Figure 2.25. Robotic endoscope holder.	51
Figure 2.26. Endoscope manipulator for nasal surgery, a) the model, b) the prototype.	52
Figure 2.27. The ROSA® system.....	53
Figure 2.28. FREEHAND® a) the present commercial system V1.2, b) the next generation (not in the market).....	54
Figure 2.29. The FREEDOM® system, a) the prototype, b) the footprint of the system.	55
Figure 3.1. Surgical workspace and pituitary gland approach.....	62
Figure 3.2. The nasal cavity.....	63

<u>Figure</u>	<u>Page</u>
Figure 3.3. An endoscope with an angular motion measuring component.....	67
Figure 3.4. Reference frame with respect to the cadaver's head	67
Figure 3.5. Frame transformation between the endoscope and the accelerometer.	68
Figure 3.6. The selected sequence of Euler angles	69
Figure 3.7. Filtered signal result for double full navigation inside the surgical workspace.....	73
Figure 3.8. The representation of the selected distances at the radiology images.....	74
Figure 3.9. Schematic diagram of surgeon-patient interaction.....	77
Figure 3.10. Schematic diagram of the handle and fixing part.....	78
Figure 3.11. Handle with motion and F/T sensor attached.....	79
Figure 3.12. The F/T sensor frame on the endoscope.....	80
Figure 3.13. The endoscope and the location of the center of gravity (including the telescope)	81
Figure 3.14. Holding the endoscope	81
Figure 3.15. Initial test setup	82
Figure 3.16. Gravitational effects by endoscope weight on reading test, a) motion information, b) force values, c) torque values.	83
Figure 4.1. The manipulator system's concept.....	87
Figure 4.2. The mechanism of the serial active robot arm and range of setup.....	90
Figure 4.3. The coordinate frame schematic of the serial robotic arm RPRP	93
Figure 4.4. The insertion distance and the inverse kinematics.	95
Figure 4.5. The prototype of the selected design of the NeuRoboScope system, the spatial parallel manipulator	97
Figure 4.6. A schematic illustration of the parallel manipulator	98
Figure 4.7. The global reference frame with respect to the patient	99
Figure 4.8. The unit vector in the global frame	100
Figure 4.9. The unit vector in manipulator's reference frame.....	101
Figure 4.10. The work plane of the 3 rd leg.....	102
Figure 4.11. A schematic illustration of leg 3.....	104
Figure 4.12. The center of masses for leg 1.....	106
Figure 4.13. Load distributions on the center of masses	110
Figure 4.14. The motion trajectory of A) the trajectory of the required motion, B) the generated motion at the actuators.	114

<u>Figure</u>	<u>Page</u>
Figure 4.15. The comparison results for A) The calculated torques, B) The error between the calculated and simulated torques, C) The percentages of the error in torque calculation	115
Figure 4.16. The CAD drawing of the robot endoscope holder arm	117
Figure 4.17. Schematic diagram of the passive arm	117
Figure 4.18. The parallelogram loop of the passive arm	120
Figure 5.1. Surgery zone with respect to the pivot-point and the telescope	125
Figure 5.2. NeuRoboScope system's control algorithm diagram.	126
Figure 5.3. Configuration of the passive arm with two fixing positions, a) The base beneath the head, b) The base positioned away from any singularity configuration.	129
Figure 5.4. Two cases show orientation change with respect to the position.....	130
Figure 5.5. The modification in the passive arm, a) The earlier design of the passive arm, b) The modified design	130
Figure 5.6. The gravity compensation on the modified wrist component.	136
Figure 5.7. Gravity balanced passive arm that handles the spatial parallel manipulator.....	138
Figure 5.8. The proposed design for mounting the spiral spring in the actuation system of the active parallel mechanism	140
Figure 5.9. The active mechanism's actuation systems with three spiral springs for balancing	141
Figure 5.10. The plug/release mechanism	142
Figure 6.1. A general overview of the design cycle of a surgical robot	145
Figure 7.1. The surgical robotic system NeuRoboScope.....	163
Figure 7.2. Kinematic scheme of the passive robot arm.....	164
Figure 7.3. Spectacle situation in the surgery room	166
Figure 7.4. Reference coordinate system on the surgery table	167
Figure 7.5. The change of the robot arm structure and the manipulability ellipse during the optimization routine with two design parameters	175
Figure 7.6. The change of the manipulability index of the passive arm during the optimization routine with two design parameters	176
Figure 7.7. The change of the robot arm structure and the manipulability ellipse during the optimization routine with one design parameter.....	177

<u>Figure</u>	<u>Page</u>
Figure 7.8. The change of the manipulability index of the passive arm during the optimization routine with one design parameter	178
Figure 7.9. The change of the robot arm structure and the manipulability ellipse during the optimization routine by using the modified condition number. 179	
Figure 7.10. The change of the manipulability index and singular values during the optimization routine by using the modified condition number	179
Figure 7.11. The optimization procedure with a modified condition number: a) Change of the generalized inertia matrix, b) change of components of the objective function, c) change in the values of design parameters	180
Figure 7.12. The change of the robot arm structure and the manipulability ellipse during the optimization routine by using the modified condition number and the inertia matrix	181
Figure 7.13. The change of the manipulability index and singular values during the optimization routine by using the modified condition number and the inertia matrix	182
Figure 7.14. The optimization procedure with modified condition number and inertia matrix: a) Change of the generalized inertia matrix, b) change of components of the objective function, c) change in the values of design parameters	182
Figure 8.1. Parallel RCM mechanism holding the endoscope.....	185
Figure 8.2. Motion sequence of the RCM mechanism with the endoscope for the initial study (the initial state at $t = 0$ s, intermediate state at $t = 1$ s, and final state at $t = 2$ s)	189
Figure 8.3. Actuator torque without/with springs have various properties for a specific trajectory	190
Figure 8.4. Experiment run points inside a range of workspace.....	191
Figure 8.5. Optimization objective function value versus the number of iterations.....	192
Figure 8.6. Optimization objective function value versus the number of iterations for the first scenario.....	194
Figure 8.7. Optimization objective function value versus the number of iterations for the second scenario.	195
Figure 8.8. Optimization objective function value versus the number of iterations for the third scenario.....	196

Figure

Page

Figure 8.9. The generated torques inside the workspace at the first actuator, a)
without gravity compensation, b) with partial gravity compensation 199

Figure 8.10. The generated torques inside the workspace at the second actuator a)
without gravity compensation, b) with partial gravity compensation 199

Figure 8.11. The generated torques inside the workspace at the third actuator a)
without gravity compensation, b) with partial gravity compensation 200



LIST OF TABLES

<u>Table</u>	<u>Page</u>
Table 2.1. Summary robot table devoted to the endonasal surgery.....	38
Table 2.2. Robotic endoscope holders for FESS and ESBS.....	40
Table 3.1. Summary of workspace of the relevant studies in the literature.....	66
Table 3.2. The intraoperative scenario analysis results.	71
Table 3.3. Measuring results.....	74
Table 3.4. Set of results of the initial test.	82
Table 4.1. Denavit-Hartenberg parameters.....	93
Table 4.2. The Denavit-Hartenberg parameters for the passive arm.....	118
Table 4.3. The structural parameters	118
Table 5.1. The mechanical safety features.....	123
Table 5.2. Affiliations regarding to control algorithm.....	127
Table 5.3. Sample of massages regarding to control algorithm.....	127
Table 5.4. The limits of the parallel active manipulator.....	133
Table 6.1. List of some standards published by IEC	147
Table 6.2. Control safety features presented in this study	151
Table 7.1. Joint variables of Test 2.....	176
Table 7.2. Test 3 design parameters	183
Table 8.1. The first optimization study parameters and results	192
Table 8.2. The first scenario parameters and results.....	193
Table 8.3. The second scenario parameters and results.....	194
Table 8.4. The third scenario parameters and results.	196
Table 8.5. Testing the selected design parameters in the first scenario on different....	197
Table 8.6. Optimization of the tilted robot with results.....	198

CHAPTER 1

INTRODUCTION

With the help of the fast-growing technology and improvements in medical instruments, surgical tools, and imaging devices, many changes emerged in the medical surgery industry. Medical doctors made remarkable alterations in the surgery procedures. Instead of traditional open surgeries, with the help of the new vision gadgets such as the endoscope and laparoscope, they are performing what is classified as Minimally Invasive Surgery (MIS) procedures.

In medical robots, safety is the main concern, especially for MIS systems. The most important impact of this study is the design of the robot assisted surgical system named NeuRoboScope with optimal safety criteria that can enhance this surgical technique. Throughout this dissertation, the focus is on the mechanical and control safety features' design optimization. This Chapter introduces some medical definitions related to this surgical application and presents the problems in surgery rooms that arose the need for an assistant surgical robot. The contributions are highlighted, and the Chapter ends with the outline of the dissertation.

1.1. Minimal Invasive Surgery

Technological improvements in imaging and endoscope technology made the use of MIS procedures widely common. More hospitals are starting to perform MIS on their patients due to the increasing requests for this type of surgical technique. It has many advantages outweigh open surgery; those advantages and attributes can be summarized as:

- Surgery can be done through a small incision port(s): through single-port called Single-Port Laparoscopy SPL and through multi-port called Multi-Port Laparoscopy shown in Figure 1.1.
- The surgery can be carried out by the access through small corridors in the natural orifices -Natural orifice Transluminal Endoscopic

Surgery (NOTES)- of the body, and as a result, less discomfort and small or no scars remain after surgery.

- Less painful.
- Has a better cosmetic appearance of scars.
- Less bleeding can degrade the risks of complications.
- A quicker recovery period that minimizes the surgery costs.

MIS already existed for some decades but with the assistance of robotics, many advantages added to MIS elevated this procedure to a higher level (More details are presented in Chapter 2). There are various types of surgeries that can be performed in a minimally invasive way, and in this study, the pituitary tumor surgery is considered.



Figure 1.1. The minimally invasive surgery.

(Source: Kansas, 2020)

1.2. Pituitary Tumor Resection Surgery

In pituitary tumor resection surgery, the patient suffers from skull base tumors, which are located in the pituitary gland as shown in Figure 1.2. Fortunately, this type of tumor can sometimes be removed surgically by the help of the Microscope called Traditional or open skull base surgery. Removing techniques include minimally invasive endonasal endoscopic removal surgery through the nose called endonasal endoscopic surgery and through a small incision port in the eyebrow or behind the ear which is called endoscopic craniotomy. The combined technique (both endonasal and transoral) was implemented in the surgery called Neuroendoscopic surgery (Johns

Hopkins, 2020). Endoscopic endonasal surgical technique was established (with the aid of innovative endoscopic devices by Karl STORZ® and Harald Hopkins) in the 1970s by surgeons: Stammberger and Messerklinger, for the treatment of chronic sinusitis refractory to a medical treatment called Messerklinger Technique (MT) (Stammberger and Posawetz, 1990). In 1985, Dr. David Kennedy was the first to term Functional Endoscopic Sinus Surgery (FESS) and taught the use of these techniques in many courses (Kane, 2018). By the full feedback vision to manipulate surgery tools precisely, this new technique constituted an evolution in treatment and diagnoses of nasal and sinus diseases, by altering extensive non-functional surgery into MIS designed to restore functional and physiological ventilation of the sinuses.

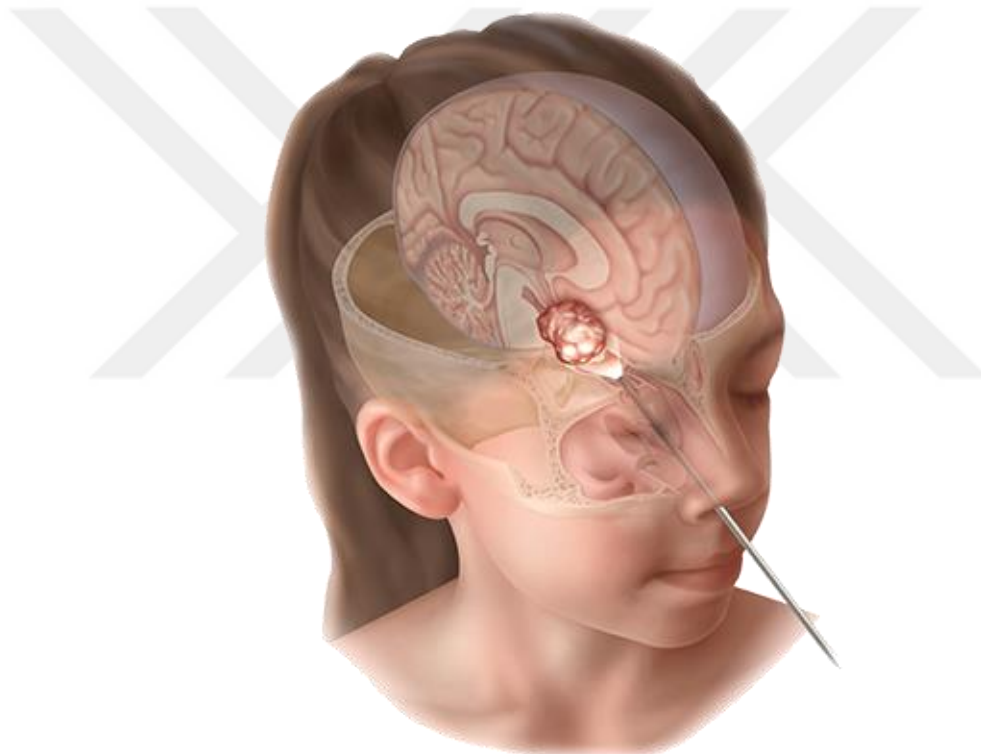


Figure 1.2. Pituitary gland position on human.

(Source: Weill Cornell Brain and Spine Center, 2020)

After years of success in the surgical treatment of common sinus diseases by FESS techniques, the applicability of these techniques for a skull base tumor approach became a new target of treatment. The pituitary tumor became a new target to apply the MIS procedure through the nasal corridor. When the surgery is minimally invasive through the nose as shown in Figure 1.3, the surgeon uses specific tools for drilling and grasping to reach the tumor and remove it. With the help of the endoscope and surgical

equipment, the surgeon can have full visual feedback inside the nostrils to manipulate the tools precisely and follow the progress of the surgery. This type of treatment technique called Endoscopic Skull Base Surgery (ESBS), (sometimes prescribed as: Endoscopic Endonasal Transsphenoidal Surgery (EETS), Endoscopic Endonasal Pituitary surgery, or Endoscopic Endonasal Skull Base Surgery).



Figure 1.3. The pituitary gland tumor surgery.

1.3. Problem Definition

In many scenarios, it has been noticed that ESBS requires the use of several tools simultaneously. As shown in Figure 1.4, one hand holds and manipulates one of the surgical tools such as the tube suction, forceps, or stripper and the other hand is reserved to hold the endoscope. Castelnovo (otorhinolaryngologist in Varese, Italy) and Nicolai (neurosurgeon in Varese, Italy) developed a new technique called “Four-hand surgery” allowing two surgeons using several tools through the two nostrils (Castelnovo et al., 2010). In this technique, the possibility of working with more than two instruments inside the nose was possible. In addition, the four-hand technique greatly minimized the duration of the surgery. Briner et al. (2005) revealed that the operating time was considerably longer (by an average of 21%) with two-hand surgery comparing with the four-hand technique. However, it requires two experienced senior surgeons.

The main problem in this surgery is the need for the surgeon to hold and control the endoscope along with the instruments such as the aspirator, curette, drill, and lancet.

Nevertheless, even a highly qualified team of surgeons can experience trembles in visualization during a long surgical procedure as stated by the surgeons. The main reason for this is that in an operation that lasts as long as four hours, the handling of the endoscope can be a very demanding task for the surgeon holding and manipulating the endoscope which results in the fatigue of the surgeon.

Sometimes, assistant surgeons handling the endoscope for the main surgeon cannot follow instructions from the main surgeon precisely. Assistant surgeons could also face various problems due to crowded and limited workspace. As a result of all these, a delay may occur in the procedure. In addition, the unstable image will increase the stress and degrade the focus of the surgeon, which is considered crucial for these surgeons. All these lead researchers to develop holding arms or robot arms to hold and direct the endoscope, and consequently, assist the surgeon.



Figure 1.4. The pituitary tumor surgery problems.

There are two categories of endoscope holders. *Passive Endoscope Holding Systems*: Passive arms/mechanisms have been used to hold the endoscope at a fixed location during the MIS procedure. In this type, the arm is passive and could be statically balanced. Whenever the surgeon needs to change the view angle, he/she will need to adjust it manually by the use of mechanical joints and then, lock them into their new position. This system is normally simple and lightweight as can be seen in Figure

1.5. Some examples of such holders are POINT SETTER[®] Holding Arm (User Manual, 2010), Martin's Arm (Martin's Arm, 2020), ENDOCRANE[®] holding arm by KARL STORZ[®] (STORZ, 2020), and ENDOFIX^{exo} by AKTORmedTM (AKTORmed, 2020). However, the passive arm solution requires a considerable effort of the surgeon or the assistant whenever a new view angle of the endoscope is necessary. In another example, the Operation Assisting Device iArmS[®] shown in Figure 1.6 is an arm-support system in which the arm is powered by the human (operates passively) while the joints brake/release by sensing surgeon's arm motion. The system is fixed to the surgeon's arm instead of the tools to compensate for the tremors that result from the long operation durations.



Figure 1.5. The passive arm solution Martin's Arm.
(Source: Martin's Arm, 2020)



Figure 1.6. Operation Assisting Device iArmS[®].
(Source: Denso, 2020)

Slave robot arm as the endoscope holder: A master-slave system can assist the surgeon during the operation. The slave robot arm, which holds the endoscope, can perform the real-time endoscope positioning during the MIS procedure. The surgeon controls the pose of the endoscope by teleoperation via a master system or suitable user-robot interfacing such as speech recognition. At the same time, he/she has the ability to work on the surgery and focus on his/her operation.

1.4. Aim of the Dissertation

Having the endoscope held by a robot arm that can follow the commands of the surgeon with high accuracy, and in an agile enough and safe way will improve quality and decrease the duration of the surgical procedure greatly. The main impact of this study is the design of the system with optimal safety criteria and the focus will be on the mechanical and control safety features. Accordingly, several safety features, which have been found in the literature and related works in the field of the surgical robot sector, are suggested to be implemented in the NeuRoboScope system. A systematic way to design and optimize these features is adopted in this dissertation. Robotic endoscope holder with teleoperation capability that is to be designed with the safety and optimal design criteria presented in this dissertation are aimed to be a benchmark for endoscopic surgical robots. In this aspect, the NeuRoboScope system will be a novel approach in the production of such robotic systems.

1.5. Contributions

- 1) Intraoperative statistical motions are analyzed to guide the choice of structure of the mechanism by an external tracking system.
- 2) A new measuring device is designed and produced for the acquisition of the loads exerted on the endoscope (by 6-dimensional force/torque sensor) while operating in the nostril corridors.
- 3) Mechanical safety features are proposed and used in a new surgical system called NeuRoboScope.

- 4) A systematic design is carried out by the selection among two novel active robot arms (one proposed in this dissertation) and by the modification of a passive arm.
- 5) Kinematic and dynamic analyses of the novel active robot arm of the NeuRoboScope system are carried out.
- 6) A particle swarm optimization method is used in the optimization of the compact gravity compensation components for the active robot arm.
- 7) A novel optimization method is proposed and used for the kinematic design and selecting the mounting position of the passive robot arm.
- 8) Control safety features are proposed for the NeuRoboScope system.

1.6. Outline of the Dissertation

In **Chapter 2**, an introduction to the categories of medical robots is made, and then, the medical robots that are used in several surgical systems. The classification is presented according to the safety features, the control algorithm, and the surgical application of these systems. A brief review of the literature for the robotic endoscopic surgery is presented focusing on the works related to the development of robot assisted endonasal surgery.

Based on the prior reviews and works, to set the necessary design requirements for the robot assisted system, the brief description and the essential measures for the surgical workspace are introduced in **Chapter 3**.

Chapter 4 starts by listing the design requirements for the NeuRoboScope system. This is followed by the conceptual design of the robot mechanisms of the system. A systematic selection between the two proposed mechanisms is discussed. Then, the kinematic and dynamic modeling of the selected active arm, which is also denoted as the parallel arm mechanism, are presented. The passive arm mechanism is introduced.

In **Chapter 5**, general mechanical safety features are listed for the robotic systems in MIS. Then, some specific adaptable safety features are proposed that are related to the active and passive arms of the NeuRoboScope system including kinematic synthesis and gravity compensation solutions.

In **Chapter 6**, safety factors and the use of systematic standards in the design of safety-critical surgical robots are presented. Several control safety features for surgical robots in MIS are listed and discussed.

A novel optimization technique is presented in **Chapter 7**. This optimization solution was applied to the kinematic synthesis of the passive arm. First, a brief description of the problem of optimization, the objective, design constraints, and design parameters are identified. Then, the results are discussed with conclusions.

The optimization of a compact partial gravity compensation solution is discussed in **Chapter 8**. The optimization is carried out by using the particle swarm optimization method for the parallel active manipulator. First, a brief description of the problem of optimization, the objective, design constraints, and design parameters are identified. Then, the results are given with discussions and conclusions. **Chapter 9** concludes all the works done in this dissertation.

CHAPTER 2

BACKGROUND ON SURGICAL ROBOTS

In the healthcare sector, robots have been employed for a wide variety of functions as can be seen in Figure 2.1. One categorization is for the healthcare outside medical centers and hospitals, usually for personal needs such as: social robots, home care servant robots, assistive exoskeletons or prosthetic robots, medical service delivery robots for medicines supplying organizer, and person carrier robots for disabled or elderly people. On the other hand, there are more sophisticated functional robots to provide services inside medical centers and hospitals. These robots have been used for functions such as: training and accelerating the process of recovery, for nursing robots, rehabilitation robots, and patient positioning. The role of robots in the healthcare system is increasing dramatically. Robotics can participate in many sectors in the healthcare system from logistics to dealing with biohazards at laboratories. There are many evidences show the shortages in medical staff people especially in catastrophic and pandemic situations. Sometimes shortages can be represented in talents when it comes to specialists in the operation room (OR).

The core and the most advanced category in medical robots is the robotic system used in surgeries. These types of surgeries are defined as Robot Assisted Surgery (RAS). RAS involves the use of a robot in general under the guidance and the direction of a surgical team. An introduction to medical robots used in RAS is the topic of this Chapter. Some known robotic systems in RAS and MIS are introduced in the next section. Then a focused review on the literature for studies of robots that used to hold and position the endoscope in MIS in general and endonasal endoscope surgeries in specific.

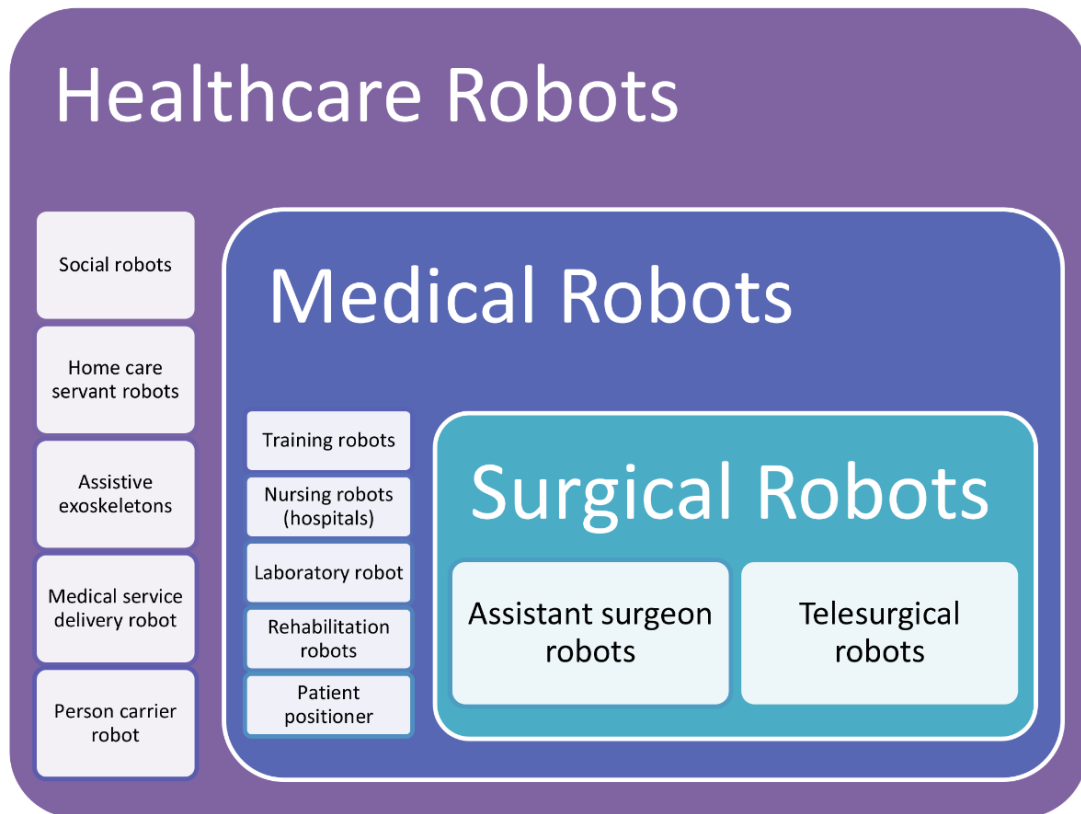


Figure 2.1. Classifications of healthcare robots.

2.1. Surgical Robotic Systems

Many hospitals started adapting RAS and force the surgeons to integrate these new facilities in their surgeries. In fact, using RAS can protect the surgeons in case of surgery complications in courts. Nevertheless, RAS systems are usually sophisticated and relatively expensive systems in training, in operating, and in supplementary and maintenance. As a result, surgeons are still looking for the use of RAS systems in which the surgical robot can cooperate with the surgeon on performing a specific task in the surgery. There are many advantages of using robots in surgeries. The most significant advantages are:

- The capability to perform surgery on a reduced scale (microsurgery)
- Improving precision, accuracy, and providing more dexterity (stereotactic surgery)
- Access through small corridors (MIS)
- The ability to process large amounts of data (image-guided surgery)
- Recording operation data for archiving

- The ability for telesurgery (for long-distance access or dangerous zone)
- Decreasing the surgeon's physiological tremor and fatigue
- Reducing the members of the surgical team required in each surgery to free them to other surgeries
- Performing with minimal invasive contact with the patients
- Reducing complications in operations and warranting faster recovery
- To minimize surgery time

As an outturn from these advantages, surgical robots may provide more safety for the surgery which is the main objective of the present dissertation.

The surgical robotic systems can be categorized into two main categories depending on the surgeon's position in the surgery. The first category can be identified by "surgeon-off the patient's site". In this category, the surgeon is on a control console (the master teleoperation side) to telemanipulate the surgical robot system with usually multiple robotic arms. For some other surgical robots, a single, usually flexible, robot arm. In these systems, the surgeon delivers and manipulates surgical tools and controls the vision camera (some with 3D vision endoscope) during the surgery. The second category is "surgeon-on the patient's site". In this type, the surgical system used to cooperate alongside the surgeon during the surgery. Generally, the robot doesn't directly perform the surgery but helps the surgeon with similar functions of an assistant surgeon or a nurse. One example is holding and positioning the endoscope during the surgery and giving the surgeon a clear and stable view of the surgery. These two categories of surgical robots can be subclassified based on the way the surgeon interacts with them.

2.1.1. Supervisory-Controlled Systems

The surgery in this type is planned earlier and the surgeon sets up the tasks to be carried on by a robot. The robot performs the same tasks automatically throughout the operation (autonomously). In this type of surgical robotic system, the surgeon is off the patient's site. However, the surgery to be performed is under the surgeon's supervisory to guarantee that there are no faults. An example of existing robots in this category is the TSolution[®] One Surgical System. In this system as shown in Figure 2.2, the TPLAN software program receives and converts the CT scan of the hip or knee joints into a 3D

graphical model. The surgeon preplans the procedure of implantation with respect to landmarks on the bones. Then the TCAT[®] with its milling tool will follow the preoperative plan on the bone with the surgeon's guidance exactly the way was planned for. A fully autonomous operative robot is a challenge, a partially autonomous surgical robot can be seen in bones and hard structures of the body. But when it comes to performing autonomous surgeries by robots on soft tissues it is still a challenging task and still a hot topic for researchers such as the STAR robotic system in the evaluation of preclinical studies (Hsieh et al., 2020; Rojas-muñoz, Cabrera, and Lin, 2020).

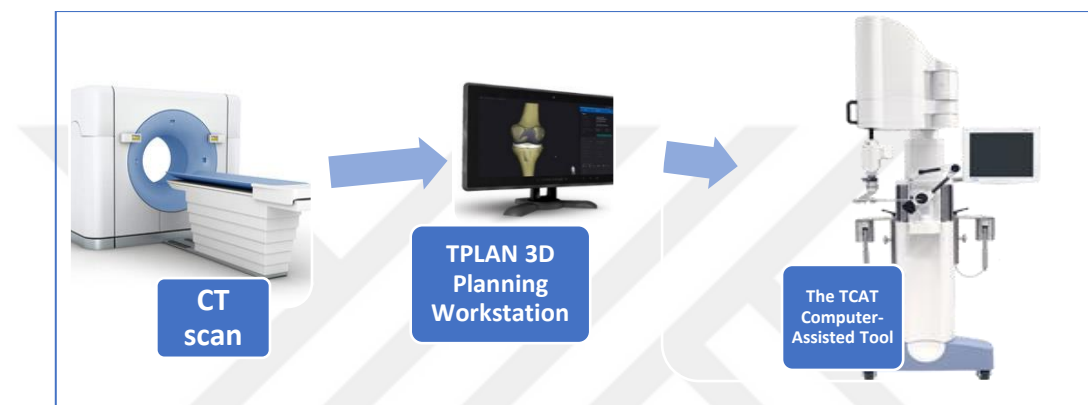


Figure 2.2. The TSolution[®] One Surgical System.
(Source: Think Surgical, 2020)

2.1.2. Telesurgical Systems

The surgeon directly performs the operation with a haptic interface through a teleoperation system. Mostly by using a force feedback master control (haptic interface). The surgeon is able to see inside the surgery zone with real-time intraoperative imaging while carrying out motions that the surgical manipulator replicates. The surgeon is able to see inside the surgery zone with real-time intraoperative imaging. Most of the robotic surgical systems that are approved and used extensively in many surgeries belong to this type. The Da Vinci systems in Figure 2.3. are important examples to be listed under this category since the earlier Da Vinci surgical system has been in ORs for many years and performed a large number of successful surgeries. Probably most of the credits for being so popular, regardless of being does not provide force feedback at the master part Figure 2.3.d, is its dexterity which is satisfactory to its unique applications. Other than this system, there are many

other important examples that serve the same function with force feedback at the surgeon side like the Senhance[®] Surgical System in Figure 2.4, the Versius[®] surgical robotic system shown in Figure 2.5 that also provide impedance control and physical Human-Robot Interaction (pHRI), and the DLR MiroSurge[®] system in Figure 2.6.

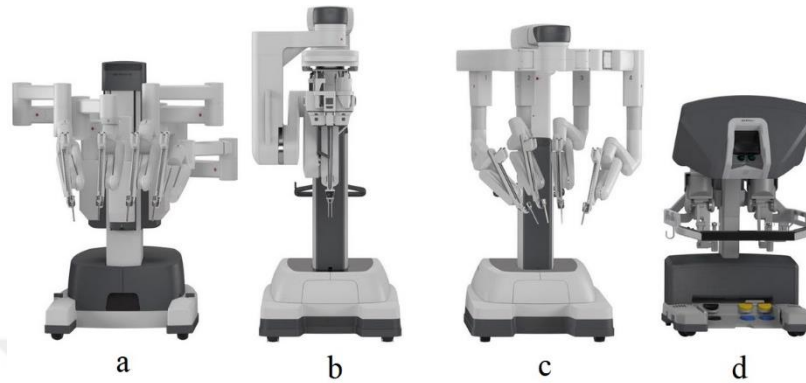


Figure 2.3. Da Vinci[®] surgical systems, a) Da Vinci x[®], b) Da Vinci SP[®], c) Da Vinci XI[®], d) Surgeon console. (Source: da Vinci Robot, 2019)



Figure 2.4. Senhance[®] surgical system Telelap Alf-X.
(Source: Senhance Surgical, 2020)

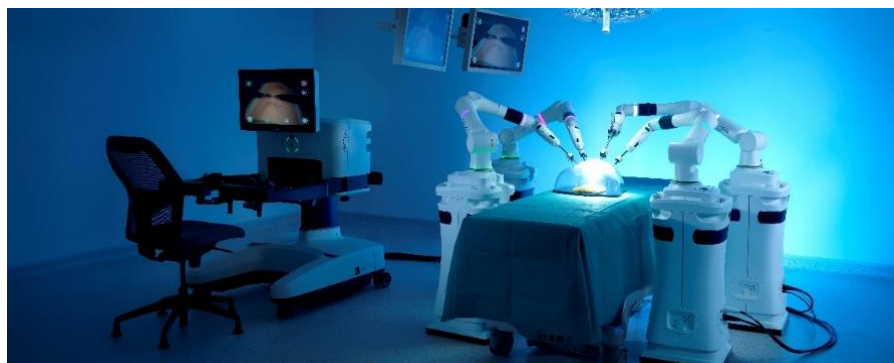


Figure 2.5. The CMR surgical, Versius[®] surgical robotic system.
(Source: CMR Surgical, 2020)

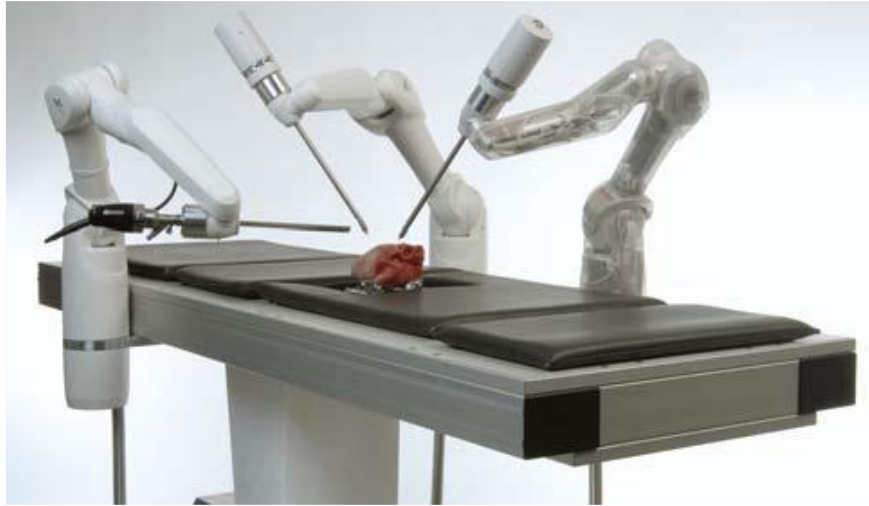


Figure 2.6. The DLR MiroSurge[®] system.

(Source: Hagn et al., 2010)

2.1.3. Shared-Control Systems

In these systems, the robot undertakes steady-hand manipulations of the surgical instrument while the surgeon controls the whole procedure. The surgeon and robot are jointly performing tasks together. Mainly, the end-effector of the robot to be used as a guidance or a trocar of the surgical tools. Such a robotic system can be seen in the Flex[®] Robotic System shown in Figure 2.7. In this robotic system, the single-port access for TransOral Robotic Surgery (TORS) is acting as a guide for the surgical tools to be used manually by the surgeon. As another example, the MAZOR X[®] surgical system shown in Figure 2.8.a which is used for spinal surgery. This surgical system performs the preoperative plan with the intraoperative 3D imaging with the guidance of the surgeon for the precise positioning of spinal implants. Another example of the same idea with a compact and frameless structure was introduced as the next generation, the Mazor[®] Robotics Renaissance as shown in Figure 2.8.b. Other examples for such types of surgical systems are ROSA ONE[®] for the brain, ROSA[®] Knee, and MAKO[®] Robotic-Arm for knee surgery shown in Figure 2.9.a, Figure 2.9.b, and Figure 2.10 respectively. Each one of these surgical robots acts as a navigational system of the surgical tools for the brain and hip/knee joints that allow the surgeon to apply an instrument on the right and accurate position. In general, the surgeon controls the position of the assistant robots in the preoperative period then the robot arm control surgeon's tools during the intraoperative period.



Figure 2.7. Flex[®] Robotic System.

(Source: Medrobotics, 2020)



Figure 2.8. The MAZOR systems, a) MAZOR[®] X (Source: Brian Feroldi, 2017), b) Mazor[®] Robotics Renaissance. (Source: MAZOR, 2020)

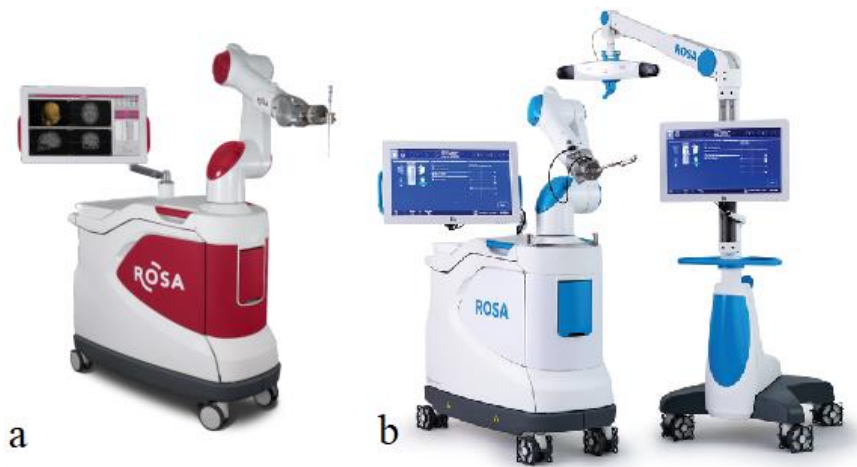


Figure 2.9. The ROSA systems, a) ROSA ONE[®] brain system, b) ROSA[®] knee system.

(Source: ROSA, 2020)



Figure 2.10. MAKO[®] Robotic-Arm Assisted Surgery.

(Source: Stryker, 2020)

2.1.4. Cooperative Systems

In these systems, the robot arm is generally employed as a holder of the endoscope or the laparoscope. During the surgery, the surgeon manipulates the instruments meanwhile he/she controls the necessary motion of the camera system (endoscope or laparoscope) intuitively. The surgeon and robot are cooperatively performing surgical tasks. An example is a surgeon-controlled robotic system shown in Figure 2.11 called KINEVO 900[®] that enhances surgical visualization and assists the surgeon to visualize structures accurately and easily. In Figure 2.12, EMARO[®] the pneumatically driven robot manipulator is used to guarantee a smooth and steady endoscopic view during surgeries. AESOP[®] shown in Figure 2.13 was the first robot that assists surgeons by manipulating the laparoscope inside the patient. The surgeon was able to direct the laparoscope via voice control commands.



Figure 2.11. The Robotic Visualization System KINEVO 900[®].

(Source: ZEISS Medical Technolog, 2020)



Figure 2.12. EMARO®.

(Source: RIVERFIELD, 2020)



Figure 2.13. The AESOP® system.

(Source: Nathan et al., 2006)

2.2. Background on Robotic Endoscopic/Laparoscopic Surgery

Many studies have produced several systems that can apply robotic principles to laparoscopic/endoscopic surgeries or MIS. There are two main different RAS systems involved in endoscopic assistance in MIS: a “Telesurgical system” is obtained when the robotic systems operate directly on the patient and the surgeons teleoperate and visualize the operation from a control console; a “Cooperative system” is obtained when the robotic systems are working alongside the surgeon in positioning and holding the endoscope during the surgery.

The focus here will be for robots that collaborate with the surgeons by holding and manipulating the endoscope in an active way during the surgery. Respecting mechanical design and structure, it is impossible to isolate the robot assisted systems for laparoscopic and endoscopic surgery. The endoscopic surgery referred to rhinoscopy (nose) while laparoscopic surgery referred to as laparoscopy (abdomen), and cystoscopy (urinary bladder). All these types of surgeries underly to MIS systems. It is needed to be cleared that the endoscope mentioned in this dissertation is referred to as the rigid endoscope.

Telesurgical robots are used widely in minimally invasive laparoscopy and cystoscopy surgeries. In those surgeries, the surgeons utilize an active laparoscope robot holder embedded in the robotic system and control it by the control console alongside the telesurgical tools. Those robotic systems are expensive in general. As an alternative, relatively lower cost surgical systems were developed but those robotic systems work cooperatively with the surgeon by holding the laparoscope while the surgeon is doing the operation. To this day, the most widely used commercially available robotic systems for MIS are the Da Vinci[®] system and the Medrobotics Flex[®] system. These robotic systems have dimensions and ergonomics specifically authorized for the laparoscopy and cystoscopy in Da Vinci[®] system and TORS in Medrobotics Flex[®] system. In fact, they have not been designed for FESS and they show several limitations when employed for ESBS (Bolzoni Villaret et al., 2017). These limitations make them unsuitable for this type of surgery.

In ESBS until present no robotic system developed specifically for this type of surgery. This is because that this surgery is different from laparoscopy and cystoscopy surgeries in: the surgical tools and the endoscope enter through the nostril together, surgery zone and its workspace are limited relative to the other types of surgeries, single and unique insertion port (single-port), various types of tools used in this surgery such as aspirator, drilling tool for bones, etc., and finally, no trocar used. With all of these constraints, some new Single Port Access (SPA) surgical systems have been designed to advance their technology for new areas of surgical procedures. But their systems still have a limitation which is having a wide insertion port in general that makes them inapplicable for SBES (with diameter equals 25 mm for the Da Vinci SP[®] as presented in Figure 2.3.b, and for TITAN Medical's SPORT[®] Surgical system). Some other systems do not have the rigidity that is enough for drilling the bones. Some other prototypes with smaller diameters of continuums are presented in recent works such as:

the Quadramanual robot arms with 15 mm, 35 mm workspace and 24 degree-of-freedom (DOF), 4 mm diameter by Swaney et al. (2012); The Concentric tube robot (CTR) with the multi-arm manipulator of 3 mm diameter by Wang et al. (2020). In their system, dual-arm robotic system for maxillary sinus area with 5 mm biopsy end-effector and 4 mm flexible endoscope end-effector to be arranged with 1 mm apart and within a total 10 mm outer diameter proposed by Yoon et al. (2013). Many approaches have been investigated for endonasal surgeries include transnasal navigation of the sinuses and biopsy, transnasal skull base surgery, and transnasal micro-surgery of the upper airways. A brief review was done by Orekhov et al. (2019) for snake-like robots. For the pituitary tumor removal by continuum robot, reachability and removal performance in a phantom pituitary tumor resection in anatomical skull models has been evaluated experimentally in (Swaney et al., 2015). In this dissertation, continuum robots are not the focus and the review will be concentrated on the actively controlled endoscope holder robotic systems.

A review of 27 different endoscopic and laparoscopic surgical robots developed between 1994-2009 was written by Taniguchi et al (2010). Only eight of them were able to get the technical and medical approval and commercialization to be used on patients. The other systems were proposed as a model for preclinical studies. Generally, most of these systems make use of a commercial endoscope that is directed by a robot arm.

A classification provided for the systems according to "compact and lightweight", "cleanliness" (respecting to the ability of sterilization) and "usability". As shown in Figure 2.14 just three of them satisfy all items, endoscope robots satisfying two out of three items are seven. Among those conditions, safety has the greatest importance when designing a surgical robot. Depending on these design keys, Taniguchi et al. (2010) designed a 6-DOF Stewart-Gough Platform as an endoscope holder (but not for FESS) with the focus on safety features. Some of these systems have been upgraded and some of them were expensive and not widely used. Some other systems are utilizing a flexible endoscope that is out of the scope of this dissertation.

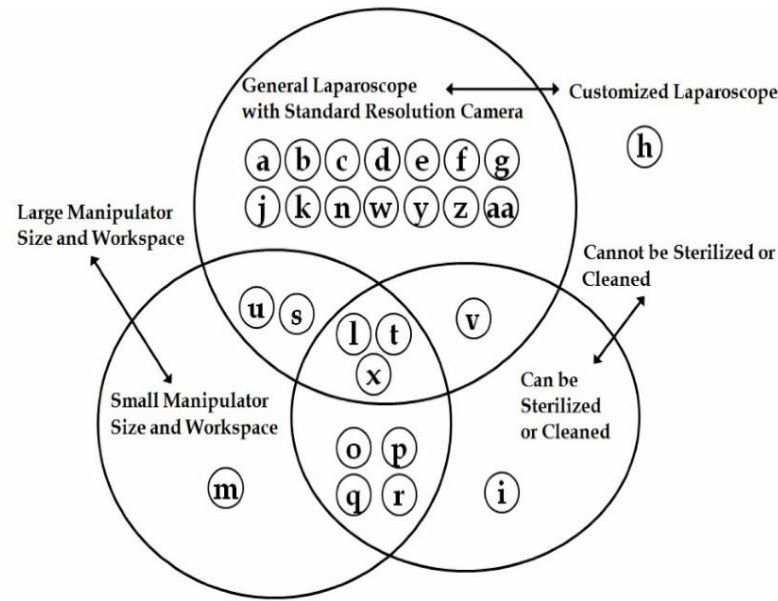


Figure 2.14. Classification results of characteristics of endoscope robots and manipulation: a) A460 CRS Plus, b) AESOP, c) LARS, d) EndoAssist (Endosista), e) Staubli Rx60, f) ERM, g) LapMan, h) RES, i) Naviot, j) PASEO, k) HISAR, l) ViKY (LER), m) 5-DOFs Laparoscopic Assistant Robot (KaLAR), n) FIPS, o) Imag Trac, p) Wide-Angle View Endoscope, q) Dual- View Endoscopic System, r) Automatic Tracking And Zooming System, s) COVER, t) P-arm, u) FreeHand, v) Robolens, w) Swarup Robotic Arm (SWARM), x) MST Laparoscope Manipulator, y) ROBOX, z) FELIX, aa) Paramis. (Source: Taniguchi et al., 2010)

2.3. Background and a Review on Robots Designed/Applicable for Endonasal Surgery

Trévillot et al. (2013) published a review paper on robotic endoscopic sinus and skull base surgery. In their paper, a focused review of robots dedicated to endonasal endoscopic surgery was presented. Most of the robots that appeared in the review were used in endonasal surgery on cadavers. Advantages, disadvantages, limitations, and risks related to the systems with respect to usability, dimensions of the robots, footprints in OR are discussed as can be seen in Table 2.1. In this table, a comparison between the systems depending on the year of development, mechanical structure, set-up time, safety, type of control interface, and some other aspects were presented.

Table 2.1. Summary robot table devoted to the endonasal surgery.
(Trévillot et al., 2013)

	Nimski	Nathan	Wurm	Strauss	Xia	Eichhorn
Robot name	Evolution 1	AESOP	A-73	None	None	Tx40
Year of development	2004	2005	2005	2007	2008	2011
Mechanical structure	Parallel M-800, Physik instrument PI, Waldbronn, Germany	7 degrees of freedom arm	Arm RV1A (MitsubishiElectric) 6 degrees of freedom	Arm PA10-6c, (Mitsubishi) 6 degrees of freedom	Neuromate Robot (Renishaw Mayfields, U)	Arm
Type of instrument	Endoscope	Endoscope	Neuroptik T30* (endoscope, drill and operating channels)	Endoscope	Drill or endoscope	Endoscope
Instrument diameter	4 mm	3 mm	5 mm	4 mm	Variable	4 mm
Set-up time	30 minutes	Several minutes	Long	Less than 20 minutes	Long	Unknown
Work space occupied	Major	Major	Major	Major	Major	Major
Precision of repetition	20 μ m	50 μ m	20 μ m	850 μ m	1 mm	Unknown
Type of control interface	Joystick	Voice-controlled	Joystick	Joystick	Co-manipulation	Joystick and automatic tracking
Safety	Satisfactory	Satisfactory	Satisfactory	Satisfactory	Satisfactory	Satisfactory
Specific characteristics	Maximum workspace: 160 \times 60 \times 100 mm Three different speeds: 0.5, 1, 2 mm/s Maximum force: 250 N	Integrated navigation system	Length 226 mm, Visual field: 105° Four channels: one for the scope, one for the drill and two for suction/irrigation Speed: 2100 mm/s Integrated navigation	Integrated navigation system	Integrated navigation system It defines the work space into three zones A forbidden zone limits A boundary zone A safe zone	Automatic washing of the endoscope lens

Another important review by Bolzoni Villaret et al. (2017) provided a literature review for robot assisted ESBS. This review constituted on papers published between 2004 and March 2016 highlighting the following items: interface, tools under robotic control, force feedback, safety systems, setup time, and operative time. However, in this dissertation, all the previously provided reviews and the very recent updated review provided in (Madoglio et al., 2020) and (Bolzoni Villaret et al., 2017) have been utilized and modified by excluding flexible endoscope solutions (including single-port entry). Also, some of the laparoscope robot holders that can be considered convenient to ESBS and transnasal sinus surgery have been added. This is a personal statement that represents personal opinion depending on the mechanical structure, sterility, safety features, footprint and the dimension of the mechanism. The applicability of such systems on the ESBS with respect to those key requirements needs to be validated by preclinical studies before any integration in the OR.

Many more databases in addition to Pubmed, Scopus, and Google scholar in this survey have been used for the review since the beginning of the NeuRoboScope project to the date of issuing this dissertation. The focus in the review of the works in the literature is in the mechanical design, footprint, and layout in OR, control algorithms (user-robot interfacing), type of surgeries performed, and mainly and most importantly on safety features developed in these works and devices are presented in Table 2.2. In the table RCM stands for remote center of motion.

In this list, many different prototypes are presented which are dedicated structures to endonasal endoscopic surgeries of different types named as: FESS, ESBS, transsphenoidal endoscopic surgery, and paranasal. Some of those systems are commercially available, and few are originally designed for other types of surgeries. Next are the introductions of the systems presented in the list.

Table 2.2. Robotic endoscope holders for FESS and ESBS

	Reference	Systems name	Type of control interface	Applied task	Safety features	Tests	Type of mechanism
1	(Nimsky et al., 2004)	EVOLUTION1	Joystick control	Transsphenoidal endoscopic surgery	Tracked by a navigation system	Phantom testing & patients	Hexapod
2	(Wurm et al., 2005)	A73	Automatic Joystick & optical tracking system	Perforation of the sphenoid sinus, puncture of the sphenoid sinus / paranasal sinus surgery	3D navigation system and redundant navigational control "loss of control" mode	Specially designed phantom model	RV-1a articulating arms Robot by Mitsubishi
3	(Nathan et al., 2006)	AESOP	Voice control	Endoscope holder / transsphenoidal approach to the pituitary gland	Three saved positions, vocal command "stop", redundancy in commands, a degree in autonomy	Cadavers	A 7-DOF & passive joints serial arm
4	By Strauß et al. (Strauß, Mathias, et al., 2007)	None	Joystick	Endoscope holder / FESS	Integrated navigation system, Easy to unfasten the endoscope, switch to manual endoscopy	Anatomical model	PA10-6c, Mitsubishi robot arm
5	(Xia et al., 2008)	None	Admittance	Endoscope or drill holder / FESS and ESBS	Visual servoing, an Integrated navigation system, forbidden zones	Phantom head model	Industrial robotic arm
6	(K. W. G. Eichhorn and Bootz, 2011)	Tx40	Joystick and autonomous tracking movements	Endoscope holder for SBES	Navigation system for different predefined zones	Phantom tests	6-DOF industrial robotic arm
7	(Fischer et al., 2011)	Endoscope Manipulator System (EMS)	Joystick	Endoscope holder for FESS	A quick attaching and release of the endoscope, Optimum power-weight ratio, Small size-specific for FESS	Phantom test	Two of five-bar planner manipulator at two offset planes
8	(Trévillot, Sobral, et al., 2013)	Hybrid	Admittance Co-manipulation mode	Endoscope holder for FESS	Force threshold security for a shutdown.	Cadaver tests	6-DOF industrial robot & passive gimble
9	(Çabuk et al., 2015)	SP (Stewart Platform) Robotic System	Joystick	Endoscope holder for ESBS	The resistance felt on the haptic arm for contact and friction with tissues	Cadaver tests	6-DOF Stewart platform with a prolonged end-effector
10	(Chan et al., 2016) (Lin et al., 2015)	FREE	Inertial measurement unit and vocal control	Endoscope holder for FESS	Force threshold for shutdown, vocal control, easy release of the endoscope	Phantom and cadaver tests	5-DOF passive and 4-DOF active arm

(cont. on next page)

Table 2.2 (cont.)

11	(Bolzoni Villaret et al., 2017)	BEAR	Head control (marked glasses)	Endoscope holder for ESBS	Multi-objective programs utilizing force sensor	Phantom tests	Industrial manipulator
12	(Madoglio et al., 2020)	Medineering® EndoscopeRobot	Foot pedal	Endoscope holder for ESBS	A commercial product, Home position saving, Avoidance of tissue contact	Commercial product Preclinical and Clinical tests,	Hybrid 7-DOF active positioner & 5-DOF active holder
13	(He et al., 2016), (He et al., 2019)	None	Main tool optical tracking control / admittance control	Endoscope holder for FESS	Virtual fixture, Force feedback, Admittance control, optical positioning	Phantom tests	7-DOF RCM double parallelogram
14	(P. Li et al., 2013)	None	Foot pedal and voice control	Endoscope holder for nasal surgeries	Safe Force threshold & passive safety mechanisms	Phantom /animal head/ human cadaver tests	4-DOF passive poisoner & 4-DOF active robot (RCM)
15	(Medtech S.A, 2020)	ROSA™	Foot pedal for activation & haptic master (admittance control)	Tool / Endoscope holder for nasal surgeries	Virtual fixture for a preprogrammed path (security zone feature)	Commercial product Clinical tests	Surgical Robot arm
16	(Freehand, 2015)	Freehand®	Headset and foot pedal	Laparoscope holder	Lightweight, Single-use of some parts for safety, RCM mechanism	Commercial product	Passive and compact RCM active arm
17	(Zhong et al., 2019)	FREEDOM®	Foot control	Endoscope holder for FESS	Passively compliant endoscope holder (PCEH), RCM mechanism, speech recognition	Commercial product	Passive 6-DOF and 3-DOF RCM active arm

- **EVOLUTION 1**

Nimsky et al. (2004) described the application of EVOLUTION 1 prototype, shown in Figure 2.15, to transsphenoidal endoscopic surgery. The prototype was initially developed for ventriculostomies and then adapted for transsphenoidal endoscopic surgery. In terms of its mechanical design, EVOLUTION 1 is based on a hexapod structure (Stewart platform) design with an additional translational axis which was designed for instrument holding. In this system, the surgeon uses a joystick to control the Stewart platform plus the additional linear axis which adds up to 7 DOF. Later, some necessary safety features to make it applicable to transsphenoidal surgery were implemented on the systems such as: the RCM at pivot-point, a quick interchange between robot-controlled endoscopic and manual holding, navigation system for tracking the endoscope, and a modified endoscope holder. This prototype was reported to be relatively large in terms of its dimensions.



Figure 2.15. EVOLUTION 1.
(Source: Vougioukas et al., 2003)

- **A73**

This robotic system was established for paranasal sinus surgery by Wurm et al. (2005). This robotic system, shown in Figure 2.16, is not designed for holding the endoscope. Instead, it punctures the sphenoid sinus' anterior wall in a fully automated method without damaging the surrounding (using a special endoscope with a drill at its end). To increase its safety, the authors installed a redundant tracking navigation system. This safety feature was not intended to increase navigation accuracy but to add potential safety features to the system. The system has a function named “loss of control” which can be considered as essential since its maneuvering is fully automated. By this function, real-time navigation feedback and robot navigation were integrated into one user interface. In case of navigation failure, the task was intended to shut down and the force/torque (F/T) sensor to be activated for softening articulated joints. Instead of the older version that was built in the concept of “all in one”, they built a modular three-component setup. Another redundancy is adding a remote-control input to correct the trajectory when needed. The main disadvantage as reported was its relatively large size (Bolzoni Villaret et al., 2017). Also, it is not tested in operations except anterior sphenoidotomy.



Figure 2.16. The A73 system.

(Source: Wurm et al., 2005)

- **AESOP**

Automated Endoscopic System for Optimal Positioning (AESOP[®]), as presented in Figure 2.13, is a commercial 7-DOF serial robotic arm gained popularity in many laparoscopic surgeries by holding a rigid endoscope and assisting the surgeons. Later, it was integrated into ZEUS[®] alongside with two tool manipulating robotic arms for telesurgery. There are plenty of studies for evaluating the AESOP[®] system in laparoscopic surgeries. However, one interesting research work was carried out by Nathan et al. (2006) for evaluating the feasibility of AESOP[®] in the transsphenoidal approach to the pituitary gland. By using this robotic system, a two-handed ESBS technique on ten fresh cadavers was conducted via controlling the endoscope direction through continuous or incremental voice control commands. The AESOP[®] system can also be controlled by foot or hand. The voice control interface has a feature of saving three positions that allow the robot to be returned to any of them by single voice command. The study concluded that this voice-controlled endoscope holder can be considered safe and has many advantages such as the ability to translate between three memorized vision settings, being tremor-free that allowed neighboring the endoscope near target organ with fewer collisions, manual shut-off by voice command or stop button, and the automatic shut-off provided by a pressure sensor.

- **Strauß et al.'s System**

Strauß et al. (2007) studied the usability of a telemanipulated endoscope holder assistance system for FESS by using the robot arm PA10–6c by Mitsubishi. Many trials were done for comparing automated endoscope holder with manual endoscope holder in

terms of maximal forces within FESS, preoperative planning time of workspace, and surgical precision and accuracy. As a safety feature, Strauß et al. designed a holder mechanism, as can be seen in Figure 2.17, to facilitate switching to a manual endoscope holder in case of an emergency (Bolzoni Villaret et al., 2017). Strauß et al. (2007) stated that from a surgical point of view, the improvement in the user-robot interface and the level of automation have greater importance compared to the improvements in the mechanical topology.



Figure 2.17. The robot arm PA10–6c with Strauß et al.’s designed holder mechanism
(Source: Strauß et al., 2007)

- **Tx40**

A research article was published by Eichorn and Bootz (2011) introducing the robot assisted endoscopy in FESS and ESBS using the Tx40 robot arm. The focus was on defining the working environment for Robot Assisted Endoscopic Sinus Surgery (RASS) of the anterior skull base and paranasal sinuses that can provide safety in visual servoing by following the tip of surgical instruments. Three different categorizations of the interior environment were proposed by the authors (1) FREE: for the region where the maximum endoscope speed is allowed, (2) SOFT: for soft structure contact that cannot be avoided, and (3) HARD for critical structures that can be considered as prohibitive zones. The system has automated lens cleaning capability. However, being an industrial robot arm the dimensions could limit the surgeon’s movements.

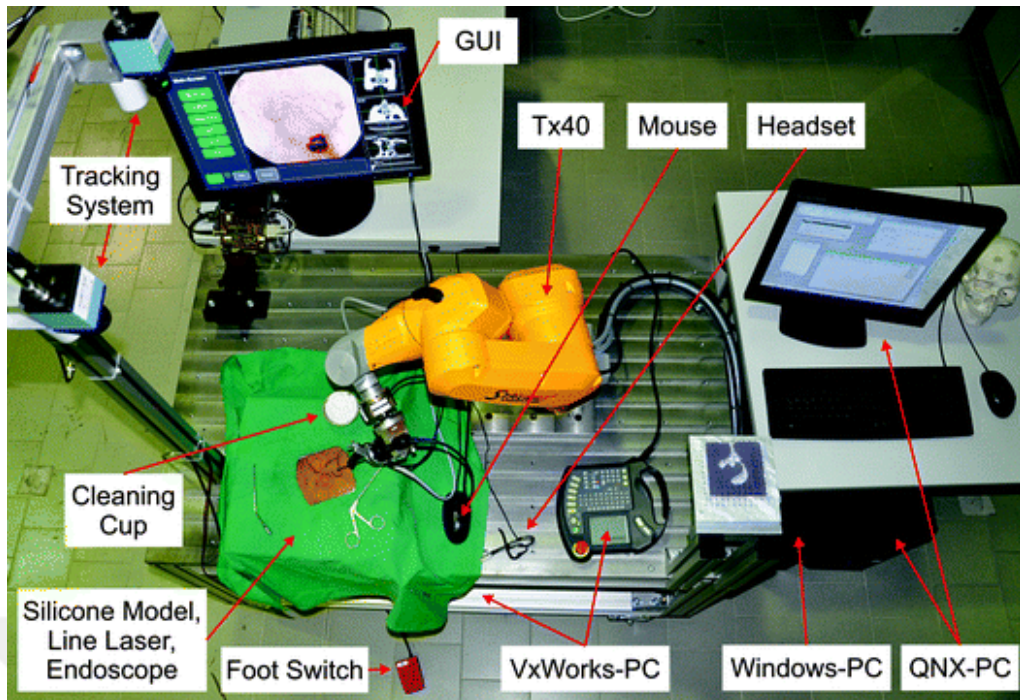


Figure 2.18. The Tx-40 for robot assisted endoscopy system
(Source: Eichhorn and Bootz, 2011)

- **Endoscope Manipulator System EMS**

Another endoscope manipulating prototype -developed for FESS by the MiMed Institute, Technical University Munich, Germany- has been examined on an artificial sinus model (Fischer et al., 2011). The EMS, as shown in Figure 2.19, consists of a passive fixing arm to carry the small active arm. The active arm has a linear module connected by two gimbal-mounted by parallel-switched 5-pivot gears. The user interface is two joysticks, one for linear endoscope movement (z-axis) and the other for pivoting and tilting in xy-plane.

To validate its feasibility, 60 tests for timing and positioning were done by the traditional technique and by EMS assistance for three target positions. It has been concluded the ability of integration of this system into the OR without prolonging endoscope guidance time. The focus of designing this system was on safety features like: a quick attach and release of the endoscope, optimum power-weight ratio, restriction of endoscope movement through the RCM. The authors concluded the best layout by the reach of the robot arm from behind the patient's head. It was reported that by this layout the surgeon's hands can have more footprint in the surgery zone.

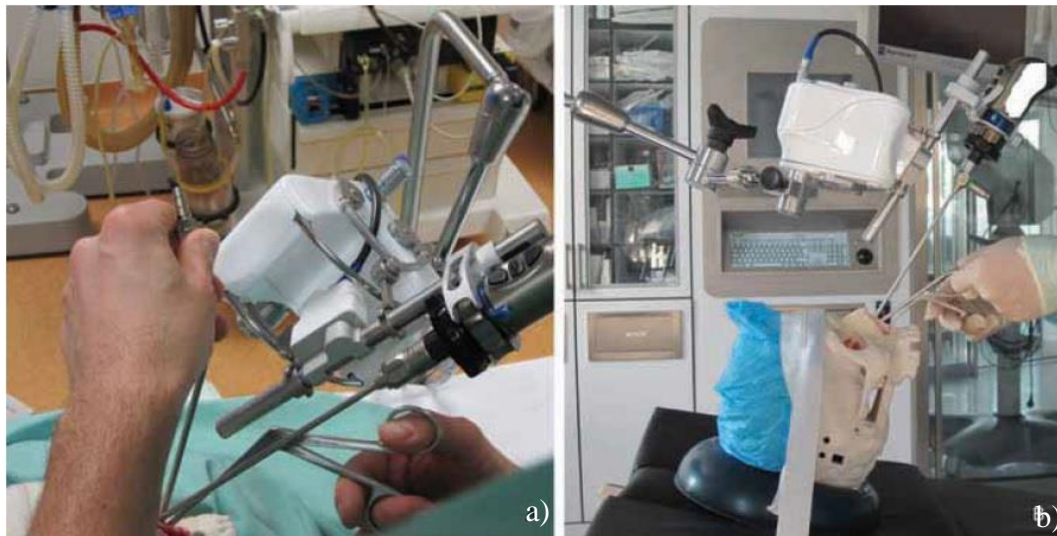


Figure 2.19. The Endoscope Manipulator System EMS with a different setup, a) beside the operation table, b) behind the operation table. (Source: Fischer et al., 2011)

- **HYBRID**

Trévilot et al. (2013) arose an important argument about whether the endoscope motion in FESS should be restricted about a specific point or not (the pivot-point). They have performed a practical test for motion and force analysis on cadaver heads to gather objective data. Then, three different mechanisms have been used on cadaver heads to perform an experimental comparative study to find out the best mechanism satisfying force and motion requirement. The first one was an RCM architecture, EVOLAP[®] (Herman et al., 2009). The second one was VIPER[®] the serial robot arm with the extended end-effector. The third one, shown in Figure 2.20.a, was a combination of VIPER[®] and the passive gimbal-like mechanism of EVOLAP[®] (Figure 2.20.b) attached to the extended end-effector of VIPER[®] arm (designated as HYBRID). They have proved that the entry point into the nostril cannot be considered as a fixed point such as the case in laparoscopic surgery, but the location of pivot-point mainly depends on the targeted sinus. Having a passive gimbal mechanism connected to a 6-DOF robot arm is considered to provide sufficient safety since the holding method of the endoscope is no more rigid. However, this method has disadvantages when applied to FESS since no fixed pivot-point exists (as the authors stated) then the image may not be stable when any external force is applied to the endoscope. Which is common for this crowded surgical workspace.

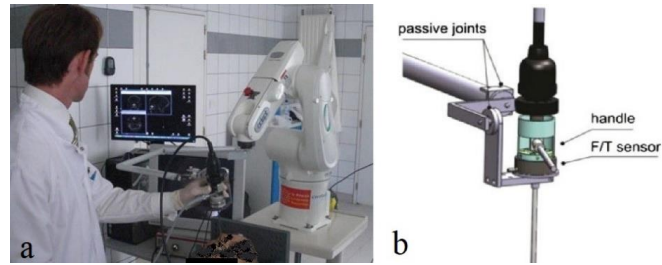


Figure 2.20. The HYBRID system, a) test scenario, b) the passive gamble holder
(Source: Trévillot, et al. 2013)

- **SP Robotic System**

A Stewart Platform with an attached passive arm endoscope holder, as shown in Figure 2.21, was developed at Kocaeli University, Department of Mechatronics Engineering. It was intended to be used in ESBS as an endoscope holder and positioner (Çabuk et al., 2015). The evaluation was done on an artificial model with a 6-DOF haptic device and a spatial mouse. The robot could change its position by an assistant to visualize sphenoid ostium, concha, and choana on six cadavers. The frictional contact with adjacent tissues was reported to be successfully felt at the master part. The disadvantages, which are similar to the one concluded by Trévillot, et al. (2013) in using the VIPER[®] robot arm, can be concluded as: the error in position due to the long attached end-effector holder, the time of mounting/unmounting the endoscope for cleaning, no rotational movement around the axis of the endoscope, and no RCM mechanical constraint. The other disadvantage that was stated by the authors was the control method by the assistant who is manipulating the endoscope by a haptic interface. Even though the assistant could feel the frictional forces at the master part, he/she needs to focus on both the remote endoscope at the patient side and the image at the screen.

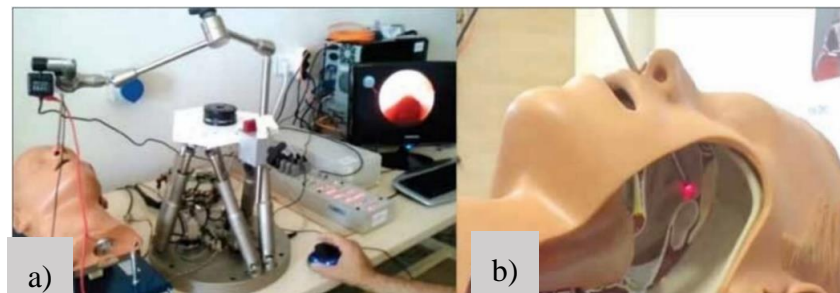


Figure 2.21. a) Stewart platform with the endoscope, b) Insertion of the endoscope to the artificial model (Source: Çabuk et al., 2015)

- **FREE**

The Foot-Controlled Robotic-Enabled Endoscope Holder (FREE) is a unique prototype designed for FESS (Lin et al., 2015). The system, as presented in Figure 2.22, consists of a 5 DOF, two rotational and three translational (2R3T), a passive arm holding an active 4-DOF (2R2T) robot arm with an RCM mechanism controlled by the foot posture. Its mechanical redundancy makes the setting up the task of bringing the endoscope to the nostril opening more fluent. Then, the active insertion of the endoscope can be performed by the surgeon's foot gestures utilizing an IMU sensor and the endoscope image feedback. Experimental studies were reported in (Chan et al., 2016; Lin et al., 2015) to validate the prototype robot's performance on cadavers. The advantages of the system are reported as: the user-robot interface was easy and intuitive that allowed the use of two hands surgery technique, the active system is relatively small, force threshold for shutting down the task was used, "start" and "stop" verbal commands were included, constant speed movement with no jerk or sudden movements, and easy removal of the endoscope can be done for cleaning, and for safety control, the sample time was selected to be the same for all components at the control units.



Figure 2.22. The FREE Endoscopic holder.

(Source: Chan et al., 2016)

- **BEAR**

Brescia Endoscope Assistant Robotic Holder (BEAR) is a prototype robot arm developed for ESBS (Bolzoni Villaret et al., 2017). The endoscope holder, as can be seen in Figure 2.23, was coupled with the 6-DOF industrial robot arm (RS03N, Kawasaki) through a force sensor positioned between them. For the surgeon-robot interfacing, a 6-Dimensional optical motion sensor was utilized to track the surgeon's head and sending motion commands to the robot. Preclinical tests for the feasibility of utilizing the system were reported.

In the BEAR system, the integration of the force sensor has many advantages to develop many features related to safety and the type of endoscope motion. Multi-objective programs were created to allow the industrial manipulator to perform many tasks and safety features so that it can be adapted to perform the surgical task. These programs and their functions are listed in (Bolzoni Villaret et al., 2017). Some programs are related to safety such as: the “DelicatedInsider” program has a function to control the position of pivot-point of the endoscope by analyzing forces exerted on the endoscope to keep them below the threshold, the “NewLeadingByNose” program is admittance control to lead the endoscope to the nose, and the “CarefulMovement” program is designed to stop the robot action and bring it to initial position after detecting force interaction beyond the assigned threshold. Being an industrial robot arm, the limitations are its excessive force and large size relative to the small surgical workspace of ESBS.

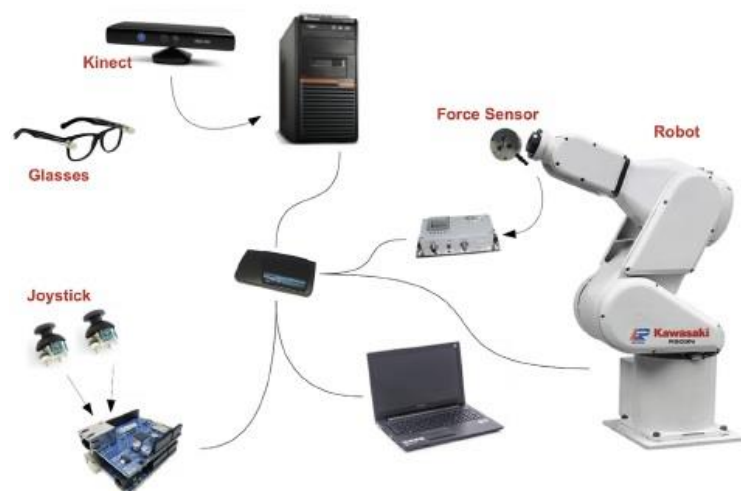


Figure 2.23. The BEAR system.
(Source: Bolzoni Villaret et al., 2017)

- **EndoscopeRobot® by Medineering**

The endoscope positioning robot system Endoscope Robot® by Medineering was developed for many surgeries including transnasal operations (Friedrich et al., 2017). This robotic system is a commercial product and received a CE mark from the European Commission (Mattheis et al., 2019). It has a hybrid mechanical structure, as shown in Figure 2.24, fixed on a surgical table that consists of a 7-DOF serial positioning robot arm and an attached hand of compact endoscope holding mechanism following the same concept of EMS by Fischer et al. (2011). This compact holding mechanism is responsible for the precise positioning of the endoscope. A commercial surgical foot pedal controller was utilized for user-robot interfacing which has the capability of saving positions. Many training tests were performed for ESBS and transnasal sinus by Friedrich et al. (2017) on cadaver heads. Patients' safety and feasibility of the system was also tested in eight patients for balanced orbital decompression through the nasal cavity by Mattheis et al. (2019). Recently, a preclinical evaluation of the system was done by Madoglio et al. (2020). This evaluation was performed by selected thirty skull base surgeons in two different dry-lab tasks. For assessment, the authors used the modified Global Evaluative Assessment of Robotic Skills in Endoscopy (GEARS-E) and completion times with and without EndoscopeRobot. In the evaluation of EndoscopeRobot in general clinical and preclinical tests, it has been reported that the surgeons prefer bimanual endoscopic surgeries. One reported criticism was that the robotic arm seems to be relatively heavy, so surgeons should get to be familiar with the system before using it (Mattheis et al., 2019).

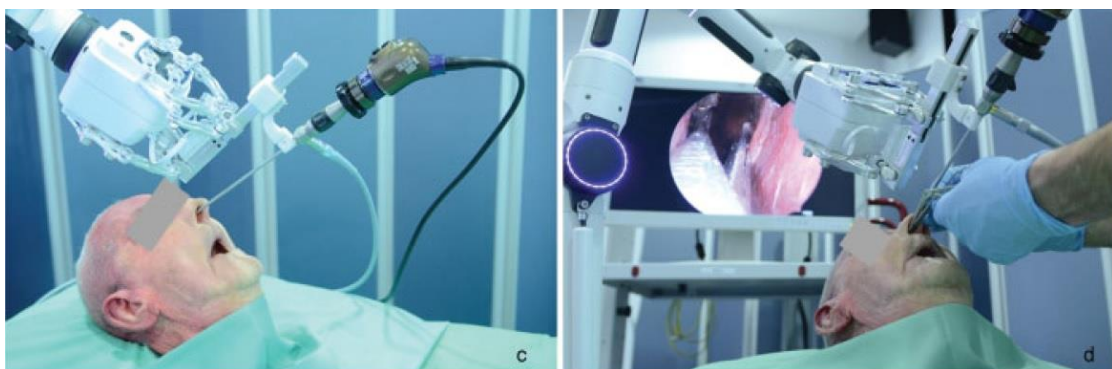


Figure 2.24. Insertion and visualization of the endoscope by EndoscopeRobot® by Medineering (Source: Friedrich et al., 2017)

- **Endoscope holding system by He et al.**

He et al. (2016) proposed a prototype, as shown in Figure 2.25, of an active robot arm with 7 DOF for positioning and orienting an endoscope in sinus surgery. The mechanism has the first three joints for compensation of the fourth joint and fifth joint (double parallelogram mechanism) to constrain pivot-point at the RCM and adjust the orientation. The sixth joint is for penetration motion along the endoscope's axis and the seventh joint is for rotation around the endoscope's axis. A F/T sensor was installed between the endoscope holder and the endoscope that shows an important role in this system. The system utilized a cooperative control method for the user-robot interface which is based on various types of virtual fixtures (VFs). The most interesting safety feature provided in this system is the use of VFs to provide safe motion of the endoscope during admittance control. He et al. (2019) have designed many types of VFs to be implemented specifically for endoscopic sinus surgery by dividing robot assisted endoscopic sinus surgery to stages. During tests on a model of "high-imitation head and fine anatomical structure", they have reported that the overall robot motion constraint method can improve the accuracy and safety of operation during endoscopic navigation. In addition to VF constraint, to avoid a collision, additional damping is used when the tip of the endoscope gets near to the nasal entrance. To realize the automatic tracking function, an optical positioning device (Polaris Vicra, NDI, Canada) was integrated into this system.

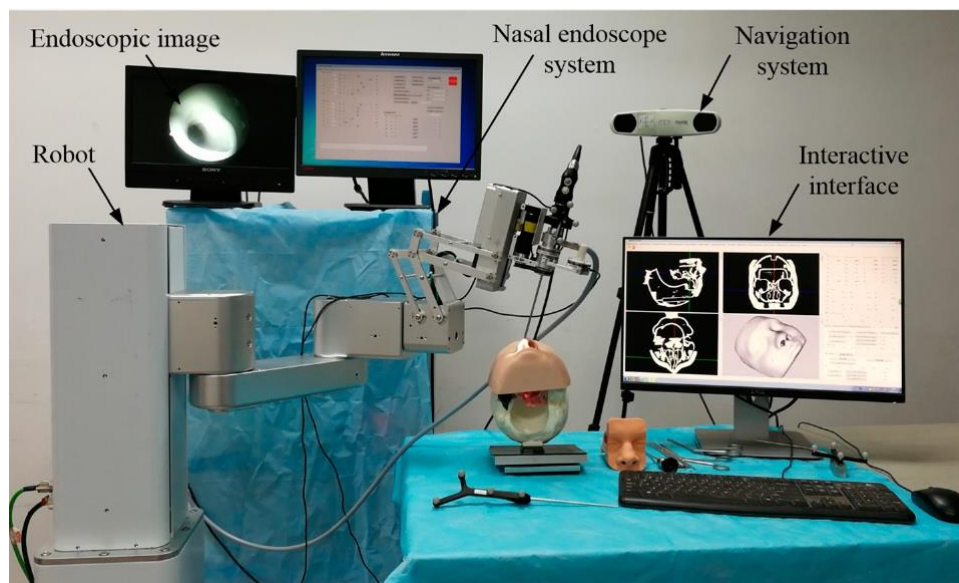


Figure 2.25. Robotic endoscope holder.

(Source: He et al., 2019)

- **Endoscope manipulator for nasal surgery by Li et al.**

Li et al. (2013) developed a custom 4-DOF wired-driven double parallelogram robot (generating an RCM) mounted on 4-DOF passive positioning platform, as shown in Figure 2.26, for nasal surgical procedures. To control the three orientation angles and the insertion depth, foot pedal and voice control interfaces have also been used to realize bimanual surgical technique. The interaction force between the tissues and the endoscope is monitored by the active force control algorithm to keep it within a safe threshold. The performance was also tested and verified on a phantom model, pig head cadaver, and human cadaver. Another important safety feature was the passive safety mechanisms that have been designed by Yip et al. (2015). The passive safety mechanisms, which limit the interaction force between the patient and the robot, were used in all DOFs of the robot. These safety mechanisms add a safety feature that can work as protection (i.e. mechanical force fuse) regardless of whether active safety control functioning or not. The passive safety mechanisms alongside the active force control algorithm intended to provide safety for the surgeons, the patient and the motors.

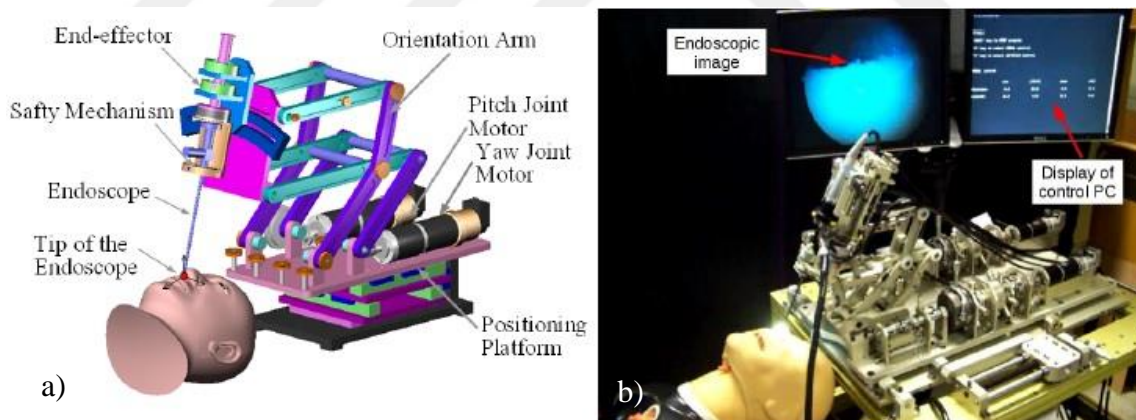


Figure 2.26. Endoscope manipulator for nasal surgery, a) the model, b) the prototype.

(Source: Li et al., 2013)

- **ROSA[®]**

Rosa is a commercial robotic arm used in joint replacement and in neurosurgery as presented previously in Figure 2.9. However, in the recently published product poster by the manufacturer, it has been stated the applicability for endoscope holding tasks, as shown in Figure 2.27, in Ventricular and Transnasal Neurosurgery (Medtech S.A, 2020). In this system, the surgeon preplans the surgery by predefining the initial

position of the endoscope with respect to the operation zone via ROSA[®]'s software. Then, at the start of the operation, the system brings the connected endoscope automatically into the initial trajectory. A foot pedal can be used to activate ROSA[®]'s “haptic mode” to manipulate the endoscope inside the constrained preprogrammed path and the “isocentric mode” constrains the path through entry port. The RCM is guaranteed by constraining the endoscope motion inside the preplanned cone which acts as a security zone. This is similar to the methodology followed by He et al. (2019) for their robotic surgery system. Another proposed safety feature is by giving a real-time endoscope position feedback with respect to the preoperative patient's anatomy to compensate for any limited visibility by the endoscope image.



Figure 2.27. The ROSA[®] system.
(Source: Medtech S.A, 2020)

- **FreeHand[®] v1.2 by Freehand Solutions**

FreeHand[®] v1.2 is a compact commercial endoscope controller that can be fixed on the operation table and has a footprint that is less than the surgeon assistant. The system is the next generation of ProSurgics[®], which was the second generation of the well-known EndoAssist[®] system. To the best of my knowledge, no one used it for ESBS. However, it has been indicated by the manufacturer (stated in its user manual) that the FreeHand is for use in “general laparoscopy, general thoracoscopy, general cardiothoracic surgery, nasopharyngoscopy, ear endoscopy, and sinuscopy, where a rigid laparoscope/endoscope is required.” (Freehand, 2015). This new generation is developed to be easier to set up, more compact in size, and considerably more

affordable than the previous generations. It has 3 DOF for an orientation around RCM and penetration for zooming. The active manipulator is attached to a simple passive positioning arm. The endoscope motion can be controlled by the surgeon's head motions, which are tracked with an optical system whenever needed by activation via a foot pedal. Many certified safety features have been considered in the design. As a safety factor of sterilization, some parts of the system are planned for single-use that allows also for fast set up for the next surgery with a simple replacement. Due to its structure and kinematics, it has potential for use in ESBS. However, preclinical and clinical tests can be done for feasibility evaluation to establish the use in ESBS.

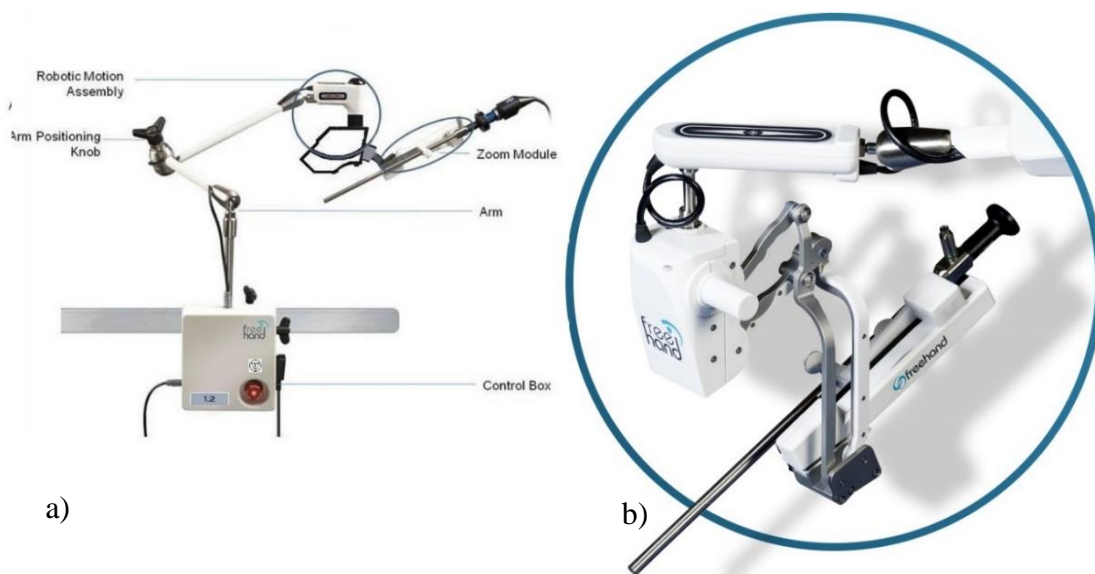


Figure 2.28. FREEHAND® a) the present commercial system V1.2, b) the next generation (not in the market). (Source: Freehand MIS Solutions, 2020)

- **FREEDOM®**

Following similar design methodology for developing the FREE system by Chan et al. (2016), Foot-controlled Robot-Enabled EnDOscope Manipulator (FREEDOM®) is another interesting robotic endoscope manipulator, presented in Figure 2.29, designed specifically for FESS by Zhong et al. (2019). Clinical considerations have been utilized in the design of this system to provide a safe and reliable endoscope manipulating with minimum restrictions. To ensure minimum interference with instrument manipulation, a 3-DOF active manipulator was designed with a rotational and arc-rack joint to produce RCM in a compact way. The active mechanism part was attached to a serial 6-DOF passive frame. This passive arm is

connected to a wheeled base and it can reach an operation table providing a space for the assistant surgeon. In addition to the user-robot interfacing by foot motion, the speech recognition algorithm was also present in the interface control loop. The surgical feasibility of the FREEDOM[®] system in FESS for endoscope manipulation has been investigated via the laboratory, cadaver, and clinical trials. These tests validated FREEDOM[®] system to be safe (according to IEC-60601-1). It is reported to have a relatively easy set up in FESS. In addition to the mechanical RCM, another introduced mechanical safety feature was the Passive Compliance Endoscope Holder (PCEH) which is the compliance connection mechanism between the robot and the endoscope body to avoid rigid endoscope-tissue contact.

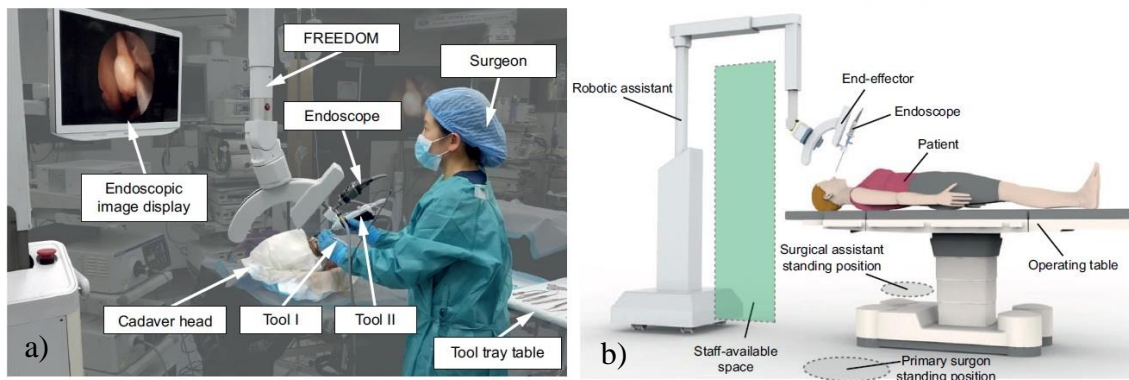


Figure 2.29. The FREEDOM[®] system, a) the prototype, b) the footprint of the system.

(Source: Zhong et al. 2019)

2.4. Discussions

Some other systems that have been designed for laparoscopic surgery such as the EMARO[®] by Hogy Medical Co. and the robotic endoscope holder MTG-H100[®] by HIWIN could also be tested and evaluated by surgical teams for their feasibility to be used in FESS. iArmS[®] by DENSO was designed to passively support the surgeon's forearm as introduced earlier in this Chapter as can be seen in Figure 1.6. It has been designed to automatically comply and support the surgeon's arm during surgery and to eliminate hand's trembling. In the study provided by Ogiwara et al. (2017), the authors reported on the applicability and the evaluation of initial experiences of this surgical device for endoscopic endonasal transsphenoidal surgery (ETSS). iArmS[®] was used on 43 patients that underwent surgery via ETSS to support the surgeon's arm that is

holding the endoscope during some period of the surgery then the endoscope is fixed to the passive arm UniArm[®] endoscope holder (Mitaka Kohki). This technique has reduced shaking image and no complications were reported. The limitations are the size of the system and its heavy base support, the relatively high price of the system, it doesn't allow a four-hand surgical technique due to its footprint. However, the authors worked to a next-generation robot that could be more suited to FESS. iArmS[®] is an intelligent arm with only brakes instead of actuators, therefore it is not included in Table 2.2.

Most of those robots for endonasal surgery were tested on cadavers, phantom models and preclinical studies, and only a few of them are tested on patients in ORs. Advantages, disadvantages, limitations, and risks related to each of these systems with respect to mechanism's usability, dimensions of the robots for these types of surgeries, footprints, and surgery layout in OR, user-robot interfacing are discussed in this Chapter to set the design requirements and the methodology to be followed in the NeuRoboScope system.

2.4.1. Safety Features

The methodological and technological tools that are used in the design and control of robotic endoscope holder systems and robotic laparoscope holder systems are considered in the design of the NeuRoboScope system. Reviews and research studies authored by surgeons/engineers utilizing/developing robotic endoscope holder in ESBS and FESS were considered to list all of the safety requirements, methods of user-robot interfacing, problems encountered, and the possible solutions provided.

In general, the observed shortcomings in the clinical application of robotic prototypes are the lack of force or haptic feedback (Bolzoni Villaret et al., 2017). This is because the master part is not a traditional mechanical structure such as the one used in telesurgeries. However, integrating the F/T sensor seems to be crucial and common in most of the reviewed systems. Plenty of safety feature algorithms depends on contact force signals. For this reason, interaction forces are measured on cadavers to find out the maximum possible contact forces to setup suitable thresholds. This is also used for determining the acceptable contact forces in selecting suitable motorization power for keeping the system functioning.

Various tracking systems are proposed as another safety feature that can be added to the system. Some systems used it as redundant feedback data to visualize the endoscope virtually with respect to the preplanned surgical zone. Overall, insufficient safety features in conceptual prototypes were the main reason for not advancing these systems to the OR.

2.4.2. Mechanical Structure

Robotic endoscope holder for laparoscopic surgeries and FESS are similar most of the time in structure and share the common function of holding and positioning the endoscope during surgery. However, the main difference is that in the laparoscope robot assistant, there can be passive joints at the endoscope holding region, but this is not practical in ESBS. These passive joints are included to map the translational motion of the end-effector of the active robot arm to a spherical motion of the endoscope holder around the virtual passive RCM (the pivot-point) located at the entrance port (the trocar). The disadvantages of using the entrance port as a passive joint are the loss of orientation control of the endoscope whenever it is outside the surgical workspace and the image is not always stable. However, what can be considered as an advantage is the compliance of the endoscope due to the free movement of the endoscope provided by this passive part (Trévillot et al. 2013). This property can cause unstable vision when applied to ESBS since there is interference with the other surgical tools that enter from the same port (for ex. the nostril). Additionally, for a tight passive joint at the gamble near the end-effector, with any fast motion, the endoscope could apply excessive load on the nose tip and nasal cavity tissues. The SOLOASSIST[®] and AESOP[®] systems are examples of systems where a mechanical RCM was not integrated. The existence of the RCM mechanism can be considered as an improvement of safety for SPA in MIS (Taylor et al., 2016).

Some laparoscope holders have dimensions that do not allow other tools to be used nearby. In such systems, the workspace at the entrance port, as can be seen in the rack and pinion disk of the Vision Kontrol endoscopY (ViKY[®]) surgical robot, is occupied (Gumbs et al., 2007).

2.4.3. Dimensions

Large dimensions of some prototypes compared to the limited operative space in EFSS and ESBS is another reason that these prototypes did not find a place in ORs. Many proposed prototypes in the literature share the same limit which is introduced as a result of the adaptation of industrial robots that had non-optimal dimensions for surgery tasks. Furthermore, preclinical tests of those prototypes indicate excessive inertia and suboptimal joint motions (Bolzoni Villaret et al., 2017). Each surgery or a group of surgeries has/have a specific surgical workspace and for this workspace, a specially designed robot arm could be recommended.

As stated by Funda et al. (1995),

It is difficult to design a general-purpose surgical robot. The workspace, ergonomic, and precision requirements associated with different procedures vary greatly. Once a promising class of applications for robots in surgery is identified, a specific mechanism and design approach may be required to adequately address the application requirements within cost constraints

In general, some surgical robots, in their second peers, are more compact, easier to set up and use, and substantially more affordable than their ancestors. Examples to this are EndoAssist® and FreeHand®, MAZOR® X and Mazor® Robotics Renaissance, Hybrid and Endoscope Robot® by Medineering, and FREE and FREEDOM®. In the next generations of these systems, the producers intend to provide new innovative but relatively affordable surgical robots. However, the robot manipulator itself is only a part of the whole system which comprises control, electronics, software and computers, user-robot interfaces, and many more components to be optimally designed (Funda et al., 1995).

2.4.4. User-Robot Interface

Reviewed studies and most of the preclinical/clinical results reveal that the user-robot interface has an important effect on surgical time prolongation. The surgeons first and foremost are very talented, they are routinely manipulating the endoscope intuitively. Any system to be devised required to be competitive so that it can be enrolled in OR. Perceiving that these systems are controlled either by hands (joysticks) or feet (pedals) or with the body's natural postures (inertial sensors, optical tracking, computer vision, etc.). The surgeon-robot interfacing methods should be designed in a

way not to put limitations or decrease the surgeon's dexterity and allow for bimanual operation during most of the surgery.

It has been concluded by Strauß et al. (2007) that from a surgical point of view, the user-robot interface has great importance compared to the other factors. Using joysticks and haptic master devices may not serve well even in the presence of a surgeon assistant. The preclinical results show low efficiency in the usage of joysticks which made it tough for the performance of the operation. However, the addition of joysticks can be favorable as a redundant input device.

Recent advances are in the optical and camera-based motion sensing and tracking systems (for example Azure Kinect[®] by Microsoft and similar systems). These state-of-the-art devices with their developed software and artificial intelligence can recognize real-time gestures with higher precision. In addition, accurate recognition of verbal commands is improved with artificial intelligence. Such modern technology can be adapted for free-hand user-robot interfacing and making the surgeon's focus on the operation.

2.5. Conclusion

In this Chapter, a general introduction is given for medical robots. Then more specific classification of surgical robots used in RAS systems is defined. Among these systems, the concept of a cooperative robot in rigid endoscope holding and positioning tasks is not new, but it is mostly used one for laparoscopic surgeries.

A detailed and focused literature review of robot endoscope holders for FESS and ESBS is introduced. All of the presented robot systems in Table 2.2 are used for endonasal endoscopic surgery (except for the Freehand robotic system) by utilizing a specially designed robotic system or modifying the existed robotic systems for this purpose. Among many details of these systems, the focus is on the safety features. These safety features, which are developed and validated in these systems, are investigated to be a starting point for proposing safety features in the design of the NeuRoboScope system. The main limitation in most of the presented systems is related to safety. Some safety features are mandatory for some of the newly developed systems such as the presence of the F/T sensor. This sensor can be defined as a standard safety feature utilized to guarantee the applicability of many safety algorithms for RAS. The

second limitation is the use of heavy and bulky mechanisms. In the next years to come, the expensive and large-sized multifunctional robots of today are expected to be replaced by more affordable and smaller robots that are custom-made to particular procedures (Marcus et al., 2015).

Many comparative studies were done by surgeons between surgeon assistant and robot assistant in laparoscopic surgeries and between different systems of passive endoscope holder and robot endoscope holder and between different robot endoscope holder on training phantoms or on cadavers and on patients. These studies show differences in the results but most of them concluded that using assistant robots during the surgeries can decrease fatigue and provide steady imaging. The most challenging demand by the surgeons is a fast and intuitive interface with the assistant robot.

Most of the commercially available systems and prototypes are designed for laparoscopic surgery however, some of them could be applicable to ESBS. This can be potential future work for surgeons, which is required for clinical approvals.

CHAPTER 3

ANALYSIS OF DESIGN REQUIREMENTS

Since the nasal cavity and skull base are vital and sensitive places in the body, identification of some physical properties of the surgical environment is of great importance. The surgeon's operational properties such as the motion analyses and the contact forces are critical information to be measured. Such analyses can provide a useful indication for the surgical workspace for setting all design requirements. In this Chapter, the surgical area and a brief anatomical definition are offered. Then two main analyses are presented for the surgery environment.

Firstly, the analysis of the surgeon's motion during surgery on a cadaver is presented. A literature survey on the previous measures of the nasal cavity and surgery workspace of various endonasal endoscopic surgeries is provided. The methodology of these measuring procedures is briefly introduced and summarized. The experimental measuring setup in this dissertation and the procedure of calculation is explained. All collected measuring data is filtered and tabulated for evaluation.

Secondly, for the analysis of the impedance characteristics of the surgical environment, a brief literature survey is done for the methodology followed. A typical mobile measuring device is designed and a methodology for higher force measuring accuracy is presented. Followed by a simple experimental test of the measuring device for the validation of its functionality a brief conclusion is given at the end of the Chapter.

3.1. The Anatomy and Physiology of the Surgical Area

The definition and development of pituitary tumor resection surgery and a brief view of the surgical workflow were introduced in Sections 1.2 and 1.3, respectively. For a detailed illustration of endonasal endoscope surgeries with steps and real surgery figures for each step, one can be directed to the manual by Schwartz and Anand (2014). In this section, a simple anatomical illustration of the surgical environment is introduced.

In the ESBS, the pituitary tumor gland can be approached by either nostril (left or right) which form both of nasal cavities. The nasal cavity has mainly two walls: the nasal septum, which is the middle bone that divides the two airways (the nostrils or nasal cavities), as can be seen in Figure 3.1. The other walls on both sides have all of the superior nasal concha, middle nasal concha, and inferior nasal concha (turbinate) as shown in Figure 3.2. The internal tissues have many distributed nerves in addition to blood capillaries. The nasal cavity has four corridors that define the endonasal endoscopic approaches: transmaxillary, transnasal, transethmoidal and transsphenoidal (Schwartz and Anand, 2014). These narrow corridors can define the first limits in the range of the endoscope motion. This environment is the surgical workspace of various surgeries and related surgical tools in addition to the endoscope to visualize the nasal cavity. However, the transsphenoidal corridor is the one related to the sella and pituitary tumor approach.

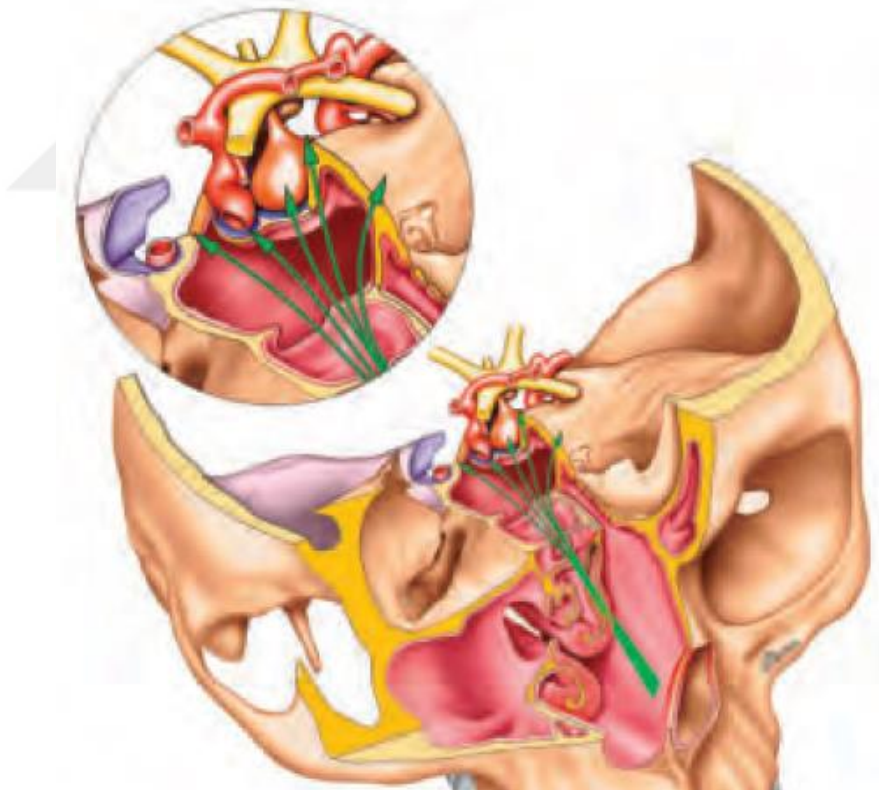


Figure 3.1. Surgical workspace and pituitary gland approach
(Source: Schwartz and Anand, 2014)

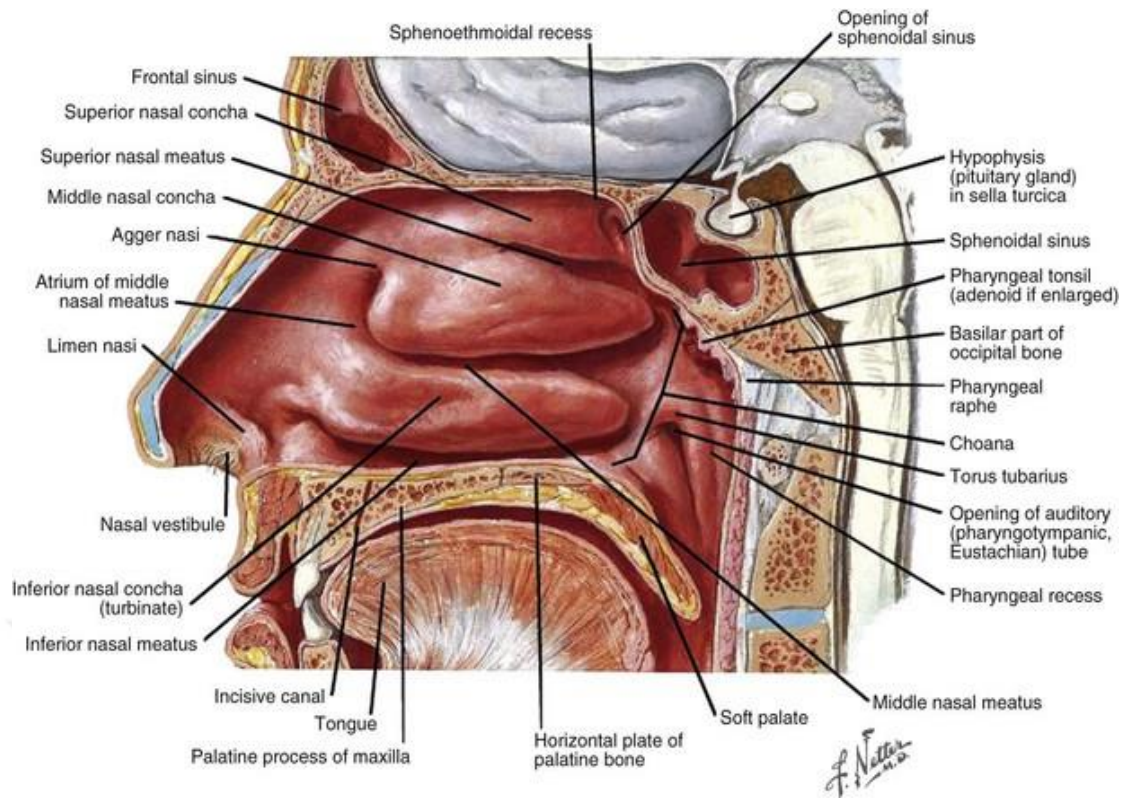


Figure 3.2. The nasal cavity
(Source: Beitler et al., 2016)

To analyze this surgical workspace, many properties for measurements can be designated immediately through observing surgery workflow. These properties are listed as follows:

- Statistically analyzing of the motions performed during a simulated surgery on a cadaver to guide the choice of the structure of the mechanism by the external tracking system,
- Measuring the ranges in endoscope motions,
- Measuring the motion rates,
- Determining the position of the pivot-point in the nostril,
- Measuring the maximum possible depth of the endoscope in the nostril,
- Measuring contact forces/ the impedance exerted on the endoscope by 6-axis F/T sensor,
- Measuring of the various resistance capacities of the structures of the nasal fossae or adjacent structures with respect to its resistance capacity to external forces.

3.2. Measurement and Analysis of the Surgeon's Motion

For most of the studies involved in the use of robot assisted endonasal endoscopy in different surgeries, many research groups had been working on investigating the workspace for the nasal cavity. On the other hand, there is not enough investigation on the workspace of the endoscope specifically for ESBS. Nor there is for the motion analysis of the endoscope with the presence of various surgical tools together in the same entry port sharing the same workspace in this surgery. One of the main challenges is the close proximity of critical regions like the anterior skull base, orbits, carotid arteries, and optical nerves to the workspace of the robot.

Strauß et al. (2007) analyzed surgical workflows in 49 FESS to provide endoscope tip point positions approximately for the design of an automated endoscope guidance system. However, they didn't study the orientation of the endoscope inside the workspace.

In FESS, there are four types of paranasal sinuses at different regions: frontal sinus, sphenoid sinus (as shown in Figure 3.2), maxillary sinus and ethmoid not shown. Among those different regions, the sphenoid sinus is the surgical workspace for pituitary gland resection surgery since the approach to the pituitary gland in ESBS is done by the nostril through sphenoidal sinus.

Another interesting investigation of the workspace and endoscope motion was done by Trévillot et al. (2013) on 13 cadavers for real sino-nasal tracts. They have used an optical tracking system to track the position, orientation, penetration and speed of the endoscope and suction tool with respect to a reference coordinate frame on the cadaver's head. Intensive statistical analyses were done specifically to show that pivot-point cannot be considered as a fixed point, but it is a fixed region represented as a box at the entry of the nostril. The position and specification of this pivot box depend mainly on the targeted sinus.

(Eichhorn et al., 2015) performed a workspace investigation on five different patients during real FESS. They observed the motion for both of the tools and endoscope by developing and using a marker-based tracking system for tracking position and orientation. The dimension of an hourglass-like workspace was defined by many statistical analyses of the data. The pivot-point was considered at the small diameter of the hourglass and defined as the point that has the smallest squared distance

to the pose of endoscope prob for all readings. This pivot-point is located out of the nasal entrance, due to the elasticity of the alar wing of the nose. It has been noticed that the pivot-point should be placed high up near the tip of the nose giving more space to the other tools to be present at the same nostril. The cuboid workspaces of the tip-point of the endoscope were investigated as well. The term resting position of the endoscope was introduced inside a small volume when the tip-point being inside this volume more frequently. In their work, nothing mentioned about the position of the workspace with respect to a global reference frame nor the angle rate for this motion.

Other studies for the workspace and pathway of EETS were done in (Chalongwongse, Chumnanvej, and Suthakorn, 2019; Chumnanvej et al., 2019). The studies aimed to investigate a pathway for safe insertion of surgical tools. For this measure, many data have been collected by an optical tracking system for the motion of a surgical tool in EETS in 70-80 cadavers. To figure out the shape and size of the workspace the data of cloud positions (140 experiments each around 800 points) was analyzed. No orientation data was recorded for the workspace. The shape of the safe pathway was shown as a cylinder with a length as the distance between entry point at the nostril and sphenoid sinus. A narrow diameter in the middle of this cylinder was observed. In this investigation, the motion of the endoscope was not studied. However, this study validated the single entrance pathway for the endoscope into the nostril for ESBS.

In the study of (Kristin et al., 2015), the motion of the endoscope during sinus surgery of 27 cadavers has been measured by tracking sensors. The endoscope had been guided by hand while linked to the SOLOASSIST. Many zones have been inspected at maximum extension. One of them was sphenoid sinuses. Since sinuses are distributed at different positions inside the nasal cavity, the range of motion generated a big and complex enveloping volume that included all maximum reached endoscope positions. The generated motion was represented as an envelope in a kidney-like shape (with respect to endoscope camera motion not the endoscope tip). A useful information for the ESBS is the insertion distance specifically for Sphenoid sinus. All of the presented studies in the literature focus on FESS. Cadaver tests show wide diversity in the results due to different anatomical structures. Some of their summary results are presented in Table 3.1.

In this Chapter, the workspace of the endoscope inside the nasal cavity throughout intraoperative pituitary gland removal surgery on a cadaver is investigated.

The presented workspace analysis algorithm is done by recording motion data of the endoscope inside the surgical workspace. By following this oriented algorithm, specific information on the workspace will be obtained. Via the analysis of this information, the required motion constraint of the endoscope during different stages of the surgery is obtained. These results are to be used for the design purpose of the mechanical system and user-robot interfacing. In addition to angular position, this work calculates the maximum reached angular rate and use it as a design parameter for actuators. By setting all these parameters the designed robot will be safer, less complex, and more efficient.

Table 3.1. Summary of workspace of the relevant studies in the literature

No	Reference	Workspace	Application	Shape
1	(Trévillot et al., 2013)	Angle with sagittal plane = 26°~66°, speed = 12~43 (°/s) Angle with axial plane 34°~68°, speed = 15~56 (°/s) Angle around endoscope 42°~71°, speed = 20~57 (°/s) Penetration = 70~100 mm	Endoscope and suction tool motion/cadaver sino-nasal tract	Conical shape
2	(Eichhorn et al., 2015)	The average length of the endonasal hourglass conus = 43.79 (range 23.50–70.37) mm The greatest (the longer axis of the ellipse) internal diameter was 28.32 (range 16.64–48.05) mm. The greatest internal diameter at pivot (range 12.28–30.88) mm.	The endoscope and five surgical tools / real FESS	The shape of an hourglass, elliptical cross-section
3	(Chalongwongse, Chumnanvej, and Suthakorn, 2019)	The average diameter = 19.08 mm (Min= 13.28, Max= 27.26) average length = 53.9 mm (Min= 36.01, Max= 70.46) Average volume =15.97 cm ³ (Min= 5.61, Max= 28.87)	Surgical tools positioning / cadavers EETS	Cylindrical tube for the tools
4	(Kristin et al., 2015)	Volume: 6.35 dm ³ (kidney-shaped) average insertion = 84 mm (Min = 54.3, Max = 113.7) Note: these values obtained from the figure in the reference	Endoscope / cadavers Sinus endoscopy	Kidney shaped (camera body position)

3.2.1. Experimentation Setup for Measurements

The experimental setup is composed of an endoscope (TH100 IMAGE1 S™ H3-Z camera head and rigid telescope with view angle of 30° by KARL STORZ) with an attached 3-axis linear accelerometer sensor and a cadaver. Multiple scenarios were planned for each functional task at different surgical stages. Two expert surgeons Prof. Dr. M.D. Mustafa Berker and Assoc. Prof. Dr. M.D. Ahmet İlkey Isikay are both from Hacettepe University, Ankara, Turkey participated in this experimentation. The surgeons are initiators and research members of the NeuRoboScope project. Statistical analysis was applied to the measured data after filtering out to damp down most of the

noises with deferent filtering parameters. This endoscope is used throughout the operation to monitor the real operation zone. The accelerometer sensor was sealed inside a plastic box and attached to the endoscope. The combination was sealed all together inside a sterilization bag as shown in Figure 3.3. The head of the patient to be positioned laying down horizontally and the reference frame is considered as shown in Figure 3.4. Several preclinical tests and evaluations to prove the proposed concept of measuring were done and verified with acceptable accuracy before the ex-vivo operation.

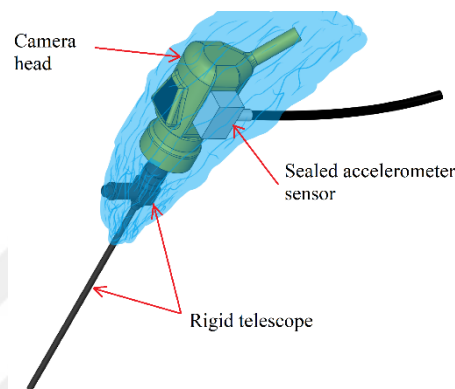


Figure 3.3. An endoscope with an angular motion measuring component

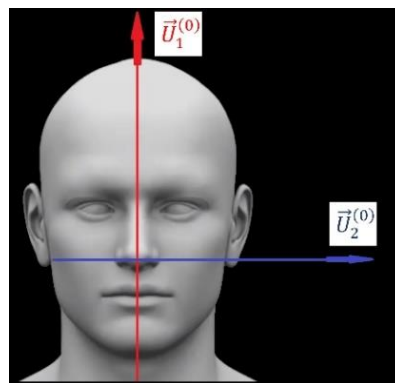


Figure 3.4. Reference frame with respect to the cadaver's head

3.2.2. Decomposition of a General Rotation into Two Elementary Rotations of Euler Angles

Considering that the third axis of the sensor is directed along the axis of the endoscope from the main body to the tip of the endoscope and directed to the ground

($\vec{U}_3^{(0)}$ in Figure 3.4 and $\vec{U}_3^{(2)}$ in Figure 3.5 for this case and $\vec{U}_1^{(0)}$ is in the direction of $\vec{U}_1^{(2)}$) as an initial position (zero rotation angles). To find the final orientation of the endoscope after some change in the orientation with unknown sequence, gravitational acceleration vector, which is always directed downward in the $\vec{U}_3^{(0)}$, is measured with respect to accelerometer's frame \mathcal{F}_2 . Considering that accelerometer frame, \mathcal{F}_2 , shown in Figure 3.5 is as a reference frame to observe the position of the gravity vector.

There are many possible sequences for Euler angles to represent this orientation. The Euler angles are the angular rotations around specified axes from initial to final orientation. The selection of the sequence can be related to the way the mechanism to be designed. The selected sequence to reach the position of the gravity vector is considered as Rotating Frame-Based (RFB). The sequence is rotation around $\vec{U}_2^{(2)}$ by α angle then following by rotation around $\vec{U}_1^{(1)}$ by β angle as presented in Figure 3.5 and Figure 3.6. this sequence and those rotational angles were selected to find joint limits of the first mechanical prototype that will be introduced in the next Chapter. The sequence is illustrated as follows

$$\mathcal{F}_2 \xrightarrow[\alpha]{\vec{U}_2^{(2)}} \mathcal{F}_1 \xrightarrow[\beta]{\vec{U}_1^{(1)}} \mathcal{F}_0 \quad (3.1)$$

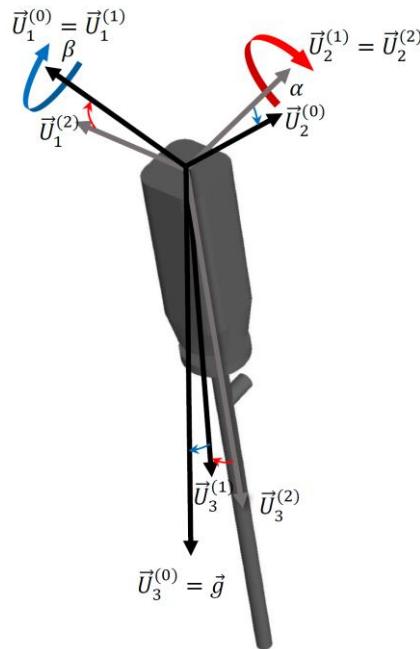


Figure 3.5. Frame transformation between the endoscope and the accelerometer.

As can be seen in Figure 3.6 the gravity vector \vec{g} is measured by the accelerometer as $\vec{g}^{(2)} = [g_x, g_y, g_z]^T$ and with respect to \mathcal{F}_0 it is $\vec{g}^{(0)} = [0, 0, g]$ where $g = 9.81 \text{ m/s}^2$ is the local gravitational acceleration of Earth.

$$\vec{g}^{(2)} = \hat{C}^{(2,0)} \vec{g}^{(0)} \quad (3.2)$$

where $\hat{C}^{(a,b)}$ is a 3×3 rotation matrix to transform from \mathcal{F}_b to \mathcal{F}_a and $\vec{g}^{(a)}$ is column matrix of the gravity vector with respect to \mathcal{F}_a .

$$\hat{C}^{(2,0)} = \hat{C}^{(2,1)} \hat{C}^{(1,0)} = \begin{bmatrix} \cos \alpha & 0 & \sin \alpha \\ 0 & 1 & 0 \\ -\sin \alpha & 0 & \cos \alpha \end{bmatrix} \begin{bmatrix} 1 & 0 & 0 \\ 0 & \cos \beta & -\sin \beta \\ 0 & \sin \beta & \cos \beta \end{bmatrix} =$$

$$\begin{bmatrix} \cos \alpha & \sin \alpha \sin \beta & \cos \beta \sin \alpha \\ 0 & \cos \beta & -\sin \beta \\ -\sin \alpha & \cos \alpha \sin \beta & \cos \alpha \cos \beta \end{bmatrix} \quad (3.3)$$

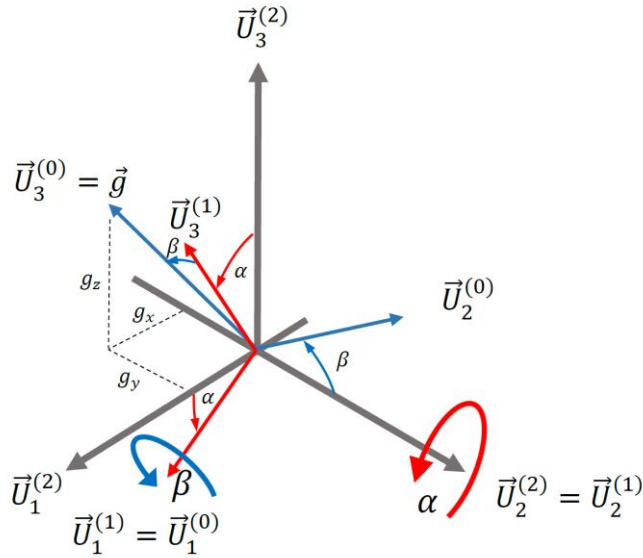


Figure 3.6. The selected sequence of Euler angles

Substituting Equation 3.3 in Equation 3.2 and divided by 9.81 to get the relationship between a unit vector of the sensor's reading and Euler Angles as follows

$$\vec{g}^{(2)} = \frac{1}{9.81} \begin{bmatrix} g_x \\ g_y \\ g_z \end{bmatrix} = \begin{bmatrix} \cos \beta \sin \alpha \\ -\sin \beta \\ \cos \alpha \cos \beta \end{bmatrix} \quad (3.4)$$

The angle value of β can be defined as presented in Equation 3.5 when $\cos \beta \neq 0$. Otherwise, it is undefined.

$$\beta = \begin{cases} \sin^{-1}(-g_y/9.81), & \cos \beta > 0 \\ \pi - \sin^{-1}(-g_y/9.81), & \cos \beta < 0 \end{cases} \quad (3.5)$$

and for α angle is related to the solution of β as shown in Equation 3.6

$$\alpha = \text{atan2}(\delta g_x, \delta g_z), \delta = \text{sgn}(\cos \beta) \quad (3.6)$$

Otherwise when $\cos \beta = 0$ i.e. $\beta = \pm \frac{\pi}{2}$, in such case, the singularity will arise and α could be any angle. This pose is not expected in the calculation by this measuring setup. The limitation of the workspace could prevent such scenario where α and β can be predicted to be in **quadrant I** or **quadrant IV**, which means that δ is always positive. In conjunction with this consideration, the external acceleration applied to the sensor from the endoscope's motion is neglected and can be filtered out.

3.2.3. Acquisition and Analysis of the Data

Each collected data was defined for its related specific motion of the endoscope when it has been recorded. After collecting all the needed data, a set of analyses is done to get angular position and angular speed information. The first analysis is done for the unfiltered raw signals to monitor the exact but noisy data. The other analysis is done by filtering all noises by using different step sizes. Considering an array x with dimension n of data that needs to be filtered, then y is the array to be calculated as

$$y(i) = \frac{1}{\text{StepSize}} \{x(i) + x(i+1) + \dots + x(i + (\text{StepSize} - 1))\} \quad (3.7)$$

for $i = (1 + 0 \times \text{StepSize}), (1 + 1 \times \text{StepSize}), \dots, (1 + (n - \text{StepSize}))$. This filtering is applied to different step sizes (5,10, and 40). The corresponding angular speed is calculated as the differentiation of angular position by the corresponding change in time as a simple ratio as

$$v = \frac{\Delta y}{\Delta t} \quad (3.8)$$

Next in Table 3.2, all 22 recorded scenarios are tabulated for each reading and filtered result corresponding to different step sizes. Figure 3.7 is presented as a sample of filtering performance and signal value illustration. The maximum and minimum angular position and maximum angular speed are highlighted by (underlined **bold** text) and summarized at the end of the table.

Table 3.2. The intraoperative scenario analysis results.

No.	Operation		Max Angle β (°)	Min Angle β (°)	Max Angular speed $\frac{d\beta}{dt}$ (°/s)	Max Angle α (°)	Min Angle α (°)	Max Angular speed $\frac{d\alpha}{dt}$ (°/s)	Note
1	Aspirator tool, right nostril entry, by Ilkay	No filtering	-15	-19		34	29		unstable
		5 step	-15	-19	19	35	28	64	
		10 step	-15	-19	6.4	35	28	33	
		40 step	-16	-18	1.7	34	27	2.8	
2	Scalpel single record	No filtering	-11	-13	5	35	29	5	
		5 step	-6	-15	29	35	27	42	
		10 step	-7	-14	8.9	35	28	12.7	
		40 step	-11	-13	1.3	34	29	2.4	
3	General, by Ilkay in endoscopy	No filtering	-7	-15	2.3	38	28	4.6~6	useful
		5 step	-7	-15	18	39	27	52.3	
		10 step	-7	-15	10.3	38	27	23	
		40 step	-8	-15	2.5	38	29	3.5	
4	General, by Ilkay endoscope inside_2	No filtering	-9	-14	4~15	33	29	~15	
		5 step	-8	-14	21.8	37	28	40.5	
		10 step	-8	-14	11.7	37	28	16.2	
		40 step	-8	-13	1.8	36	29	3.1	
5	General, by Ilkay endoscope inside_3	No filtering	-8	-17	3	34	26	~20	
		5 step	-8	-17	-20.2	34	25	23.8	
		10 step	-9	-17	-12.4	34	27	10.5	
		40 step	-10	-16	2.3	33	27	3.1	
6	General, by Ilkay endoscope inside_4	No filtering	-11	-15	1.6	35	29	12~22	
		5 step	-10	-16	16	36	29	22.7	
		10 step	-10	-16	5.4	35	29	10	
		40 step	-10	-15	1.5	35	29	3	
7	Double full round	No filtering	-5	-17	4	44	22	5.2	useful
		5 step	-4	-18	36.7	45	22	29.4	
		10 step	-4	-18	21.2	44	22	15	
		40 step	-5	-17	4	43	23	7.4	
8	Bleeding checking	No filtering	-3	-10	4	38	23	10~37	
		5 step	-2	-10	48.6	39	22	74.2	
		10 step	-3	-10	11	38	23	33.5	
		40 step	-3	-10	2.6	38	29	5.7	
9	Kirwan, by Ilkay	No filtering	-15	-19	5	38	31	3~6.8	
		5 step	-15	-22	42.3	38	30	50.6	
		10 step	-15	-20	11	38	31	11.9	
		40 step	-15	-19	1.8	37	32	2.1	

(cont. on next page)

Table 3.2 (cont.)

10	Kirwan, single record	No filtering	-8	-16		30	16	4	
		5 step	-4	-20	105~65	33	12	114	
		10 step	-5	-17	34	33	14	40	
		40 step	-9	-15	3.2	29	19	7	
11	Three-tool s bipolar, by Mustafa	No filtering	-4	-9		30	24	7.5	unstable
		5 step	1	-13	111	39	22	102	
		10 step	-3	-11	24.8	34	24	28.5	
		40 step	-4	-9	2	31	25	2.7	
12	Three-tool s bipolar, by Mustafa	No filtering	-12	-15		33	29		
		5 step	-11	-15	13.6	33	28	16.5	
		10 step	-12	-15	5.6	33	29	5.5	
		40 step	-	-	-	-	-	-	15 s
13	Three-tools, by Ilkay_2	No filtering	-8	-14	10	37	30	20	
		5 step	-2	-22	42.9	36	25	50.9	
		10 step	-4	-21	29.5	35	27	17.7	
		40 step	-	-	-	-	-	-	8 s
14	Three-tools, by Ilkay_3	No filtering	-14	-16	-	35	30	8~30	
		5 step	-4	-14	50.8	37	23	66.2	
		10 step	-5	-12	16	34	24	26	
		40 step	-8	-12	2.2	34	26	4.8	
15	Three-tools, record	No filtering	-10	-17	20~30	35	26	20	
		5 step	-10	-18	40.6	36	25	28.8	
		10 step	-10	-17	13.4	35	26	16.7	
		40 step	-	-	-	-	-	-	18 s
16	Three-tools, record_2	No filtering				36	26		unstable
		5 step	-2	-22	42.9	36	25	51	
		10 step	-4	-21	29.5	35	26	17.7	
		40 step	-	-	-	-	-	-	8 s
17	Three-tools, record_3	No filtering	-7	-12	8	35	25	25	useful
		5 step	-4	-14	50.8	37	23	66.2	
		10 step	-5	-12	16	34	24	26	
		40 step	-8	-12	2.2	34	26	4.8	
18	Three-tools, by Ilkay	No filtering	-15	-20		40	36		
		5 step	-16	-20	14.8	40	36	22	
		10 step	-17	-20	5.8	40	36	8.5	
		40 step	-	-	-	-	-	-	12 s
19	Tumor removal, by Ilkay_2	No filtering						2	
		5 step	-13	-16	30.7	32	16	94	
		10 step	-13	-16	45	31	21	18.2	unstable
		40 step	-	-	-	-	-	-	8 s
20	Tumor removal, by Ilkay	No filtering	-9	-12		32	28		
		5 step	-9	-12	11	32	28	13.3	
		10 step	-9	-11	2	31	29	3.2	
		40 step	-	-	-	-	-	-	12 s
21	Tumor removal three-tools, two aspirators, by Mustafa	No filtering	-5	-10		34	31		
		5 step	-3	-11	33.5	34	29	43	
		10 step	-4	-10	8.8	34	29	17.5	
		40 step	-	-	-	-	-	-	25 s
22	Tumor removal, three-tools, by Mustafa	No filtering	-10	-14		35	28	~29	
		5 step	-8	-15	39.6	35	27	36.4	
		10 step	-9	-14	17.5	34	28	22.4	useful
		40 step	-10	-14	1.9	33	29	3.7	
23	Summary	No filtering	-3	-20	20~30	44	16	37	
		5 step	1	-22	55.5	45	12	52.3	
		10 step	-3	-21	45	44	14	40	
		40 step	-3	-19	4	43	19	7.4	

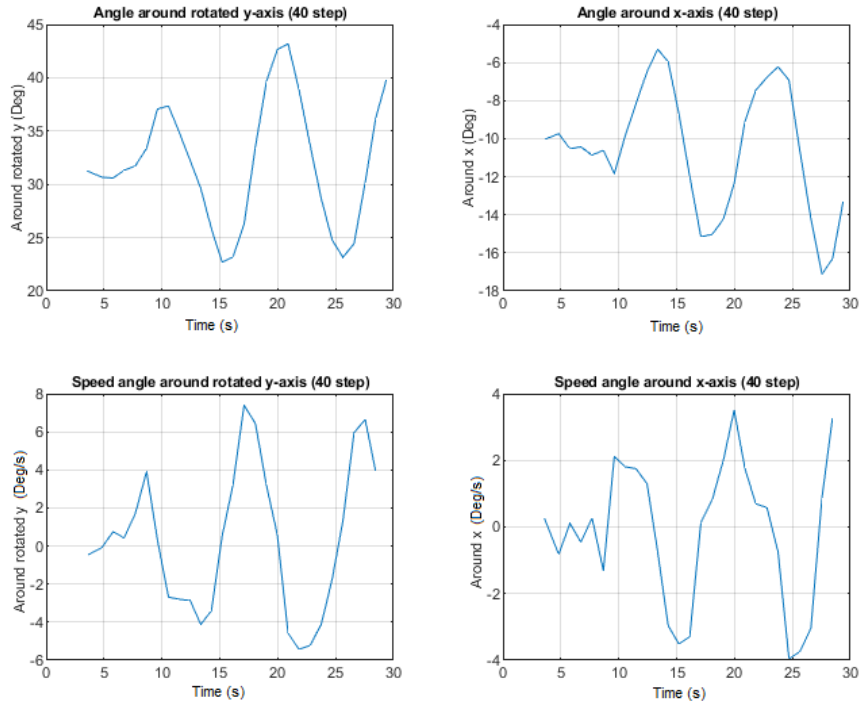


Figure 3.7. Filtered signal result for double full navigation inside the surgical workspace

These results are related to the workspace of the right side (of the cadaver) of the nasal cavity where the endoscope was inserted in. It can be noticed that for some operation sections there is an unexpected error in the data. Such error can be classified as error resulted from sudden motions or impact of the endoscope which can cause high jerks and error in speed calculation. In this case, it was classified as unstable and disregarded. The useful information is selected as shown in the summary at the end of the table. It can be concluded that the rotation angle β around x-axis is between 1° and -22° and the rotation angle α around $\vec{U}_2^{(2)}$ and $\vec{U}_2^{(1)}$ (the rotated y-axis) is between 12° and 45° . Some stable results for the angle rate show the approximate results around $50\sim 55^\circ/s$ that agree with the angle rate provided by Trévillot et al. (2013). To compare these results with the results by Eichhorn et al. (2015), to find the pivot-point or measure the distance of insertion of the telescope inside the nostrils, another measuring technique was used. But considering the maximum angle measurements, it can generate a pyramid-like shape with a rectangular cross-section. However, the corners of this rectangle may not be reached in real surgery. In this case, the results will agree with the shape of a cone-like volume with an elliptic base as declared by Eichhorn et al. (2015). The limitation of the method of using an accelerometer is that at the beginning and during the measuring, the surgeon should try not to rotate the endoscope around its axis

during the translation from the initial pose to guarantee correct measurement with respect to the reference frame shown in Figure 3.4. This could look a very demanding and tedious task for the surgeons but when realizing that their feedback is the endoscope vision on the screen it will be easy to follow. The surgeon was asked to navigate freely but to keep the camera image on the screen not tilted to follow this demand. It has been observed that when there are three tools, the range of motions was more limited due to the crowded space. To obtain more accurate results, a visual tracking system can be recommended in such cases, especially with the new high accuracy generations of advanced tracking devices. The position of the pivot-point is not unique. It depends mostly on the position to be visualized by the endoscope. To find the maximum insertion distance of the telescope, another study related to the NeuRoboScope system was done using radiology data by Dede et al. (2018). To extend the results for a wide diversity of anatomy (with respect to ages and gender for the distances inside the nasal cavity) statistical analysis was done. The radiology tests were carried out on 28 patients who were suffering from pituitary tumors (17 women and 11 men in ages of 45.9 ± 16.5 years). In these tests, four anatomical distances at carefully selected points inside the nasal cavity were measured (Figure 3.8). The resulting statistics were summarized in Table 3.3.

Table 3.3. Measuring results.

(Source: Dede et al., 2018)

Measurement (in <i>cm</i>) of	Average \pm Standard Deviation (<i>Avg</i> \pm <i>SD</i>)	95 % confidence interval (<i>Avg</i> + 2 <i>SD</i>)	99.7 % confidence interval (<i>Avg</i> + 3 <i>SD</i>)
(A) The workspace depth	9.5 ± 0.5	8.5 – 10.5	8 – 11
(B) The workspace height	2.7 ± 0.5	1.7 – 3.7	1.2 – 4.2
(C) The mid width	3.0 ± 0.4	2.2 – 3.8	1.8 – 4.2
(D) The maximum width	3.4 ± 0.5	2.4 – 4.4	1.9 – 4.9

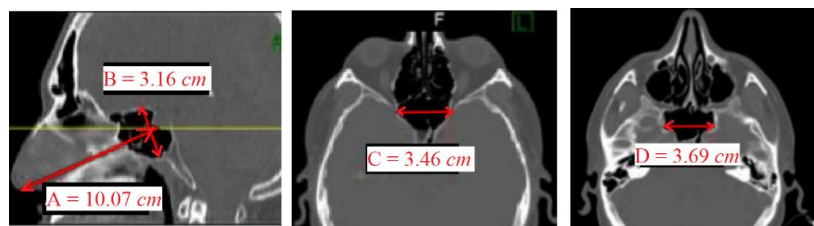


Figure 3.8. The representation of the selected distances at the radiology images.

(Source: Dede et al., 2018)

3.3. Measuring the Impedance Characteristics of the Surgical Environment

To measure all the load thresholds that can be generated during the contacts between the endoscope and the patient, a self-developed mobile F/T measuring algorithm is designed. These load thresholds are necessary for identifying the loads that can be generated on the endoscope during the insertion and manipulation inside the nasal cavity. Maximum loads can identify the safe contact loads that are not to be exceeded. In addition, these thresholds can identify the loads that are necessary to be generated by the actuators so that the robot can be able to function. Many experimental tests have been done in the literature for measuring contact and threshold forces. However, it mostly focuses on the contact forces applied to FESS.

Strauß et al. (2007) measured the maximum forces within FESS by 40 trials but on an anatomical model. They have measured the forces on the mucous membrane to be between 5.9–9.8 N.

In the study of (Trévillot et al., 2013), the friction and contact forces on the endoscope were measured during FESS on 13 cadavers. At the end of each test, they measured the minimum forces for damage on vital structures such as sella turcica, and internal carotid in the sphenoid sinus, and other structures inside the nasal cavity. These structures are sharing the same surgical workspace with ESBS. They have measured a range of 10~20 N friction and normal forces on the endoscope while damaging forces measured greater than 40 N.

In an earlier work by Wagner et al. (2008), five cadaver heads were used to test forces acting on the endoscope (for contacts with the middle turbinate, the alar wing, and the septal cartilage) for FESS. The forces did not exceed 5 N most of the time and a peak value of 8 N is measured for a short time. On the same tests, 24 different points (at bones and tissues) were tested for elasticity and damage force measures.

Again on five cadavers performing 20 FESS's, Eichhorn et al. (2008) found that the forces applied at the tip of the endoscope has values below 7 N. Moreover, they found that the force measurements recorded for maxillary and frontal sinuses are relatively higher.

Lin et al. (2015) applied forces to the tissues of the nasal cavity on five cadavers by a special force measuring tool. They have found that 25 N was the minimum force

that can cause damages to the tissue. As a result, having 10 N as a maximum force that may be applied by a robot to these tissues has been suggested. In a recent test of their designed robot, Zhong et al. (2019) used these measurements to test their designed PCEH, the compliance safety mechanism, by applying normal forces to endoscope's axis and taking into account the weight of the endoscope camera and the cables.

For the NeuRoboScope system design, the static contact forces were measured for some selected points inside the surgical environment of a cadaver in a related thesis study by Işıtman (2018). However, the focus was on the tissue modeling to apply the results on the design of an accurate interaction controller during teleoperation. The results show an approximate maximum contact force of 2 N at the tip of the nose, 3 N of frictional force with the tip of the nose due to the insertion of the telescope, and 12 (6.2) N of normal (frictional) force with nasal concha. The parameters were also reported for some spots of tissues by considering the model as each of Kelvin Boltzmann, Kelvin Voight, elastic, Maxwell, and Hunt Crossley.

For measuring the interoperation contact loads, a 6-axis F/T sensor was used in the literature. Some attached it to surgical tools with some modifications applied to the tools. Others attached it directly to the endoscope to measure contact forces on real surgeries. The best method of fixation is by attaching the sensor between the telescope and the endoscope camera. However, a sophisticated modification will be required to secure the mechanical connection and to ensure a clear vision due to the changing in focal length. The other easier method is by designing a handle so that the sensor will be between the handle and the endoscope. In the second connection method, errors in reading can be generated due to first, the forces applied by endoscope cables (camera and illumination cables), and second, weight of the endoscope. The proposed solution in this work is by designing a special handle that allows for obtaining intraoperative contact force readings more precisely. The proposed force measuring device is designed for tests of contact forces that can be performing ex-vivo real-like ESBS. These loads with the calculated dynamic loads of the mechanism within the estimated motion ranges are useful as designing tools for selecting the appropriate actuators for the NeuRoboScope system.

3.3.1. Measurement Device Design

The 6-axis F/T sensor to be used is Nano17 transducer from ATI[®]. This sensor is small in size and has a satisfactory precision. The methodology to be followed for the development of the F/T measuring device is by attaching the F/T sensor in between a handle and the endoscope as illustrated in Figure 3.9. In this connection method, an amount of bias can be present in the sensor's reading due to the weight of the endoscope, the camera cable and the illumination cable. A possible partial solution to this problem is by applying gravity cancellation for eliminating the endoscope's gravitational force from the F/T sensor's reading.

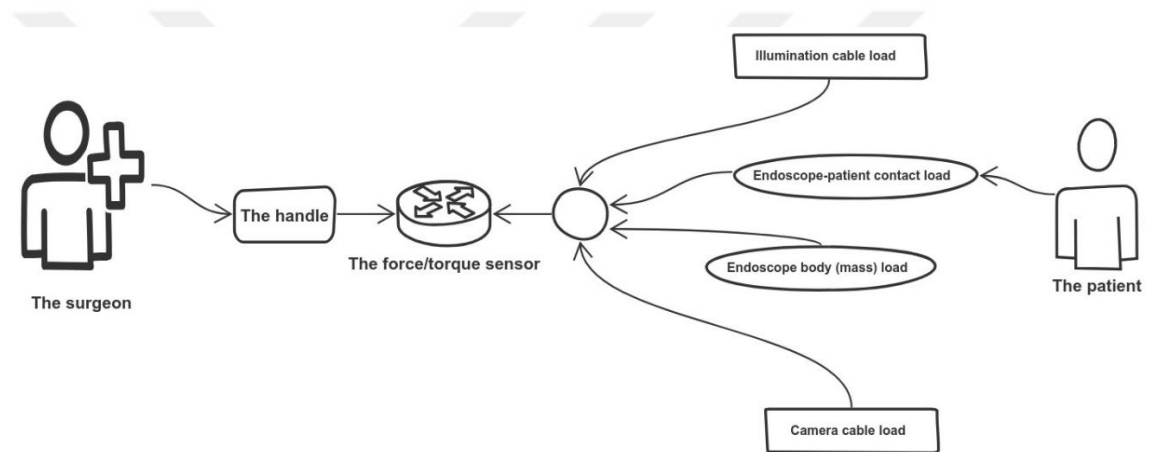


Figure 3.9. Schematic diagram of surgeon-patient interaction

Following this methodology, as the first step in the design of the loads measuring device, all necessary design requirements are listed below:

- To find the experimentally approximated mass value of the Endoscope (including the telescope)
- To find experimentally the approximate position of the center of gravity with respect to the frame of the F/T sensor
- Designing a handle so that it can be grasped by the surgeon easily without effort and connected to the F/T sensor
- Designing a connection part that can be fixed on both the endoscope and the F/T sensor. This unit should be fitted inside the handle without any possible contact even after any possible deflections

- To integrate a motion sensor to the handle to read the orientation at the endoscope

The motion sensor (Adafruit® BNO055 Absolute Orientation Sensor) is connected to data interfacing (Arduino® MEGA was selected) and connected to the PC through a USB port. While the F/T sensor (Nano17 transducer) is connected to the NET Box amplifier by ATI (with three types of calibrations and the selected one is: F_x , $F_y = 12$ N, $F_z = 17$ N, T_x , T_y , and $T_z = 120$ N·mm as maximum ranges, resolutions: F_x , F_y and $F_z = 1/160$ N, T_x , T_y , and $T_z = 1/32$ N·mm) and connected to the PC through LAN Cable. MATLAB® is used to gather and process all reading signals with a rate of 100 Hz. The handle with fixing part shown in Figure 3.10 was manufactured by the aid of a 3D printer. This design can make the grasping by the surgeon easy and doesn't affect the workflow of the real surgery.

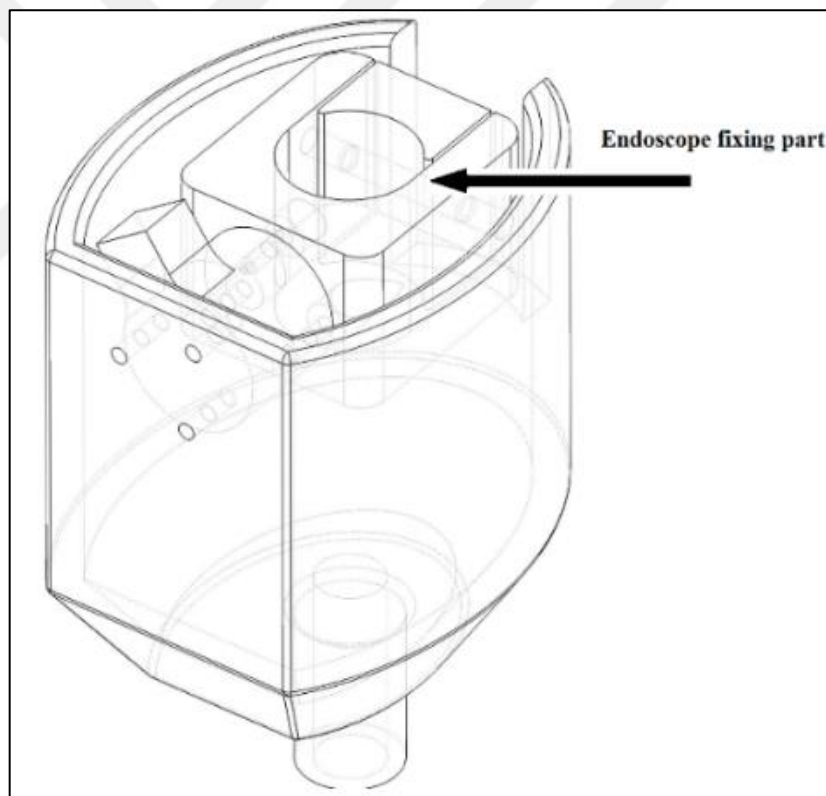


Figure 3.10. Schematic diagram of the handle and fixing part.

Next, the components of the device are integrated together as shown in Figure 3.11. The motion sensor is attached to the handle so that the coordinate frame of motion sensor is coincident (no relative rotation between them otherwise rotation matrix needed to be added) with the coordinate frame of the F/T sensor.

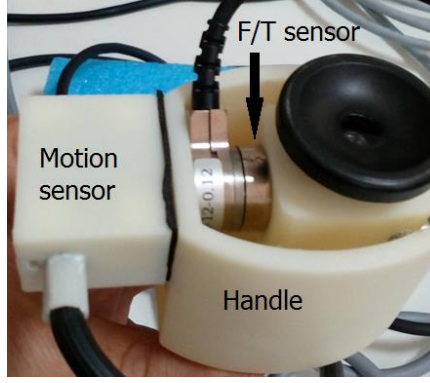


Figure 3.11. Handle with motion and F/T sensor attached

3.3.2. Gravity Cancellation for Higher Accuracy in Measurements

The weight effect of the endoscope on the F/T sensor is studied here in order to cancel the bias resulting from the gravitational effects and get a more accurate reading of external loads on the endoscope. These effects are variable because of the continuous change in the angular position of the endoscope. However, considering the small range of motion inside the surgery zone, the inertial force/moments have been neglected. To do this, first, the mass value of the endoscope is defined as m (measured approximately since there is also the additional mass of the camera cable) and the position of the center of mass vector as \vec{l} with respect to the reference frame of the F/T sensor shown in Figure 3.12. These two parameters are constant and can be measured. Then the moment exerted on the F/T sensor by the gravity effect can be calculated as

$$\vec{T}_G = \vec{l} \times \vec{F}_G. \quad (3.9)$$

where \vec{F}_G is the weight of the endoscope defined in the F/T sensor's reference frame. It can be determined as

$$\vec{F}_G = m \hat{R} \vec{g} \quad (3.10)$$

when \vec{g} is the gravity vector with respect to the global frame (the global frame is assumed to be coincident to the F/T sensor's reference frame when the endoscope is vertically positioned), \hat{R} is the rotation matrix to relate the global frame to the F/T

sensor's frame after changing the orientation. The Euler angles selected with respect to the F/T sensor's reference frame shown in Figure 3.12 as the first rotation angle α around z-axis then β around the x-axis.

$$\hat{R} = \hat{R}_{z,\alpha} \hat{R}_{x,\beta} = \begin{bmatrix} \cos \alpha & -\sin \alpha & 0 \\ \sin \alpha & \cos \alpha & 0 \\ 0 & 0 & 1 \end{bmatrix} \begin{bmatrix} 1 & 0 & 0 \\ 0 & \cos \beta & -\sin \beta \\ 0 & \sin \beta & \cos \beta \end{bmatrix} \quad (3.11)$$

Finally, by substituting Euler angles α and β to Equation 3.11 and by using the calculated force and moment in Equation 3.9 and Equation 3.10 then, the gravity cancellation can be done as

$$\bar{F}_e = \bar{F}_s - \bar{F}_G \quad (3.12)$$

$$\bar{T}_e = \bar{T}_s - \bar{T}_G. \quad (3.13)$$

Each of \bar{F}_s , \bar{T}_s are the measured force and torque at the F/T sensor. As a result, the external force and torque \bar{F}_e , \bar{T}_e respectively are representing the external loads applied on the endoscope.

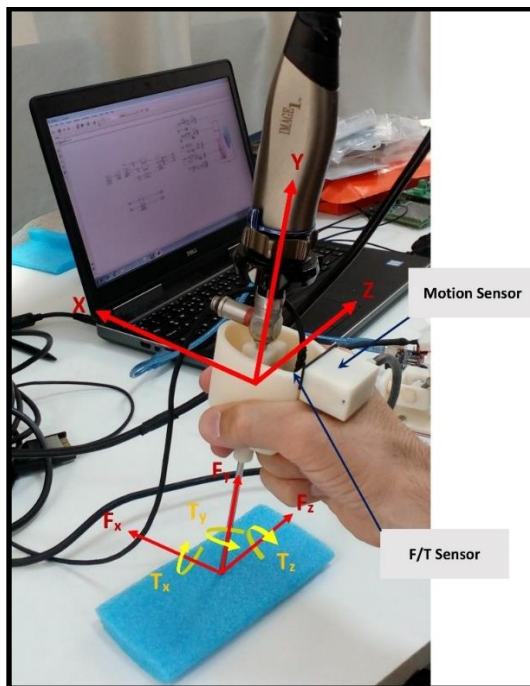


Figure 3.12. The F/T sensor frame on the endoscope

3.3.3. Experimental Tests of the Device

Since the endoscope camera and its telescope are almost symmetrical in shape, it is easy to locate the center of mass as shown in Figure 3.13. To perform a successful measuring of the external loads the handling of the holding part should be as shown in Figure 3.14. The body of the endoscope with the telescope should be isolated from any external contact except the contact needed to be measured. However, this is impossible since there is the cable of the camera and the fiber-optic cable for illumination. Those cables are the dominant part of the error that appears in the measurements.

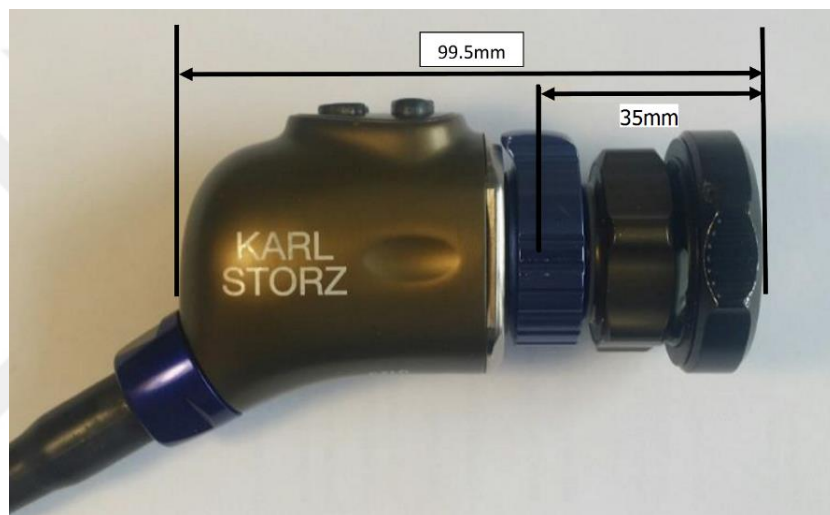


Figure 3.13. The endoscope and the location of the center of gravity (including the telescope)

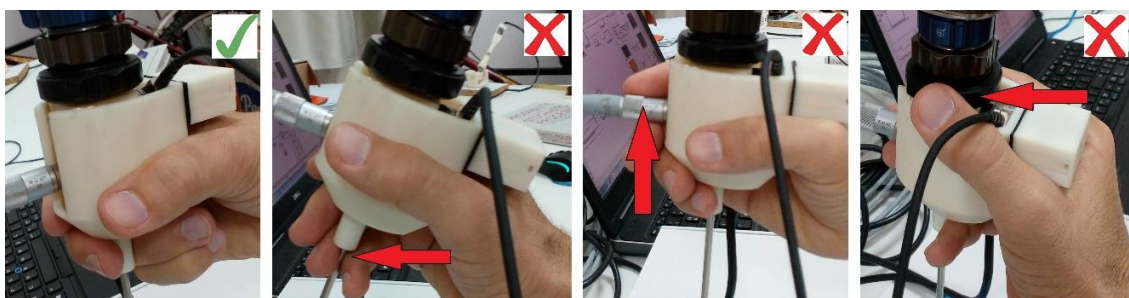


Figure 3.14. Holding the endoscope

To find the performance of the F/T measuring device, two simple tests were applied. In the first test the handle was fixed rigidly and lying horizontally as shown in Figure 3.15. A set of forces has been applied in different positions (scale masses are

used) to find out the reading of the applied forces and the corresponding generated torques on the F/T sensor. Then, the distance arm of the applied force was calculated and measured from the F/T sensor. The results are presented in Table 3.4. For a random selection of applied forces at different positions, the maximum error was about 3.4%. This error can be considered acceptable which is mostly generated by the inaccuracy of distance measurement of the arm for the applied loads.



Figure 3.15. Initial test setup

Table 3.4. Set of results of the initial test.

No.	Applied force (N)	Generated torque (N·mm)	Measured arm distance (mm)	Calculated arm distance (mm)	Error %
1	0.705	64	88	91	-3.4
2	0.700	83	115	118	-3.13
3	0.727	106	143	147	-2.8
4	0.750	137	177	182	-2.8
5	0.194	40	205	206	-0.58
6	0.192	32	163	166	-1.8
7	0.193	15	75	77	-2.66

In the second test, the gravitational effect was tested theoretically. To perform this test, first the parameters have been defined with respect to the reference frame shown in Figure 3.12 as $\bar{l} = [0.0144 \ 0.045 \ 0]^T$ m , the total mass $m = 0.46$ kg, and $\bar{g} = [0 \ -9.81 \ 0]^T$ m/s². The endoscope camera has a mass of 270 g but in the test, the total mass including the telescope mass and the effect of the cables as well.

The amount of the forces and torques generated in this test are presented in Figure 3.16 with respect to the motion limits found in Section 3.1.3. This result was not

performed experimentally but to show the pure effect of gravitational loads and exclude any other source of error. The maximum force observed is 4.5126 N when one of the force axes is coincident to the gravity vector and the maximum torque occurs when the endoscope is inclined with an angle of $\alpha = 45^\circ$.

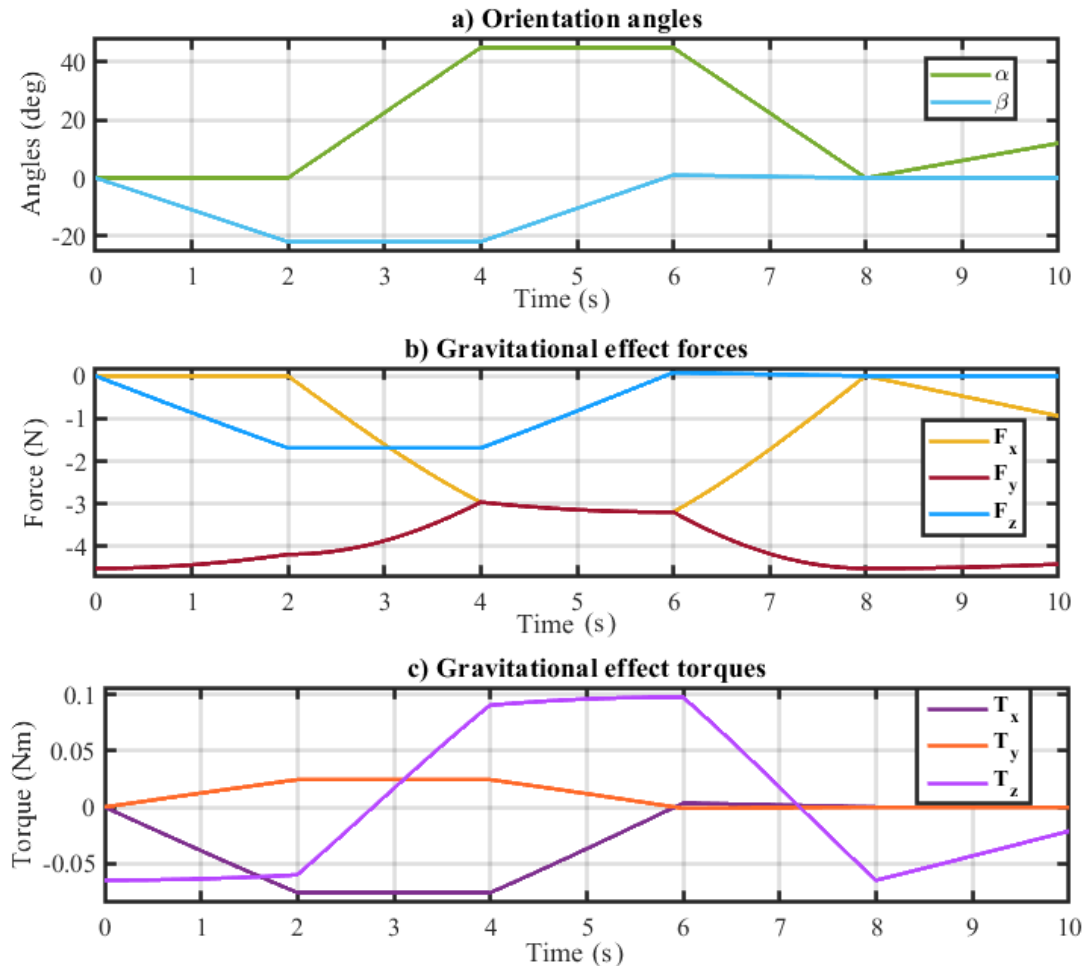


Figure 3.16. Gravitational effects by endoscope weight on reading test, a) motion information, b) force values, c) torque values.

When there is no external F/T applied on the endoscope and while manipulating the endoscope in slow motion the maximum change in torque values was noticed as ± 30 N·mm and for the forces ± 200 mN. These changes are mainly due to the cables connected to the endoscope (Data cable and illumination cable) which are out of control. When the cables are fixed with a band to the handle, more reliable results were noticed. However, other loads are generated from the bending moments of the elastic cables. This is the only limitation generated the aforementioned error range in this load measuring endoscope.

3.4. Conclusion

In this Chapter, a brief introduction to the anatomy of the surgical environment is presented. For more investigation, the surgical environment is defined by two main analyses. Firstly, the analysis of the endoscope motion during a real pituitary gland approach and removal scenario on a cadaver is carried out. In this scenario, the endoscope motion is recorded by the use of an accelerometer attached to the endoscope. The required calculations are done to determine the rotation matrix of the frame attached to the endoscope with respect to the fixed coordinate frame. An Arduino board is used for interfacing with a computer for the calculations and recordings. 22 short functional tests are recorded while performing a simulated ESBS on a cadaver. The results are collected and filtered to find the extreme ranges with acceptable accuracy.

The earlier works on the literature survey for the dimensions of the nasal cavity were mostly specific to other functional surgeries. However, the sphenoidal sinus surgery presents the closest results to the pituitary gland in ESBS. These two surgeries mostly share the same surgical workspace for the endoscope. The methodology of this measuring procedure was helpful for measuring the extreme angular positions of the endoscope and its angular rate during the surgery. However, to find the approximate insertion amount of the endoscope, another study is carried out by using radiology data of patients. These data are also used for the teleoperation design (the surgeon-robot interface) in the NeuRoboScope system's related studies (Ateş, 2018; Dede et al., 2018). However, these results show limitations when a statistical study is needed for the entire surgery. The optical navigational system could be a great solution for such analysis and can provide increased accuracy in the angular rate measurements.

Secondly, to study and analyze the impedance characteristics of the surgical environment, a mobile contact force measuring device is developed for the intraoperative ESBS on a cadaver. A brief literature survey is introduced for the methodologies followed and results obtained in the earlier studies. A technique for contact force measuring is developed. To cancel the gravitational forces due to the endoscope's mass, a motion sensor is also attached to the endoscope. Simple experimental tests of the force measuring device for the validation of its functionality are done. The tests of the contact forces are carried out on a cadaver's head and the

required parts of the surgical environment are modeled in another thesis study by Işıtman (2018) which was a part of the NeuRoboScope project tasks.



CHAPTER 4

DESCRIPTION AND DESIGN OF THE NEUROBOSCOPE SYSTEM

Considering the proposed research problem in Section 1.3 and the available solutions in robot assisted MIS, the requirements are listed for the design of the NeuRoboScope system. In this Chapter, the design requirements are proposed along with the general description of the concept that represents the basis to select and design the mechanical structure. Following this description, the design requirements are then utilized to design and select the most suitable prototype for enhanced safety in a systematic way. Two novel designs of the active robot arm are presented. The selected design was the topic of another thesis study about the structural synthesis and kinematic analysis of the mechanism which is also related to the NeuRoboScope project. Afterward, kinematic and dynamic analysis are presented for the selected active robot arm. The first prototype of the passive arm is presented with its kinematic analysis at the end of this Chapter.

4.1. General Description of the System

The NeuRoboScope system has a passive arm that is used by the surgeon manually to position an active robot arm that is attached to its moving platform. The endoscope is attached to the end-effector of the active robot arm. These components represent together the whole system as shown in Figure 4.1. The active robot is driven by the control demands sent from the surgeon (user-robot interface) while the passive arm has brakes at every joint in order to generate a fixed frame for the active arm inside the surgery zone. The passive arm is fixed at a point on the operation table behind the patient's head. The user-robot interface is to be designed in a way to allow bimanual operation of the ESBS.

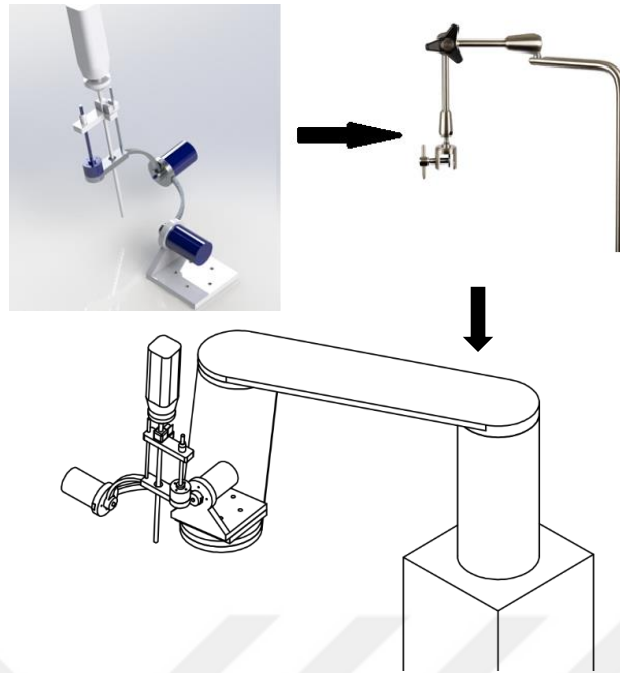


Figure 4.1. The manipulator system's concept

4.2. Design Requirements for the Robot Assisted Endoscope Holder System

The following design requirements are the general and fundamental requirements that can be applicable to MIS systems. The addition to these and optimization studies of the designs are discussed in the next Chapters.

1. DOF of the manipulator: this criterion can be selected depending on the necessary controllable motion of the endoscope.
2. Workspace: the necessary motion range of the whole system and the necessary motion range of the endoscope inside the surgery zone.
3. Mechanism of the manipulator: surgical robots in MIS require a motion that guarantee motion around a RCM of the endoscope/tool at the pivot-point (mechanically or by control).
4. Layout of the OR: depending on the area of application, dimension and positioning of the surgical robot can be decided.
5. Footprint of the robot system: considering a footprint that allows the surgeon to have as much free space as possible for his own movements and movements of surgery tools.

6. Passive arm: having a passive arm with minimum impedance to hold the active manipulator nearby the operation workspace that guarantees enough rigidity of the system while keeping the system's size and weight at minimal values.

For control and surgeon-robot interface, the following requirements are set. These requirements are presented here as parts of the design considerations of the NeuRoboScope system. However, the study of developing and optimizing surgeon-robot interface is another study outside the scope of this dissertation (Dede et al., 2018; Ateş, Majani, and Dede, 2019):

- The endoscope robot arm holder should be able to follow the command of the surgeon in a real-time and fast response.
- Intuitive human-robot interface to ease the operation of the surgeons.
- A wearable master system to acquire the surgeon's commands to be sent to the active robot arm.
- A foot pedal to activate/deactivate the interface.
- Wireless communication to send the necessary motion demands to the active robot arm.

In contrast to conventional industrial robot cells the workspace is inside the patient in surgical robots. In the development of the NeuRoboScope surgical system, safety is a critical concern. In order to meet the general safety requirements:

A F/T sensor is to be integrated to the system in order to have contact feedback information for safety and keep the interaction forces at desired values.

- Electrical/electronic safety requirements for OR standards areas are to be met.
- Emergency switches are to be integrated.
- Preclinical tests are to be performed.

In general, an endoscope holder system needs to have a special design for ESBS to minimize its size and components, as well as to decrease the dependency on the availability of the surgeon's assistants.

4.3. Description of the Active Arm and its Analysis

The active robot arm is intended to hold and position the endoscope inside the surgical workspace. This workspace is entered from a nostril, which is a natural incision port. For this reason, the mechanical design has most of its criteria shared with the robot assisted MIS systems. An intensive review of such a robotic system was given in Section 2.3. It has been concluded that it is necessary to have a fully active actuation system for controlling the orientation of the endoscope in ESBS without the engagement of the entry port as a passive mechanical constraint. Using the nostril as a passive mechanical constraint can both apply unnecessary forces and result in a backlash. Such a drawback results in trembles in the vision received as the feedback image provided by the endoscope on the monitor especially with the presence of other surgical tools at the same entry port can collide with the endoscope. There are three main solutions for the mechanism of the active robot arm to hold and position the rigid endoscope in ESBS. The first option is a serial manipulator, the second option is a parallel manipulator and the third option is a hybrid manipulator. These alternative manipulator architectures can be classified into other two subcategories: a mechanically constrained RCM and RCM by the control algorithm. When the RCM is located at the pivot-point at the tip of the nose, the telescope of the endoscope moves with only 4-DOF 3R1T (three rotation and one translation along telescope's axis). There are many possible solutions for the design of an active robot arm with this type of a motion capability in the literature. One of the most common RCM mechanisms is the double parallelogram structure that presents mechanical RCM constraint. This type of solution was first introduced for a MIS system in a patent by Taylor et al. (1995) and applied in the LARS system for MIS and has been adopted in many other commercial systems such as DaVinci Surgical Robot and other research prototypes (Taylor, 2018). Therefore, an RCM mechanism that provides a pivot-point became one of the key aspects in the design of safe robot assisted FESS (Eichhorn et al., 2015). However, in the NeuRoboScope project, two different types of prototypes are proposed and among them, the parallel mechanism with mechanically constrained RCM is selected for developing.

4.3.1. A Conceptual Design of the Active Arm: RPRP Serial-Arm

In the first proposed system, the active mechanism is a serial robot arm RPRP (R for revolute and P for prismatic joints) as shown in Figure 4.2. The telescope of the rigid endoscope held by the end-effector is directed toward the last prismatic joint. The first actuated revolute joint is to make the end-effector rotate around the first revolute joint's axis (called a swivel axis, and the angle is called a swivel angle). The second actuated prismatic joint is to provide linear motion to the end-effector along an axis parallel to the swivel-axis. The third actuated revolute joint is responsible for controlling the angle (called rotated sagittal angle) between the endoscope's axis and the swivel-axis. The fourth and final actuated prismatic joint controls the insertion amount along the telescope's axis.

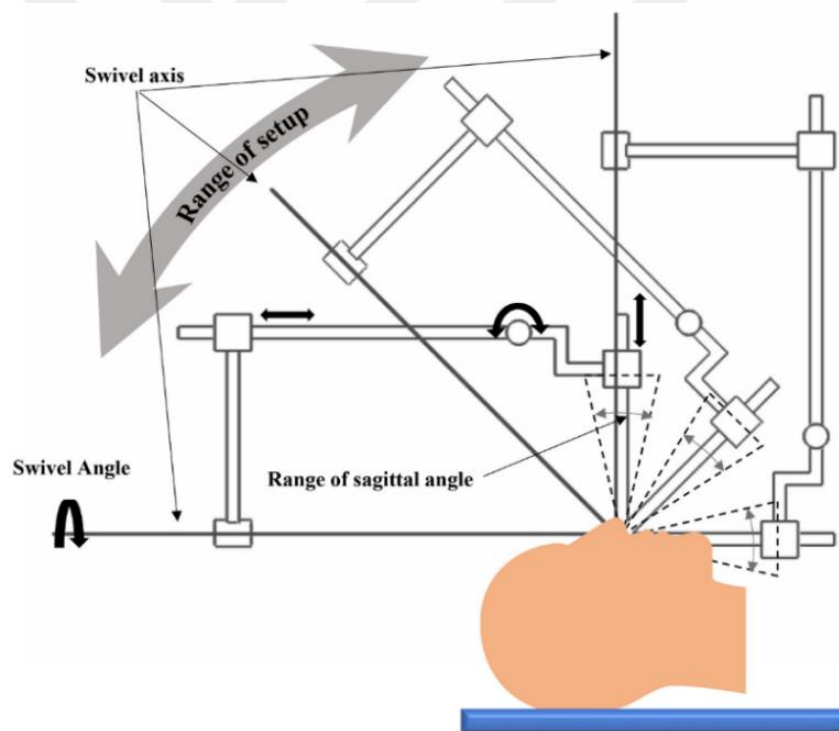


Figure 4.2. The mechanism of the serial active robot arm and range of setup

By considering the motion of this mechanism, it can be seen that the generated workspace consists of two translational motions inside a cylindrical space (one is for the height of the cylinder and the other is for the radial motion) and two rotational motions (one angle around the longitudinal axis / swivel axis of the cylinder and the other angle between the longitudinal and the telescope's axes). As a result, the developed

mechanism has 4-DOF that can operate in a 4-dimensional workspace. However, the workspace of the ESBS and MIS, in general, has a 3-dimensional workspace (excluding the rotational motion around the endoscope's axis).

To make this mechanism convenient for MIS the following steps of setup should be considered:

- The telescope axis should be intersecting with the swivel axis with a convenient initial angle (near 90°).
- The initial intersection angle (the rotated sagittal angle) depends on many aspects such as the dimensions of the links of the mechanism, the orientation of the swivel axis (the range of setup angle) with respect to the needed workspace of the surgery and the operation table, and the limits of the actuated joints.
- To generate RCM, the position of the pivot-point at the swivel axis should be defined. In this way, 1 DOF of the active robot arm will be constrained. The active robot arm will then be constrained to have 3 DOF to manipulate the endoscope in the needed 3-dimensional workspace (two rotation and one translation).
- The position of the RCM depends directly on the position of the active robot arm with respect to the pivot-point located on the patient. The information of the pivot-point with respect to the position of the active robot arm during the setup can be used to define the extra 1 DOF.
- To move the endoscope towards the pivot-point in a 3-dimensional workspace, the remaining 2 DOF in the Cartesian space can be produced by an additional passive arm that can hold and position the active robot arm.
- The range of setup and setup angle can be changed by a manual passive joint that can be readjusted and locked one time before the operation. As a result, a 3-DOF (two translation, one rotation) passive arm is needed.
- All joints (the active and passive joints) need to be backdrivable. Additionally, an admittance control algorithm can be applied to the robotic system with the aid of an F/T sensor.
- Joints that are responsible for the motion of masses in the vertical direction can be statically balanced and therefore, gravitational loads can be compensated.

This mechanism is intended to carry and position the endoscope to the entry port (by two passive and one active DOF) and control the orientation and the insertion of the endoscope (by 3 DOF) to generate a novel 6-DOF assistive robot arm for MIS.

The most important criterion of designing this robot is that the motion should be performed around a virtual RCM and to keep the position of the RCM with the desired insertion value of the telescope there are three coupled actuated joints collaborated. These can be considered as critical points in terms of safety. However, with the advancements of the F/T sensors, the capability of the new actuation system that measure the applied loads, and the compliant actuators or variable stiffness actuators VSAs, what was used to be considered as limitations no more exist in the new generations of surgical robots. Moreover, a degree of compliance at the actuation or control level can be added at the first prismatic actuator to have a flexible range for the pivot-point along the swivel axis. As a result, a small pivot line with compliance can add a degree of safety. This prototype can be considered lightweight. It has a small footprint and its kinematics facilitates the controller design. The next two subsections present the kinematic analyses of the proposed prototype.

4.3.1.1. Forward Kinematic Analysis of RPRP Serial-Arm

After assigning the coordinate frames to the active robot arm as shown in Figure 4.3, the forward kinematic analysis is carried out according to the Denavit-Hartenberg convention presented in Table 4.1.

In the presented DH convention, the variables S_2 and S_4 are the linear displacement variables of the prismatic actuators, whereas θ_1, θ_3 are the angular displacements of the rotary actuators. The other variables a_1 and a_3 are the design parameters of the mechanism. According to DH convention, all rotation matrices and position vector for the reference frames at each link are calculated as follows:

$$\hat{C}^{(0,1)} = e^{\tilde{u}_3(\theta_1)}, \quad \bar{r}_{01}^{(0)} = \hat{C}^{(0,1)} a_1 \bar{u}_1^{(1)} \quad (4.1)$$

$$\hat{C}^{(1,2)} = e^{\tilde{u}_1 \frac{\pi}{2}}, \quad \bar{r}_{12}^{(1)} = S_2 \bar{u}_3^{(1)} \quad (4.2)$$

Table 4.1. Denavit-Hartenberg parameters

DENAUIT-HARTENBERG PARAMETERS				
FRAME NO. (i)	d_i	q_i	a_i	α_i
1	0	θ_1	a_1	0
2	S_2	0	0	$\pi/2$
3	0	θ_3	a_3	$-\pi/2$
4	S_4	0	0	0

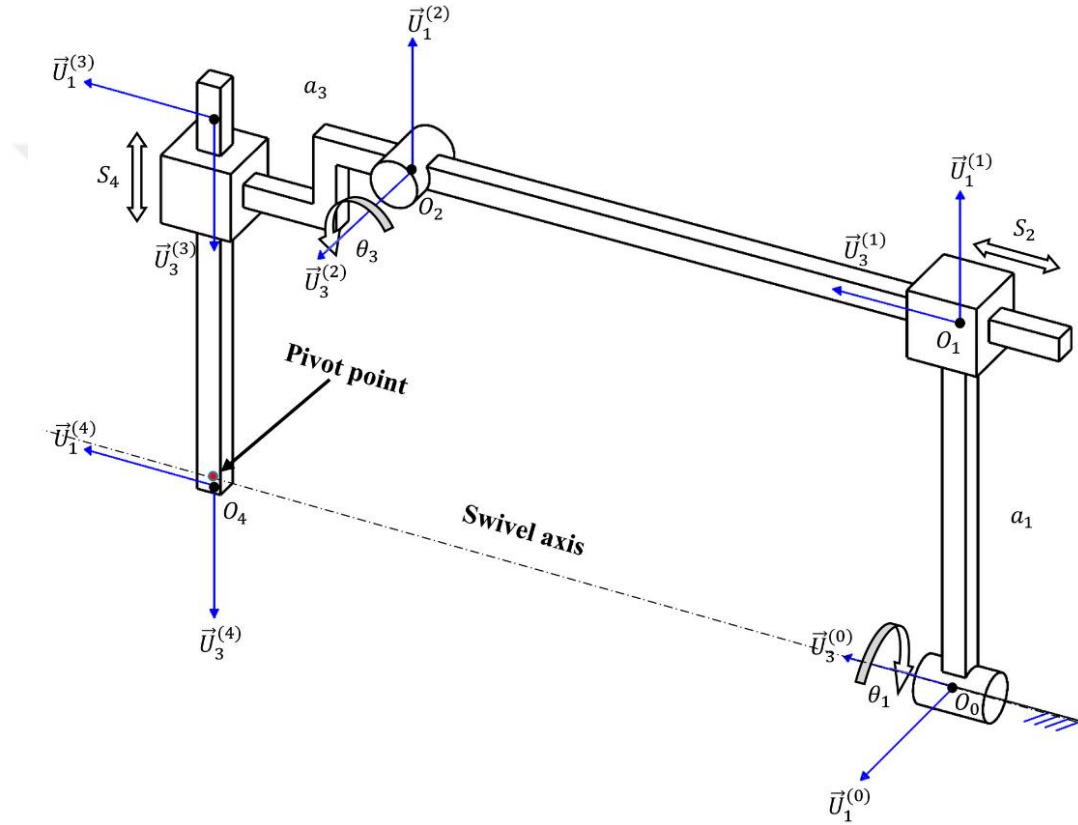


Figure 4.3. The coordinate frame schematic of the serial robotic arm RPRP

$$\hat{C}^{(2,3)} = e^{\tilde{u}_3(\theta_3)}, \quad \bar{r}_{23}^{(2)} = \hat{C}^{(2,3)} a_3 \bar{u}_1^{(3)} \quad (4.3)$$

$$\hat{C}^{(3,4)} = \hat{I}, \quad \bar{r}_{34}^{(3)} = S_4 \bar{u}_3^{(3)} \quad (4.4)$$

End-effector position as introduced at O_4 with respect to the base frame can be represented as

$$\bar{r}_{04}^{(0)} = \bar{r}_{01}^{(0)} + \hat{C}^{(0,1)} \bar{r}_{12}^{(1)} + \hat{C}^{(0,1)} \hat{C}^{(1,2)} \bar{r}_{23}^{(2)} + \hat{C}^{(0,1)} \hat{C}^{(1,2)} \hat{C}^{(2,3)} \bar{r}_{34}^{(3)} \quad (4.5)$$

To find the position with respect to the world frame (which can be any selected frame), Equation (4.5) can be pre-multiplied by the transformation matrix given in Equation (4.6):

$$\hat{C}^{(w,0)} = e^{\tilde{u}_1 \delta} \quad (4.6)$$

where δ represents the setup angle with respect to the world reference frame.

4.3.1.2. Inverse Kinematic Analysis of RPRP Serial-Arm

To calculate the motion at each actuator for the required motion at the end-effector, inverse kinematic analysis is needed. Endoscope motion inside its workspace is considered as a spherical motion, in this case, the motion at the revolute joint will be calculated directly from the input of spherical coordinate that is obtained from the workspace analysis in Chapter 3 as follows:

$$\theta_1 = -\psi \quad (4.7)$$

$$\theta_3 = \phi \quad (4.8)$$

where $\psi = \beta$ is the angle around the swivel axis and $\phi = \alpha$ is the angle in the rotated sagittal plane. For the proposed robotic arm, the end-effector position is required to be fixed at the pivot-point. The pivot-point is located at $[x, 0, 0]^T$ with respect to the attached selected reference frame on the active robot arm. This pivot-point is on the swivel axis (x is measured along the swivel axis) and its location depends on the structural parameters of the proposed robotic arm and actuator limits. After specifying the RCM position and by using the information of orientation, the other two actuated joints (the two prismatic joints) are calculated geometrically as shown in Figure 4.4 to have:

$$l = \frac{a_1}{\cos(\theta_3 - \pi/2)} \quad (4.9)$$

$$s = a_3 \tan(\theta_3 - \pi/2) \quad (4.10)$$

$$p_2 = l - s \quad (4.11)$$

Then, the displacement of the last prismatic joint can be calculated as

$$S_4 = p_2 + i \quad (4.12)$$

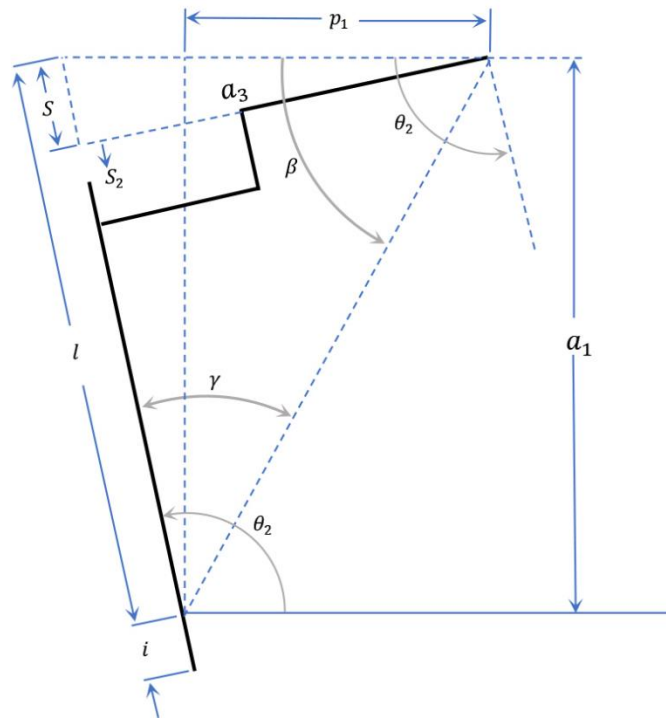


Figure 4.4. The insertion distance and the inverse kinematics.

where S_4 is considered to be the displacement of the second prismatic actuator which is a function of the orientation angle θ_3 and insertion value i . The insertion value is the input along with the telescope beyond the pivot-point. Each of the variables i and S_4 sign positive toward the patient as shown in Figure 4.4. The displacement of the first prismatic actuator can be calculated as follows:

$$\gamma = \tan^{-1} \frac{a_3}{p_2} \quad (4.13)$$

$$\beta = \theta_3 - \gamma \quad (4.14)$$

$$p_1 = \frac{a_1}{\tan \beta} \quad (4.15)$$

The value of p_1 , represents the distance between the position of the pivot-point and the reference frame point O_2 in the swivel axis. Then,

$$S_2 = x - p_1 \quad (4.16)$$

where S_2 is the displacement of the first prismatic actuator. Considering the selected design parameters of the link lengths, actuators limits, and pivot-point position x then the inverse kinematics and needed actuators' values can be obtained. As can be seen from Equation 4.12 and Equation 4.16, with the given information of the rotated sagittal angle, the desired pivot-point location, and the required insertion value, the corresponding actuator inputs can be obtained. It can also be noted that while changing the rotated sagittal angle to compensate for the pivot-point position and the insertion value, the two prismatic actuators are coupled through these equations. By applying these simple equations and with a high performance of the actuation system and controller, the RCM can be guaranteed in this mechanism. The velocity analysis can be conducted by driving the Jacobian matrix to find actuator velocity limits that can guarantee a synchronized motion and fixed RCM during path trajectory. However, further investigations of structural and dynamic analyses of this prototype have not been performed due to the selection of the other option of the active robot mechanism that is presented in the next section.

4.3.2. Mechanism of the Selected Spatial Parallel Manipulator

The second design is the spatial parallel mechanism which was first presented by Yaşır and Kiper (2018). The mechanism comprises of three legs as shown in Figure 4.5. Each i^{th} leg has the links of length a_i , b_i , and c_i connected by revolute joints. Each leg is connected with the ground by a universal joint. The last link in the 3rd leg (the leg in the middle) is connected rigidly to the moving platform, whereas 1st and 2nd legs are connected by revolute joints with identical axes concurrent with the telescope axis and therefore passing through the RCM. This mechanism can produce 2R1T (two rotational

motion and one translational along with the endoscope) and guarantees the telescope to pass through the RCM by its mechanical constraints inherently. To generate and control these motions, three actuators to be mounted. The three actuators provide input motion for the angles θ_1 , θ_2 , and θ_3 as shown in Figure 4.6. The axes of rotations of the angles θ_1 and θ_2 are intersecting at point D that represents the position of the RCM at the pivot-point. These two input angles are responsible for the orientation of the endoscope in a decoupled manner. On the other hand, the third angle θ_3 is for controlling the insertion amount of the endoscope.

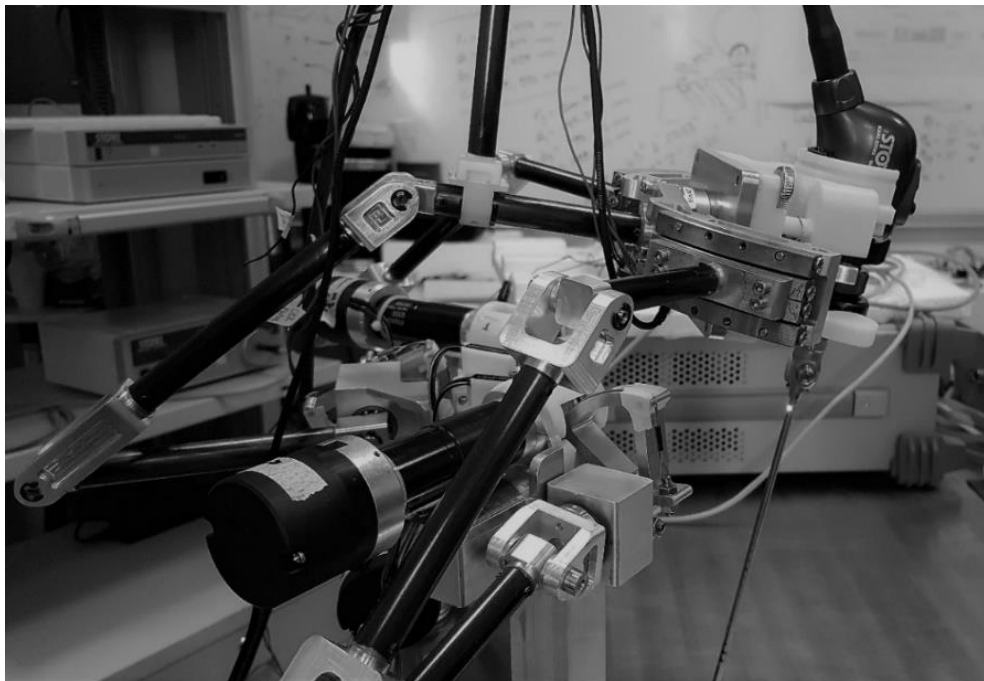


Figure 4.5. The prototype of the selected design of the NeuRoboScope system, the spatial parallel manipulator

This special parallel mechanism has 3 DOF to generate a 3-dimensional workspace. All of the dimensions have been designed to cope with this surgical workspace as can be seen in (Yaşır, Kiper, and Dede, 2020). It needs to be noted that the motion of the third angle θ_3 is coupled with the motion for each of the angles θ_1 and θ_2 to maintain a constant insertion value. For this reason, to make the motion smooth, the coupled input angles need to operate synchronously. The feature of mechanical RCM can provide valuable safety to the patient. This feature leads to the decision of selecting this design for the NeuRoboScope system. However, a failure of θ_3 in leg 3 can lead to a motion of the endoscope to fall downward to undesired insertion value.

The next Sections are the kinematic and dynamic analyses of the proposed active parallel manipulator.

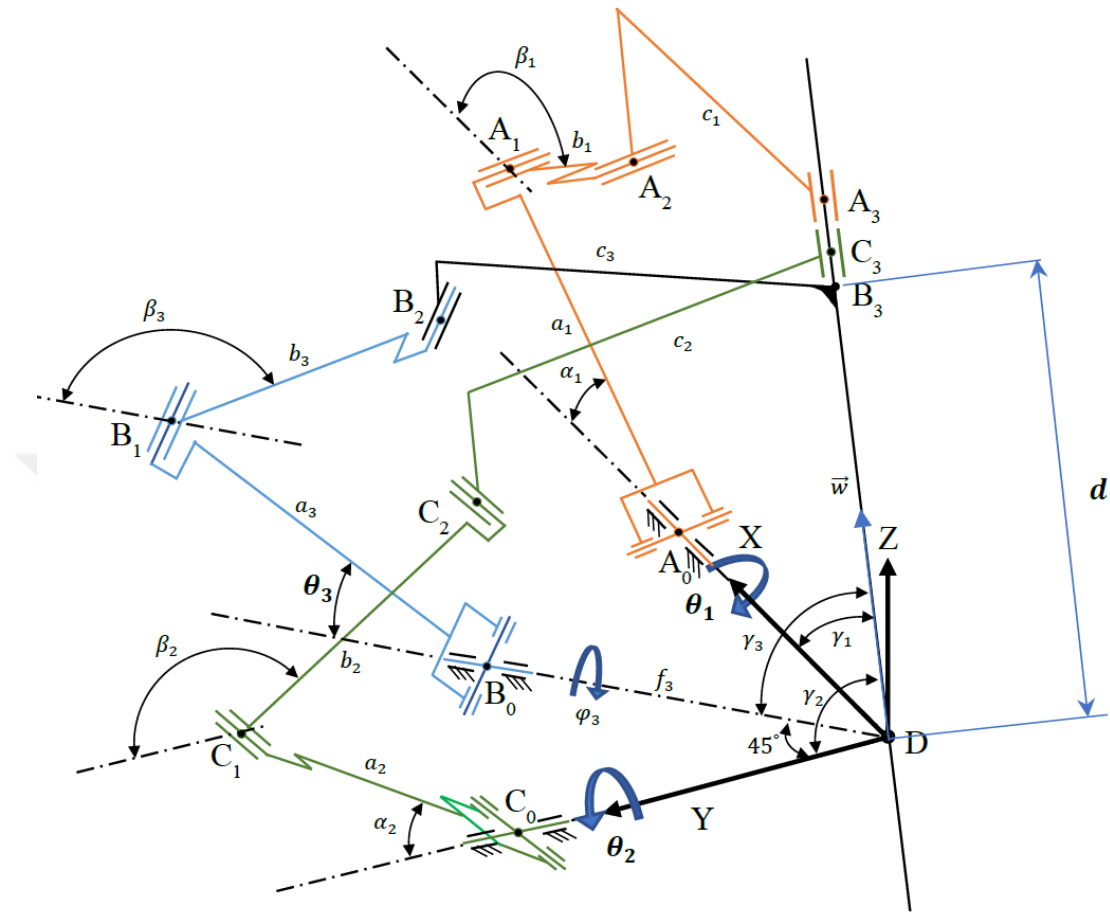


Figure 4.6. A schematic illustration of the parallel manipulator

4.3.3. Kinematic Analysis of the Selected Spatial Parallel Manipulator

The following subsections represent the kinematic analysis of the proposed spatial parallel manipulator. This kinematic analysis is used in the inverse dynamic problem in the next section.

4.3.3.1. Inverse Kinematic Analysis of the Spatial Parallel Manipulator

In the inverse kinematics, active joint variables θ_1 , θ_2 and θ_3 are needed to be determined depending on the desired pose of the endoscope. The motion of the endoscope is represented by the desired position and orientation at the workspace as d ,

ψ , and ϕ . Based on the definitions in Chapter 3, the angle ψ is the rotation angle around the y-axis and the angle ϕ is the rotation angle around the rotated x-axis as shown in Figure 4.7.

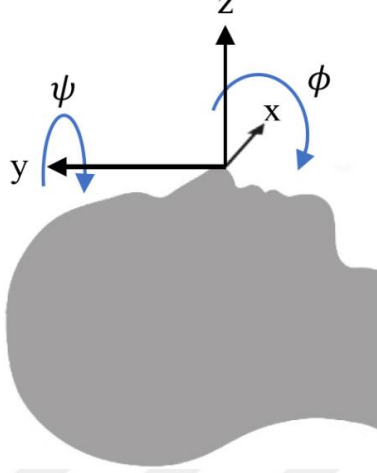


Figure 4.7. The global reference frame with respect to the patient

The direction of the endoscope's location with respect to the reference frame of the parallel manipulator is represented by a unit vector \vec{P} . This unit vector represents the position vector of the endoscope (directed upward) as a function of ϕ and ψ angles with respect to the global frame as shown in Figure 4.8.

The rotation matrix for desired endoscope orientation introduced as a rotation around the y-axis by ψ angle then followed by a rotation around the rotated x-axis by ϕ angle.

$$\hat{R}_y = \begin{bmatrix} \cos \psi & 0 & \sin \psi \\ 0 & 1 & 0 \\ -\sin \psi & 0 & \cos \psi \end{bmatrix}, \hat{R}_x = \begin{bmatrix} 1 & 0 & 0 \\ 0 & \cos \phi & -\sin \phi \\ 0 & \sin \phi & \cos \phi \end{bmatrix} \quad (4.17)$$

Then these successive rotations are written as the rotation matrix \hat{R}_{GE} as the rotation from the global to the endoscope frame

$$\hat{R}_{GE} = \hat{R}_y \hat{R}_x \quad (4.18)$$

$$\vec{P} = \hat{R}_{GE} \begin{bmatrix} 0 \\ 0 \\ 1 \end{bmatrix} = \begin{bmatrix} \sin \psi \cos \phi \\ -\sin \phi \\ \cos \psi \cos \phi \end{bmatrix} \quad (4.19)$$

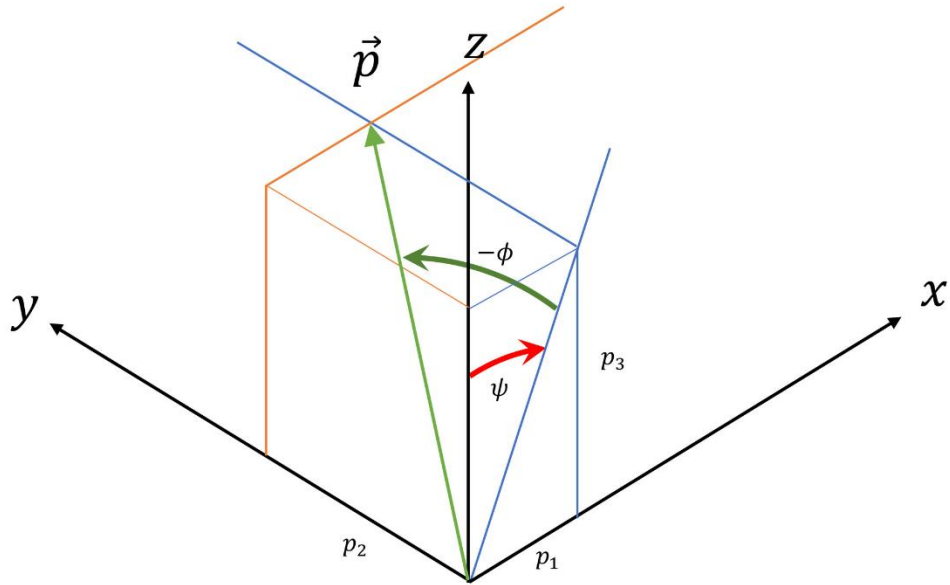


Figure 4.8. The unit vector in the global frame

Considering the forward kinematics of the passive arm, \hat{R}_{GM} represents the transformation matrix from the global frame to the manipulator's frame. Now the same unit vector \vec{p} can be represented in the manipulator's frame to obtain,

$$\vec{w} = \begin{bmatrix} w_1 \\ w_2 \\ w_3 \end{bmatrix} = \hat{R}_{GM}^{-1} \vec{p} \quad (4.20)$$

Noting that θ_1 and θ_2 are the angle of rotations around fixed X-axis and fixed Y-axis of the manipulator's frame respectively in the parallel manipulator. The defined unit vector \vec{w} can be related to θ_1 and θ_2 as shown in Figure 4.9 by the following equations

$$w_1 = w_3 \tan(\theta_2) \quad (4.21)$$

$$w_2 = w_3 \tan(-\theta_1) \quad (4.22)$$

$$w_3 = \sqrt{\frac{1}{1 + (\tan \theta_2)^2 + (\tan \theta_1)^2}} \quad (4.23)$$

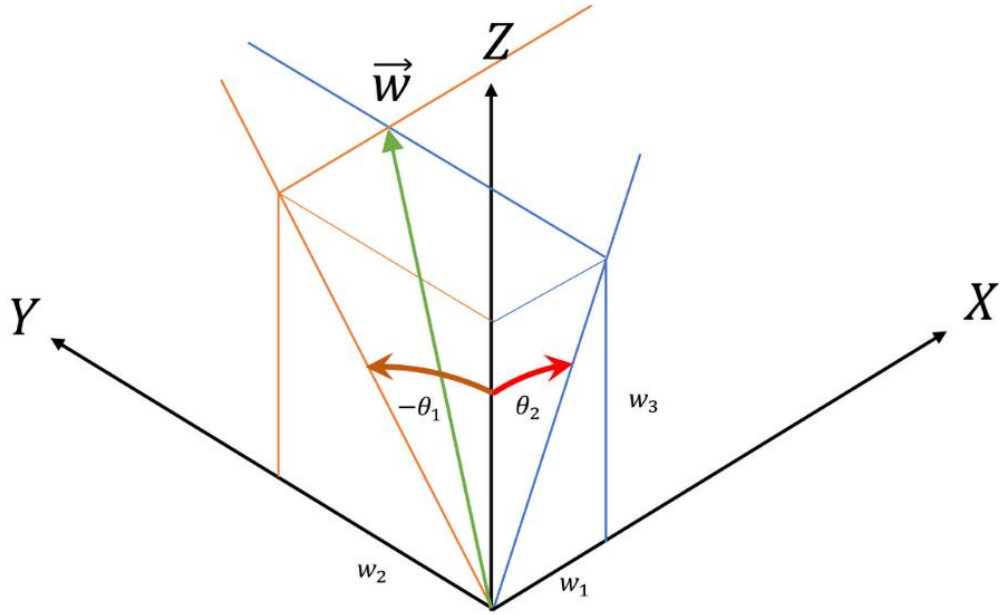


Figure 4.9. The unit vector in manipulator's reference frame

Then, each of θ_1 and θ_2 can be calculated as

$$\theta_1 = \tan^{-1} \left(\frac{-w_2}{w_3} \right) \quad (4.24)$$

$$\theta_2 = \tan^{-1} \left(\frac{w_1}{w_3} \right) \quad (4.25)$$

To find angular speed and acceleration, the first and the second time derivatives of θ_1 and θ_2 are obtained as $\dot{\theta}_1$, $\ddot{\theta}_1$, $\dot{\theta}_2$ and $\ddot{\theta}_2$.

The 3rd leg with the axis of the endoscope generates a subsystem of a closed-loop slider-crank mechanism. This subsystem acts on the virtual plane, as presented in Figure 4.10, and consists of three revolute joints and one virtual prismatic joint along the intersection of the virtual planes of leg 1 and leg 2.

This linear motion is generated as a result of the mechanical constraint imposed by these two legs. The necessary inputs for this analysis are γ_3 angle and the link length d which is considered as the desired value of the sliding/prismatic joint. Noting that γ_3 is a function of θ_1 and θ_2 and it can be calculated as

$$\gamma_3 = \sin^{-1}(w_3). \quad (4.26)$$

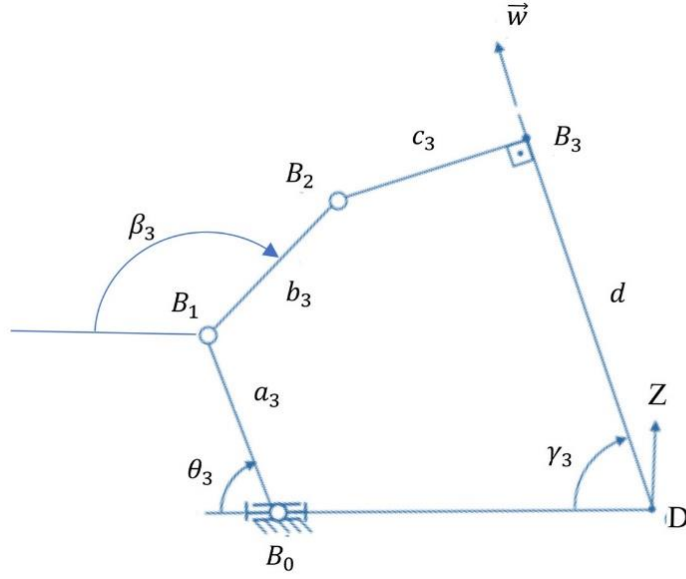


Figure 4.10. The work plane of the 3rd leg.

By taking the first and the second time derivatives of Equation 4.26, $\dot{\gamma}_3$ and $\ddot{\gamma}_3$ can be obtained. To find θ_3 , the Euclidean norm of $\overline{B_1B_2}$ represents the scalar value which is the link length b_3 and it can be calculated as:

$$\|(d - ic_3)e^{-i\gamma_3} - f_3 - a_3e^{-i\theta_3}\| = b_3. \quad (4.27)$$

The variable d is the distance from the moving platform (the gripper of the endoscope) to the RCM. Equation 4.27 have a relation between θ_1 , θ_2 , θ_3 and d and can be rewritten as

$$C = A \cos \theta_3 + B \sin \theta_3 \quad (4.28)$$

where

$$A = 2d a_3 \cos \gamma_3 + 2c_3 a_3 \sin \gamma_3 - 2f_3 a_3 \quad (4.29)$$

$$B = 2d a_3 \sin \gamma_3 - 2c_3 a_3 \cos \gamma_3 \quad (4.30)$$

$$C = (d \cos \gamma_3 + c_3 \sin \gamma_3 - f_3)^2 + (d \sin \gamma_3 + c_3 \cos \gamma_3)^2 + a_3^2 - b_3^2. \quad (4.31)$$

Remembering that γ_3 is a function of θ_1 and θ_2 , by these equations θ_3 can be found as a function of θ_1 , θ_2 and d as follows

$$M = \sqrt{(A^2 + B^2)} \quad (4.32)$$

$$\sigma = \tan^{-1}\left(\frac{B}{A}\right) \quad (4.33)$$

$$N = \cos^{-1}\left(\frac{C}{M}\right) \quad (4.34)$$

$$\theta_3 = \sigma - N \quad (4.35)$$

The first and second time derivative of θ_3 lead to obtain $\dot{\theta}_3$ and $\ddot{\theta}_3$, respectively.

To this point, all required motion (position, velocity, and acceleration) information at actuators θ_1 , θ_2 and θ_3 are found as functions of the corresponding motion of the endoscope attached to the moving platform.

4.3.3.2. Forward Kinematic Analysis of the Spatial Parallel Manipulator

In this section all the remaining passive joint variables between the links are calculated as functions of θ_1 , θ_2 and θ_3 so that they will be used later in calculating positions, velocities, and accelerations of the center of mass of each connecting link. To find φ_3 , first, the unit vector defined as $\vec{w}^{(b)}$ as the same unit vector \vec{w} but defined in the new rotated frame (b) along the base of leg 3 (rotation around Z-axis by 45° , so the x-axis of frame (b) is pointed toward point B_0) in Figure 4.11 as

$$\vec{w}^{(b)} = \hat{R}_{z,-45} \vec{w} \quad (4.36)$$

$$\varphi_3 = \tan^{-1} \frac{-w_{b2}}{w_{b3}} \quad (4.37)$$

The first and second derivatives of φ_3 are obtained as $\dot{\varphi}_3$ and $\ddot{\varphi}_3$ respectively. Since the variables are θ_1 and θ_2 , the resulted equations have the derivatives of these variables as well.

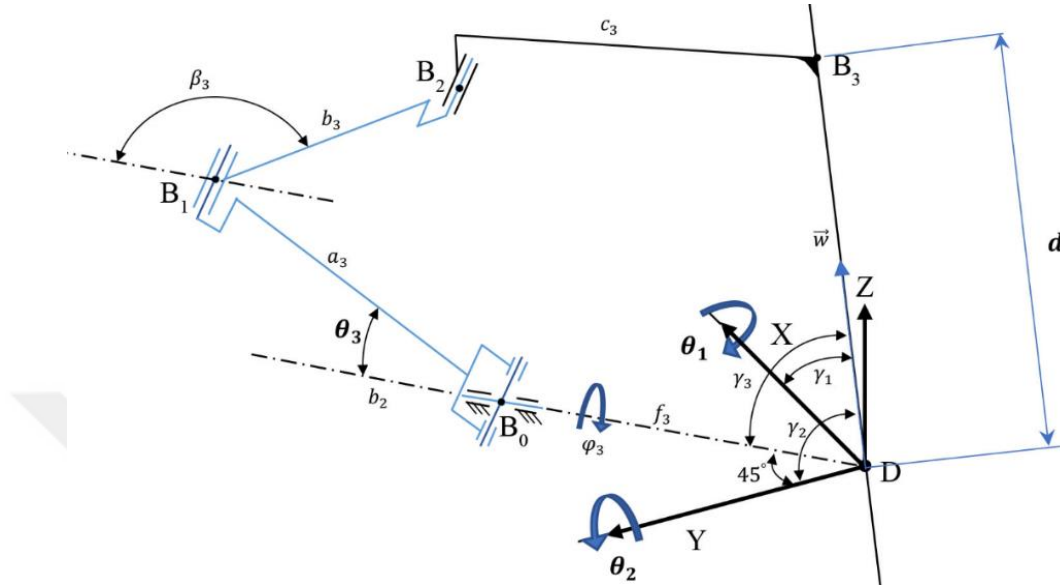


Figure 4.11. A schematic illustration of leg 3

Similar to the determination of γ_3 , γ_1 and γ_2 can be calculated as follows. Considering the positive values of the angles for the solutions below:

$$\gamma_1 = \cos^{-1} w_1 \quad (4.38)$$

$$\gamma_2 = \cos^{-1} w_2 \quad (4.39)$$

As a part of the forward kinematic solution, the distance d as a function of θ_1 , θ_2 and θ_3 is calculated by recalling the Euclidean norm calculated in Equation 4.27. Then, Equations 4.28 ~ 4.31 can be rewritten to have a quadratic form of the equation as:

$$d^2 + B_d d + C_d = 0 \quad (4.40)$$

Among the available two solutions that can be generated in having two possible configurations of $\pm\beta_3$, the positive solution is considered as the value of d . However, when two positive roots obtained then the greater value to be selected to have the

moving platform away up from the patient's head. The first and second derivatives are calculated by differentiating the equation of d with respect to time.

To find β_3 , the position of B_2 is calculated in two ways to determine the loop-closure equation:

$$f_3 + a_3 e^{i\theta_3} + b_3 e^{i\beta_3} = (d - ic_3) e^{i\gamma_3} \quad (4.41)$$

Then it can be rewritten as

$$XB = d \cos \gamma_3 + c_3 \sin \gamma_3 - f_3 - a_3 \cos \theta_3 \quad (4.42)$$

$$YB = d \sin \gamma_3 + c_3 \cos \gamma_3 - a_3 \sin \theta_3 \quad (4.43)$$

$$\tan \beta_3 = \frac{YB}{XB} \quad (4.44)$$

Time derivatives can be taken to find speed and acceleration information related to β_3 value, $\dot{\beta}_3$ and $\ddot{\beta}_3$. Since, there are three similar series of links in the legs, the same steps can be followed in finding θ_3 and β_3 to find $\alpha_1, \dot{\alpha}_1, \ddot{\alpha}_1, \alpha_2, \dot{\alpha}_2, \ddot{\alpha}_2, \beta_1, \dot{\beta}_1, \ddot{\beta}_1, \beta_2, \dot{\beta}_2,$ and $\ddot{\beta}_2$.

Having the angular speed and acceleration of each link in hand makes it easy to compute the acceleration of the centers of masses. This can be done by taking the first and the second time derivative of the position of the center of masses for each link. Next, a sample calculation for leg 1 that is shown in Figure 4.12 is presented

$$\bar{p}_{r_1} = \begin{bmatrix} f_1 \\ 0 \\ 0 \end{bmatrix} + \hat{R}_{x,\theta_1} \bar{c}_{r_1} \quad (4.45)$$

where \hat{R}_{x,θ_1} is a rotation matrix around X-axis with angle θ_1 , \bar{c}_{r_1} is the position vector of the center of mass of the first link r_1 of leg 1 with respect to the reference frame of the link. f_1 is a scalar distance value between the two points D and A_0 , and \bar{p}_{r_1} is the position vector of the center of mass of the first link with respect to the manipulator's

reference frame. The double derivative of any center of mass position can be calculated to find the vector of the linear acceleration of the link's mass center

$$\ddot{\vec{p}}_{r_1} = \frac{d^2 \vec{p}_{r_1}}{dt^2} \quad (4.46)$$

Following the same steps, all linear acceleration vectors can be found for all center of masses for each moving part of this mechanism as

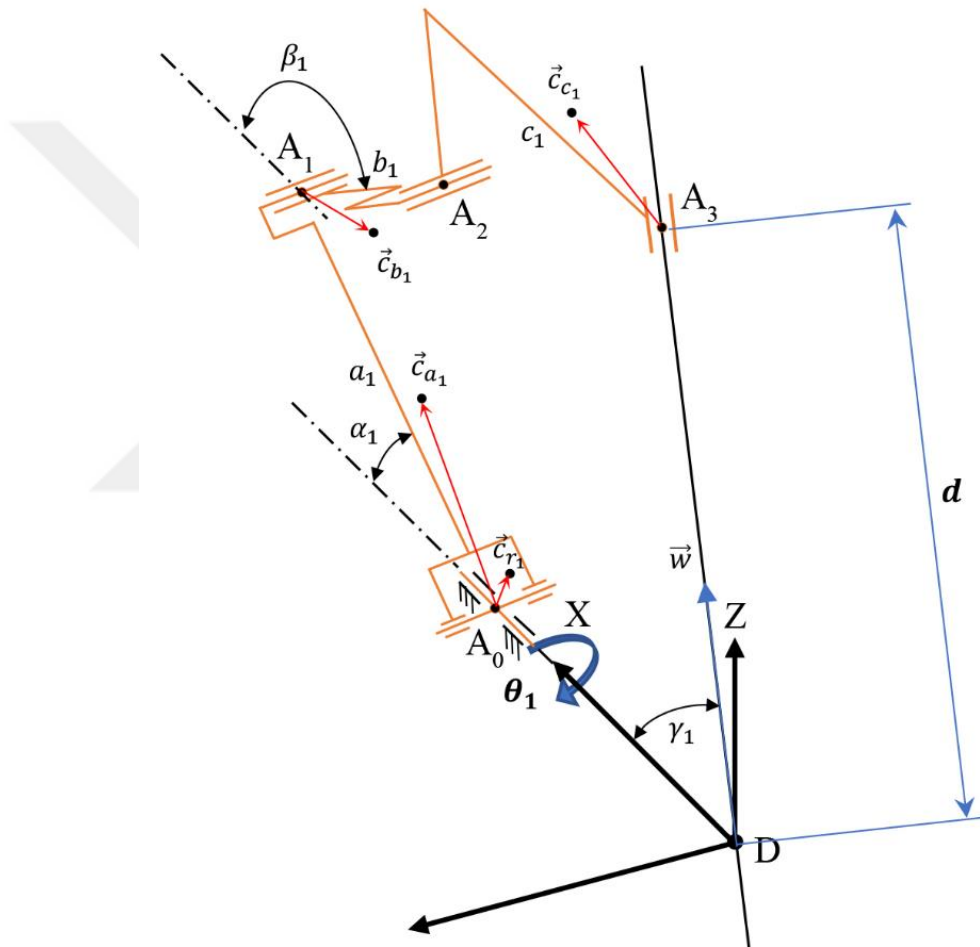


Figure 4.12. The center of masses for leg 1

$$\vec{p}_{a_1} = \begin{bmatrix} f_1 \\ 0 \\ 0 \end{bmatrix} + \hat{R}_{x,\theta_1} \hat{R}_{y,-\alpha_1} \vec{c}_{a_1} \quad (4.47)$$

$$\vec{p}_{b_1} = \vec{p}_{A_1} + \hat{R}_{x,\theta_1} \hat{R}_{y,-\beta_1} \vec{c}_{b_1} \quad (4.48)$$

where \vec{p}_{A_1} is the position vector of the point A_1 with respect to the manipulator's reference frame.

$$\bar{p}_{c_1} = d\bar{w} + \hat{R}_{x,\theta_1} \hat{R}_{y,-\gamma_1} \bar{c}_{c_1} \quad (4.49)$$

Position and acceleration vectors of the moving parts of leg 2 and leg 3 can be calculated following a similar procedure.

4.3.4. Dynamic Analysis of the Selected Spatial Parallel Manipulator

The solution of the inverse dynamic problem consists of finding the torque/force amounts that are required to actuate the input link to produce the specified trajectory. Dynamic analysis of spatial parallel manipulators has to be studied since the dynamic analysis provides fundamental information in system modeling to be used in simulation tests and in application of nonlinear control algorithms (Maarroof, Gezgin, and Dede, 2012). This dynamic model can also be used in the design process and in the analysis of the capability of the manipulator. There are many approaches for solving dynamic analysis of serial manipulators and also applied for spatial parallel mechanisms such as: recursive Newton-Euler method, Lagrange formulation method (Lee and Shah, 1988), virtual work based method (Wang and Gosselin, 1998); Hamilton's principle (Miller, 2004), the D'Alembert's principle, Kane method (Kane and Levinson, 1983); and Gibbs-Appell method (Abedloo, Molaei, and Taghirad, 2014).

Some simplification approaches of these methods were proposed such as in (Elgolli et al., 2019; Özgür, Andreff, and Martinet, 2013). A classification of the classical dynamic approaches in the literature for parallel manipulators has been presented by Müller (2020). The classification is done as analytic and synthetic approaches with regard to: the formulation of the coordinates, the formulation in redundant coordinates, and in minimal independent coordinates. Müller (2020) presented a systematic Lie Group formulation for modeling approach on the majority of spatial parallel manipulators. In some cases, more than one method can be used simultaneously such as the decomposition of the mechanism and using the Lagrange and the Newton-Euler methods in (Dede, Maarroof, and Ceccarelli, 2018), and the

improved method by Elgolli et al. (2019) using the D'Alembert's principle and Kane method to get to the overall dynamic equation of a mechanism.

The most frequently used method is the recursive Newton-Euler formulation. By this approach, the free-body diagrams of each link of the manipulator are considered and the Newton-Euler equations can be applied to compute forces and moments between links. Even though the constraint forces and moments are useful for the design process, they are not presented in the control of manipulators (Wang and Gosselin, 1998). In the case of spatial parallel mechanisms, the number of moving masses is much more than the number of DOF of the mechanism. This makes the number of contact forces and moments high and the number of generated equations by Newton-Euler is high as well. This is observed in the first attempt for the inverse dynamic solution of the selected spatial parallel mechanism.

The Lagrangian approach provides an analytical formulation of the dynamic equations of motion. Most of the moving links are dependent on more than one input value of the actuators as known for the forward kinematics solution of parallel manipulators, and this makes the application of this approach relatively more complex in general. Nevertheless, due to the complexity of the kinematics of the spatial parallel manipulators, some simplifications are essential for simplifying the terms of kinetic and potential energy. Therefore, this method is not always efficient for dynamic analysis of parallel manipulators. The selection of the method depends on various criteria such as type of the mechanism, the details and complexity of its components, algorithm of control to be used, capability of the computer for computations, the tolerance of the error and finally the assumptions to be applied in the calculations.

The virtual work approach proposed by Wang and Gosselin (1998) can be a practical approach for the dynamic analysis of planar and spatial parallel mechanisms and can lead to faster computational algorithms when compared with the Newton-Euler approach. Accordingly, in this study, the frictional forces are omitted, and the mechanical system is considered to be under the influence of only conservative forces and moments. The dynamic analysis used of the system is based on the principle of virtual work. First, the inertial force and moments are computed using the linear and angular accelerations of each moving link. In the principle of this method, the manipulator is assumed to be in equilibrium and the principle of virtual work is applied to derive the equilibrium equations. Since constraint forces and moments are not needed

to be computed, this approach leads to faster computational algorithms, which is an important advantage for the control of a manipulator.

The objective of this subsection is to define the dynamical model of the mechanism that gives the exact analytical solution. The inverse dynamic calculation will provide enough information for designing and selecting of actuation methodology and capabilities. The exact complex dynamic solution can also be used to optimize the simplified dynamic solution to be used in the controller design task with optimum performance in real-time control.

4.3.4.1. Calculation of the Inertia Forces and Moments

The inertia force and moment acting on a rigid body are exerted at the center of mass of the body. Following D'Alembert's principle (Wells, 1967), the direction of the applied forces and moments are in a direction opposite to the direction of the linear and angular acceleration vectors. Identifying these forces and moments allows one to consider the mechanism in an equilibrium condition. As the linear accelerations of the center of masses and angular accelerations of the links are computed earlier, one can easily compute the forces acting at the center of masses and moments on each moving link as shown in Figure 4.13. These forces and moments are including inertial forces and moments and the weights of each link. A general form of forces can be written as

$$\bar{F}_i = -m_i \bar{a}_i + m_i \bar{g} \quad (4.50)$$

When, \vec{F}_i is the force vector acting on the center of mass of link i , which composed of the forces due to the motion of the center of mass and gravitational force. m_i is the mass of link i , \vec{a}_i is the linear acceleration vector of the center of mass, and \vec{g} is the gravitational acceleration vector. In Equation 4.50, all of the vectors on link i are resolved in manipulator's reference frame.

A sample of calculation performed on leg 1 is shown in Figure 4.13 and formulated as follows

$$\bar{F}_{r_1} = -m_{r_1}(\ddot{p}_{r_1} - \bar{g}) \quad (4.51)$$

$$\bar{F}_{a_1} = -m_{a_1}(\ddot{p}_{a_1} - \bar{g}) \quad (4.52)$$

$$\bar{F}_{b_1} = -m_{b_1}(\ddot{p}_{b_1} - \bar{g}) \quad (4.53)$$

$$\bar{F}_{c_1} = -m_{c_1}(\ddot{p}_{c_1} - \bar{g}) \quad (4.54)$$

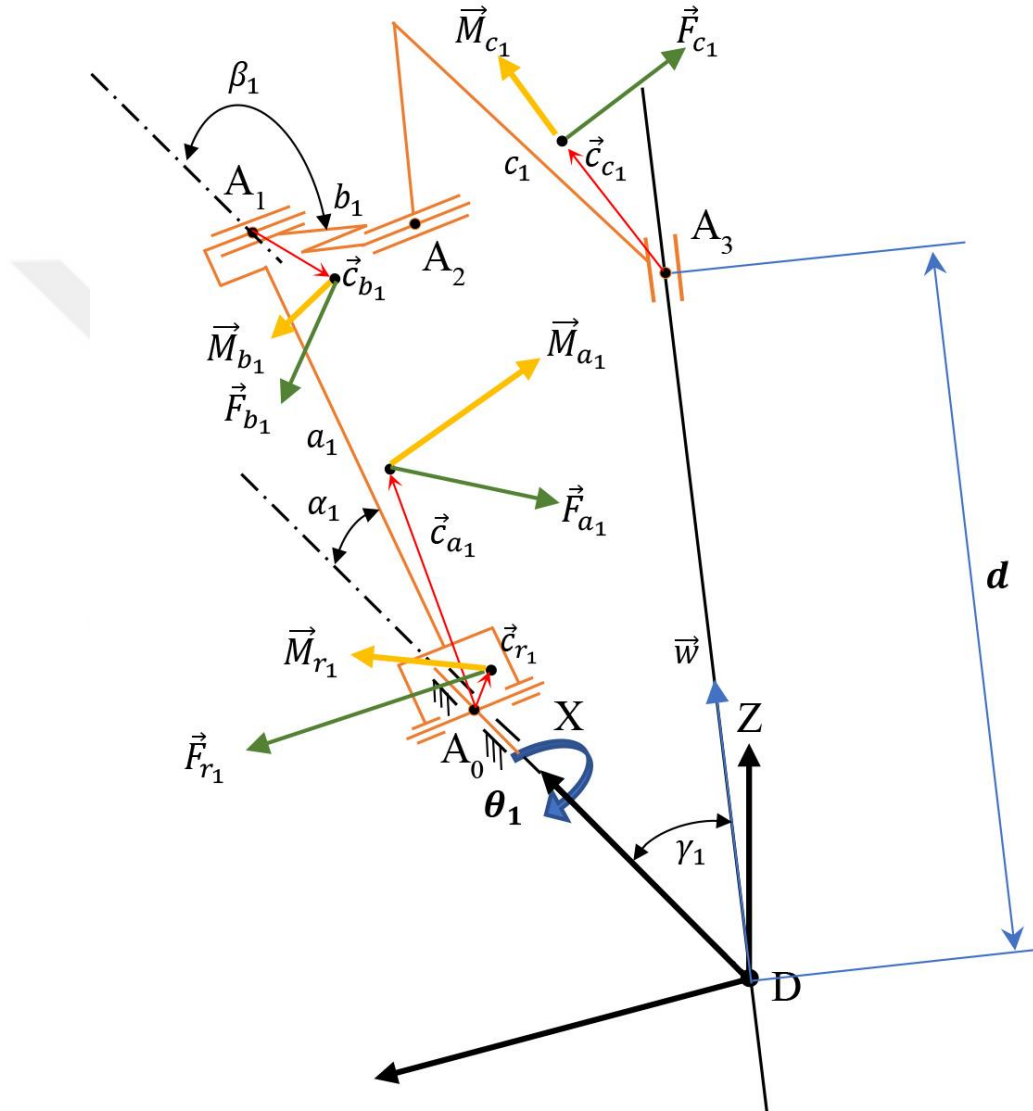


Figure 4.13. Load distributions on the center of masses

The moment is written in a general form as a vector \bar{M}_i , which is generated from the inertial moment acting on the link i related to the link's motion relative to the manipulator's reference frame.

$$\bar{M}_i = -\hat{I}_i \dot{\omega}_i - \tilde{\omega}_i (\hat{I}_i \bar{\omega}_i) \quad (4.55)$$

where, \hat{I}_i is the inertia matrix of link i about its center of mass resolved in manipulator's reference frame, $\vec{\omega}_i$ and $\dot{\vec{\omega}}_i$ are the angular velocity and angular acceleration vectors respectively as resolved in the manipulator's reference frame. The tilde term represents a cross product matrix (the skew symmetric matrix representation of a column matrix). The angular velocities for each link can be written as a summation of angle rate vectors as resolved in the manipulator's reference frame:

$$\vec{\omega}_{r_1} = \begin{bmatrix} \dot{\theta}_1 \\ 0 \\ 0 \end{bmatrix} \quad (4.56)$$

$$\vec{\omega}_{a_1} = \begin{bmatrix} \dot{\theta}_1 \\ 0 \\ 0 \end{bmatrix} + \hat{R}_{x,\theta_1} \begin{bmatrix} 0 \\ -\dot{\alpha}_1 \\ 0 \end{bmatrix} \quad (4.57)$$

$$\vec{\omega}_{b_1} = \begin{bmatrix} \dot{\theta}_1 \\ 0 \\ 0 \end{bmatrix} + \hat{R}_{x,\theta_1} \begin{bmatrix} 0 \\ -\dot{\beta}_1 \\ 0 \end{bmatrix} \quad (4.58)$$

$$\vec{\omega}_{c_1} = \begin{bmatrix} \dot{\theta}_1 \\ 0 \\ 0 \end{bmatrix} + \hat{R}_{x,\theta_1} \begin{bmatrix} 0 \\ -\dot{\gamma}_1 \\ 0 \end{bmatrix} \quad (4.59)$$

Angular accelerations are determined by taking the time derivative of the angular velocities as follows:

$$\dot{\vec{\omega}}_{r_1} = \begin{bmatrix} \ddot{\theta}_1 \\ 0 \\ 0 \end{bmatrix} \quad (4.60)$$

$$\dot{\vec{\omega}}_{a_1} = \begin{bmatrix} \ddot{\theta}_1 \\ 0 \\ 0 \end{bmatrix} + \hat{R}_{x,\theta_1} \begin{bmatrix} 0 \\ -\ddot{\alpha}_1 \\ 0 \end{bmatrix} + \frac{d(\hat{R}_{x,\theta_1})}{dt} \begin{bmatrix} 0 \\ -\dot{\alpha}_1 \\ 0 \end{bmatrix} \quad (4.61)$$

$$\dot{\vec{\omega}}_{b_1} = \begin{bmatrix} \ddot{\theta}_1 \\ 0 \\ 0 \end{bmatrix} + \hat{R}_{x,\theta_1} \begin{bmatrix} 0 \\ -\ddot{\beta}_1 \\ 0 \end{bmatrix} + \frac{d(\hat{R}_{x,\theta_1})}{dt} \begin{bmatrix} 0 \\ -\dot{\beta}_1 \\ 0 \end{bmatrix} \quad (4.62)$$

$$\dot{\bar{\omega}}_{c_1} = \begin{bmatrix} \dot{\theta}_1 \\ 0 \\ 0 \end{bmatrix} + \hat{R}_{x,\theta_1} \begin{bmatrix} 0 \\ -\dot{\gamma}_1 \\ 0 \end{bmatrix} + \frac{d(\hat{R}_{x,\theta_1})}{dt} \begin{bmatrix} 0 \\ -\dot{\gamma}_1 \\ 0 \end{bmatrix} \quad (4.63)$$

According to the rotational motion information of each link, the inertial moments formed at each link of leg 1 is calculated as follows:

$$\bar{M}_{r_1} = -\hat{I}_{r_1} \dot{\bar{\omega}}_{r_1} - \tilde{\omega}_{r_1} (\hat{I}_{r_1} \bar{\omega}_{r_1}) \quad (4.64)$$

$$\bar{M}_{a_1} = -\hat{I}_{a_1} \dot{\bar{\omega}}_{a_1} - \tilde{\omega}_{a_1} (\hat{I}_{a_1} \bar{\omega}_{a_1}) \quad (4.65)$$

$$\bar{M}_{b_1} = -\hat{I}_{b_1} \dot{\bar{\omega}}_{b_1} - \tilde{\omega}_{b_1} (\hat{I}_{b_1} \bar{\omega}_{b_1}) \quad (4.66)$$

$$\bar{M}_{c_1} = -\hat{I}_{c_1} \dot{\bar{\omega}}_{c_1} - \tilde{\omega}_{c_1} (\hat{I}_{c_1} \bar{\omega}_{c_1}) \quad (4.67)$$

4.3.4.2. The Virtual Displacements of Each Link

Regarding the virtual angular displacement of the input $\delta\theta_k$ at leg j , the virtual displacement in linear displacement of the center of mass of link i and angular displacement of link i can be defined as the vectors $\delta\bar{p}_{i_j}$ and $\delta\bar{\Omega}_{i_j}$ respectively as seen in manipulator's reference frame. Then, the partial derivative (the ratio of the virtual displacements \bar{p}_{i_jk}) of the general virtual linear displacement of link i with respect to the virtual displacement at the actuator ($\delta\theta_k$) can be defined as

$$\bar{p}_{i_jk} = \frac{\delta\bar{p}_{i_j}}{\delta\theta_k} \quad (4.68)$$

Then, Equation 4.68 can be used for all centers of masses for each link.

First the vector $\bar{\Omega}_{i_j}$ can be defined as the vector of the principal angular rotation around the manipulator's reference frame for link i at leg j . Then, the partial derivative of the general virtual angular displacement of link i with respect to the virtual displacement of the actuated joint ($\delta\theta_k$) can be defined as follows

$$\bar{\Omega}_{ijk} = \frac{\delta \bar{\Omega}_{ij}}{\delta \theta_k} \quad (4.69)$$

For leg 1, as an example, the partial derivative with respect to the angle θ_1 in the links r , a , b , and c are:

$$\bar{\Omega}_{r_11} = \bar{\Omega}_{a_11} = \bar{\Omega}_{b_11} = \bar{\Omega}_{c_11} = \begin{bmatrix} 1 \\ 0 \\ 0 \end{bmatrix} \quad (4.70)$$

Then, the problem being for a spatial parallel mechanism, each of the translational and rotational virtual displacement for all links of the three legs can be derived by the partial derivative with respect to each of θ_1 , θ_2 , and θ_3 .

4.3.4.3. The Generalized Input Torques

By applying the principle of the virtual work, the generalized input torques to actuate the parallel manipulator regarding the desired input motion can be obtained as:

$$\begin{aligned} & T_1 + \bar{M}_{r_1}^T \bar{\Omega}_{r_11} + \bar{M}_{a_1}^T \bar{\Omega}_{a_11} + \bar{M}_{b_1}^T \bar{\Omega}_{b_11} + \bar{M}_{c_1}^T \bar{\Omega}_{c_11} \\ & + \bar{M}_{r_2}^T \bar{\Omega}_{r_21} + \bar{M}_{a_2}^T \bar{\Omega}_{a_21} + \bar{M}_{b_2}^T \bar{\Omega}_{b_21} + \bar{M}_{c_2}^T \bar{\Omega}_{c_21} + \bar{M}_{r_3}^T \bar{\Omega}_{r_31} \\ & + \bar{M}_{a_3}^T \bar{\Omega}_{a_31} + \bar{M}_{b_3}^T \bar{\Omega}_{b_31} + \bar{M}_{c_3}^T \bar{\Omega}_{c_31} + \bar{F}_{r_1}^T \bar{p}_{r_11} + \bar{F}_{a_1}^T \bar{p}_{a_11} \\ & + \bar{F}_{b_1}^T \bar{p}_{b_11} + \bar{F}_{c_1}^T \bar{p}_{c_11} + \bar{F}_{r_2}^T \bar{p}_{r_21} + \bar{F}_{a_2}^T \bar{p}_{a_21} + \bar{F}_{b_2}^T \bar{p}_{b_21} \\ & + \bar{F}_{c_2}^T \bar{p}_{c_21} + \bar{F}_{r_3}^T \bar{p}_{r_31} + \bar{F}_{a_3}^T \bar{p}_{a_31} + \bar{F}_{b_3}^T \bar{p}_{b_31} + \bar{F}_{c_3}^T \bar{p}_{c_31} = 0 \end{aligned} \quad (4.71)$$

Noting that T_1 can be used to find the necessary amount of torque for the first actuator for input motion of the first leg defined by θ_1 . Same steps can be followed for obtaining the other generalized input torques T_2 and T_3 . As a result, the inverse dynamic analysis is derived by using D'Alembert's principle of virtual work approach. For testing the derived inverse dynamic equations, MATLAB Simulink® tools are used for comparison. The comparative study is between the derived inverse dynamic equation and the Simscape tool called SimMechanics™ that is used for the performance analysis of the mechanical system. As a case study, two rotational and one translational motion

of the endoscope with sufficient frequency are designed as shown in Figure 4.14. A half sinusoidal function of time t is selected for the position trajectory as

$$\phi = \begin{cases} 40^\circ \sin t\pi/2, & \text{for } t < 2; \\ 0, & \text{otherwise} \end{cases} \quad (4.72)$$

$$\psi = \begin{cases} -25^\circ \sin t\pi/2, & \text{for } 2 \leq t < 4; \\ 0, & \text{otherwise} \end{cases} \quad (4.73)$$

$$d = \begin{cases} 170 + 100 \sin t\pi/2, & \text{for } t \geq 4; \\ 170, & \text{otherwise} \end{cases} \text{ (mm)} \quad (4.74)$$

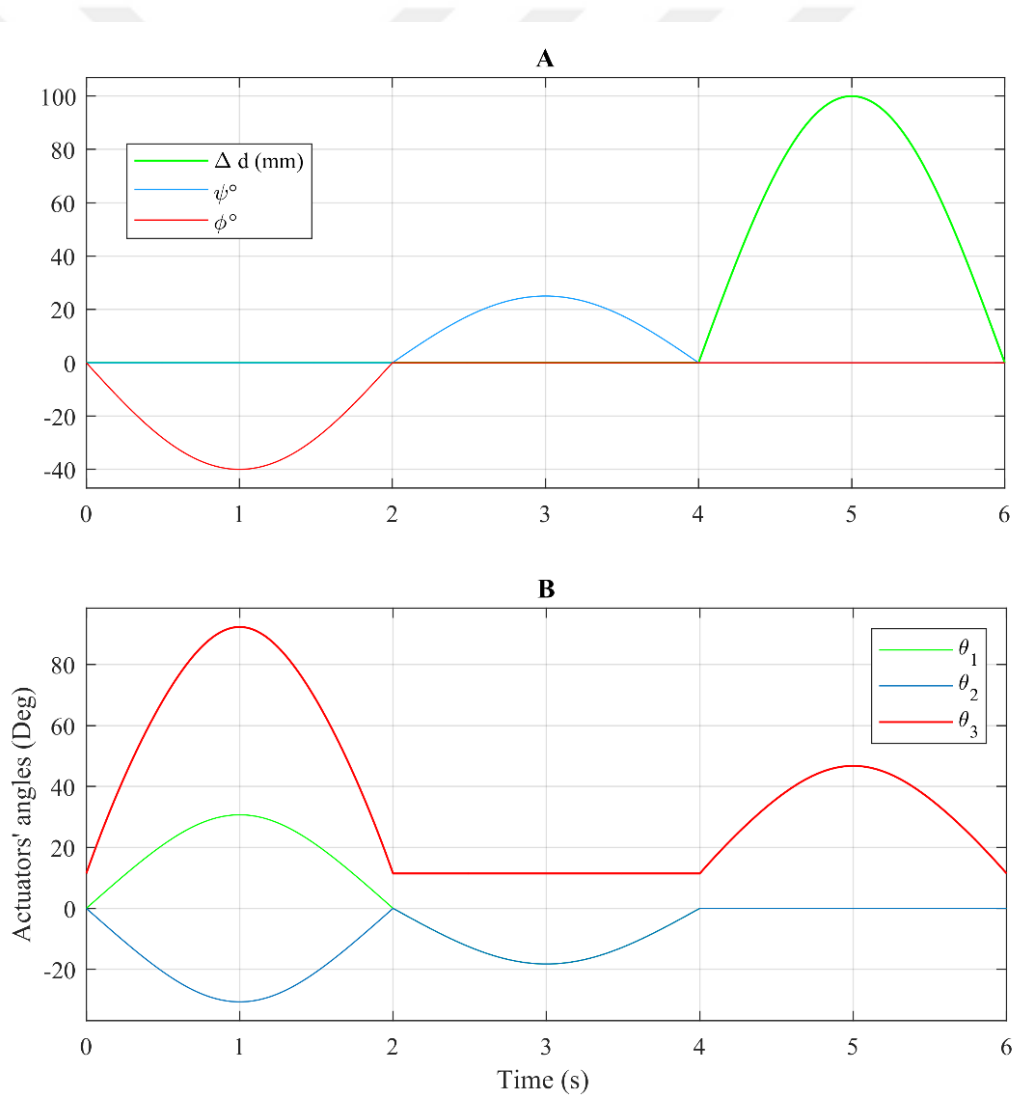


Figure 4.14. The motion trajectory of A) the trajectory of the required motion, B) the generated motion at the actuators.

In this test setup, the mechanical parameters of the spatial parallel manipulator are obtained from its CAD model. The results are presented in Figure 4.15. The maximum torque for this trajectory, which occurred in the second actuator, is 3.2 N·m in the 3rd second. The maximum error in terms of the calculated and simulated torques is 0.0029 N·m determined for the second actuator at the 1st second. The percentage of this error is 0.14% of the maximum torque at the same time.

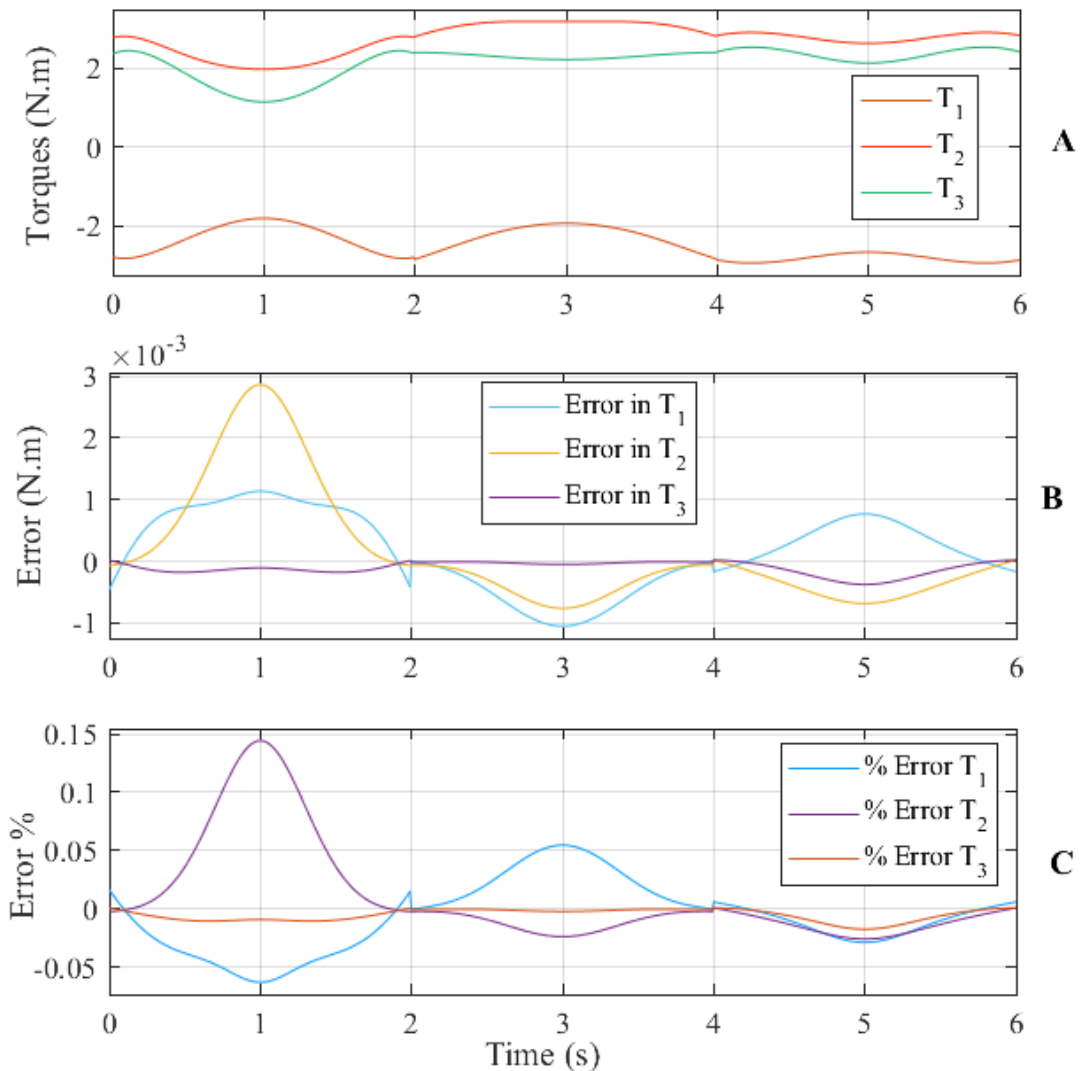


Figure 4.15. The comparison results for A) The calculated torques, B) The error between the calculated and simulated torques, C) The percentages of the error in torque calculation

This solution presents satisfactory accuracy. However, the derived dynamic equations take a relatively long time to be applied for real-time computation. The number of arithmetic operations is minimized for improving the solution time.

Neglecting the small effect of some specific links was also done by Ayit et al. (2018) for this spatial parallel manipulator to see the effect on both the simulation (for verification) and on the real-time controlled manipulation. The satisfactory error value can be decided by an optimum cancellation with the help of this analytical solution along with the control algorithm based on the real-time performance.

4.4. Description of the Passive Arm and Its Kinematic Analysis

The initial design of the passive arm has 5 DOF. Three of them are responsible to restrict the motion for positioning the active arm in Cartesian space. This positioning is done by the horizontal planar motion of the passive joints θ_1 and θ_2 . The third passive joint θ_3 can be considered as the input for the parallelogram loop to have the dependent output angle at the fourth joint θ_4 . This parallelogram loop is responsible for the elevation motion of the active arm. However, the linearly actuated level adjuster shown in Figure 4.16 adds redundancy in elevation amount together with the parallelogram loop. This makes the selection of motion range of the parallelogram loop possible.

These motions help the surgeon to position the active arm with the endoscope to the surgery zone and sometimes for repositioning after cleaning the endoscope. Brakes and encoders are integrated at each independent passive joint to lock the passive arm at a desired pose and record the joint angles to be used in forward kinematics to calculate the location of the RCM, respectively.

Position and orientation of the end-platform of the passive arm are required to be monitored in real-time for checking the position of the RCM with respect to a predefined pivot-point at the surgery zone. On the other hand, orientation monitoring is essential to monitor the working range of the active parallel manipulator within the surgical workspace as well as for the calculation of the required actuators torques in the inverse dynamic equations. To find this information, absolute angular position sensors are used in the design of the passive arm joints.

Forward kinematic analysis is carried out by attaching reference frames on the passive arm joints as shown on the schematic diagram in Figure 4.17. Although the passive arm presented in Figure 4.16 has 5 DOF, the passive arm went through some modifications and optimization that lead to the design presented in Figure 4.17. These

modifications as a result of optimizations are presented in the next Chapters. In this section, the kinematics of the modified passive arm is presented.

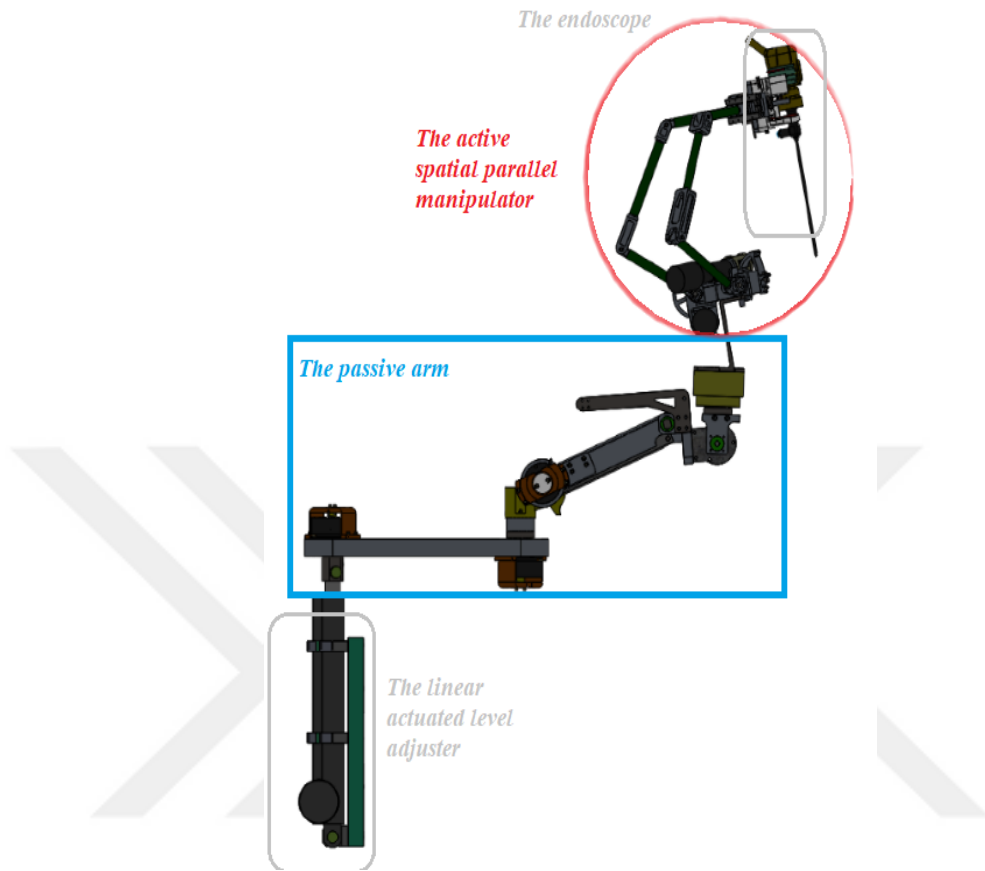


Figure 4.16. The CAD drawing of the robot endoscope holder arm

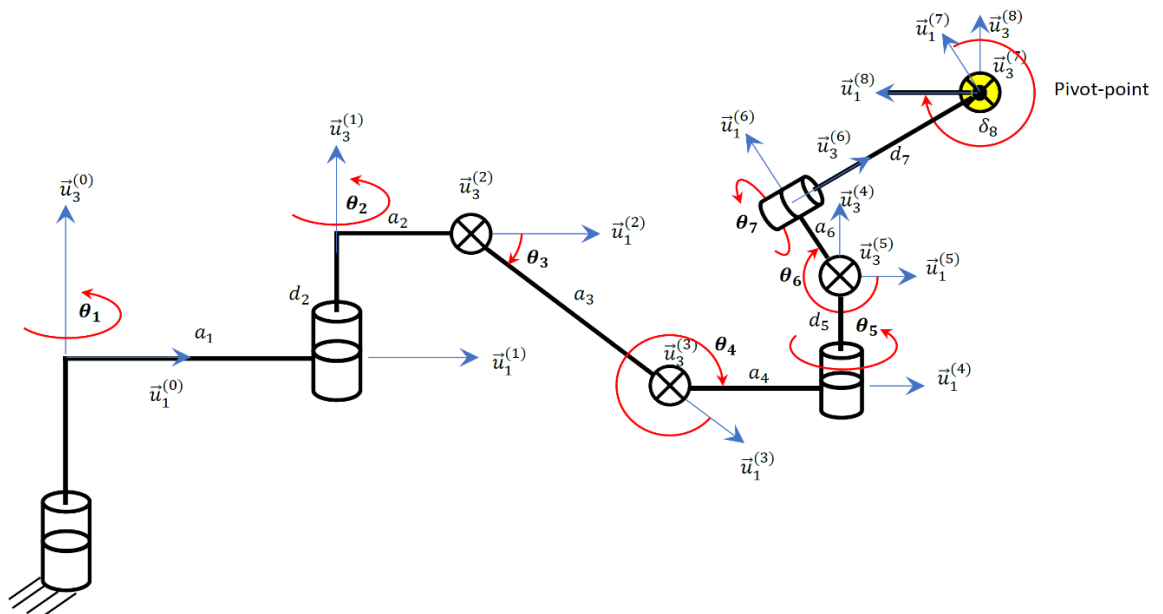


Figure 4.17. Schematic diagram of the passive arm

4.4.1. Forward Kinematic Analysis of the Passive Arm

To relate the coordinate frames and the end-effector pose as shown in Figure 4.17, transformation matrices can be derived using the Denavit-Hartenberg parameters that are tabulated in Table 4.2.

Table 4.2. The Denavit-Hartenberg parameters for the passive arm.

k	d_k	θ_k	a_k	α_k
1	0	θ_1	a_1	0
2	d_2	θ_2	a_2	$-\pi/2$
3	0	θ_3	a_3	0
4	0	θ_4	a_4	$\pi/2$
5	d_5	θ_5	0	$-\pi/2$
6	0	θ_6	a_6	$-\pi/2$
7	d_7	θ_7	0	$\pi/2$

The structural parameter values for the passive arm that are presented in Figure 4.17 and shown in Table 4.2 are listed in Table 4.3.

Table 4.3. The structural parameters

Links' parameters	
a_1	300 mm
a_2	35 mm
d_2	81 mm
a_3	216 mm
b_3	216 mm
c_3	21 mm
d_3	21 mm
a_4	89.5 mm
d_5	45.45 mm
a_6	45 mm
d_7	111 mm
δ_8	282.44°

The corresponding transformation matrices are calculated as

$$\begin{aligned}
\hat{C}^{(0,1)} &= e^{\tilde{u}_3 \theta_1} \\
\hat{C}^{(1,2)} &= e^{\tilde{u}_3 \theta_2} e^{-\tilde{u}_1 \pi/2} \\
\hat{C}^{(2,3)} &= e^{\tilde{u}_3 \theta_3} \\
\hat{C}^{(3,4)} &= e^{\tilde{u}_3 \theta_4} e^{\tilde{u}_1 \pi/2} \\
\hat{C}^{(4,5)} &= e^{\tilde{u}_3 \theta_5} e^{-\tilde{u}_1 \pi/2} \\
\hat{C}^{(5,6)} &= e^{\tilde{u}_3 \theta_6} e^{-\tilde{u}_1 \pi/2} \\
\hat{C}^{(6,7)} &= e^{\tilde{u}_3 \theta_7} e^{\tilde{u}_1 \pi/2} \\
\hat{C}^{(7,8)} &= e^{\tilde{u}_3 \theta_8} e^{-\tilde{u}_1 \pi/2}
\end{aligned} \tag{4.75}$$

Position of RCM can be calculated with respect to the defined global frame as follows

$$\begin{aligned}
\bar{p}_p &= a_1 \hat{C}^{(0,1)} \bar{u}_1 + d_2 \hat{C}^{(0,1)} \bar{u}_3 + a_2 \hat{C}^{(0,2)} \bar{u}_1 + a_3 \hat{C}^{(0,3)} \bar{u}_1 + a_4 \hat{C}^{(0,4)} \bar{u}_1 \\
&\quad + d_5 \hat{C}^{(0,4)} \bar{u}_3 + a_6 \hat{C}^{(0,6)} \bar{u}_1 + d_7 \hat{C}^{(0,6)} \bar{u}_3
\end{aligned} \tag{4.76}$$

4.4.2. Description of the Parallelogram Loop for Gravity Compensation

To keep the orientation stable while the vertical positioning motions provided, a parallelogram loop is used with input and output joint variables as θ_3 and θ_4 . This loop is used in spring-balanced passive arms. To compensate for the gravity, a compression helical spring is installed in the original model along the line h_3 in Figure 4.18. The methodology of gravity compensation provided by the manufacturer is as follows: the vertical force component provided by the compression of the spring axially is designed to keep it equal to the weight regardless of the configuration of the parallelogram loop. To adjust for variable loads, a cam profile is used to realize a variable contact point between a roller fixed at the end of the spring and the point p_3 in Figure 4.18. The preload force applied to the spring can be adjusted to compensate for the change in the masses at the end-effector. The relation between the variables that are shown in Figure 4.18 and the relation between input and output angles can be defined easily.

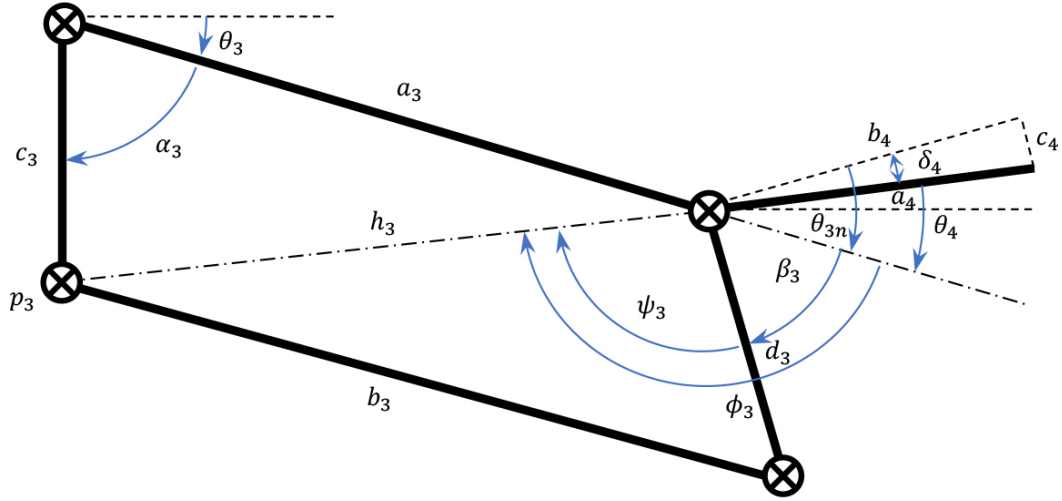


Figure 4.18. The parallelogram loop of the passive arm

$$\alpha_3 = \frac{\pi}{2} - \theta_3 \quad (4.77)$$

$$h_3 = \sqrt{c_3^2 + a_3^2 - 2c_3a_3 \cos \alpha_3} \quad (4.78)$$

$$\bar{p}_3 = \begin{bmatrix} c_3 \cos \alpha_3 - a_3 \\ c_3 \sin \alpha_3 \end{bmatrix} \quad (4.79)$$

$$\phi_3 = \text{atan2}(c_3 \sin \alpha_3, c_3 \cos \alpha_3 - a_3) \quad (4.80)$$

$$\psi_3 = \cos^{-1} \left(\frac{h_3^2 + d_3^2 - b_3^2}{2h_3d_3} \right) \quad (4.81)$$

$$\beta_3 = \phi_3 - \psi_3 \quad (4.82)$$

For a parallelogram, when $a_3 = b_3$ and $c_3 = d_3$ then the output angle equals to the input angle as $\beta_3 = \alpha_3$. Then, the angle on the fourth joint can be calculated as

$$\theta_4 = \beta_3 - \frac{\pi}{2} + \delta_4 \quad (4.83)$$

For $\delta_4 = 0$, $\theta_4 = -\theta_3$, which means that the input angle of the parallelogram loop is equal to the output angle. In this case, the orientation is kept constant, and the

change in position is in a 2-dimensional workspace. The inverse kinematic analysis is not calculated for the passive arm since the mechanical arm is passively driven by the surgeon during operation.

4.5. Conclusions

The general description of the concept that represents the NeuRoboScope is proposed. To select and design the mechanical structure of this surgical system, first, the design requirements are defined. These design requirements are then utilized to have systematic design and selection for the most suitable one considering safety criterion. Two novel designs of the active robot arm are presented. Afterward, a kinematic analysis of the two alternatives is done. Then the dynamic analysis is presented for the selected robot arm. The exact analytical dynamic solution can also be used to optimize any simplified dynamic modeling for optimum performance at real-time controlling of the system. Finally, the first prototype of the passive arm is presented with its kinematic analysis.

CHAPTER 5

MECHANICAL SAFETY FEATURES FOR SURGICAL ROBOTS

Safety features in robotic systems used in RAS can be categorized under many areas. The safety features presented in this Chapter are related to functional mechanical safety features. First, mechanically oriented safety feature additions to the surgical robotic systems that are found in the literature are investigated. Then, specific solutions for the NeuRoboScope system are presented. In this objective, the mechanical effects can be force, vibration, fatigue, or any other mechanical effects that can cause injury directly or indirectly (by the failure of the system). In this Chapter, all added functional mechanical safety features to NeuRoboScope system are force related safety features. The list in Table 5.1 is for the features added by this study, for those added by other studies, and for potential safety features that can be added optionally to the system.

5.1. Surgery Zone Definition

It is necessary to define the surgery zone for safety reasons. Defining the surgery zone can provide precise information about the position of the RCM and the telescope with respect to the pivot-point located on the patient. In addition to the RCM position, for safety reasons, both telescope's tip point and RCM are to be observed whether they are inside or outside the predefined surgery zone (**MSF01**). For collecting this information, in addition to the actuated joints at the active parallel manipulator, all independent joints at the passive arm have encoders installed (**MSF02**). The insertion amount of the endoscope is essentially needed which can give feedback to the surgeon as an indicator of the real amount of the insertion of the telescope's tip point beyond the pivot-point.

Table 5.1. The mechanical safety features

No	Code	Description
1	(MSF01)	Defining the surgery zone
2	(MSF02)	Encoders for all independent joints
3	(MSF03)	Footprint and layout management
4	(MSF04)	Maximizing manipulability/minimizing the impedance at the end-effector
5	(MSF05)	Brakes for all independent joints
6	(MSF06)	Mechanical joint limits
7	(MSF07)	Wall guard for the patient's head
8	(MSF08)	Balancing spring in the passive arm for gravity compensation
9	(MSF09)	Balancing spring in the active manipulator for gravity compensation
10	(MSF10)	Using compression spring within a guide
11	(MSF11)	Minimizing the number of joints for the vertical path of motion
12	(MSF12)	Moves away from the contact by default
13	(MSF13)	The smaller size of actuators
14	(MSF14)	Backdrivability at actuators
15	(MSF15)	Light-weight design of active robotic arm
16	(MSF16)	Using spiral spring with packed case
17	(MSF17)	Minimizing tension on cables
18	(MSF18)	F/T fuse/ limiters at the capstan
19	(MSF19)	Mechanical remote center of motion (RCM)
20	(MSF20)	Integration of the F/T sensor
21	(MSF21)	Mechanical compliances at the endoscope
22	(MSF22)	The easy plug/release mechanism for the endoscope
13	(MSF13)	Small size of actuators
14	(MSF14)	Backdrivability of actuators
15	(MSF15)	Light-weight design of active robotic arm
16	(MSF16)	Using spiral spring with packed case
17	(MSF17)	Minimizing tension on cables
18	(MSF18)	F/T fuse/limiters at the capstan
19	(MSF19)	Mechanical remote center of motion (RCM)

(cont. on next page)

Table 5.1 (cont.)

20	(MSF20)	Integration of the F/T sensor
21	(MSF21)	Mechanical compliances at the endoscope
22	(MSF22)	The easy plug/release mechanism for the endoscope

The surgery zone is predefined to be in the vicinity of the center of a sphere with radius r as shown in Figure 5.1. The position of this sphere can be set during the initial setup before the surgery.

As can be noticed in Figure 5.1, \vec{w} is the unit vector that is related to the orientation of the telescope. Then, the distance $d_i = d_t - d$ is defined as the insertion distance of the endoscope beyond the RCM which located at the pivot-point position \vec{p}_p during the surgery. After locating \vec{p}_p with respect to the pivot-point located on the patient during surgery setup, the position of the center of a sphere \vec{p}_c with radius r can be selected relative to a desired distance s_d (from zero up to r) between the center of the sphere and the pivot-point position \vec{p}_p in the opposite direction of \vec{w} at the instant of setup.

$$\vec{p}_c = \vec{p}_p + s_d(-\vec{w}) \quad (5.1)$$

If s_d is selected to be zero, then the center of the surgery zone will be the pivot-point itself. After finishing the setup, the position of tip-point of the endoscope \vec{p}_t can be continuously calculated as follows:

$$\vec{p}_t = \vec{p}_p + d_i(-\vec{w}) \quad (5.2)$$

Each of the \vec{p}_p and \vec{p}_t can be used for checking whether these two points are inside or outside the sphere of the surgery zone or how far is \vec{p}_p (the RCM) from the pivot-point on the patient. This direct procedure can be done by using the equation of the sphere or by simply calculating the Euclidean norm of $\|\vec{p}_t - \vec{p}_c\|$ and $\|\vec{p}_p - \vec{p}_c\|$ to be compared with the radius r or any desired smaller value.

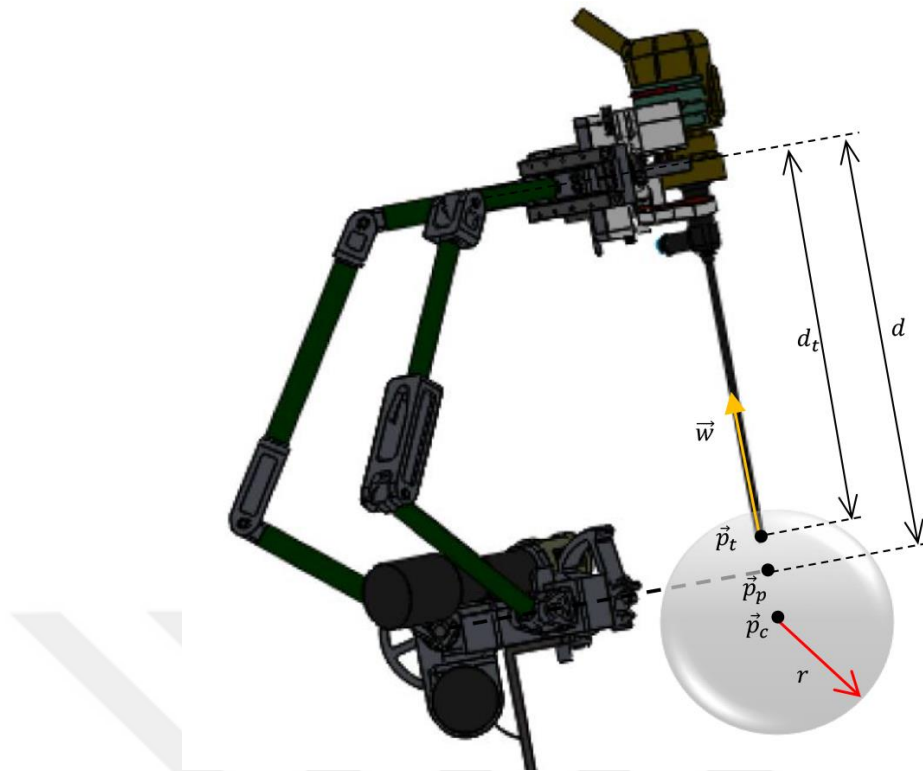


Figure 5.1. Surgery zone with respect to the pivot-point and the telescope

After all, the checking process will be related to the center of the sphere. All this information will be useful for performing the home positioning of the active robotic arm when the telescope and pivot-point are outside the surgery zone as can be seen in the control algorithm in Figure 5.2 which is related to the information in Table 5.2 and Table 5.3. Finding this information: (1) can give an indication to the surgeon or (2) can half activate the joint brakes to slow down the passive arm motion or (3) can be utilized to prevent uncontrolled motion such as performing the homing position of the active arm.

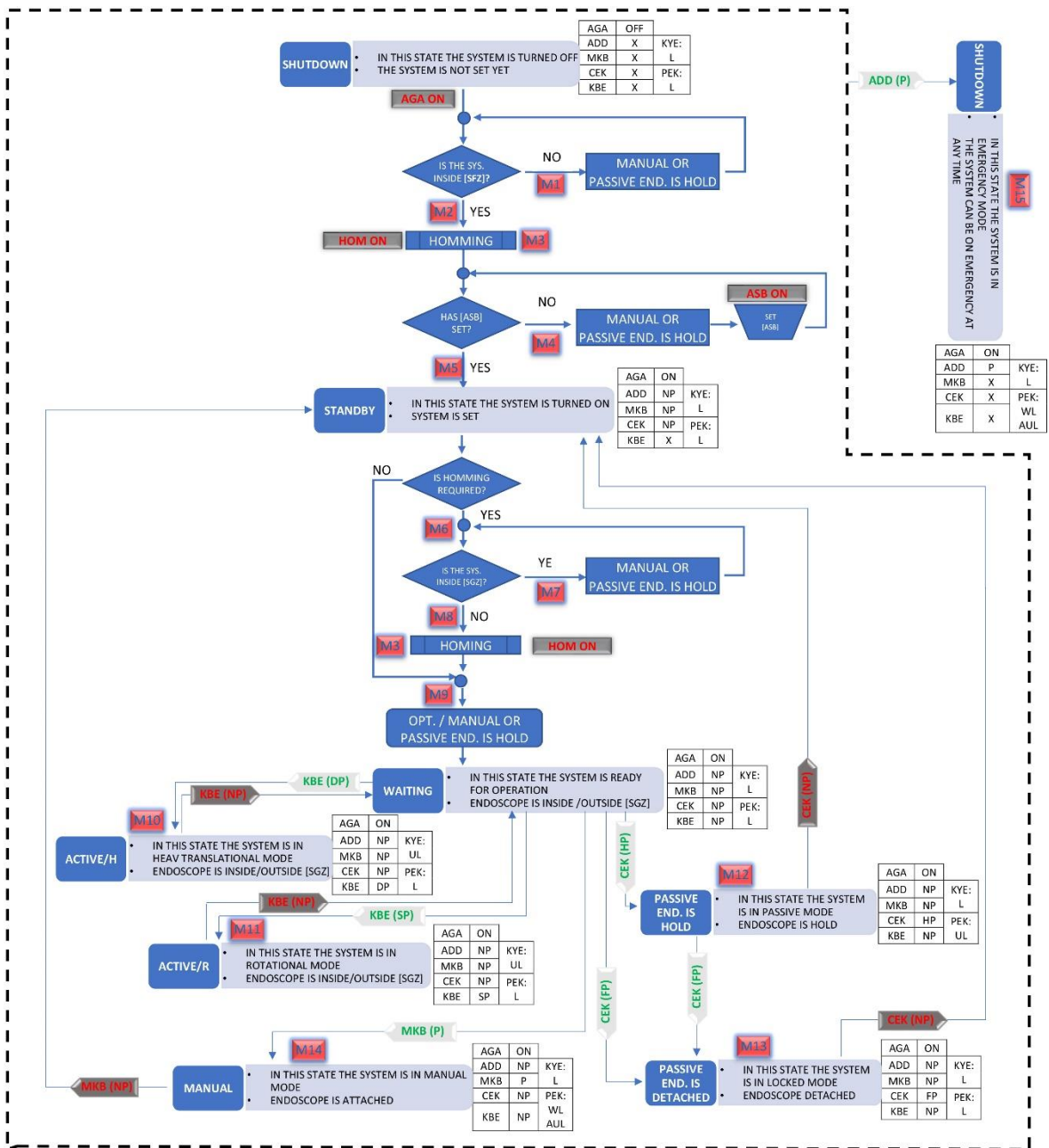


Figure 5.2. NeuRoboScope system's control algorithm diagram.

Table 5.2. Affiliations regarding to control algorithm.

Affiliations			
SFZ	SaFety Zone	CEK	Quick Release Mechanism
SGZ	SurGery Zone	MKB	To drive manually with a locked wrist and active arm
ACTIVE H	Active Heave	AGA	Main Switch of the System
ACTIVE R	Active Rotational	ADD	Emergency Push Button
L	Locked	KBE	Pedal Control
UL	UnLocked	ASB	Recorder Push Button to define the SGZ
UP	UnPressed	KEY	Active Endoscope Holder Arm
FP	Fully Pressed	PEK	Passive Balanced Arm
HP	Half Pressed	AKS	Main Control Unit
SP	Single Press		
DP	Double Press		
X	Not available		
WL	Wrist Locked		
AUL	Arm UnLocked		
OPT.	OPTional		
END.	ENDoscope		
HOM	Homing		

Table 5.3. Sample of messages regarding to control algorithm.

Messages	
M1	Move to Safety Zone!
M2	You are inside Safety Zone, press homing!
M3	Homing in progress! → Done!
M4	Set ASB!
M5	ASB has set! → STANDBY MODE
M6	Homing is required!
M7	Move outside Surgery Zone!
M8	You are outside Surgery Zone, press homing!
M9	Waiting Mode, Inside/Outside SGZ
M10	Active Heave Mode, endoscope is Inside/Outside SGZ
M11	Active Rotational Mode, endoscope is Inside/Outside SGZ
M12	Passive Mode Endoscope is Hold
M13	Endoscope Detached, Go to out of SGZ to reattach the endoscope
M14	MANUAL MODE
M15	EMERGENCY MODE

5.2. Positioning and Setting-up the System

The NeuRoboScope system comprises all of its components according to the design presented in Chapter 4: the passive arm, the active spatial parallel manipulator, and the endoscope unit. Various scenarios can be followed to set up the system, since positioning the endoscope along with the active robotic arm to be done manually through the passive arm. However, selecting the fixing position of the system is related to the position of the surgery zone as well as its footprint that is affecting the surgeons and the layout of the OR. The probability of collusion with the patient, the surgery table, and other equipment should also be considered (**MSF03**). As a first decision, the robotic endoscope holder system was selected to be fixed on the surgery table and to be located behind the patient's head. In this configuration, the symmetrical alignment of the endoscope on both sides of the nostril can be achieved (Fischer et al., 2011). Additionally, this layout can also prevent collisions between the manipulator and surgery instruments to provide necessary space for the surgeon's hands. Therefore, passive arm is to be fixed on the operation table. Having a separate robot mounting cart has disadvantages of being large and heavy in general to rigidly support the system as have been observed from the literature review in Chapter 2. In some systems, a small mounting base is used which has the ability to be connected rigidly to the operation table. For this specific surgery, many surgical tools (such as the operative endoscopic system, navigation systems, drilling systems, and electrocoagulation system) in OR must be set near the surgeon (Ogiwara et al., 2017). In addition to these systems, the surgeon, the assistant surgeon, and the surgeon assistant should have a comfortable movement inside the OR layout.

Maximizing the manipulability and minimizing the impedance at the end-effector of the passive arm near the surgery zone can give advantages in terms of safety (**MSF04**). In fact, maximizing the manipulability means minimizing endurance force at end-effector (Maarouf and Dede, 2016). In case of emergency and system failure, the surgeon should be able to relatively easily overcome brake's load and move the endoscope along with the active arm away in any direction. Such scenarios are denoted in Figure 5.3 with red arrows. In the first scenario presented in Figure 5.3.a, the movability is almost zero in one direction due to the singularity configuration of the

passive arm when the base of the passive arm is fixed on the table exactly beneath the patient's head.

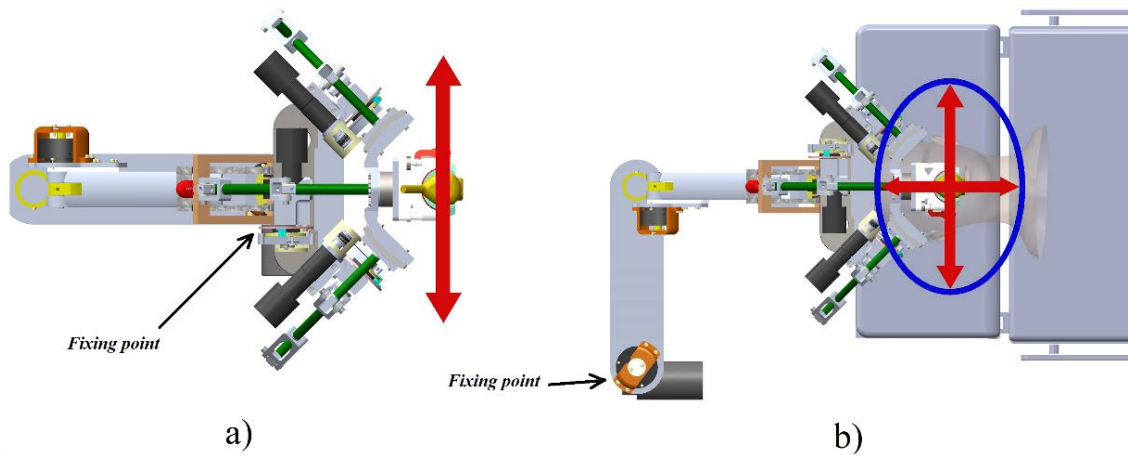


Figure 5.3. Configuration of the passive arm with two fixing positions, a) The base beneath the head, b) The base positioned away from any singularity configuration.

While in Figure 5.3.b, when the fixing point is located at a position away from any singularity configuration, the dimension of manipulability ellipse/ellipsoid can change drastically. The selection of fixing position and the other design parameters of the links have a direct effect on this safety feature. These are extensively discussed and worked out as a case study for the optimization problem presented in Chapter 7.

5.3. Modification of the Passive Arm's Kinematics

Spatial positioning of the wrist of the passive arm can be obtained by three passive joints θ_1 , θ_2 , and θ_3 . The first two joints are responsible for positioning in the horizontal plane. To compensate for the orientation in this plane, another revolute joint should be installed which is not considered in the first prototype. It can be seen in Figure 5.4, the orientation around the z-axis (the normal axis to the operation table) is dependent on the position of the end-effector and fixing point. This prototype could allow a single fixing point and a unique positioning of the patient's head on the table to have a convenient initial orientation with respect to the surgical workspace.

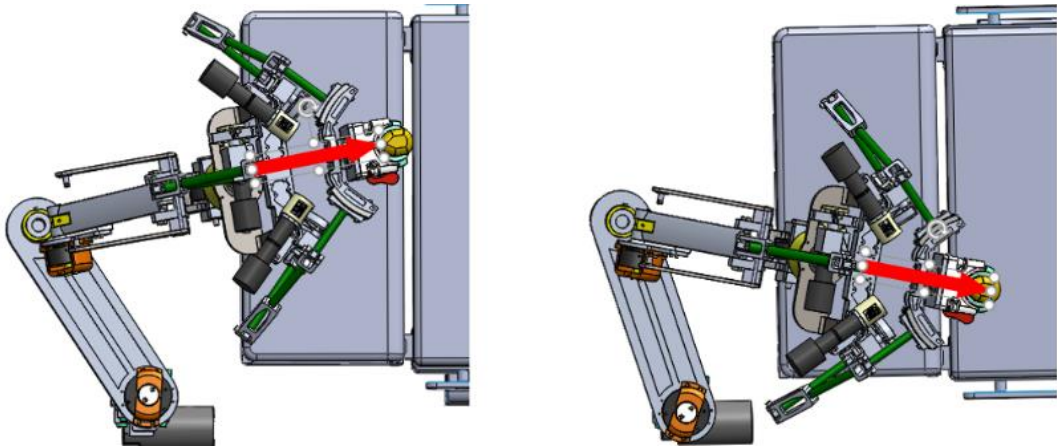


Figure 5.4. Two cases show orientation change with respect to the position

Since the rotational angle around the z-axis is not important for the endoscope image, it can be important due to the angular positioning limitations of the active parallel manipulator. For the scenario illustrated in Figure 5.4, the manipulator's workspace does not comply with the workspace of the surgery. As an alternative, switching between the 5th and 6th passive joints, which are responsible for the orientation of the active arm, is done. This change is presented as the old and new prototypes in Figure 5.5. By this modification, the 5th passive joint rotates the active manipulator around the z-axis (yaw-angle) to comply with both of the workspaces. The 6th passive joint is for setting the pitch angle of the wrist of the passive arm.

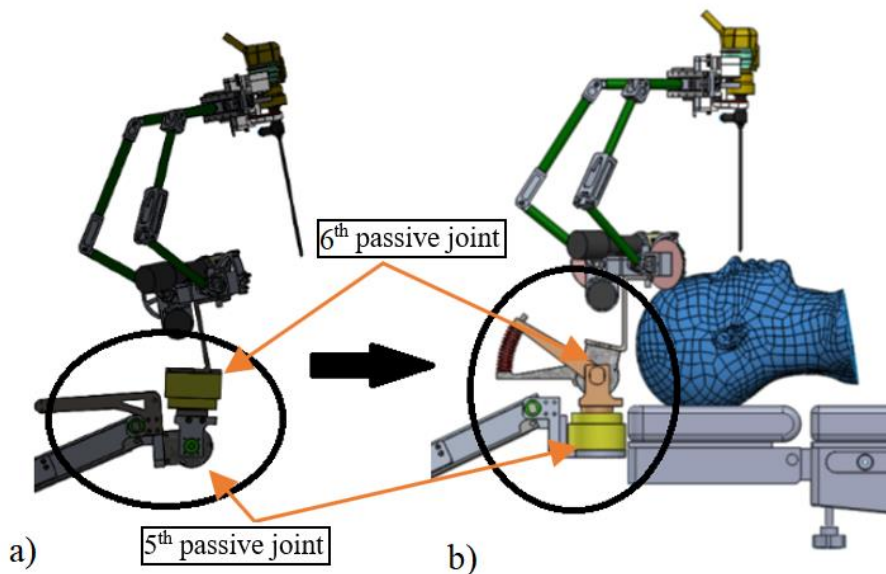


Figure 5.5. The modification in the passive arm, a) The earlier design of the passive arm, b) The modified design

This modification can provide flexibility while the surgeon reinserts the endoscope to the surgery zone via changing the passive arm's wrist orientation after the endoscope's lens is cleaned. This complies with the fact that the insertion pathway has a cylindrical shape through the nostril between the entry port and the anterior sphenoid bone as defined by Chalongsongse et al. (2019). The 6th passive joint has another main function which is to increase the range of the active manipulator's ϕ angle as defined in the discussions on the surgical workspace.

5.4. Reachability and Joint Limits

Setting up joint limits is beneficial in general for surgical robots. In addition to safety brakes in joints, they can function as variable joint limits (**MSF05**). For some joints adding mechanical joint limits will implement additional safety features (**MSF06**). Mounting of the mechanical joint limits is not intended to provide restriction inside the workspace and surgery zone nor restricting the movability but to enhance safety by making some motion restricted in a way not to cause injuries. For the presented surgical robot system, NeuRoboScope, the passive arm has six independent joints. These joints are responsible for positioning the active manipulator to a desired position and orientation. This positioning procedure is to be conducted by the surgeons where the arm stays passive. However, the surgeon needs to be aware of the workspace limitations of the active parallel manipulator with respect to the patient's pose. Otherwise, some spots on the workspace will be out of reach for the endoscope to visualize. When excessive orientation ranges are implemented, gravity compensation will not serve the purpose it is aimed for, which will be discussed in Chapter 8. The surgeons' skill can be improved by practice to follow these instructions intuitively. This is the reason to modify the first prototype of the passive arm as presented in subsection 5.3.

The mechanical joint limits can be essential for specific joints. However, other joints can be free from any restrictions. The need for movability, restrictions, and the change in potential energy are the main things to evaluate to decide on the joint limits. There is various risk levels that can be generated by undesired joint motion. In general, the joints that are responsible for the movability of masses in a vertical direction have a

higher level of risk due to their potential energy and risk of dropping down. Safety can be enhanced by installing mechanical joints limits to these joints.

5.4.1. The Passive Arm Joint limits

The first and second passive joint axes with variables θ_1 and θ_2 are both along the normal of the horizontal plane and it will be better to have them as free-range joints since they have a direct effect on the manipulability at the end-effector as discussed in Section 5.2. However, a protection shield can be installed behind the patient's head (to act as a helmet) to protect the patient from any collision by the structure of the passive arm and active robotic arm during a horizontal motion (**MSF07**). The third passive joint (θ_3) is the input of the parallelogram loop and it is limited by the mechanism and the compression spring integrated in the mechanism (as can be seen in Section 5.5.1). As a result, the fourth dependent joint θ_4 is limited by the third passive joint's limits hence it is the output of the parallelogram loop. As shown in Figure 5.5, the fourth independent passive joint (shown as θ_5 in Figure 4.17) is acting on the horizontal plane and it is also responsible for the positioning the RCM and changing the RCM's orientation about the z-axis. This revolute joint, with joint variable denoted by θ_5 , is required to be free to rotate. The mechanical safety limit is added to the new pitch angle (the sixth passive joint indicated with the joint variable θ_6) to ensure that the tilting of the active robotic arm does not exceed 20° (which is the angle selected to extend the range of the active parallel manipulator).

5.4.2. The Active Arm Joint limits

For the robot assisted endoscope holder system, the active robot arm has normally three actively controlled motions. Two are for the orientation of the endoscope and the third input is responsible for the insertion of the telescope. Mechanical limits should be set so that the workspace of the active robot manipulator and the task space of the surgery (surgical workspace) are equivalent. For the selected active parallel manipulator, the workspace that can be generated is a right rectangular pyramid. On the other hand, the surgical workspace has a conical shape with ellipse cross-section. In the current setup of the active parallel manipulator, the measured ranges of the surgical

workspace (rotational angles) are not coincident with the active manipulator's angular ranges. For example, all of θ_1 , θ_2 , and θ_3 produce the motion in ϕ and both of θ_1 and θ_2 produce the motion in ψ . The insertion value is related to the actuator angle θ_3 which is the most critical motion regarding the patient's safety. The variable d for the insertion relies only on θ_3 , but the range of θ_3 is not unique. Its range varies depending on the current position of θ_1 and θ_2 . All of these coupling in motion prevents the transformation of the surgical workspace limits into the active arm's limits. As a result, the installation of mechanical joint limits in the active parallel manipulator is not practical.

These changes in the ranges and limits at each position can be seen in Table 5.4 from test No. 1 to test No. 8 for various positions inside the workspace (extreme positions) at pitch angle 0° and at 20° . Test No. 9 is for 10^6 equally distributed positions inside the surgical workspace limits for pitch angle 20° .

Table 5.4. The limits of the parallel active manipulator

No. i	Workspace limits at Pitch angle $= 0^\circ (20^\circ)$			Joints' positions/ranges at Pitch angle $= 0^\circ$ (20°)		
	ϕ_i ($^\circ$)	ψ_i ($^\circ$)	d_i (m)	θ_1 ($^\circ$)	θ_2 ($^\circ$)	θ_3 ($^\circ$)
1	-12	-1	0.17	9.24 (-4.98)	-7.86 (6.36)	36.75 (-8.16)
2	-45	-1	0.17	35.74 (18.75)	-34.79 (-17.75)	104.77 (61.93)
3	-12	12	0.17	0.19 (-13.73)	-16.91 (-2.98)	36.75 (-7.04)
4	-45	12	0.17	29.80 (12.56)	-41.13 (-24.51)	104.77 (62.57)
5	-12	-1	0.18 (0.24)	9.24 (-4.98)	-7.86 (6.36)	40.21 (-4.04)
6	-45	-1	0.18 (0.24)	35.74 (18.75)	-34.80 (-17.75)	114.94 (65.83)
7	-12	12	0.18 (0.24)	0.19 (-13.73)	-16.91 (-2.98)	40.21 (-2.97)
8	-45	12	0.18 (0.24)	29.80 (12.56)	-41.13 (-24.51)	114.94 (66.49)
9	(-45 \rightarrow -12)	(-1 \rightarrow 12)	(0.17 \rightarrow 0.24)	(-13.73 \rightarrow 18.75)	(-24.51 \rightarrow 6.36)	(-8.16 \rightarrow 101.03)

The last test shows the range of the actuators' angles at these 10^6 positions. However, these ranges are not useful for developing a safety region since what can be considered as a safe minimum/maximum angle at a specific position is not the same at

the other positions. For example, the minimum angle in test No. 1 is $\theta_3 = 36.75^\circ$ for resulting $d = 0.17$ m cannot be considered as the lower limit to be applied to test No. 2. The minimum angle on test No. 2 is $\theta_3 = 104.77^\circ$ for the same $d = 0.17$ m. Also, the surgical workspace is changing from one patient to another as indicated in Chapter 4 during the surgical workspace analysis. For these reasons, no mechanical joint limits are added to the active parallel manipulator in the NeuRoboScope system.

5.5. Gravity Compensation

Numerous design concepts for passive gravity compensation in mechanism design are studied in the literature in order to achieve static equilibrium at any condition and/or to reduce the actuator's load due to gravity. A review of the available techniques is presented in the work of Arakelian (2016) by presenting the advantages and drawbacks of the methods with examples. Passive gravity compensation via counter-masses or springs can be considered as a fundamental way in the design of the statically balanced robot arms. A comparison between these two techniques is presented in (Mahalingam and Sharan, 1986). In fact, these two techniques can also be used simultaneously (Yaşır et al., 2019). A design tool was proposed in (Martini, Troncossi, and Rivola, 2019) to determine a feasible gravity compensation solution by selecting appropriate mixtures of counter-masses and springs. The authors evaluated the performance of an unbalanced/balanced mechanism in terms of energy efficiency, peak motor loads, and joint reactions to assess the most convenient balancing solution.

Consequently, there should be safety features in case of possible failures in the surgical systems. Potential scenarios of these failures are the malfunction of the actuators and brakes of these robotic mechanisms or the malfunction of the control systems. In this case, the manipulator should be statically balanced so that it will not drop on the patient during these types of failures (**MSF08**). Another obvious advantage of passive gravity compensation is that the actuator's effort will be mostly spent on the control of the motion which improves the control performance. Hence, peak loads of the actuators will be smaller which leads to the use of less powerful actuators which is safer for the pHRI (Lessard, Bigras, and Bonev, 2007). Due to the induced advantages in backdrivability as suggested by Perret and Vercruyssen (2014) for medical applications, gravity balancing can be a great tool for this approach.

Among the gravity compensation methods, an obvious and relatively easier option is integrating counter-masses which is a superior method for its independency of the direction of gravity vector when the base of the robot has rotational motion. Nevertheless, this solution results in increased mass/inertia of the moving bodies. High gravitational loads can cause deflections at the end-effector point which can affect the dynamics, stiffness, and accuracy performance of the parallel manipulator (Lian et al., 2016). This increase in moving mass/inertia poses a problem for the specific application (the NeuRoboScope system) in terms of the backdrivability of the passive arm. Additionally, in contrast to using a spring-balanced system, using counter-masses increases the required power of the actuators and results in a lower bandwidth of the system (Carricato and Gosselin, 2009). In the application of industrial robots, usually, the serial robot arms designed to have partial gravity compensation for their shoulder and elbow that are in general working against gravity. In the case of parallel industrial robotic manipulators, the actuators are fixed on the base platform and the moving links and the mobile platform are usually made of lightweight structures. Gravity compensation has been used in medical applications such as in wearable rehabilitation mechanism for lower limbs by Nakayama, Araki, and Fujimoto (2009) and for upper limbs by Stienen et al. (2007), in an exoskeleton supporting the body parts by Altenburger, Scherly, and Stadler (2016), in a backdrivable and counterbalanced robotic arm carrying the ultrasound probe for ultrasound examination in (Lessard, Bigras, and Bonev, 2007; Salcudean et al., 1999). In the area of surgical robotics, in (Chung et al., 2016), a passive gravity compensation mechanism based on springs and wires with a scotch-yoke mechanism was introduced for a laparoscopic robotic arm. In the next subsections, the gravity compensation solutions proposed in the NeuRoboScope system are introduced.

5.5.1. Gravity Compensation for the Passive Arm

For a more efficient and reliable design, the passive arm is designed to have gravity compensation (**MSF09**). Both the parallelogram loop after the third joint and the pitch angle are related to the vertical motion of the center of gravity in the new modified passive arm. In the original design of the parallelogram loop, a compression spring with adjustable length is used. Failure of compression springs is less likely to occur and if it

happens, it is not as risky as tension springs especially when placed within a guide (**MSF10**). The third passive joint is nonlinearly related to the vertical displacement of the center of gravity. In the original design of the passive arm, to gain better and accurate performance, a curved profile at the contact point with the spring, which is acting as a cam and a roller follower, was installed. This method leads to having another design parameter added to the variable h_3 shown in Figure 4.18 to be selected by using the synthesis method of the mechanism. The compression spring can be adjustable with respect to the carried loads at the end-effector of the passive arm, for this reason, the original design of gravity compensation at the parallelogram was used without any modifications.

The other advantages provided with the new modified design compared with the former design of the passive arm is that just the fifth passive joint, with joint variable θ_6 , needs gravity compensation within the wrist architecture since the fourth passive joint, with joint variable θ_5 , is acting on the horizontal plane as shown in Figure 5.6. In the former design, both θ_5 and θ_6 contribute to the vertical motion of the center of gravity of the active robot. As a result, fewer joints contribute to the vertical motion and hence safety (**MSF11**) is enhanced in the system. Similar to the parallelogram, for safety reasons, a compressive counter-spring is selected for balancing the wrist's pitch angle with a guidance (**MSF10**) as shown in the modified wrist component and the auxiliary linkages in Figure 5.6.

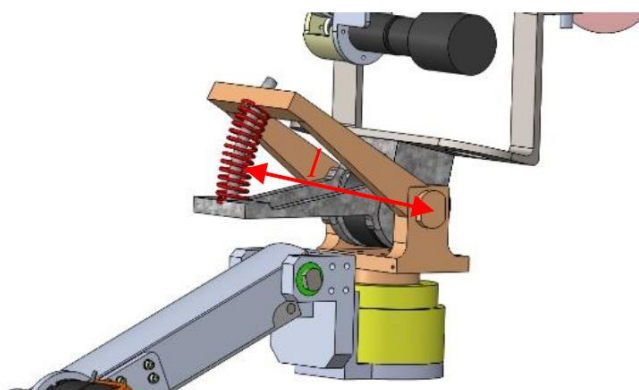


Figure 5.6. The gravity compensation on the modified wrist component.

As can be noticed from this figure, to calculate the torque provided by the compression spring for balancing and to design/select the stiffness value the following formula is used:

$$T = \Delta c k_6 l = (\theta_6 + \theta_i) k_6 l^2 \quad (5.3)$$

- T The counter torque provided by the spring on the passive joint θ_6
- Δc The change in curve's length and it equals to $l (\theta_6 + \theta_i)$
- k_6 The stiffness of the compressive spring
- l The dimension of the auxiliary linkages
- θ_i Initial angle measured from the non-deflected spring angle on the passive joint θ_6

Since the active parallel manipulator has masses that continually move during the operation and the equivalent center of the mass for the component is not constant, the generated torque of these loads is considered at their extreme values. This strategy was implemented in (Taniguchi et al., 2010). In this strategy, Taniguchi et al. (2010) used pneumatic actuators that maximally stretch (in default) when no control applied on the actuators for safety reasons. By following this strategy, the torque to be provided by the gravity compensation is designed slightly higher (and can be adjustable) than the torque generated at the passive joint as a result of the gravity when the pitch angle is at its maximum values (20°). Then, stiffness value and dimension l are designed for approximated gravity compensation. Any failure in the brakes or the controller will make the active parallel manipulator with the endoscope to rise instead of falling onto the patient's head (**MSF12**) and the failure could be mitigated. The gravity compensation spring at the parallelogram can be adjusted following this strategy as well.

5.5.2. Gravity Compensation for the Active Arm

The passive gravity balancing is advantageous to be used in the active parallel manipulator of the NeuRoboScope surgical system. These advantages can be listed as:

- ***The system shall have an inherent safety feature.*** Since this active parallel manipulator is designated to be used for a surgical system, in case of total system failure, the mechanism should be able to maintain its position or minimizing failure effects.
- ***Minimizing the actuation load (MSF13).*** As it is observed from the first functional prototype an endoscope that is handled at the tip of the

mechanism is relatively heavy with respect to any other moving mechanical component. Thus, during the tests, it was observed that most of the actuation load is spent on the gravity balancing of this payload (the endoscope). By integrating passive gravity balancing, since the actuation loads are lower, the use of a high-speed reduction system can be avoided. As a result, the low-speed reduction ratio capstan drives can be used to cancel the gear backlash effects. Thus, control quality will be improved.

- ***The capability of using capstan drives.*** With a reduction system that has a reduction ratio lower than 1:10, the backdrivability of the active mechanism can be obtained (**MSF14**). As a result of this, the surgeon can backdrive the system if there is a need for or in case of system failure. Hence, this capability enhances the inherent safety of the system.

The robot mechanism in the NeuRoboScope is designed to work on top of the head of the patient during a pituitary tumor surgery as illustrated in Figure 5.7. One practical limitation of the specific application of this spatial parallel manipulator is its total mass. The passive arm is backdriven by the surgeon to place the endoscope in and out of the surgery zone. An increase in the total mass of the manipulator degrades the backdrivability of the passive arm since the total moving mass/inertia is increased.

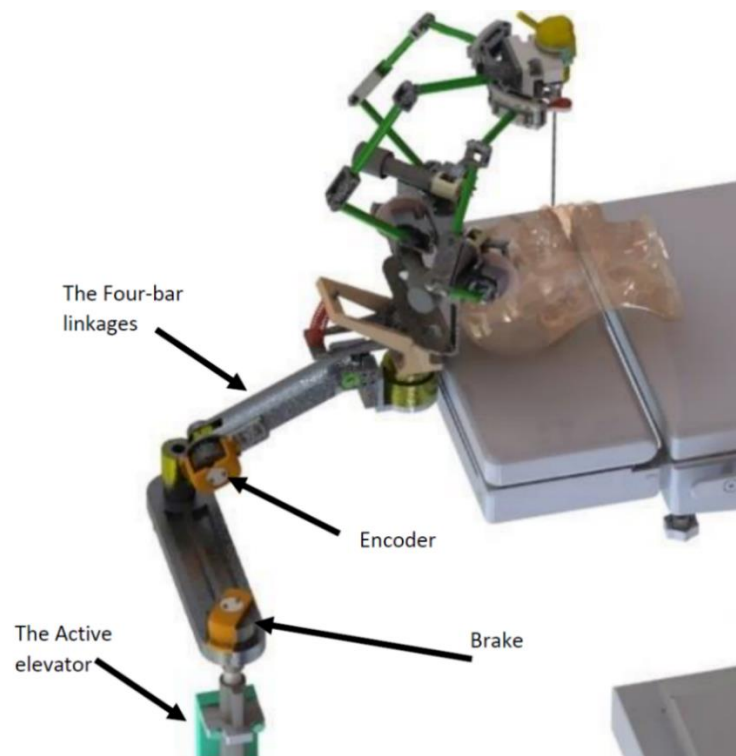


Figure 5.7. Gravity balanced passive arm that handles the spatial parallel manipulator

Recently, a study was conducted using only counter-masses and a combination of counter-mass and spring for the NeuRoboScope system's active arm (Yaşır et al., 2019). The increase in the total moving mass was observed when only counter-masses are used. In order to reduce the total moving mass, the use of springs was proposed for the links that are connected to the base platform. Nevertheless, total gravity balancing could not be achieved, having a variable orientation range of the endoscope.

In this subsection, partial gravity balancing for the parallel manipulator is proposed without using counter-masses in order to reduce the total mass of the mechanism for safety reasons (**MSF15**). Another concern is the compactness and small footprint of the design which is required for having a minimal number of components that can cause a collision with the surgeon's hands and patient's head or for vision blockage during the surgery.

In the literature, various design studies have been carried out for implementing passive gravity balancing methods. There are two main arrangement methods that are usually used when using springs (Lian et al., 2016): first, direct connection of spring to the link; second, via utilizing an auxiliary linkage with the spring. During the implementation of these methods, the main design consideration is the use of simple mechanisms to result in a cost-effective and easy to maintain design while reducing power demand from the system actuators (Chheta et al., 2017). In (Okada, Uchida, and Uemura, 1999), a solution is proposed to have smaller size springs by the arrangement of springs with different diameters located inside each other. A smaller and compact spring element was produced but the total weight was not the focus of their design.

Usually, gravity compensation with spring components is used in spatial parallel manipulators with a fixed base platform. In (Lian et al., 2016), three tension springs were used for 3-RPS parallel robot manipulator to compensate for gravitational loads. The geometric parameters of these springs were optimized by minimizing gravitational potential energy fluctuation within a prescribed workspace. However, using tension springs on links in parallel manipulator requires a fixture point connected to the base platform of the parallel robot manipulator which needs auxiliary fixture structures that increases the total weight of the whole system as well. With a fixed-base platform, there is no problem with fixing the one end of the springs to a static inertial frame. However, in the NeuRoboScope system, the spatial parallel robot manipulator is mounted on a passive arm which has the feasibility to change the orientation/position of the base platform. Hence, there is no fixed frame on the structure to be used for fixing one end of

the spring, as demanded by design constraints, neither adding an auxiliary linkage for this purpose. Earlier work proposed another solution by adding torsional springs (Lessard, Bigras, and Bonev, 2007). In their work, torsional springs were placed at active and some selected passive revolute joints of the manipulator to meet two objectives. The first objective is to keep the vertical load always upward so that in case of a failure, the medical tool to be out of contact with the patient for safety reasons. The second objective is to minimize peak loads at actuators.

For a compact design, the proposed idea in the NeuRoboScope system is to enclose the spring within the actuation system. Therefore, a spiral spring (coil spring) is chosen to be mounted directly on the rotating shafts with customized packaging for safer design as presented in Figure 5.8. In this design, the adjustment of the preload on the springs can be done easily and while the spring is in its case.

Within the design of the active parallel manipulator, the most practical place to locate the spiral spring is to embed it inside the capstan drive's follower wheel. As this spiral spring is enclosed within the capstan drive, in case of a failure in the spring, the spring will remain in its casing (**MSF16**). The radius of the spring is bounded within two limits in this design. Due to this constraint in the motion of the spring, it is unlikely that the spring will experience a fracture due to excessive bending stresses. It is also possible to change the initial preload value with ease if a different endoscope with different inertial properties will be used. Putting the spring component at the capstan directly can contribute to having less tension/elongation on the cables (**MSF17**). In this case, force fuse can be applied at the cables with a small threshold or mechanical torque limiters, as proposed by Yip et al. (2015), which can be installed at the capstan/motor shaft (**MSF18**). The F/T limiters can allow for the advance in the motion of the actuators while the end-effector is obstructed at the same contact force.

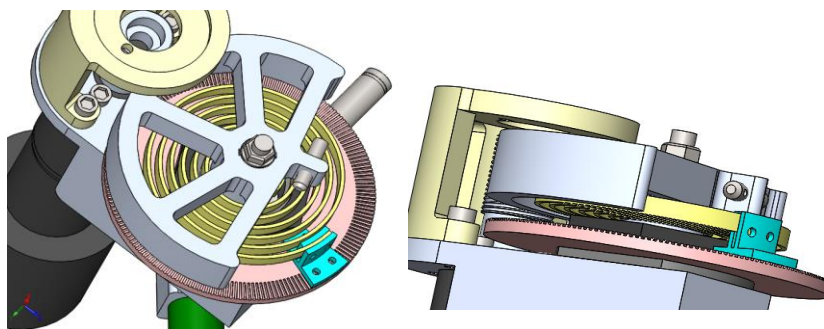


Figure 5.8. The proposed design for mounting the spiral spring in the actuation system of the active parallel mechanism

Since, it is an impossible solution to minimize the complete unbalanced masses, in order to partially minimize the unbalanced masses throughout the entire workspace, optimal design of the three installed spiral springs in Figure 5.9 and their initial angles for preload must be carried out. This optimization procedure along with the design parameters are explained in Chapter 8.

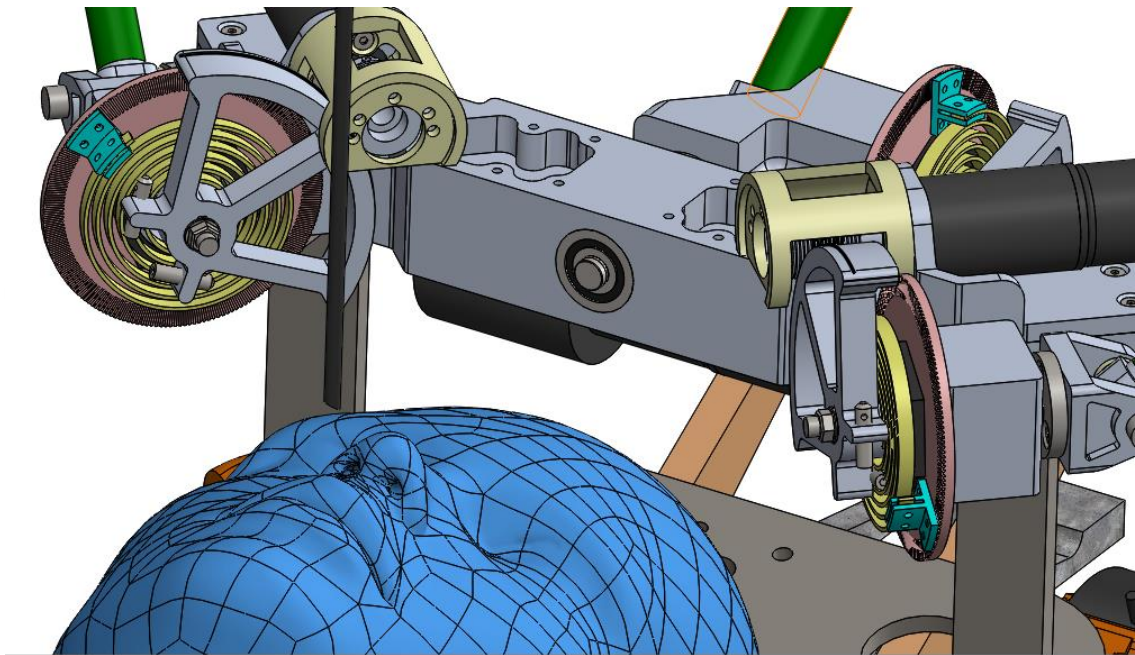


Figure 5.9. The active mechanism's actuation systems with three spiral springs for balancing

5.6. Mechanical Safety at Endoscope Holder

In addition to the many safety features presented for both the passive arm and the active parallel manipulator, other functional mechanical safety features are presented for the endoscope holding system. First, the RCM feature provided with the active parallel manipulator guarantees the movement of the telescope part of the endoscope around and through a single-entry port by an inherited mechanical constraint the RCM. This feature can provide safety to the entry port region in case of controller malfunctioning (**MSF19**). To have a reliable safety feature in case of any failure the F/T sensor has been mounted in series between the moving platform of the active manipulator and the endoscope holder (**MSF20**) in the NeuRoboScope system. The measured F/T can provide direct feedback in real-time for the contact between the

telescope and the patient. The addition of a mechanism at endoscope holder that allows a degree of compliance at the very end of the system can provide another safety feature (**MSF21**). By this compliance mechanism, the endoscope will have a tilt angle when an excessive force of contact exerted between the patient's tissue and the telescope. This can allow a short amount of time between collision and the action to save the situation. Also, the point of contact at the relatively sharper end of the telescope will be changing to a line of contact at the telescope prob. This has been observed in the Passive Endoscope Compliance Holder (PECH) designed by Zhong (2019). As a last backup solution, the ability to plug/release the endoscope in a simple and intuitive manner can be implemented (**MSF22**). Such feature can provide important role in safety by easily and fast switching to manual endoscopy at any stage of the surgery. For this purpose, a novel mechanism design was done for the NeuRoboScope system by a team of project researchers. This mechanism allows for a passive rotation of the endoscope around its axis and has a two functional (two-step) button as shown in Figure 5.10. These two functions can be used for: first, by a half-press of the button the passive arm brakes will be released so the surgeon can passively manipulate the endoscope holder robot arm, second, by a full press the endoscope will be released and the surgeon will be conveyed to manual endoscopy mode. As haptic feedback addition for this button, a vibrator is attached to this compound. These scenarios are presented in the control algorithm introduced in Figure 5.2.

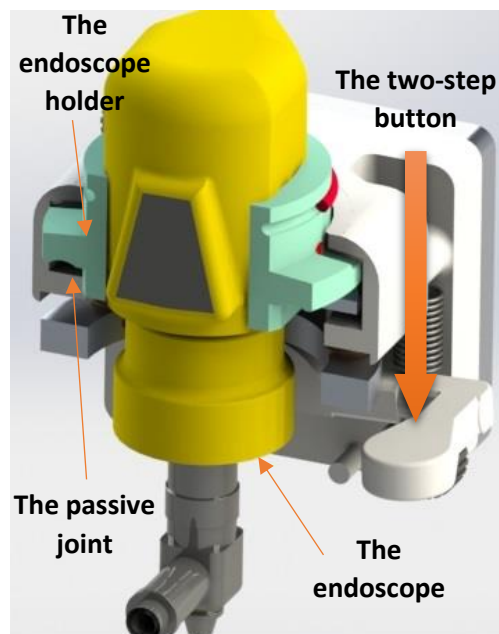


Figure 5.10. The plug/release mechanism

5.7. Conclusions

This Chapter focused on the safety enhancement methods that are related to mechanical safety features. For this objective, a list of mechanical safety features added in this study, those added by other studies, and potential safety features that can be optional to the system are presented. Then, specific solutions for the NeuRoboScope system are presented. Those solutions include modifications and additions to the system to enhance its safety. Gravity compensation with the methodologies to be followed for both of the passive arm and active robot were studied. A compact solution for the partial gravity compensation is proposed for the active parallel manipulator. This solution can result in adding more safety to the system in various ways.

CHAPTER 6

CONTROL SAFETY FEATURES FOR SURGICAL ROBOTS

There are always potential errors that can cause dangerous and unexpected movement by the robot from some sources. Risk assessment, system testing, following the safety standards, and following systematic design procedures can adequately minimize and restrict such sources of errors. In addition to the MSFs, other features can also be added as complementary potential safety features titled as the Control Safety Features (CSFs). This chapter presents some of the important points for the functional design of the surgical robotic system and provides some thoughts that can be applied in the design of the NeuRoboScope system. In this chapter, Control Safety Features (CSFs) are proposed for robot assisted surgical systems to be complementary to the previously proposed mechanical safety features. The main objective of this work is to introduce available control safety enhancement methods that already studied by other researchers and applied in surgical robot systems.

6.1. Systematic Design for Safety

Control safety features deal with electric, electronic, software, and operational techniques. The design of a surgical robotic system could be considered as a tough research project because of the complexity of the system. It is a combination of the effort of engineers, surgery specialists and industrial designers. During decades, many research teams worked on the design of surgical robotic systems. However, not all of them could make all the way to the OR. Many studies in the literature deal with the assessment and improvement of the safety of surgical robots in systematic methods.

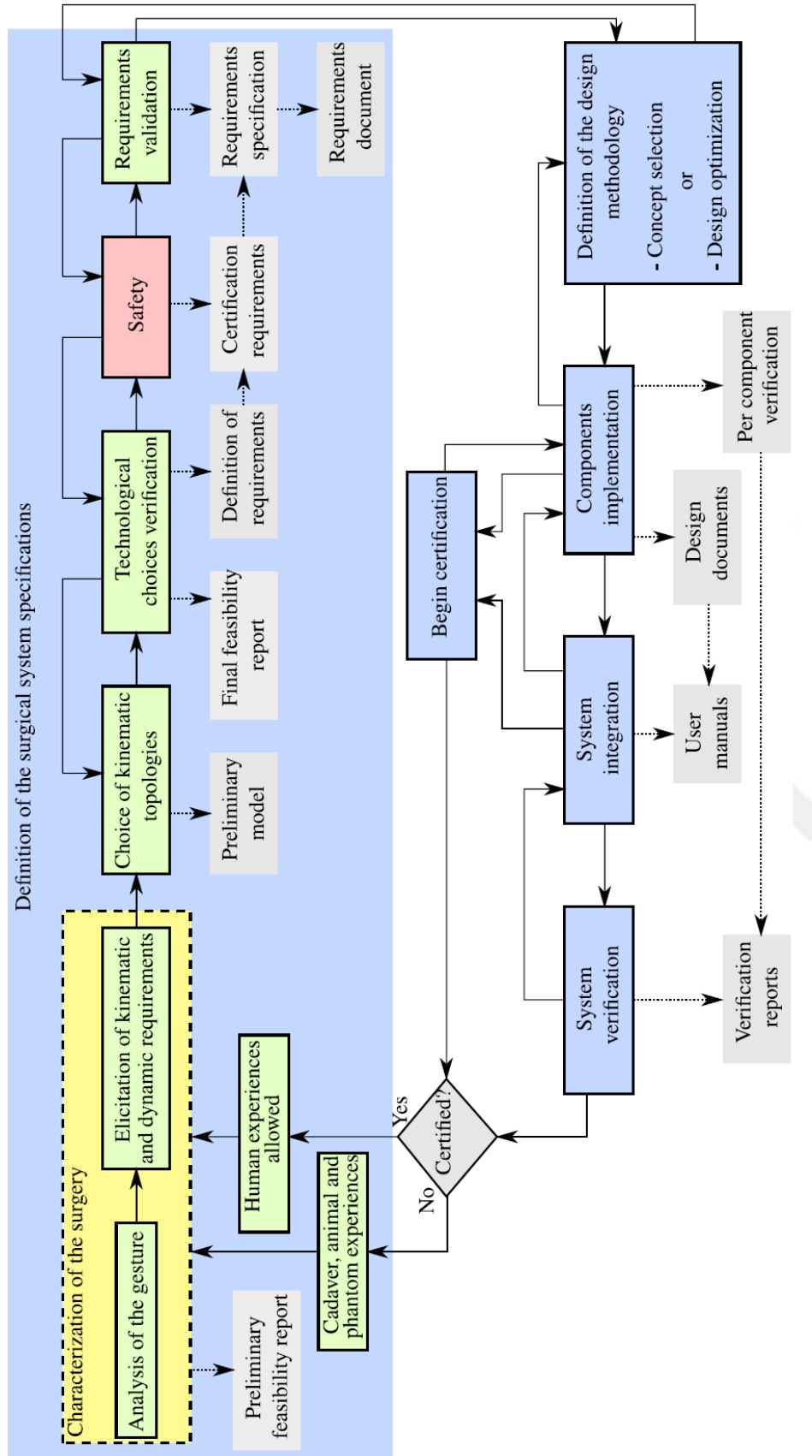


Figure 6.1. A general overview of the design cycle of a surgical robot (Source: Sánchez et al., 2014)

In this outlook, researchers in (Fei et al., 2001) proposed a systematic method to analyze safety factors by three axes: software, hardware and control. This systematic method is called HISIC and consists of seven principles including hazard identification and safety insurance control. However, the software safety feature is the most reliable one in medical devices for safe and proper operation of the system (Kazanizides, 2009).

A framework shown in Figure 6.1 was introduced by Sánchez et al. (2014) to be a foundation for the design and transformation of surgical robots to the OR with respect to European medical device regulations. Also, important safety guidelines for a robotic surgical system were proposed in this work.

The frequently used safety features in the literature of medical robots were investigated in the study presented by Jung et al. (2014) to better understand and describe the design-time and run-time in a structured and systematic way. In their study, Safety Design View (system view and mechanism view) was proposed as a framework to be taken into consideration for this application with respect to both functional components and deployment options of safety features.

Many researchers tried to regulate safety design factors that should be considered in the design of surgical robots. The work of Ryu et al. (2017) was based on the available trend of standardization for the identification of the degree of autonomy and in this work, they proposed safety design methods with respect to hazard analysis, required performance, and elementary safety of surgical robots.

Some practical design aspects were proposed by Dibekci and Bebek (2018) for the improvement of the design of a safe surgical robot called OzU Knee Robot through safety guidelines. Safety improvement was achieved through various concepts of design such as alternative designs, variables of designs, constraints, and limitations. In this work, a similar approach is used in the design of the NeuRoboScope system along with presenting functional safety features and optimization of the design for this purpose.

6.2. Safety Standards of Robot Assisted Surgical Systems

Robot developers and researchers intend to get into the medical devices market for its benefit of investment and to improve human life. Throughout several years of improvement in robotic fields, the use of advanced technology in robotic systems makes make these systems more complex system but as a result, these systems gained multiple

functionalities. As a result, the urge to follow standards and the specific regulatory requirements related to the medical field were present to make this technology widely accepted. However, when it comes to the surgery room, it requires the ultimate advanced techniques in engineering fields. In this application, other complicated aspects come across such as safety, real-time interacting and processing, the cooperation between human and robot, design of the mechanism, force/vision-based control, etc.

For many years, several series of robot safety standards have been published by standards organizations such as the International Organization for Standardization (ISO) and International Electrotechnical Commission (IEC). For example, the Technical Committee of Robotic Industries Association (ISO/TC 299, Robotics) has published a list of safety requirements for industrial robots (ISO 10218-1:2011 and ISO 10218 2) and (ANSI/RIA R15.06-2012). Although these safety principles can be considered useful to other specific robotic functions outside the industry, they are barely applicable to medical robots. The most relevant one to the safety of medical robots is the safety requirements regulation for collaborative industrial robotic systems (also called cobot) and their working environment with the technical specifications ISO/TS 15066:2016. Nonetheless, medical devices need a specific regulation to be accepted in the market and in the OR.

Another list can be related to safety standards provided by the IEC which is also collaborating closely with ISO on electrotechnical standardization. The list presented in Table 6.1 is for standards that are related to the safety of medical devices and can be utilized to generate a new safety procedure. Such safety procedures can be transformed into the domains of robot assisted surgical systems.

Table 6.1. List of some standards published by IEC

	Standard code	Application
1	IEC 60601-1	<i>Medical electrical equipment- Part 1: General requirements for basic safety and essential performance</i> - gives general requirements of the series of standards
2	IEC TR 60513	Fundamental aspects of safety standards for medical electrical equipment
3	IEC 62304	Medical Device Software – Software Life Cycle Processes
4	IEC TR 80002	Medical device software
5	IEC 61508, ISO13849, IEC 62061	Some assessments of robotic-specific functional safety requirements

These standards may not guarantee the effectiveness of robot assisted surgical systems but can be considered as inception for safety enhancement. Nevertheless, researchers for many years depended on these standards for inventing and developing medical devices and surgical robots. Guiochet et al. (2012) pointed out the challenges for standardization and the application of several existent standards to the creation of a medical robot. O'Sullivan et al. (2019) provided discussions and recommendations for improving and developing standards and frameworks for robotic surgeries depending on the literature. They have also discussed the responsibility of autonomous robotic surgery in three aspects: Accountability, Liability, and Culpability. They provided specific suggestions for managing reliability with respect to the first two aspects while Culpability produces less clarity.

Regarding safety for robot assisted surgical systems, robots are not always censurable. As stated in the report of complications and adverse events related to robotic surgery by the Pennsylvania Patient Safety Authority, most of the incidents were caused by the lack of the skills of surgeons who perform robotic procedures (Dubeck, 2014). The best method to relatively guarantee patient safety is to have competent surgeons, who are well trained and talented to perform RAS as he/she is feels himself/herself as a part of the system. Medical errors by surgeons are always presented but within acceptable limits. Various techniques are used to minimize these medical errors to a minimal level. A study showed that a decrease in post-surgical deaths in Scotland between 2000 and 2014 is 36.6% due to the implementation of a safety checklist created by the World Health Organization (WHO) (Ramsay et al., 2019). In RAS, the use of a safety checklist can also provide an influential effect on safety level when robot assisted surgical systems involved.

To understand safety in robot assisted surgical systems, a team of surgeons and developers have started a long term project, the SAFROS Patient Safety in Robotics Surgery (SAFROS, 2019). In this project, they preplanned to develop the required procedures and techniques for patient safety. The SAFROS project and similar projects are assigned to provide WHO Patient Safety with global safety guidelines for patient surgery.

In the SAFROS project, WHO Patient Safety was intended to make clear how to guarantee the integration of patient safety in the development of new technology of robotic surgery systems and to formulate suitable methodologies for this ambition.

WHO defines the patient safety term as

the absence of preventable harm to a patient during the process of health care and reduction of risk of unnecessary harm associated with health care to an acceptable minimum. An acceptable minimum refers to the collective notions of given current knowledge, resources available and the context in which care was delivered weighed against the risk of non-treatment or other treatment (WHO, 2019).

Finally, a joint working group (as proposed by eight collaborated countries) from ISO and IEC involving many experts in both ISO/TC 299 and IEC/TC62/SC62D was established in July 2015. As a result, on July 9, 2019, the IEC issued both of: “IEC 80601-2-77: 2019 Medical electrical equipment - Part 2-77: Particular requirements for the basic safety and essential requirements of robotically assisted surgical equipment” and “IEC 80601-2-78 for safety requirement of RECA (rehabilitation, assessment, compensation or alleviation) medical robots for supporting impaired patients” (*ISO Standardization IEC-80601-2-772019, 2019; ISO Standardization IEC-80601-2-782019, 2019*). Noting that those specific standards are to be used with IEC 60601-1 and its collateral standards for the safety of medical electrical equipment. These recently released standards will contribute significantly to augment the development of medical robots in general and Robotically Assisted Surgical Equipment (RASE) specifically.

6.3. Risk Assessment for Safety

Identification of hazards in robot assisted surgical systems before it happens can be represented by the value of risk assessment. In RAS, implementing actions to mitigate the potential risks is related to using robot assisted surgical systems on the patients by surgeons. The safety assessment process for robot assisted surgical systems is important to certify that their performance is as intended to. In general, anticipated risks are identified as acceptable when balanced with the profits.

A good tool for initial risk assessment is the risk level decision matrix (according to ISO 13849-1) by tracking the three order of severity, exposure, and avoidance to assure the accurate risk level in the matrix. It is directed across the three stated critical aspects to quantify and qualify the suitable risk levels. This is the first step needed for the risk management process which is required by ISO 14971 titled “Application of risk management to medical devices”.

The risk assessment method called Fault Tree Analysis (FTA), which shows the cause and effect graphically with logic symbols. This method is presented by IEC

61025. Another tool presented by IEC 60812 which covered both tools: FMEA/FMECA Failure Modes Effects Analysis/and Critical Analysis. A simple tutorial overview of the application of these tools can be seen in the work by (Kazanzides, 2009). Some researchers define their own safety assessment method to evaluate the effectiveness of their design for safety (Ning, Wang, and Jing, 2017). These tools are needed in the early stage of design to identify the hazard and decide on the need and the efficiency of all kinds of safety features. However, risk assessment is directly related to the efficiency assessment of the designed system. The systematic tool for the assessment of the designed system can be applied by the Global Evaluative Assessment of Robotic Skills (GEARS). By applying a systematic and accurate assessment of the designed robot assisted surgical system, risk assessment can be more accurate and reliable. After risk assessment, the risk level can be identified and all corresponding tools for the enhancement of safety can be recognized to device effective control safety features in the surgical system.

According to the literature most of the research works have risk reduction and management as the main method to be considered in surgical system design. These methods are usually derived from the industry and military sectors (Sánchez et al., 2014). At each stage of design and test of the surgical systems, a risk assessment should exist. Accordingly, appropriate corrective actions should be developed and documented at each stage and a corresponding safeguard should be applied for each one. Risk assessments need to be done by applying a diversity of opinions, thoughts, and experiences by a team of engineers, operators, surgeons, etc. All of this can be documented as a reference to support proactive safety engineering as an alternative to the reactionary afterthought. Brainstorms by the team could be a great approach to this objective.

6.4. Control Safety Features

In this section, all added or proposed control safety features to the NeuRoboScope system are related to system failure avoidance and risk reduction techniques. The list presented in Table 6.2 is for the features added by this study and for those added by other studies. Noting that some features do not add safety directly to the

system but instead, they make controlling of the system easier for the surgeon and make the attention of the surgeon directed to his main task.

Table 6.2. Control safety features presented in this study

No	Code	Description
1	(CSF01)	All CSFs should be activated/supervised during operations
2	(CSF02)	Single main control-unit
3	(CSF03)	Auxiliary stand-alone sub-controllers for selected additional safety
4	(CSF04)	Current change detection of the motors
5	(CSF05)	Having a degree of autonomy
6	(CSF06)	Using computer-aided surgery for workspace analysis
7	(CSF07)	Estimating the workspace by simply measuring sets with intelligent learning technique
8	(CSF08)	Laser-based projection system for the placement of RCM point with respect to the patient
9	(CSF09)	Threshold on critical signals
10	(CSF10)	Assigning workspace limits at the software level
11	(CSF11)	Assigning predefined VFs to enhance safety and accuracy
12	(CSF12)	Instrument Delivery Virtual Tubes (IDVTs) or the virtual trocar
13	(CSF13)	Visual warning/alarmed signals
14	(CSF14)	The admittance control at the active robot arm
15	(CSF15)	Collision detection
16	(CSF16)	Intuitive touch screen with step-by-step guidance
17	(CSF17)	Selected physical buttons for the ease of accessibility
18	(CSF18)	Test-setup run
19	(CSF19)	Lockout tools
20	(CSF20)	Get instantaneous pose of the endoscope
21	(CSF21)	Redundancy in the controller
22	(CSF22)	Redundant passive landmarks for tracking system

(cont. on next page)

Table 6.2 (cont.)

23	(CSF23)	Redundancy of sensors
24	(CSF24)	Cable loose or cut detection
25	(CSF25)	Redundancy in teleoperation commander
26	(CSF26)	Twice confirmation on critical decisions
27	(CSF27)	Emergency switches (red mushroom head switch)
28	(CSF28)	Voice command
29	(CSF29)	Dead Man Switches (DMS) for safety

6.5. Robot Assisted Surgical Systems Control for Safety

In addition to the function of a controller unit in robot assisted surgical systems for moving and tracking in real-time, it is responsible for activation and monitoring the control safety features that added to the system and all control safety features should be activated during operations (**CSF01**). In the case of using a single main control unit, the wiring of signals will be less, and the response is quicker (**CSF02**). Nevertheless, using auxiliary stand-alone sub-controllers for selected additional safety devices can make the system safer in case of main control unit failure (**CSF03**). In the NeuRoboScope system, one main controller board was used to implement the main programming codes and realize the communications between the components' signals of the system (Ateş, 2018).

Signals between the mainboard and the other components can be monitored for unusual behavior. During the activation of motion, the current in the motors can be checked for any anomalous change which can serve as an indicator for impact or collision with objects. For example, if a sudden increase is detected in the current of the motors, it can be considered as a sign of collision, and the power of motors is needed to be turned off for safety reasons (**CSF04**).

As noticed from the user-robot interfacing methods in the literature, surgeons send motion commands to the robot assisted surgical system by various methods. The master part of this teleoperating system is usually not a traditional haptic device with

force feedback. The sensible feedback at the master side is usually the visual feedback. An image-based tracking technique to follow predefined points on the tool and assign them as landmarks of the transferred picture of the endoscope is another method of teleoperation. In this case, the motion can be autonomously commanded (CSF05). The autonomy of the surgical robot system does not mean to replace the surgeon by the robot but to increase the efficiency and dexterity of the surgeon by computer-aided guidance which can be effective in MIS (Yip and Das, 2018). By these means, the surgeon can have more concentration on the flow of the procedure.

6.6. Modeling and Analysis of Patients for Safety

Computer-assisted surgeries (CAS) techniques can be used to model each patient (CSF06). A database for patients will be available to be used on estimating the workspace by a simple measuring set such as the tests done for the NeuRoboScope project by radiology (Dede et al., 2018). For example, by using artificial intelligence (AI) and machine learning techniques (CSF07), the surgical workspace and the corresponding surgical task space of the robot can be investigated systematically. This technology can be used to improve the safety and efficiency of the surgery. A knowledge-based system is presented for MIS (Weede, Mehrwald, and Wörn, 2012) for planning all of the pose and configuration of the robot and ports of entrance during setup.

In pituitary tumor surgery, the surgeons are normally operating in small corridors and normally they get into proximity to some critical regions. Pre-modeling the organ to be treated in a 3D graphical presentation is beneficial as it gives surgeons a clear view of the data provided by medical scans. Rendering can provide even additional dimensions for the model of the organ and provides surgeons sensing ability like force interaction closer to reality.

Various techniques are used for implementing augmented reality after modeling and analysis of patients. In the work of (Wörn and Hoppe, 2001; Zeng et al., 2017), they used a common video projector to project necessary modeling information on the patient. The laser-based projection system was used as guidance for the robot system (Weede, Mehrwald, and Wörn, 2012). Applying a laser-based projection system can significantly contribute to the placement of RCM points with respect to the patient's

pivot-point at the entry port in MIS and improve time and safety (**CSF08**). In addition to mechanical and software limits, any critical signal can be considered for applying thresholds such as the exchange of forces and anomalous motion signals (**CSF09**).

As shown in Chapter 5, the difficulties of implementing mechanical limits for limited surgical workspace were discussed. However, by knowing the anatomical structure of the nasal cavity, software level workspace limits can be assigned to the control system as forbidden regions. (**CSF10**). Such information can leverage the design of VFs. He et al. (2019) designed and implemented a composition of three regular VFs designated for ESBS. They mainly depended on the trajectory of the endoscope and added a cloud of points by CT images to generate constrained motion and forbidden spots inside the surgery zone. Then by adopting admittance control, the user-robot cooperative method can guide the endoscope within the predefined VFs in a safe and accurate manner (**CSF11**). Since in NOTES, trocars are not available as commonly used in laparoscopic surgeries, VF techniques can be applied to have Instrument Delivery Virtual Tubes (IDVTs) as a virtual trocar (**CSF12**).

Data can be collected from encoders and saved as a data recorder for tracking the motion of the robot system. This dataset can be used as a tool for statistics, skill assessment, training, and authorization for surgeons (Taylor, 2006). Such important data can even be used along with the surgeon's commands data as a shred of evidence if needed at courts in case of complications.

6.7. Contact Force Information for Safety

The implementation of the force sensor was presented in Chapter 5 as an MSF. The feedback information of the contact force can be used in many scenarios as presented in the literature survey in Chapter 2. Plenty of safety feature algorithms depend on contact force signals that can be adapted. The simplest one is by setting a force threshold value for the contact force. Such a threshold should not be selected very low otherwise the robot would have a potential risk of unjustified motion (Bolzoni Villaret et al., 2017). By exceeding this threshold, the robot can be programmed to stop operating immediately. Multi-objective programs can be adapted to perform the surgical task. In the NeuRoboScope system, the contact F/T signals are sent to visual monitoring lights to warn the surgeons for exceeding the predefined levels of the F/T values

(CSF13). Many examples of force feedback related safety algorithms and functions can be found in (Bolzoni Villaret et al., 2017). External contact forces and collisions can be also tested at other location than the end-effector region. In the robots designed for pHRI, actuators are usually designed with embedded torque sensors. With the help of torque information at the joint level, external forces can be tested both in the contact points at the end-effector and the forces that can be presented at the links. An example is the Versius[®] surgical robotic system (CMR Surgical, 2020). This surgical system can allow for implementation of the admittance control **(CSF14)** so the surgeon can push the active robot arm away from the surgery zone. To test collision and external impact forces, Birjandi et al. (2020) proposed a new method of collecting motion information by IMU sensing at robot links. This method allowed real-time detection and increased the bandwidth that outweighs the other observer techniques **(CSF15)**.

6.8. Setup and Operation for Safety

Setting up and operating the main control unit should be easy and interactive considering that the surgeons are not technicians. For example, during the setup procedure, there should be instructions (See the control algorithm in Figure 5.2) that can be followed up easily and guide them through what should be done on each sequence and who should do each step. An interactive touch screen with a graphical user interface can be a useful tool so that the surgeon can follow up step by step intuitively **(CSF16)** (Ng and Tan, 1996).

Setup task accomplishment should be self-driven via a Graphical User Interface (GUI). The operating system in the main screen can provide pop-up windows and pull-down menus for simplicity and effectiveness in explanations. Additionally, using graphical representing icons for each function in the real physical system can increase simplicity. Using stylus or light pen for selection and vocal feedback can reduce the error and increases the accuracy of selection.

In addition to the other control methods, main and critical functions can be controlled or selected by the physical button for ease of accessibility **(CSF17)**. These physical buttons can be normal buttons, a mouse, a keyboard, or a joystick. Not too many functions should be assigned for the keys on the keyboard. They can be reserved for the functions that are frequently used during the surgery. This will help the user to

get used to effortlessly and improve the learning curve. From the surgical point of view, the most critical concerns for the surgeons are the development of intuitive user-robot interface and the automation level. It could be even more important than the selection of the special topology of the robot manipulator as has been stated by Strauß et al. (2007).

The reliability of the design at software and electromechanical hardware level should be guaranteed. Programed code at the software level that is prepared to be compiled and implemented to the control unit is needed to be pretested and checked thoroughly during design. Modeling of the NeuRoboScope system was done at the first stage of the project (Uzun et al., 2016). The predesign modeling was carried out by using the UPPAAL model checking tool. This modelling allowed validating the requirements of the system. As well as verifying the system against the vital system characteristics by focusing on the safety critical conditions. However, software and hardware tests can be performed at each setup for the system.

Since brakes and motors are integrated as a single unit in the active parallel manipulator, hardware test-run (**CSF18**) can be performed during setup to check for the brakes whether they are functioning or not. This can be initiated by activating brakes and motors simultaneously for a while and monitoring the potential motion in encoders. Another test setup can be carried out for encoders by providing motion to predefined reference positions and check if the motion of the robot is correlated to those reference positions. Lockout tools can be attached to the mechanical parts used in the setup (the fixture at the passive arm in NeuRoboScope and its elevator level) as well as attaching them to any needed switches and buttons (**CSF19**).

6.9. Redundancy for Safety

For the tracking method, all independent joints are in general have encoders which can provide accurate motion information of the joints. With an accurate forward kinematic solution, the end-effector can be tracked in real-time. However, any delay in the control unit can lead to misleading information to the controller. For safety reasons, an external navigation system for image-guided motion tracking can be added for the position of the endoscope at the end-effector or any other surgical tool needed to be tracked regarding the patient. In this way, the instantaneous pose information of the endoscope can be obtained (**CSF20**). Furthermore, an auxiliary external control unit can

be utilized independently of the main controller of the robot assisted surgical system to have redundancy in the controller (**CSF21**). For marker-based tools, redundant passive landmarks can be added to the active landmarks to improve the reliability of the tracking system (**CSF22**). Such a tracking system can be implemented in the NeuRoboScope system as an optional add-on, especially it is mostly available in the hospitals and provided with the commercial endoscope systems. Similarly, the redundancy of sensors is an important safety feature (**CSF23**). Adding additional encoder in passive joints is a good solution in the parallel active manipulator. Since these joints have a room for auxiliary sensors and can verify kinematic calculations on these joints. Besides, using reliable extra encoders at passive joints could significantly reduce forward kinematic calculations load of parallel robots if the obtained data used instead of calculating it. This can significantly contribute to the simplification of the dynamic equation. These secondary encoders can also be mounted on the capstan while the primary fine encoder is mounted on actuators. This can be used as an indicator tool for any shifting/backlashing within a tolerance between the position of motor's shaft and capstan position which can be potentially caused by loose or cut in the cable used in capstan. This safety feature can be called as cable cut/loose detection tool (**CSF24**). If any failure in the used commander in the teleoperation or loss of communications happened, an auxiliary manual joystick-like commander can take the responsibility to teleoperate the robotic arm. Such auxiliary commander could be attached to the main control unit in a reachable position (**CSF25**).

Another level of redundancy is in the autonomy of some functions of the surgical robotic system. This can be called redundancy in the Human-Robot level when a robot can overtake the human role whenever necessary (**CSF05**). This can be seen in the supervisory-controlled system and the examples presented in Section 2.1.1. A lower level of autonomy in the surgical robot can be noticed in the use of virtual limits for the joints or the workspace (**CSF07**). It is usually the surgeon's responsibility for being aware of the workspace but whenever he/she go beyond the previously defined workspace the robot will warn or proceed. As an example, in the MAKO[®] system, the surgeon can maneuver the milling tool inside a virtually constrained volume which is called the virtual fixture (Rosenberg, 1993). Adding to that, redundancy at different levels such as (watchdog, emergency switches, etc.) can always be an essential solution for safety.

6.10. Other Control Safety Features

Whenever a critical decision is being asked for, a surgeon can be asked to confirm twice (**CSF26**). In case a decision has been taken, the surgeon can always be able to interrupt the action by various options of emergency mechanisms. In addition to the emergency mechanisms that can be performed by the aid of the MSFs, which are proposed in Chapter 5, such as the passive guidance out of surgery zone; the admittance control; and the easy plugging/releasing of the endoscope, other emergency devices in CSFs can be added such as: Emergency switches (**CSF27**) and stopping voice command (**CSF28**). Emergency switches can be added in many reachable positions (near joysticks, near foot pedal, close to the assistant, etc.) to interrupt any stage of the processes as shown in the control algorithm in Figure 5.2. As another CSF, the so-called Dead Man Switch (DMS), can be utilized. This needs the surgeon to exert continuous action to permit the robot arm to interact (**CSF29**). Even though more switches can provide more safety, they will limit the mobility of the surgeon. In general, a pedal can be added as a second DMS so that if it is not pressed the robot will stop/decelerated.

6.11. Conclusions

This Chapter presented some of the important points used to be implemented in the design of robot assisted surgical systems and provides some thoughts that can be applied in the design of the NeuRoboScope system. A brief discussion on the safety standards and systematic approaches are presented for surgical robotic systems. Implementing safety features to the surgical system can only be verified by following safety standards and extensive preclinical tests. Risk assessment methods are discussed, and related assessment tools and hazard identification methods are pointed out. Many of these control safety features are inspired by researches and considered to be a crucial element of safety features in surgical robotic systems. However, additional safety features can provide the system with more safety but can make the system more complicated. A high level of safety can increase the chance of acceptance of the surgical robot system for being in the operation room which is the main goal of surgical robot systems developers.

CHAPTER 7

PASSIVE ARM'S DESIGN OPTIMIZATION

In this Chapter, a redundancy resolution technique that is used normally in robot arms is employed in mechanical design optimization. Although the robot arm can be a non-redundant one, the proposed method modifies the robot arm kinematics by adding virtual joints to make the robot arm a kinematically redundant one. In this way, a suitable objective function is selected for optimizing the robot arm's kinematic parameters by enhancing one or more performance indices. In the procedure of this optimization method, the robot arm's end-effector is fixed at critical positions of the workspace while the redundancy resolution algorithm moves all the joints including the virtual joints as a result of the self-motion capability of a redundant robot arm. In this way the optimum values of the virtual joints are determined, and the design of the robot arm is modified accordingly. In this work, the passive arm that is used in the NeuRoboScope system and introduced in Section 4.3, is considered and the optimization task is defined as the determination of the optimum base fixing location (as firstly introduced in Section 5.3) and the first link's length for maximizing the manipulability and minimizing the impedance.

7.1. Optimization Methods

Most optimization techniques depend on numerical and/or algorithmic approach. With the improvement and availability of powerful computers, many techniques for optimization studies are presented. Such methods can be listed as genetic algorithms (GA) (Holland, 1973a), Ant Colony Optimization (ACO) (Colorni, Dorigo, and Maniezzo, 1991), and Particle Swarm Optimization (PSO) method (Kennedy and Eberhart, 1995). These methods are categorized as modern and nontraditional optimization methods. Each individual optimization technique has rewards and drawbacks. Many improvements and modifications to these techniques have been studied. The readers are directed to related books on optimization methods, review papers of optimization methods, and comparative studies such as the comparative study

in (Ab Wahab, Nefti-Meziani, and Atyabi, 2015) and the review of the seven stochastic optimization methods preferred in industrial design optimization (Erten, Deveci, and Artem, 2020).

In this Chapter, a new optimization approach for mechanical design optimization is presented. The proposed optimization technique is potentially able to adopt any one of redundancy resolution techniques (introduced in the next section), which are originally developed for the control of kinematically redundant robot arms, for optimization tasks.

A structural optimization process is carried out in this Chapter considering the design constraints to verify the applicability of this new method. The mechanical design optimization procedures followed generally in the design of industrial robots (Briot and Goldsztejn, 2018) and the design of haptic devices (Vulliez, Zeghloul, and Khatib, 2018) are utilized in this work in terms of analyzing the requirements, stating the problem, assigning design constraints, and nominating objective functions. Consequently, performance indices such as manipulability, the impedance at the end-effector, and the modified condition number are utilized to evaluate kinematic and/or dynamic performances of robot arms (Iqbal and Aized, 2014). Specifically, in the present work, the objective function that is used in redundancy resolution via null-space optimization is derived by using these two indices and the performance index of the Generalized Inertia Matrix (GIM).

7.2. Redundancy Resolution Techniques

Optimization is employed in a wide range of study areas from economical sciences to design processes in engineering applications. All of those systems that need optimum solutions are inherently redundant. In robotics, kinematic redundancy has been an attractive research area since kinematically redundant robot arms may be used to perform additional functions on top of their main tasks. This is due to the infinite number of solutions received for the inverse kinematics analysis of a redundant robot resulting in an infinite number of configurations of the robot for the same end-effector pose. Consequently, the motions of the links of a robot that are not affecting the motion of the end-effector are named “self-motion” by Nakamura (1990).

A variety of redundancy resolution methods was introduced in the literature such as the Jacobian pseudo-inverse method, weighted pseudo-inverse method, and singularity robustness method (damped least-squares DLS). All of those redundancy resolution methods are Jacobian based. A common result of these techniques is to have the minimum norm of joint-space velocities.

By adding constraints in the form of additional tasks to redundancy resolution, the infinite number of solutions are narrowed down to a specific/bounded solution. This is exactly equivalent to establishing design constraints in design optimization techniques. To incorporate an additional task, which is usually called the subtask, to the resolution process of kinematic redundancy, a null-space based method can be applied. In this method, the gradient of a differentiable objective function is projected in the null-space of the Jacobian matrix so that it has no effect on the main task. Here, the main task is the task that is usually assigned as the tracking of the end-effector's motion trajectory.

Another method of redundancy resolution is the decomposition method which decomposes joint-space variables into two groups (two minor Jacobian matrices) as they are related to the main-task and the additional task. Afterward, constraint objective equality is utilized as an implicit function to reduce the gradient of optimization objective function (De Luca and Oriolo, 1990). This method has the attribute of eliminating the unnecessary intensive computation of pseudo-inverse which increases the efficiency of calculation time.

In the task augmentation null-space based method, the Jacobian matrix is extended by the addition of an auxiliary task (Peng and Adachi, 1993) to result in a square augmented Jacobian matrix. In this method, the pseudo inverse is not to be used (Seraji, 1989) and the kinematic solution is no longer redundant.

Multi-task priority is another null-space based method (Nakamura, Hanafusa, and Yoshikawa, 1987). In this method, other than the Jacobian matrix related to the main-task, for each additional subtask, another Jacobian matrix exists. The self-motion of the first subtask is projected to the null-space of the main-task's Jacobian matrix. The motion of the second subtask is projected into the null-space of the first subtask's Jacobian matrix. In the same means, other lower-order priority subtasks can be embedded in the earlier subtask that has higher priority. Another redundancy resolution at the acceleration level was presented in the work of (Luca, Oriolo, and Siciliano, 1992). At the acceleration level, acceleration is used instead of velocity command.

Using redundancy at the acceleration level is useful for dynamic control methods (Wang, Li, and Zhao, 2010; Maarroof, Gezgin, and Dede, 2012).

Kinematic control is essential to execute both the main-task and the subtask of redundant robots (Dubey, Euler, and Babcock, 1991). Previously, for control of kinematically redundant robots, a neural network method is used in (Li and Leong, 2001) (Cerebellar Model Articulation Controller). Others works on the control include the optimization of the torque signals through dynamic control of the system, which performed redundancy resolution of torque signals (Baillieul, Hollerbach, and Brockett, 1984; Hollerbach and Suh, 1987; Al Khudir et al., 2019).

Depending on the redundancy resolution studies, Özbay et al. (2008) classified the redundancy resolution into two major approaches. In the first one, the formulation of the task space is extended into a new dimension by adding as many augmented constraints as the degree of the redundancy. As a result, the new system is no more redundant. In the second one, the pseudo-inverse of the Jacobian matrix is used for the formulation of the control system. By this approach, whenever the manipulator is near singularity the bounded solution cannot be guaranteed.

7.3. Applications on Redundancy Resolution

In the previous studies, redundancy resolution has been also used as an optimization tool for different applications such as the enhancement of safety through optimization of redundant robot posture during human-robot interaction (Maarroof and Dede, 2016). It has been used in the optimization of the stability in machining operation through the control of the robot posture (Mousavi et al., 2017). In (Uzunoglu, Dede, and Kiper, 2016), optimization to resolve a special type of kinematic redundancy, the macro–micro manipulation, was employed for task duration reduction. These auxiliary functions are used to be controlled online by changing the posture of the arm during performing the main function which is an online optimization procedure. The extra DOFs have been used for other optimization approaches such as the obstacle avoidance in (Dede, Maarroof, and Tatlicioğlu, 2016), mechanical joints limit avoidance (Tatlicioğlu et al., 2009), minimization of joint velocities and accelerations (Maarroof, Gezgin, and Dede, 2012), and reducing interaction forces in physical human-robot Interaction (Maarroof and Dede, 2016). In most redundancy resolution methods, the

definition of the objective functions to fulfill specific additional tasks are involved in manipulation. In accordance, in this proposed optimization technique that is presented in this Chapter, these objective functions are used as potential performance indices to assign design constraints in the optimization problems for the first time in structural synthesis.

7.4. Description of the Case Scenario

The passive arm that is designed to carry the active parallel manipulator mounted on its last link as shown in Figure 7.1 is the optimization problem. It can be also considered as a case study for the verification of the proposed optimization technique. In this system, the passive arm is required to be backdriven by the surgeon to the designated locations of the surgical workspace with minimal effort. Therefore, its performance measures related to both kinematic and dynamic manipulability are studied in this work as objective functions to be used in the optimization of the passive arm's structure.



Figure 7.1. The surgical robotic system NeuRoboScope

Its kinematic architecture is shown in Figure 7.2. The MP is identified as the manipulation point at which the manipulability of the passive arm is designated to be calculated. Denavit-Hartenberg parameters of the passive arm are provided earlier in Table 4.2. In this table, a_1 length is kept as to be designed (TBD) on purpose since this is the link length to be optimized for this manipulator in addition to the fixing position of the passive arm.

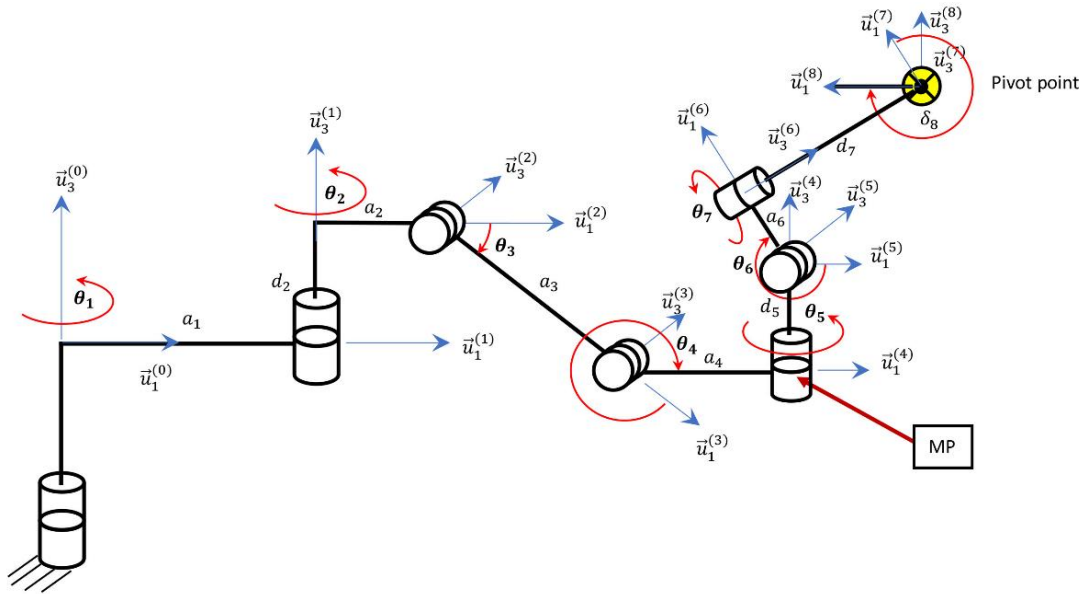


Figure 7.2. Kinematic scheme of the passive robot arm

7.5. Description of the New Design Optimization Method

Redundancy resolution by using pseudo-inverse and null-space optimization technique has been used for the control of redundant robots. In order to conduct redundancy resolution algorithms for robot arms, the n -DOF of the robot arm should be higher than the m -DOF needed for the task. For the specific task of any robot arm, structural synthesis can be included while the robot is performing that task through introducing p number of additional virtual joints. In this way, even if the original robot arm for the specified task is not redundant ($n = m$), the modified robot arm has $n + p$ DOF and becomes a redundant one. The additional virtual joints number is assigned to represent the design optimization parameters. In the structural synthesis of a robot arm, design optimization parameter/s can be any Denavit-Hartenberg (Denavit and Hartenberg, 1955) parameter/s other than the joint variable. Accordingly, the self-

motion of the robot arm is a consequence of the change of the real joints and design parameters.

As a next step, by assigning a suitable objective function to be minimized or maximized as a subtask, optimum values for the virtual joint variables (design parameters) are searched for. The objective functions are generally selected to represent a performance index usually defined for robot arms such as manipulability or condition number but the performance to be tested on the real robotic system. The robot can then be tested for a specific main task, which might be a static position/s of the end-effector. Finally, optimal values for the virtual joints are calculated regarding the objective function via a redundancy resolution algorithm, and thus, the design parameters are selected.

7.6. Design Optimization Constraints

In this section, and related to this specific case scenario, the design constraints for the NeuRoboScope system are provided. With respect to this special use of the passive arm, design constraints defined below are set.

1. The endoscope can be inserted from either nostril.
2. The endoscope and the active parallel manipulator should not interfere with the surgeon's hands and they should not block the surgeon's view of the monitors (Figure 7.3).
3. The passive arm should locate the active manipulator inside the surgery zone by approaching from behind the patient's head.
4. The passive arm should be fixed to the surgery table.
5. Physical dimensions of the links should not be large and heavy while keeping the compliant displacements at a minimal level.
6. When the passive arm's brakes are released, the surgeon should be able to move the endoscope freely while the endoscope is still attached to the active robot manipulator.

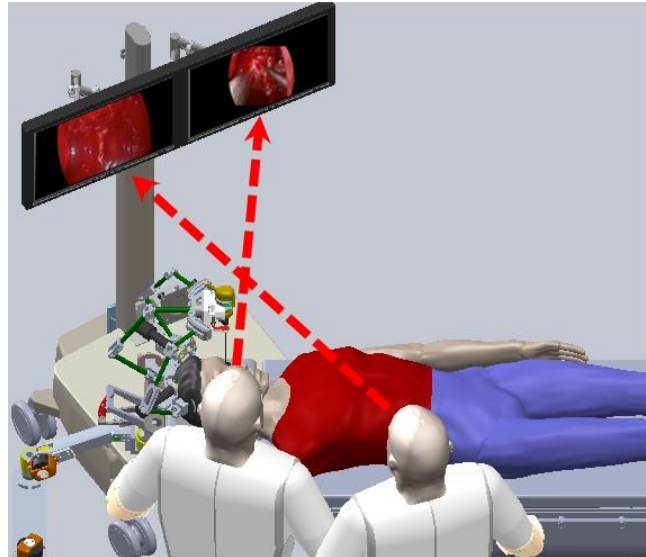


Figure 7.3. Spectacle situation in the surgery room

In this case study, the only motion of the passive arm on the horizontal plane will be considered. By this consideration, the passive arm is considered as a two-link planar arm with 2 DOF. Design parameters that are considered are the effective link length of the first link and the ground frame origin of the passive arm, which is the location when the passive arm is fixed on the surgery table.

7.7. Optimization by Using Mechanical Redundancy

Depending on the previously defined design constraints, some conditions for the passive arm are set in order to facilitate the optimization procedure by considering the necessities and conditions of the surgery:

The surgeon should have minimal effort when he/she intends to push the active robot manipulator into or away from the surgery zone. Hence, the optimization objective function that makes the manipulability maximum of the base of the active manipulator and having maximum movability in all directions is selected for this goal.

1. The parallelogram loop in the passive robot arm is utilized with no modifications since it is designed with counter-spring for gravity compensation. This linkage is responsible for providing vertical motion of the base of the active arm.

2. Optimization will be related only to the manipulability on the horizontal plane.
3. The fixing point position on the y-axis (with respect to reference-frame in Figure 7.4) is selected as a design parameter, which is related to the first link's length that is needed to be designed.
4. The position of the manipulation point (MP), shown in Figure 7.2, is considered to be fixed nearly at coordinates (-20, -30) cm with respect to the reference frame in Figure 7.4.
5. The effective link length of the first link should be limited depending on its manufacturability, final weight, and allowed compliant displacements due to loads.
6. The linear density of the first link is taken as follows: mass/length = 1 kg/m.
7. The third joint variable θ_3 in Figure 7.2 is fixed at -30° which is the condition when the endoscope is located just above nostrils (with the help of the adjustable first active level motor on the passive arm).

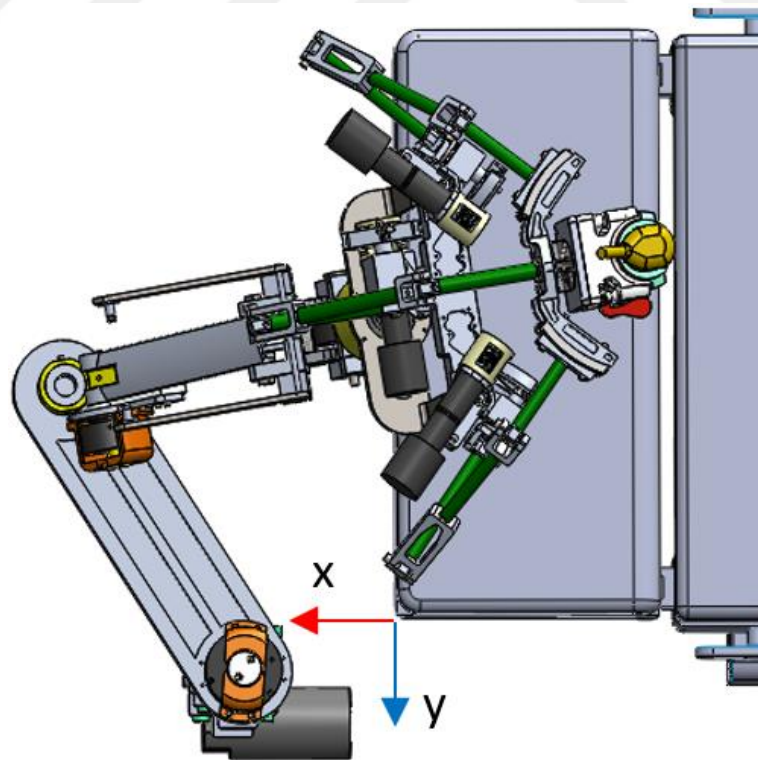


Figure 7.4. Reference coordinate system on the surgery table

Since the objective of the optimization is to obtain maximum manipulability at MP, which is denoted in Figure 7.2, forward and inverse kinematics, and the Jacobian matrix calculations are presented in this Chapter for MP. Hence, these calculations are used for the proposed optimization method.

Forward kinematics: The position of MP is assigned as the manipulation point which is essential for being a critical consideration for optimization.

$$\bar{p}_{MP} = a_1 \bar{u}_1^{(1)} + d_2 \bar{u}_3^{(1)} + a_2 \bar{u}_1^{(2)} + a_3 \bar{u}_1^{(3)} + a_4 \bar{u}_1^{(4)} \quad (7.1)$$

In Equation 7.1, there are $d_2, a_2, a_3,$ and a_4 as fixed parameters. The only variable is the design parameter that is selected for this optimization study which is the effective link length of the first link, a_1 .

The joint variables are $\theta_1, \theta_2, \theta_3$ and θ_4 , three of which are independent parameters so that the position in the Cartesian space is to be considered as moving on a horizontal plane as related to θ_1 and θ_2 . Apart from that, θ_3 is related to the vertical motion and it is selected as a constant value as explained previously. In this way, the passive arm is reduced into a planar revolute-revolute (RR) manipulator.

Inverse Kinematics: Since the workspace that the surgeon uses while locating the endoscope in and out of the nostrils is known, the position of the MP can be considered as another constraint for design. With respect to this position on the horizontal plane, while considering the base of the passive arm fixed at a specific point on the surgery table, two possible configurations can be calculated as elbow-up and elbow-down. One of the two solutions is selected to find the initial position for each of θ_1 , and θ_2 during the optimization study. In addition, an initial value for the design parameter a_1 is selected to calculate the inverse kinematics calculation. The inverse kinematics solutions are not presented here since it is trivial for a planar 2-DOF RR arm.

Jacobian Matrix: For verifying and constituting the objective function on the actual passive arm, the original Jacobian matrix is selected as $\hat{J}_{2 \times 2} \in \mathfrak{R}^{2 \times 2}$ matrix for the planar arm with 2 DOF. However, for optimization study, virtual joints are added to the original passive arm and the Jacobian matrix is modified as $\hat{J}_{2 \times 4} \in \mathfrak{R}^{2 \times 4}$ and also $\hat{J}_{2 \times 3} \in \mathfrak{R}^{2 \times 3}$. The dimension of the Jacobian matrix is related to the DOF of the workspace and DOF of the original or modified passive arm. In the next set of Equation

7.2 ~ 7.4, Jacobian matrix with two virtual joints, one virtual joint, and no virtual joints are presented respectively.

$$\hat{J}_{2 \times 4} = \begin{bmatrix} 0 & c_1 & -a_1 s_1 - (a_2 + a_4 + a_3 c_3) s_{12} & -(a_2 + a_4 + a_3 c_3) s_{12} \\ -1 & s_1 & a_1 c_1 + (a_2 + a_4 + a_3 c_3) c_{12} & (a_2 + a_4 + a_3 c_3) c_{12} \end{bmatrix} \quad (7.2)$$

$$\hat{J}_{2 \times 3} = \begin{bmatrix} c_1 & -a_1 s_1 - (a_2 + a_4 + a_3 c_3) s_{12} & -(a_2 + a_4 + a_3 c_3) s_{12} \\ s_1 & a_1 c_1 + (a_2 + a_4 + a_3 c_3) c_{12} & (a_2 + a_4 + a_3 c_3) c_{12} \end{bmatrix} \quad (7.3)$$

$$\hat{J}_{2 \times 2} = \begin{bmatrix} -a_1 s_1 - (a_2 + a_4 + a_3 c_3) s_{12} & -(a_2 + a_4 + a_3 c_3) s_{12} \\ a_1 c_1 + (a_2 + a_4 + a_3 c_3) c_{12} & (a_2 + a_4 + a_3 c_3) c_{12} \end{bmatrix} \quad (7.4)$$

In the Equation 7.2 ~ 7.4, the abbreviations c_i and s_i represent $\cos \theta_i$ and $\sin \theta_i$ respectively. While c_{ij} and s_{ij} represent $\cos(\theta_i + \theta_j)$ and $\sin(\theta_i + \theta_j)$ respectively.

7.8. Implementation of the New Optimization Strategy

When there is kinematic redundancy, there is a free motion of the mechanism even if the end-effector is fixed. This so-called self-motion happens in the null space of the Jacobian matrix. In the implementation of the proposed optimization strategy, this property is used. However, in order to use this property, the non-redundant passive arm has to be modified to have more joints.

The DOF of the RR planar arm is increased by two by adding virtual prismatic joints to move the fixing point along $\vec{u}_2^{(0)}$ axis (y-axis in Figure 7.4) defined with a joint variable Y_0 and to change the effective link length of the first link defined with a joint variable a_1 . Consequently, the new planar arm is a 4-DOF PRPR operating in a 2-DOF planar workspace. Since the objective is to find optimum design parameters, these new joint variables are included in the control of the self-motion of the resultant redundant arm. The design constraint of having maximum manipulability at MP is used as the main objective function for controlling the self-motion of the robot arm.

A previously designed controller for redundant robot manipulators is utilized for this optimization task. The design of this controller is explained in (Maarroof, 2012; Maarroof, Gezgin, and Dede, 2012). However, only the kinematic part is used in this

work, which is acceleration-based control. This controller can be used to control both the main-task in task-space defined by the MP point's position \vec{x} , and the desired sub-task in joint-space defined by joint variable in the array \bar{q} .

An error term is defined as $\bar{e} = \vec{x}_d - \vec{x}$ is defined as the tracking error, and \vec{x}_d is defined as the desired position in task space. The designed controller is presented in Equation 7.5 where \hat{K}_v and \hat{K}_p are diagonal constant feedback gain matrices related to the PD controller of the main-task.

$$\ddot{\bar{q}} = \hat{J}^+ \left(\ddot{\vec{x}}_d + \hat{K}_v \dot{\bar{e}} + \hat{K}_p \bar{e} - \dot{\hat{J}} \dot{\bar{q}} \right) + \ddot{\bar{\theta}}_N \quad (7.5)$$

The joint variables are represented in $\bar{q} \in \mathfrak{R}^n$, where n , from now on, is the summation of actual and virtual joints in this approach. A column function $\bar{z}(\cdot) \in \mathfrak{R}^n$ is calculated as a gradient of optimization objective function $f(\bar{q})$ for a specific optimization objective function (which may be time-dependent function, design parameters, constraints, etc.), and the projection of \bar{z} onto the null space of \hat{J} needs to be as the joint velocities in the null space of \hat{J} . Since the projection of any vector can be done by premultiply the vector by $(\hat{I}_n - \hat{J}^+ \hat{J})$. The error in the velocity of the joints in the null space can be calculated in Equation 7.6, which converges to zero. Here, \hat{J}^+ represents the pseudo-inverse of \hat{J} and $\hat{I}_n \in \mathfrak{R}^{n \times n}$ is the identity matrix.

$$\dot{\bar{e}}_N = (\hat{I}_n - \hat{J}^+ \hat{J}) \dot{\bar{z}} - \dot{\bar{\theta}}_N \quad (7.6)$$

Considering the manipulator is away from a singularity condition, it is needed to design for $\ddot{\bar{\theta}}_N$ corresponding to the desired subtask objective as:

$$\ddot{\bar{\theta}}_N = (\hat{I}_n - \hat{J}^+ \hat{J}) \ddot{\bar{z}} - (\dot{\hat{J}}^+ \hat{J}^+ + \hat{J}^+) \dot{\bar{z}} + \hat{K}_N \dot{\bar{e}}_N \quad (7.7)$$

In Equation 7.7, \hat{K}_N is a diagonal positive definite feedback matrix. This designed control law guarantees that the error will be bounded and converged to zero (Maarroof, Gezgin, and Dede, 2012).

After the description of the controller to be used in the proposed optimization method, the performance indices that are used to formulate the objective function are explained in the next subsections.

7.8.1. Manipulability Ellipse and (SVD) Singular Value Decomposition

Manipulability of a selected point in a mechanical linkage can be represented as a scalar value related to the area/volume of velocity ellipse/ellipsoid. It is first developed in (Yoshikawa, 1985a) as a performance index. Since the motion of any point on a mechanical linkage can be related to the motion of the joints by the Jacobian matrix, the scalar representation of the manipulability index Mp is provided in the following equation.

$$Mp = \sqrt{\det(\hat{j}\hat{j}^T)} \quad (7.8)$$

In addition to the manipulability index shown in Equation 7.8 another manipulability measure in Equation 7.9 was also formulated by Paul and Stevenson (1983). Both of Equation 7.8 and Equation 7.9 are identical when the Jacobian matrix is a square matrix (which is the case of the proposed 2-link planar arm).

$$Mp = |\det(\hat{j})| \quad (7.9)$$

The objective set when using the manipulability index is to maximize this value via changing the positions of joints by staying inside the null-space when MP is fixed at the desired position. During this motion, the effective link length of the first link (a_1) and the position of the fixing point of the passive arm will be changing to reach the optimum value in this optimization. Singular value decomposition on the matrix $\hat{j}\hat{j}^T$ is used to solve for singular values of \hat{j} , which also represents the semi-axes of manipulability ellipse during the simulation. The rank of \hat{j} represents the number of singular values, which is 2 in this case since the Jacobian matrix used in the objective function is for the real arm.

7.8.2. The Modified Condition Number

Another way to represent force/motion relation of a point in the workspace of a mechanism is done by a scalar number called condition number (Salisbury and Craig, 1982). Manipulability represents ease of manipulation of the end-effector at a certain location of the workspace and the condition number relates the maximum and minimum axes of manipulability ellipse achieved along with different directions at that specific location of the end-effector. The condition number can be defined by the ratio of the maximum singular to the minimum singular values of the Jacobian matrix. The singular values represent the radii of the manipulability ellipse or as so-called the velocity transmission ratio by Chiu (1988). In an ideal case, the performance index is 1, which means at that specific point, the ease of manipulation is the same in all directions.

Force condition number and velocity condition number are calculated in similar ways. Salisbury and Craig (1982) found force condition number by introducing the amplification of the relative force error at the workspace to the relative torque error at joint-space. While Merlet (2006) found a velocity condition number using relative motion error in joint-space and relative motion error in the workspace.

In this work, the difference between the maximum and minimum singular values is used instead of the condition number and it will be referred to modified condition number from this point on. By the use of the modified condition number in this way, the problem of having near infinity number of the objective function at singularity configurations can be eliminated. The objective function is shown in Equation 7.10 is then used in the optimization to be decreased to an acceptable amount or to zero.

$$C_n = \sigma_{max} - \sigma_{min} \quad (7.10)$$

7.8.3. Generalized Inertia Matrix

To include a dynamic orientated design constraint for the design of the passive arm, the dynamic of the arm is studied via finding its dynamic equation of motion and inertia matrix. This is essential to find the dominant effective part of design parameters in the relation between the forces shown at the end-effector and the motion in the same space. In this work, since the end-effector is moved at a slow rate, Coriolis and

centripetal forces, and the viscous frictional forces are neglected. Consequently, the remaining part of the dynamic equation is the part with the inertia matrix as shown below.

$$\bar{\tau} = \hat{M}\ddot{q} \quad (7.11)$$

To represent Equation 7.11 in the task space where the interaction is taking place, the task space forces are mapped to the joint space by using the Jacobian matrix as follows:

$$\bar{\tau} = \hat{J}^T \bar{F} \quad (7.12)$$

where \bar{F} is the array of external forces acting at the end-effector. For the slow-motion of the end-effector, where $\dot{q} \rightarrow 0$, then considering $\ddot{q} = \hat{J}^{-1}\ddot{x}$. Subsequently,

$$\hat{J}^T \bar{F} = \hat{M}\hat{J}^{-1}\ddot{x} \quad (7.13)$$

As a result of this expression in Equation 7.13, Generalized Inertia Matrix (GIM) \hat{M}_G is defined in the task space as shown in Equation 7.14.

$$\hat{J}^{-T} \hat{M} \hat{J}^{-1} = \hat{M}_G \quad (7.14)$$

The dynamic performance of the passive arm can be represented by the ellipse (in the case of 2-DOF manipulator) which can be plotted with respect to the eigenvalues and eigenvectors of \hat{M}_G matrix (Asada, 1983). On the other hand, the dynamic manipulability (the determinant of $\hat{J}\hat{M}^{-1}$) as defined by Yoshikawa (1985a) relates the loads at actuators to the acceleration output at end-effector as shown in Equation 7.15.

$$\ddot{x} = \hat{J}\hat{M}^{-1}\bar{\tau} \quad (7.15)$$

For the design optimization study of the passive arm, the objective is to minimize the resistance shown to the operator during the surgeon backdrives the arm,

which can be termed as the mechanical impedance (Colgate and Brown, 1994) of the passive arm. By doing so, the end-effector can be moved freely inside its workspace with minimum force reflected to the user. This can be achieved by minimizing the numerator part of GIM hence the inertia matrix, and/or maximizing the denominator part of GIM, which corresponds to the manipulability index since $\det(\hat{f}^T \hat{f}) = \det(\hat{f} \hat{f}^T)$.

7.9. Test Setup and Simulation Results

Three simulation tests were conducted to verify the presented approach. The number of design parameters is different in the first two tests. The Jacobian matrix developed for the MP of the actual passive arm (RR manipulator version) is used to determine the desired objective function consisting of the manipulability index in the first two tests and the modified condition number in the third test and the addition of part of the GIM in the final test. All tests are carried out in MATLAB[®] Simulink[®]. The position of MP is selected as a design constraint on the horizontal planar workspace at -20, -30 cm, which is determined with respect to the reference frame described in Figure 7.4. The initial value of the first link is chosen as $a_1 = 30$ cm and the initial value of fixing position (first joint's axis) along the y-axis is selected to be $Y_0 = 0$. The other parameters of the passive arm are fixed. It should be noted that the actual passive arm's Jacobian matrix is used only to find the objective function of self-motion, while the virtual/modified Jacobian matrix used in the control law.

7.9.1. Test 1: Two Design Parameters

In this test, the optimization procedure is carried out for the first link length (a_1) and fixing position of the base of the passive arm along the y-axis of the surgery table (Y_0). Here, two virtual joints added to result in a modified Jacobian matrix with the dimension of the 2-by-4 matrix. This matrix is used in the controller while the self-motion is regulated by the change in the rates of new joint space parameter set consisting of Y_0, a_1, θ_1 , and θ_2 .

It is observed from Figure 7.5 that the design parameters continue to change. This leads to divergence in the solution as observed in Figure 7.6 and hence, no feasible

design can be obtained. In Figure 7.6, σ_1 and σ_2 refer to the singular values. The reason for this phenomenon is that as the design parameters get larger values, the manipulability continues to increase without bounds. Consequently, simulation time is terminated at 1.5 (s) since the increase in the length of link 1 will not stop at a specific value because of the absence of boundary conditions.

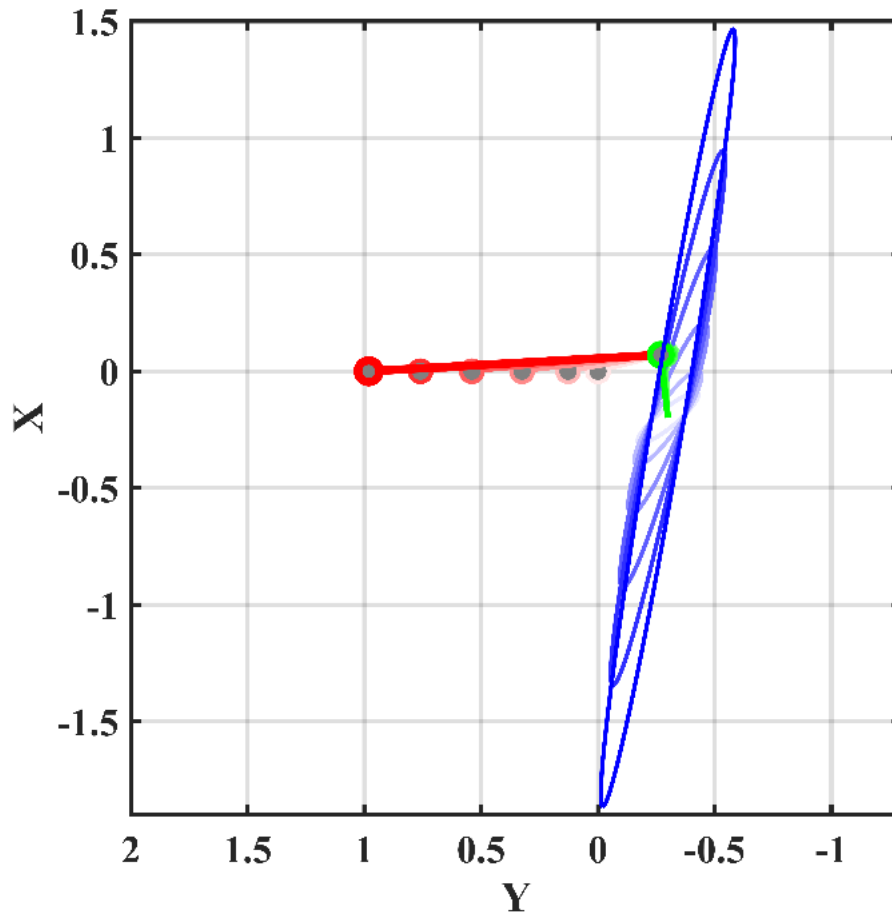


Figure 7.5. The change of the robot arm structure and the manipulability ellipse during the optimization routine with two design parameters

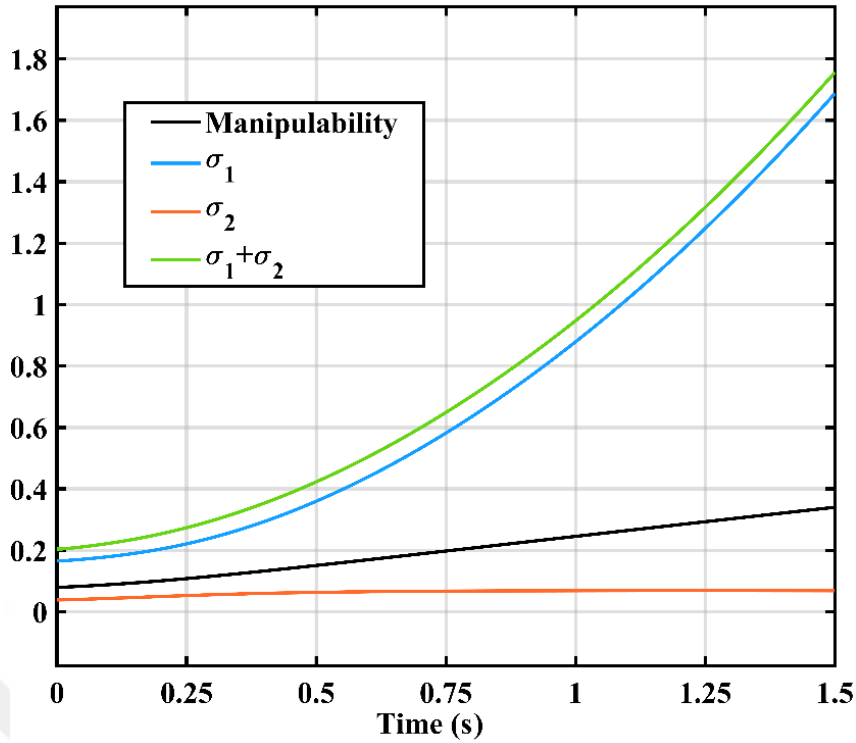


Figure 7.6. The change of the manipulability index of the passive arm during the optimization routine with two design parameters

7.9.2. Test 2: One Design Parameter

In this simulation test, a single virtual prismatic joint is used for the optimization of only the length of link 1, a_1 . In this case, the modified Jacobian matrix is $\hat{J} \in \mathbb{R}^{2 \times 3}$. Simulation test results indicate that the manipulability of the passive arm is increased to the maximum value and parameter change of rate for the length of the first link is stopped at an optimum value, 0.4515 m, as shown in Figure 7.7. Any link length dimension for the first link less than this value will lead to having decreased manipulability at the MP. Hence, the length of the first link can be selected via this analysis in order to have reasonable link length and have satisfactory manipulability.

Table 7.1. Joint variables of Test 2

i	Joint parameters	q_i
1	a_1 (m)	0.4515
2	θ_1 (rad)	-1.512
3	θ_2 (rad)	-2.217

Manipulability ellipses in this test are shown in Figure 7.7. The maximum area of the ellipse is obtained at the final presented configuration is near the 20th s and stayed constant at this optimum solution. This can also be noticed in Figure 7.8 for manipulability and singular values. It can be noticed that the orientation of the second link is perpendicular to the virtual line that can be drawn between the fixing-point and MP. Hence, this configuration is obviously the maximum manipulability one. This property of orthogonality makes it easier to select the value of Y_0 considering its relation to the first link's length and orientation. However, this could seem different than the previously provided results by Yoshikawa (1990) but both are identical. The analytical form of the determinant of the Jacobian matrix can be written as $Mp = |l_1 l_2 \sin \theta_2|$. In the results provided by Yoshikawa, to maximize manipulability with fixed link lengths, maximum $\sin \theta_2$ can be obtained by assigning the second angle $\theta_2 = \mp 90^\circ$. This is not the case here. To increase the manipulability in this equation $\sin \theta_2$, l_1 , and l_2 can be maximized if there are no constrained. However, in the specific case presented in this optimization test the position of the MP is fixed regarding the fixture point and the second link length as well. In this case, increase this scalar value of manipulability can only be done by the manipulation of l_2 and θ_2 . For a fixed tip-point θ_2 is also related to l_1 to keep the position of MP with respect to the fixture point. So, there is a unique solution for this equation when it has a maximum value. This can be a verification of the solution obtained in this test and a verification of the proposed optimization method.

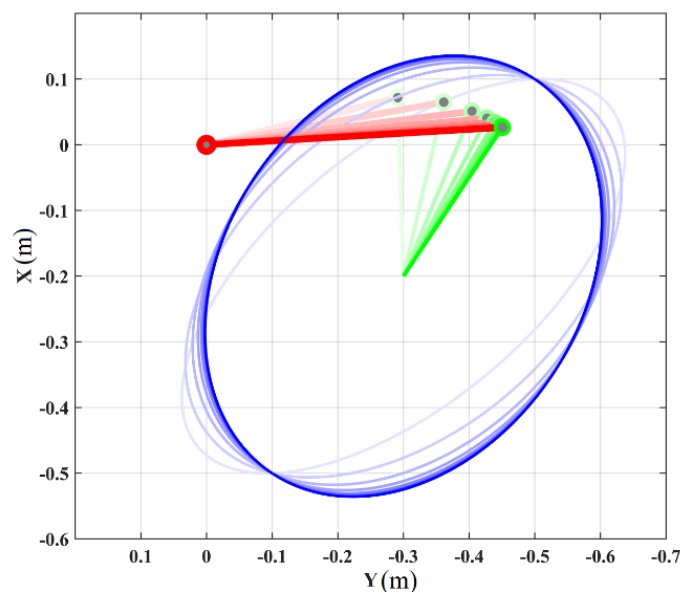


Figure 7.7. The change of the robot arm structure and the manipulability ellipse during the optimization routine with one design parameter

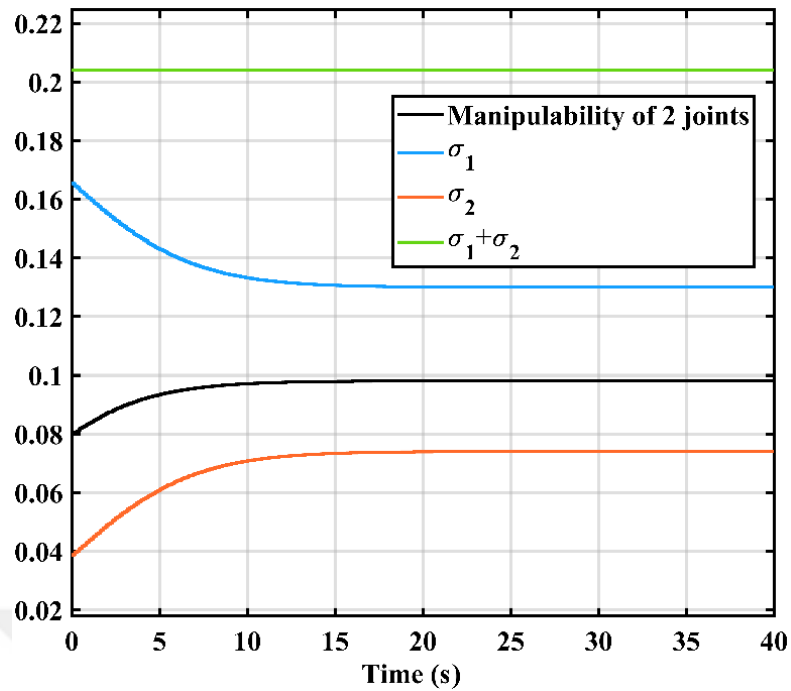


Figure 7.8. The change of the manipulability index of the passive arm during the optimization routine with one design parameter

7.9.3. Test 3: With the Modified Condition Number as the Performance Index

In this test, the modified condition number is used as an alternative to the manipulability index. Both fixing point and the first link's length are selected as design parameters which are the same condition of Test 1 in Section 7.9.1. However, in this case, the use of the modified condition number includes an extra design constraint. Two different results are obtained in this test which is related to the selection of the objective function as follows:

Test 3.1: By only using the modified condition number, which is explained in Equation 7.10, as the only performance index informing the objective function. Singular values are forced to be equal to each other during the optimization procedure. As a result, the manipulability ellipse is reshaped to be a circle and the robot arm moves into an isotropic pose, which is also discussed in (Yoshikawa, 1990), as it can be noticed in Figure 7.9. The results in the dimension are exactly as expected for the isotropic pose which is the first link length a_1 equals to the second link length multiplied by $\sqrt{2}$. The design parameters are presented in Table 7.2.

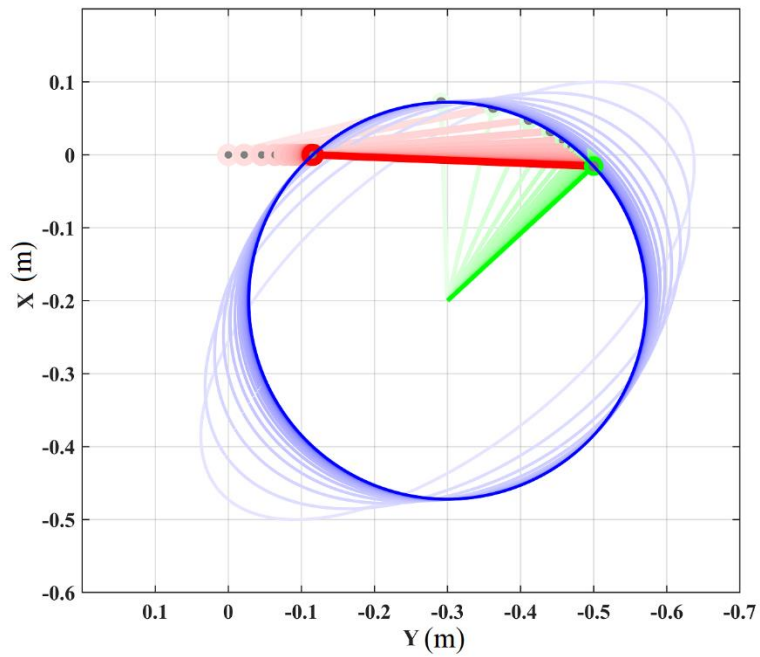


Figure 7.9. The change of the robot arm structure and the manipulability ellipse during the optimization routine by using the modified condition number

It is observed in Figure 7.10 that the manipulability index is decreased while decreasing the modified condition number index hence toward making maximum and minimum singular values to be equal to each other.

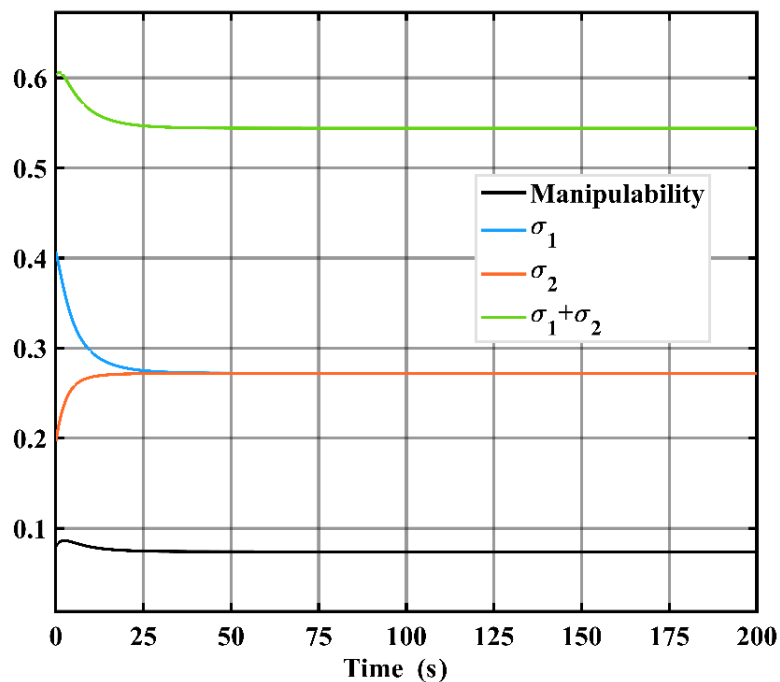


Figure 7.10. The change of the manipulability index and singular values during the optimization routine by using the modified condition number

As another consideration of the optimization routine, the inertial properties are investigated. From Figure 7.11.a, it can be noticed that the determinant of the GIM is increased as a result of this optimization. This is due to the increase of first link length and decrease of overall manipulability. Also, the determinant of the inertia matrix (the numerator of GIM) is increased as can be seen in Figure 7.11.b, which is represented by ImN in this figure. ImD represents manipulability (the denominator of GIM). During the optimization process, design parameters change to a final value. In Figure 7.11.c, the increase in the length of the first link can be seen due to this optimization which leads to an increase of the determinant of the inertia matrix (a decrease in dynamic manipulability) and as a consequence increase in the determinant of GIM. This can be considered as a drawback but the objective in using the modified condition number is to result in an isotropic pose in terms of manipulability index.

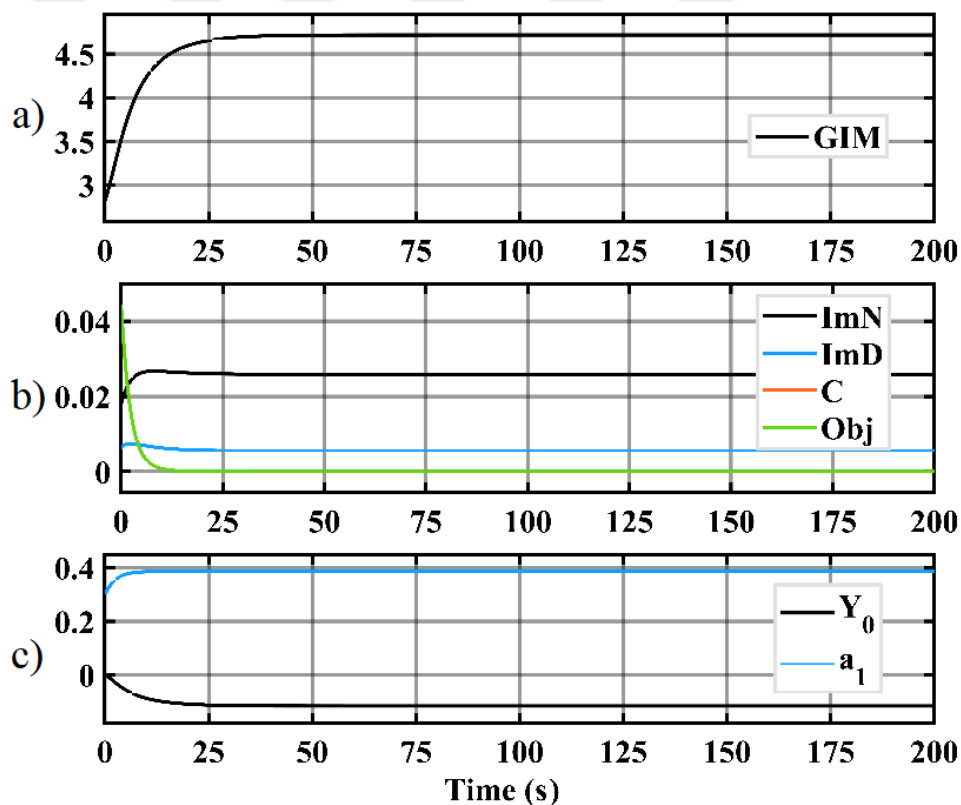


Figure 7.11. The optimization procedure with a modified condition number: a) Change of the generalized inertia matrix, b) change of components of the objective function, c) change in the values of design parameters

Test 3.2: In this final test, the summation of the modified condition number and the numerator part of the generalized inertia matrix, which corresponds to the inertia

matrix, are used with selected weights of 1 and 2 in reforming the objective function, respectively. In this way, the objective function is modified to have both the effect of the modified condition number and the determinant of the inertia matrix. As a result, shorter length for the first link is obtained and manipulability ellipse is reshaped as can be noticed in Figure 7.12.

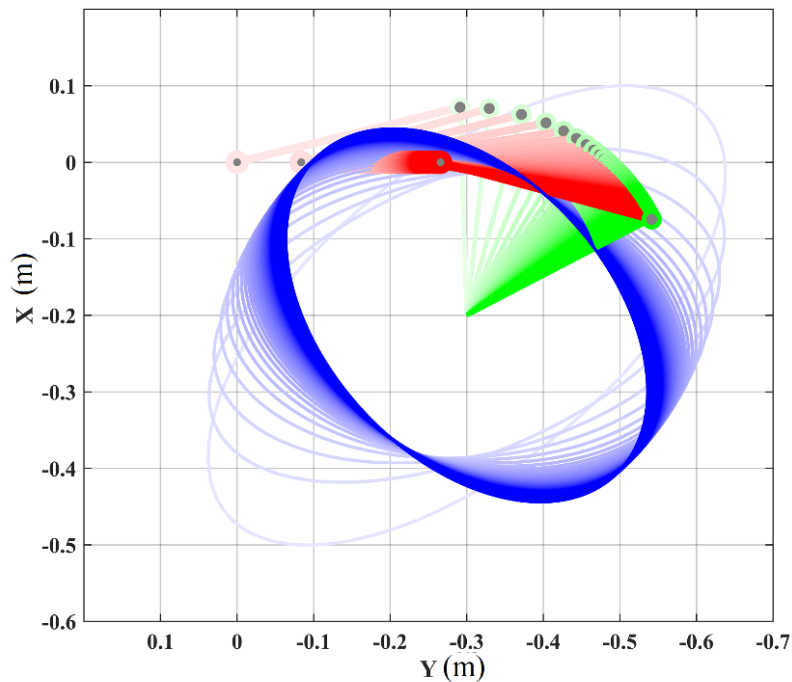


Figure 7.12. The change of the robot arm structure and the manipulability ellipse during the optimization routine by using the modified condition number and the inertia matrix

This decrease in manipulability, which is shown in Figure 7.13, and the decrease of the determinant of inertia matrix ImN , which is shown in Figure 7.14.b resulted from this optimization procedure. However, the determinant of GIM, which is shown in Figure 7.14.a, is increased. The positive result of this optimization is obtaining a smaller dimension for the first link's length, which is shown in Figure 7.14.c. Nevertheless, the weights used for the influence of the modified condition number and the inertia matrix on the objective function is critical. The choice of these weights depends on the desire of which performance index to be emphasized. The choice that could decrease the velocity transmission ratio in one direction to near to zero would minimize the backdrivability in that direction.

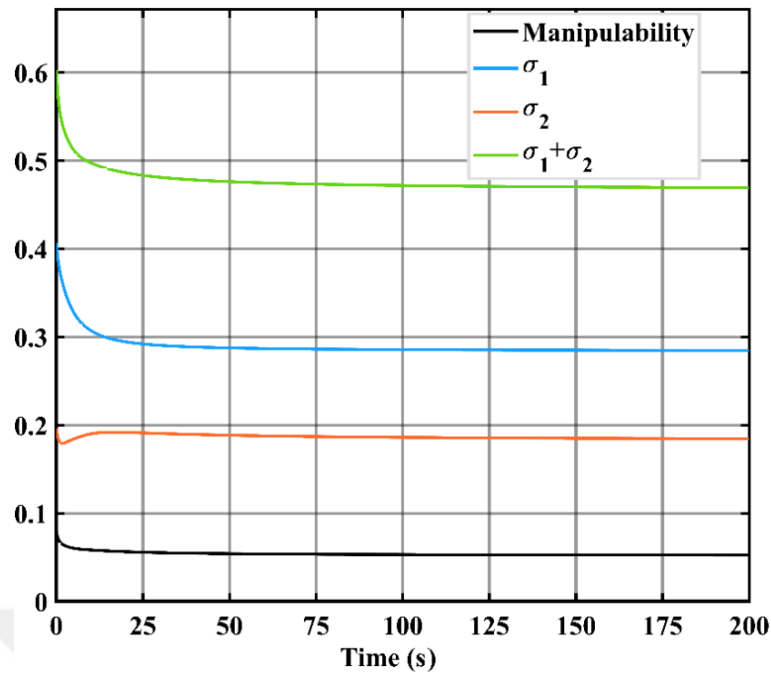


Figure 7.13. The change of the manipulability index and singular values during the optimization routine by using the modified condition number and the inertia matrix

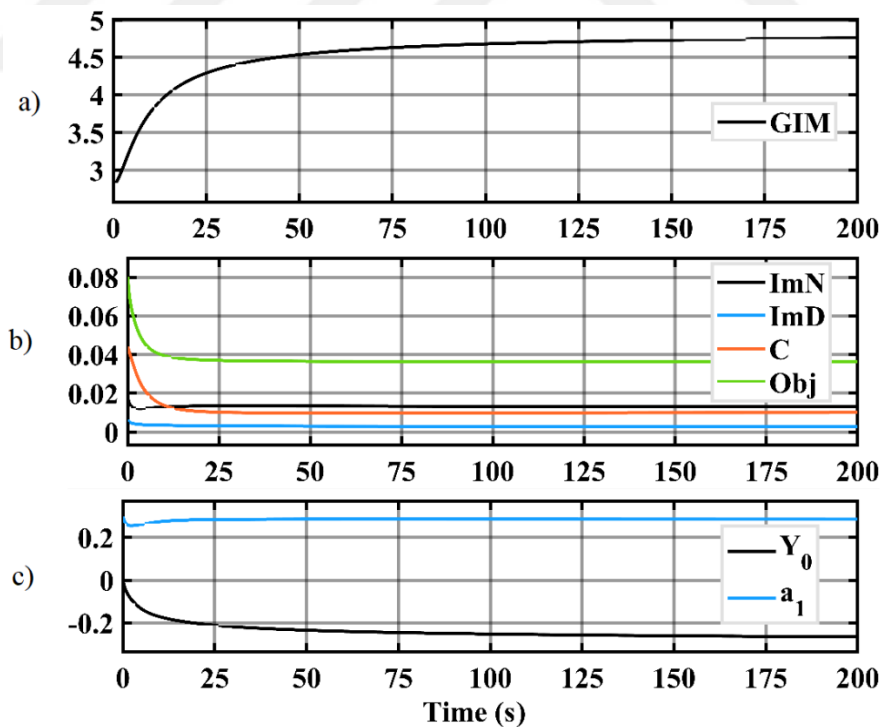


Figure 7.14. The optimization procedure with modified condition number and inertia matrix: a) Change of the generalized inertia matrix, b) change of components of the objective function, c) change in the values of design parameters

The optimized design parameters for Test 3 are summarized in Table 7.2.

Table 7.2. Test 3 design parameters

Design parameters	Test 3.1	Test 3.2
Y_0 (m)	-0.1157	-0.2657
a_1 (m)	0.3847	0.2855

7.10. Conclusions

A new approach of mechanical optimization through mechanical redundancy and the use of the null-space controller designed for redundant robots is studied and proposed in this chapter. Optimum solutions for various design parameters can be obtained by including these design parameters as virtual joints of a virtual redundant robot. These variables are adjusted in the null-space of the modified Jacobian matrix through redundancy resolution techniques so that it will not affect the main-task or design constraint. However, the manipulation affects directly the selected subtask hence the optimization procedure's objective function. Thus, the design parameters are optimized with respect to the selected objective function that includes the necessary performance indices of the real robot.

This new technique is experimented on the passive arm optimization for determining the fixing point and the first link's length. The main concern for the optimization is increasing the backdrivability of the passive arm of the surgical system. The presented results with various numbers of design parameters and various use of performance indices in the objective functions show the applicability of this method for the mechanical design and optimization of robots. At the same time, these results show agreement with the perspective presented by Yoshikawa (1990) for the manipulability performance of the two-link robotic arm. Finally, this new approach is a promising method for optimization procedures for any robotic system.

CHAPTER 8

ACTIVE ARM'S GRAVITY COMPENSATION DESIGN OPTIMIZATION

Spring-based passive gravity compensation methods are used especially when there are total mass restrictions in a mechanism. For a spatial parallel mechanism that has links and mobile platform performing the spatial motion, these limitations result in partial static balancing. The previously proposed compact and safe way of using springs for partial gravity compensation of an RCM is investigated in this Chapter for optimum performance. Optimum stiffness values and the amount of initial angle values of the springs are calculated. The optimization method used in this work is the Particle Swarm Optimization (PSO) method. In the next sections, the case scenario followed by the general description of PSO and the specific procedure followed in this optimization problem are presented. Various design constraints are set to select the proper optimization objective function. According to these various design constraints, many scenarios have been considered for optimization. The resulted design parameters have been tested and the dropping in the actuator torques are presented.

8.1. Description of the Case Scenario

The robot mechanism considered in this study is the functional prototype presented in Section 4.3.2. The kinematic sketch of this active parallel manipulator is presented in Figure 8.1. The three input angles θ_1 , θ_2 and θ_3 are used for controlling the two rotations ϕ and ψ , and one linear motion d of an endoscope about the RCM which is called the pivot-point. The proposed balancing spring for gravity compensation introduced in Section 5.5.2 is the design optimization problem in this Chapter.

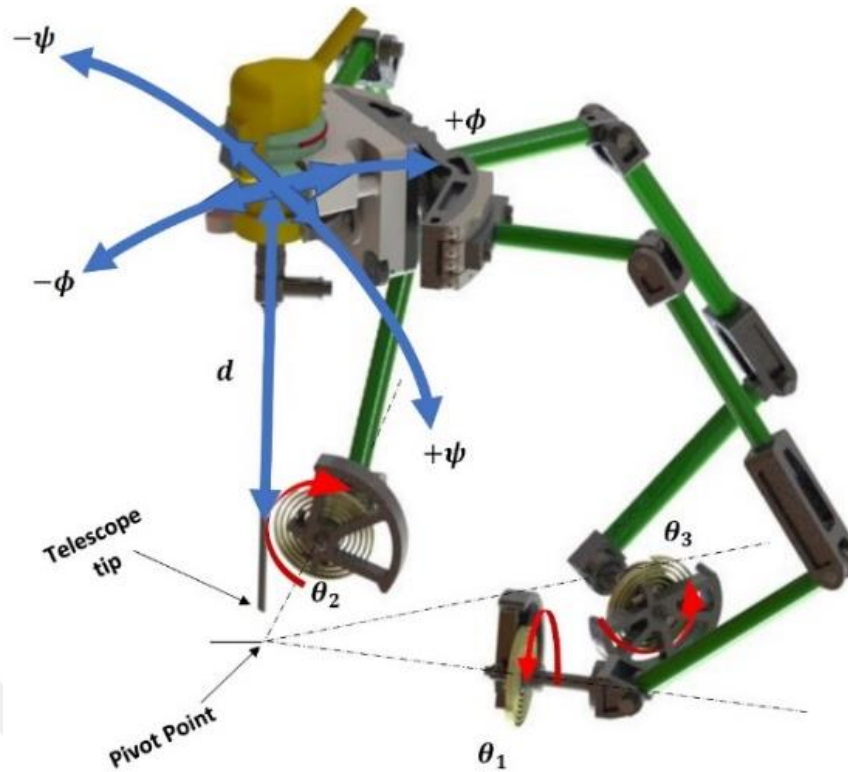


Figure 8.1. Parallel RCM mechanism holding the endoscope

8.2. Particle Swarm Optimization Method

Several new optimization methods that are theoretically different from the traditional ones have been advanced during the last years. These methods are characterized as nontraditional or modern methods of optimization and some of such methods can be listed as the genetic algorithms (GA) (Holland, 1973b), the PSO method (Kennedy and Eberhart, 1995), and the ant colony optimization (ACO) (Colomi, Dorigo, and Maniezzo, 1992). Most of them require only the function values without the need of their derivatives, the formulation of the objective functions, or the constraint functions. Most of these methods are based on swarm intelligence. As opposed to the genetic algorithms, such methods are called behaviorally inspired algorithms or the evolution-based procedures (Rao, 2019).

PSO was formulated by Edward and Kennedy in 1995. The idea behind the algorithm was inspired by the social behavior of animals, such as bird flocking or fish schooling. The advantages of PSO are that it is easy to implement, it does not require the mathematical gradient in order to optimize a problem, and there are only a few parameters to be adjusted. In this algorithm, each particle moves about the cost surface

with a velocity. Each particle studies its own previous best solution for the optimization problem and its group's previous best. The optimal value will be found by repeating this process. The PSO algorithm updates the velocity vector for each particle and then adds that velocity to the particle position or its value:

$$v_{i,j}^{\text{new}} = w v_{i,j}^{\text{old}} + \Gamma_1 r_1 (p_{i,j}^{\text{local-best}} - p_{i,j}^{\text{old}}) + \Gamma_2 r_2 (p_{i,j}^{\text{global-best}} - p_{i,j}^{\text{old}}) \quad (8.1)$$

$$p_{i,j}^{\text{new}} = p_{i,j}^{\text{old}} + v_{i,j}^{\text{new}} \quad (8.2)$$

where v is particle velocity, w is inertia weight which affects directly the behavior of the particles with respect to their motion toward the optimum solutions, p is particle position or variable, r_1 and r_2 are independent uniform random numbers, $p_{i,j}^{\text{local-best}}$ is the best local solution for the current iteration, $p_{i,j}^{\text{global-best}}$ is the best global solution until the current iteration, i is particle index, j is the dimension of the variable (the swarm dimension), Γ_1 is a cognitive parameter which has the effect of the convergence of design parameters within its local position, and Γ_2 is a social parameter that is responsible for the convergence within the global best solution in the swarm. The selection of these parameters depends on the desired upcoming information from the particles. The optimization and tuning of these parameters have been a research topic for many papers (Trelea, 2003; Shi and Eberhart, 1998; Van Den Bergh, 2007; Cui et al., 2017)

In the comparative study of Swarm Intelligence (SI) based methods for thirty standard functions, it has been found PSO as the second-best method that performed/outperformed the other SI based methods of 18 out of 30 benchmark functions (Ab Wahab, Nefti-Meziani, and Atyabi, 2015). The disadvantages of traditional PSO are premature and local optimum convergence. However, PSO variants are discovered in order to increase its performance and they increase the algorithm's ability to solve a wide range of optimization problems (Chavan and Adgokar, 2015). In this work, due to its simplicity and ease of implementation, the PSO technique is used as an optimization tool for the selection of optimum design parameters.

8.3. The Procedure Followed in PSO Method

The following procedure is used to generate the PSO program:

- Set the parameters of the optimization method,
 1. Set the size of the iteration,
 2. Set constants: inertia (w) and $r_1 = r_2$ values,
 3. Set the swarm size/population (pp),
 4. Set the ranges/boundaries of design parameters (dp),
 5. Set the matrix of an initial random population of the particles within the bound, the initial sets of (dp),
 6. Set swarm matrix,
 7. Set column array of initial best values (nonlogical value in general),
 8. Set column array of initial velocities and initial best positions of the particles (nonlogical value in general),
- Start the iteration,
 - Start another iteration to the size of (pp),
 - Using the current position (old position), calculate the new position for each particle of (dp) as in Equation 8.2. By adding the old position plus the new calculated velocity in Equation 8.1,
 - Checking can be used for the physibile particles of (dp) before using for the calculation of the objective function,
 - The objective function can be examined now with the older local best value at the current set of particles,
 - If it's better than the older local best value, then the used set of particles can be saved as the best local (dp) for the new best local best value (to be replaced with the older one). Else, keep the previous (dp) and the previous local best value,
 - Now, the objective function is calculated with respect to each set of (dp) until the end of the (pp).
 - All the saved local best values for all sets of (dp) are examined with each other to set the best global value (updated at each iteration) of the objective function and its corresponding particles are assigned as global best (dp),

- Now, all initial velocity values (old velocities) are updated with the earlier calculated velocity values for each particle.
- The process to be repeated for several swarms until the end of the iterations.
- The last updated global best value and its corresponding set of particles (dp) will be the global best design parameters that give the closest solution of the desired objective function.
- The end of the processes.

8.4. Design Optimization Constraints

To find the static balancing torque at actuator shafts, the previously derived dynamic equation of the active parallel manipulator has been utilized by omitting the inertia force/moment terms. The gravity compensation is designed for the static gravitational forces, so just the gravitational related torques at the actuators are considered. In general, there are six independent design parameters to be optimized. Three design parameters are k_1 , k_2 , and k_3 for stiffness values of the first, second, and third spiral springs respectively. The other three design parameters θ_{01} , θ_{02} , and θ_{03} are for the initial angle values for each of the three spiral springs for preloading. Noting that each of the spiral springs mounted directly on the first link of each leg so the relation between the angle and torque is considered to be linear to have a compact design without adding an auxiliary mechanism. The previously prescribed workspace is the constraint for selecting the optimum design parameters regardless of the objective used in the tests. The fixed platform of the parallel manipulator is considered fixed in orientation during the first optimization process as an additional constraint. Later, this consideration was investigated for more general cases on different orientation. Different swarm sizes were selected at each test; however, some boundaries of the design parameters were assigned to find the solution of each particle inside the swarm around the range of these boundaries.

8.5. Optimization Test Results

In this section, the optimization of spiral spring is presented which is to be included in a robot mechanism for passive gravity balancing. It is worth noting that the spiral spring is mounted to the joint directly so that the relation between the angle and torque can be considered to be linear. This produces a compact design without adding an auxiliary mechanism for passive gravity balancing. Three types of optimization studies are conducted. In the first one, the effect of adding a spring for passive gravity balancing is investigated. In the second and third studies, the PSO method is used to find optimum stiffness value and initial angle for each spring used for each actuation system. The selection of the objective function depends directly or indirectly on the change in potential energy inside a previously prescribed workspace. Other different specific design constraints are used on each test and discussed in the next subsections.

8.5.1. Spring Utilizing Effect on the Partial Gravity Compensation

Initially, a specific scenario for the motion of the parallel manipulator is selected so that all actuators will be operating simultaneously. The devised motion trajectory is presented in Figure 8.2. The designated motion is a single axis rotation for a range of ϕ angle from 0° to -40° in which ψ is kept at 0° and d is kept at 17 cm, which means the Telescope tip is inserted beyond pivot-point by 6.1 cm.

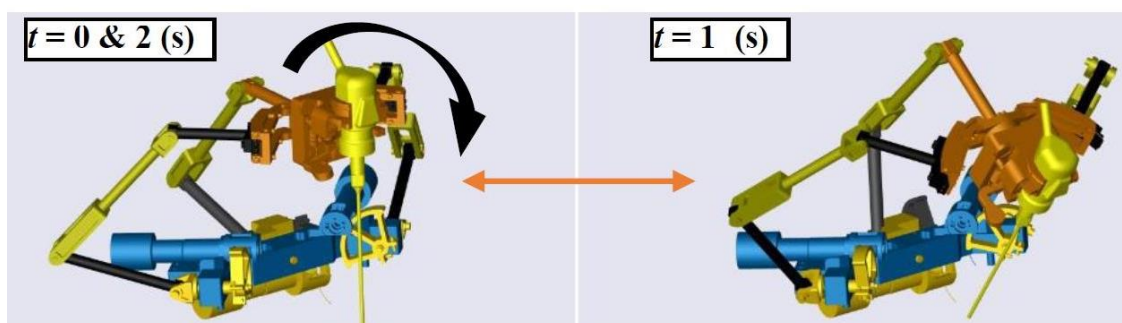


Figure 8.2. Motion sequence of the RCM mechanism with the endoscope for the initial study (the initial state at $t = 0$ s, intermediate state at $t = 1$ s, and final state at $t = 2$ s)

As a first case study, just for the third joint, various spring stiffness values are selected manually as 0.3, 0.5, 0.7, and 0.9 N·m/rad. The effect of these springs is examined in the simulation tests and presented in Figure 8.3. The initial angle is also selected relative to stiffness and loading conditions in order to shift the results near zero torque as a resultant torque.

It is observed that changing stiffness value and initial angle have a direct effect on the required torque by the actuator. In that respect, minimized maximum torque or minimized energy consumption by the actuator can be obtained by selecting optimum values of the stiffness and initial angle of the spring. The initial angle is used to shift the actuator torque's value to the desired value while changing stiffness value affects the shape of required torque function with respect to the followed motion trajectory as can be noticed in Figure 8.3. Within the workspace of the parallel manipulator, the required torque for the three actuators is in one direction and no zero-torque crossover happens for the unbalanced case. This allows for the attachment of the balancing springs with an initial angle. For obtaining the optimum results, the selection of the stiffness and initial angle are to be studied within the entire workspace. To achieve this goal, in the next subsection the PSO is used.

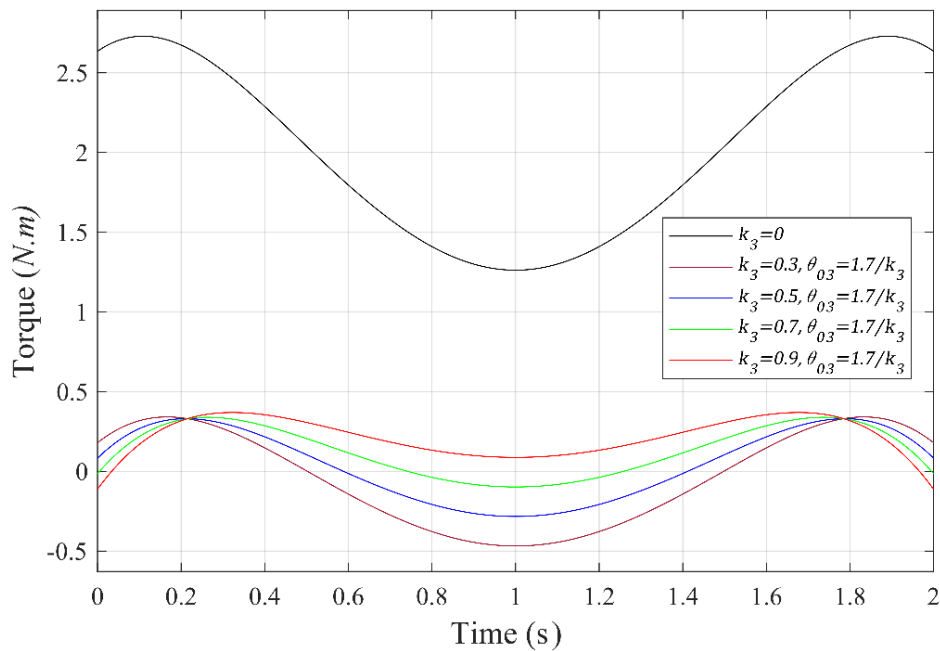


Figure 8.3. Actuator torque without/with springs have various properties for a specific trajectory

8.5.2. Optimization Study by Minimizing the Summation of Actuator Torques

In this optimization test, PSO is used to select all three springs' stiffness and their initial angle for optimum design. The objective function for this optimization process is defined as the sum for the squares of the three actuators' torques calculated at the preselected points of the workspace. The selection of the points is generated by the companion of the Box-Behnken Design (BBD) technique and Central Composite Design (CCD) for experiment runs. BBD is based on the cube edge midpoints and CCD is based on the corner points, with the center of the cube 3 factors by 3 levels can be generated (NIST/SEMATECH, 2013). These points inside the workspace are selected at extreme loci and in the midpoint of the extreme loci inside the workspace. As a start, $3 \times 3 \times 3$ loci for the three independent variables are selected which result in 27 loci inside the workspace range shown in Figure 8.4. the range (dimensions) of the cube is defined as $\phi = -35^\circ \rightarrow -12^\circ$, $\psi = -1^\circ \rightarrow 12^\circ$, and $d = 17 \rightarrow 20$ cm. This workspace is related to the left nostril of the patient.

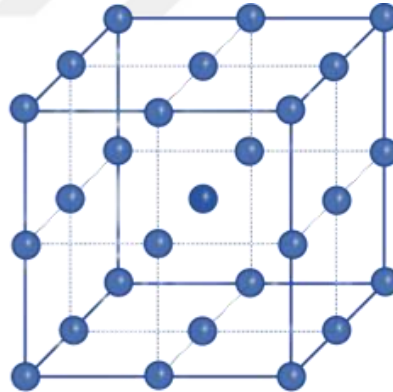


Figure 8.4. Experiment run points inside a range of workspace

In this run of optimization, many tests have been done to select the best solution. The best-resulted objective function (Best OpObVa) is presented in Table 8.1 with corresponding optimum design parameters. The parameters among all tests are selected to have acceptable optimization performance of the swarm with respect to the number and convergence of the particles to the results inside the appropriate size of the swarm (the population of the swarm). The bounds are selected with regard to the potential solution of the design parameters

Table 8.1. The first optimization study parameters and results

Selected parameters		Selected results	
Iteration	300	Best OpObVa	9.6775
Swarm size	120	Maximum torque	$T_1 = 0.57875 \text{ N}\cdot\text{m}$
Inertia weight	1	Sum of square torque	9.6775
$\Gamma_1 = \Gamma_2$	2		
Boundaries		Best parameters	
k_1	$0 \rightarrow 2$	k_1	$4.505(10)^{-2} \text{ N}\cdot\text{m}/\text{rad}$
k_2	$0 \rightarrow 2$	k_2	$9.226(10)^{-2} \text{ N}\cdot\text{m}/\text{rad}$
k_3	$1 \rightarrow 2$	k_3	$1.2315 \text{ N}\cdot\text{m}/\text{rad}$
θ_{01}	$3 \rightarrow 9$	θ_{01}	41.481 rad
θ_{02}	$-33 \rightarrow -10$	θ_{02}	-23.188 rad
θ_{03}	$-2 \rightarrow 0$	θ_{03}	-1.7093 rad

The solution converges to the optimum value $9.6775 (\text{N}\cdot\text{m})^2$ after approximating 220 iterations as shown in Figure 8.5. However, this value does not give any indication about the upper limit possible torque for actuators calculated among these loci. Among these loci, one of the loci could have the highest actuator's torque value regarding the other loci. To better observation of the optimization process, in the next optimization tests, another optimization objective function is defined.

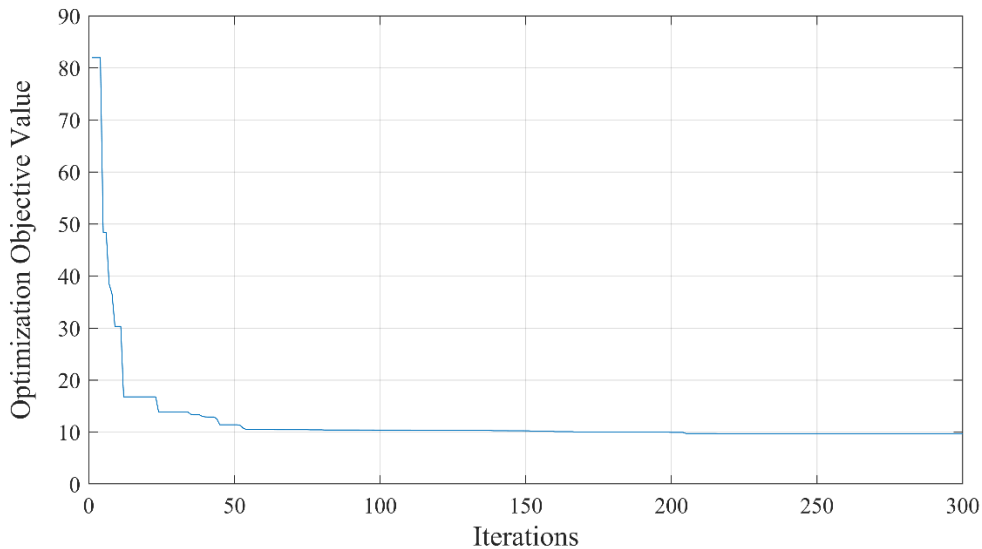


Figure 8.5. Optimization objective function value versus the number of iterations

8.5.3. Optimization Study by Using the Minimum Upper Limit of Actuator Torques

To obtain a minimum upper limit for torque magnitude of the actuators, optimization objective function has been modified for having minimum upper torque value at all loci and for all actuators. Another condition was added to result in a physically possible solution for the stiffness values of the springs, which is considering a solution with only positive values of the springs' stiffness. In this optimization test, three different scenarios were introduced to relate the selected solution with design constraints:

The First Scenario: three different spring stiffness values (k_1, k_2 and k_3) are considered with three different initial angle values θ_{01}, θ_{02} and θ_{03} . Minimized upper torque limit is to be obtained by defining optimization objective function to be as the maximum torque for any of the actuators tested at all loci. The role of the PSO solution here is to minimize this objective function. As a result, the optimum solution of dominant design parameters will be the one with the solution of the lower upper torque of all actuators inside the workspace. Table 8.2 presents the optimum design parameters that result in the best OpObVa value at 0.555 N·m as the minimized upper torque calculated at the first actuator at the iterations presented in Figure 8.6.

Table 8.2. The first scenario parameters and results.

Selected parameters		Selected results	
Iteration	300	Best OpObVa	0.555
Swarm size	300	Maximum torque	$T_1 = 0.55502$ N·m
Inertia weight	1	Sum of square torque	15.529
$\Gamma_1 = \Gamma_2$	2		
Boundaries		Best parameters	
k_1	$0 \rightarrow 10$	k_1	0.1454 N·m/rad
k_2	$0 \rightarrow 10$	k_2	0.20617 N·m/rad
k_3	$1 \rightarrow 10$	k_3	1.3954 N·m/rad
θ_{01}	$3 \rightarrow 20$	θ_{01}	12.450 rad
θ_{02}	$-33 \rightarrow -10$	θ_{02}	-10.123 rad
θ_{03}	$-20 \rightarrow 0$	θ_{03}	-1.7812 rad

It can also be noticed that the sum of squares of actuator torques becomes higher than the former result since it is no more the objective of this optimization and due to this additional new constraint.

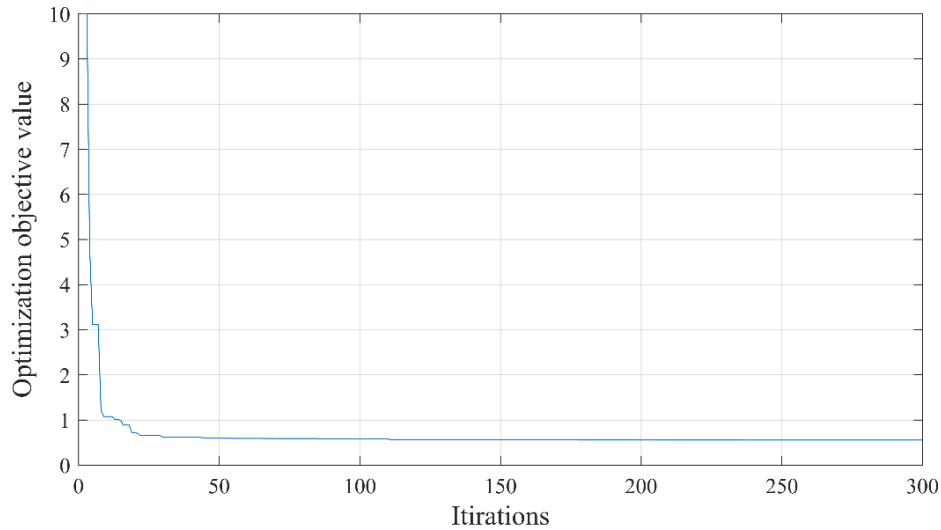


Figure 8.6. Optimization objective function value versus the number of iterations for the first scenario

This scenario presented dissimilar results between the first and second actuators compilation in spite of the symmetry of the presented parallel manipulator. That difference derived from the selection of the workspace which is related to the left nostril. However, with these parameters, the symmetry of gravity compensation components is dysfunctional when the workspace is the right nostril.

The Second Scenario: Considering only two springs in the optimization process to be solved as an additional design constraint ($k_1 = k_2$ and k_3) with three different initial angle values θ_{01} , θ_{02} and θ_{03} . By the addition of this design constraint, symmetry regarding the structural compilation of the gravity compensation component is achieved as presented in Table 8.3.

Table 8.3. The second scenario parameters and results.

Selected parameters		Selected results	
Iteration	300	Best OpObVa	0.6169
Swarm size	200	Maximum torque	$T_l = 0.6169 \text{ N}\cdot\text{m}$
Inertia weight	1	Sum of square torque	25.074
$\Gamma_1 = \Gamma_2$	1		
Boundaries		Best parameters	
k_1	$0 \rightarrow 2$	k_1	$0.8300 \text{ N}\cdot\text{m}/\text{rad}$
k_2	k_1	k_2	k_1
k_3	$1 \rightarrow 2$	k_3	$1.1531 \text{ N}\cdot\text{m}/\text{rad}$
θ_{01}	$1 \rightarrow 7$	θ_{01}	1.9738 rad
θ_{02}	$-5 \rightarrow 0$	θ_{02}	-2.1632 rad
θ_{03}	$-2 \rightarrow 0$	θ_{03}	-1.4141 rad

The solution converges to 0.6169 N·m as shown in Figure 8.7. However, each time the workspace is modified due to design constraints (left/right nostril), initial angles need to be readjusted.

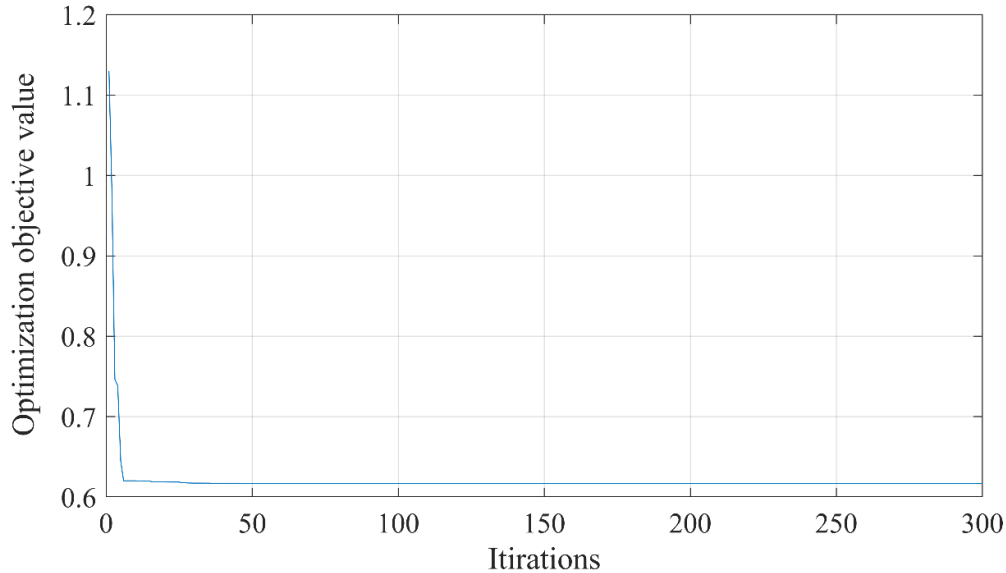


Figure 8.7. Optimization objective function value versus the number of iterations for the second scenario.

The Third Scenario: two different springs are considered as $k_1 = k_2$ and k_3 with two different initial angle values $\theta_{01} = -\theta_{02}$ and θ_{03} . In this optimization test, the RCM mechanism is considered to be used in the right or left side of the nostril. In this case, the symmetry of the springs and the initial angular values of the first and second actuators facilitate to obtain a result conveniently for the insertion through the right or left nostril.

The selected parameters for the optimization procedure are presented in Table 8.4. After approximating 70 iterations as shown in Figure 8.8 the optimized objective value is obtained as 0.6817 N·m. This is also the maximum torque for the first actuator with the selected dominant parameters which happens to be close to the prior results.

Table 8.4. The third scenario parameters and results.

Selected parameters		Selected results	
Iteration	150	Best OpObVa	0.6817
Swarm size	200	Maximum torque	$T_l = 0.6817 \text{ N}\cdot\text{m}$
Inertia	1	Sum of square torque	14.024
$\Gamma_1 = \Gamma_2$	2		
Boundaries		Best parameters	
k_1	$0 \rightarrow 2$	k_1	$0.2679 \text{ N}\cdot\text{m}/\text{rad}$
k_2	k_1	k_2	k_1
k_3	$1 \rightarrow 2$	k_3	$0.85108 \text{ N}\cdot\text{m}/\text{rad}$
θ_{01}	$2 \rightarrow 7$	θ_{01}	7.0747 rad
θ_{02}	$-\theta_{01}$	θ_{02}	$-\theta_{01}$
θ_{03}	$-2 \rightarrow 0$	θ_{03}	-2.2232 rad

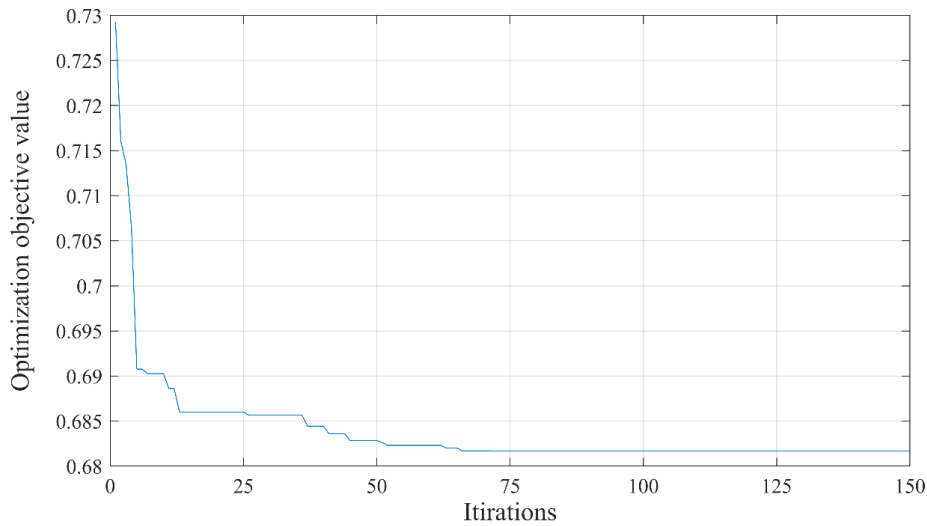


Figure 8.8. Optimization objective function value versus the number of iterations for the third scenario

8.5.4. Discussion on the Design and Improvements

Initially, to test the optimization results inside the previously defined workspace, the boundaries and midpoints of the range of motion in each direction are selected as 27 loci. However, the design parameters are tested in simulations for randomly generated 100000 loci within different ranges inside the workspace. The selected design parameters used for these tests are the results presented in Table 8.2 from the first scenario in subsection 8.4.3. It is observed that the minimum upper torque limit for selected parameters in the first scenario is calculated to be $0.555 \text{ N}\cdot\text{m}$ at the locus $(-35^\circ, 12^\circ, 0.2 \text{ m})$. Whereas the other maximum torques calculated among the 100000 loci are

0.551 N·m, 0.526 N·m, and 0.514 N·m for the first, second, and third actuators, respectively as shown during test No. 2 in Table 8.5. These results indicate that the selected design parameters in the optimization process can be tested by using only the selected 27 loci in the optimization process.

Other tests for the selected design parameters in the first scenario for the extended range of the workspace are presented at test No. 3 in Table 8.5. The change in maximum torques was observed when the points are in the extended workspace out of the one tested for during the optimization process.

Table 8.5. Testing the selected design parameters in the first scenario on different points in the workspace

Test no	Specification of the workspace, No. of points (n), the orientation of the manipulator	Maximum recorded torques	
		With gravity compensation (N·m)	Without gravity compensation (N·m)
1	$\phi = -35^\circ \rightarrow -12^\circ$, $\psi = -1^\circ \rightarrow 12^\circ$, $d = 17 \rightarrow 20$ cm. $n = 27$ Pitch angle = 0°	$T_1 = 0.555$ $T_2 = 0.529$ $T_3 = 0.523$	$T_1 = 2.389$ $T_2 = 2.656$ $T_3 = 2.067$
2	$\phi = -35^\circ \rightarrow -12^\circ$, $\psi = -1^\circ \rightarrow 12^\circ$, $d = 17 \rightarrow 20$ cm. $n = (10)^5$ Pitch angle = 0°	$T_1 = 0.552$ $T_2 = 0.526$ $T_3 = 0.515$	$T_1 = 2.386$ $T_2 = 2.652$ $T_3 = 2.067$
3	$\phi = -45^\circ \rightarrow -12^\circ$, $\psi = -1^\circ \rightarrow 12^\circ$, $d = 17 \rightarrow 18$ cm. $n = (10)^5$ Pitch angle = 0°	$T_1 = 0.814$ $T_2 = 0.854$ $T_3 = 0.517$	$T_1 = 2.36$ $T_2 = 2.591$ $T_3 = 2.067$
4	$\phi = -35^\circ \rightarrow -12^\circ$, $\psi = -1^\circ \rightarrow 12^\circ$, $d = 17 \rightarrow 20$ cm. $n = (10)^5$ Pitch angle = 20°	$T_1 = 1.066$ $T_2 = 0.973$ $T_3 = 1.898$	$T_1 = 2.874$ $T_2 = 3.085$ $T_3 = 2.014$
5	$\phi = -35^\circ \rightarrow -12^\circ$, $\psi = -1^\circ \rightarrow 12^\circ$, $d = 17 \rightarrow 20$ cm. $n = (10)^5$ Pitch angle = 10°	$T_1 = 0.880$ $T_2 = 0.812$ $T_3 = 1.044$	$T_1 = 2.697$ $T_2 = 2.935$ $T_3 = 2.092$
6	$\phi = -45^\circ \rightarrow -12^\circ$, $\psi = -1^\circ \rightarrow 12^\circ$, $d = 17 \rightarrow 24$ cm. $n = (10)^5$ Pitch angle = 20°	$T_1 = 1.163$ $T_2 = 1.127$ $T_3 = 1.895$	$T_1 = 2.966$ $T_2 = 3.231$ $T_3 = 2.073$

Optimum design parameters are tasted again for the condition when the base platform of the parallel manipulator is rotated by 10° and 20° at θ_6 (the pitch angle) in

the passive arm for different ranges during the tests No. 4 to No. 6. However, 20° is the maximum pitch rotation that was foreseen to happen during the surgery. In this case, it is observed that maximum torque increased from $0.555 \text{ N}\cdot\text{m}$ to $1.897 \text{ N}\cdot\text{m}$ at one of the extreme loci during test No. 6. The change in the values is due to the change of the orientation of the gravity vector with respect to the active robot arm.

Test No. 4 to test No. 6 with different ranges of workspace and pitch angles show divergence in the maximum torques and deficient of the selected design parameters in gravity compensation design. For this reason, another optimization was performed.

To obtain improved results, other details have been added to the system during optimization. First, the maximum pitch angle is considered during optimization. The maximum pitch angle is to be needed during operation since it allows for extending the range of the workspace of the parallel manipulator. Second, the accurate amount of endoscope, telescope, and approximated cable effects for a total mass of 400 g was also added to the mass of the moving platform to realize approximate real scenarios. The best selected optimized parameters are presented in Table 8.6.

Table 8.6. Optimization of the tilted robot with results

Selected parameters		Selected results	
Iteration	300	Best OpObVa	0.895
Swarm size	300	Maximum torque	$T_l = 0.895 \text{ N}\cdot\text{m}$
Inertia weight	1	Sum of square torque	45.97
$\Gamma_1 = \Gamma_2$	2		
Boundaries		Best parameters	
k_1	$0 \rightarrow 10$	k_1	$0.34 \text{ N}\cdot\text{m} / \text{rad}$
k_2	$0 \rightarrow 10$	k_2	$0.616 \text{ N}\cdot\text{m} / \text{rad}$
k_3	$1 \rightarrow 10$	k_3	$0.592 \text{ N}\cdot\text{m} / \text{rad}$
θ_{01}	$1 \rightarrow 20$	θ_{01}	9.106 rad
θ_{02}	$-20 \rightarrow -1$	θ_{02}	-5.562 rad
θ_{03}	$-20 \rightarrow -1$	θ_{03}	-2.711 rad
Specification of the workspace, No. of points (n), the orientation of the manipulator		Maximum recorded torques $\text{N}\cdot\text{m}$	
		With gravity compensation	Without gravity compensation
$\phi = -45^\circ \rightarrow -12^\circ$, $\psi = -1^\circ \rightarrow 12^\circ$, $d = 17 \rightarrow 24 \text{ cm}$. $n = (10)^6$ <i>Pitch angle = 20°</i>		$T_1 = 0.915$	$T_1 = 3.992$
		$T_2 = 0.876$	$T_2 = 4.348$
		$T_3 = 0.911$	$T_3 = 2.714$

The optimization was performed inside the maximum range of the workspace and pitch angle = 20° and tested during the optimization process on 27 points. For

testing the selected optimum design parameters, a cube of $(10)^6$ equally distributed points inside this workspace was generated. The torques in Nm inside the $(10)^6$ equally distributed points for the first, second, and third actuators are presented in Figure 8.9, Figure 8.10, and Figure 8.11 respectively. The results show the maximum torque considering all actuators is $0.915\text{ N}\cdot\text{m}$ when the gravity compensation is activated and $4.348\text{ N}\cdot\text{m}$ when deactivated. The amounts of the torques that can be dropped at the three actuators are approximately 77, 80, and 66% respectively. However, by a suitable selection of the actuators, the unbalanced parts of the gravitational loads can be compensated by the actuator efforts.

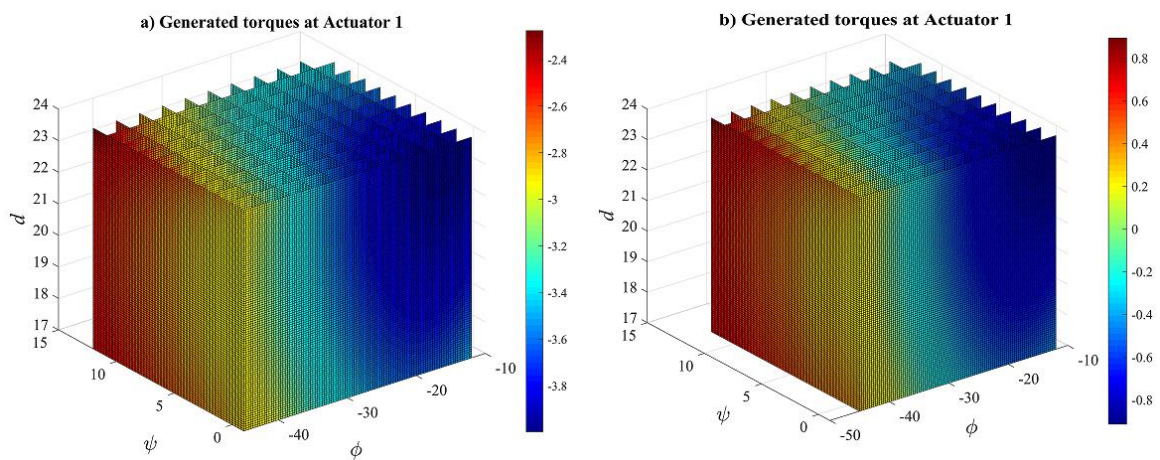


Figure 8.9. The generated torques inside the workspace at the first actuator, a) without gravity compensation, b) with partial gravity compensation

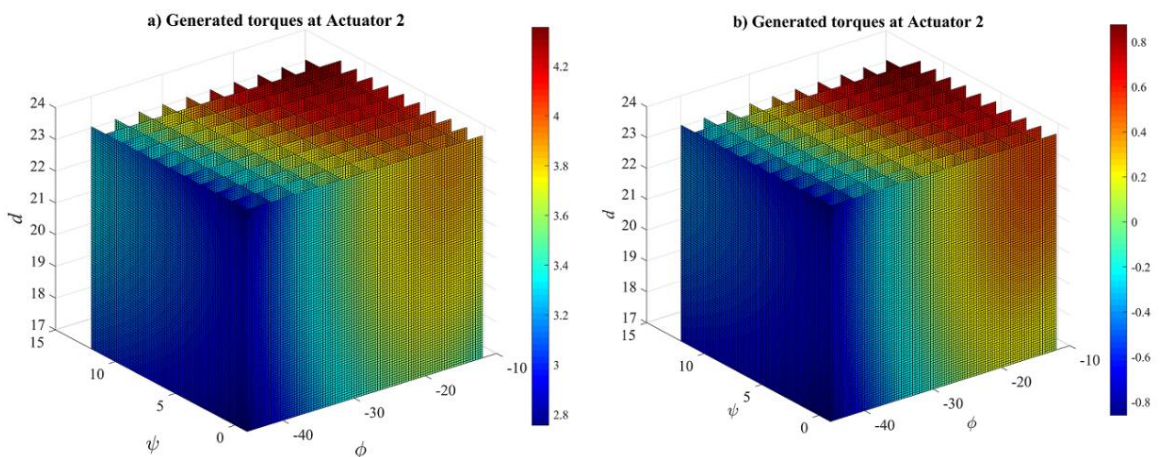


Figure 8.10. The generated torques inside the workspace at the second actuator a) without gravity compensation, b) with partial gravity compensation

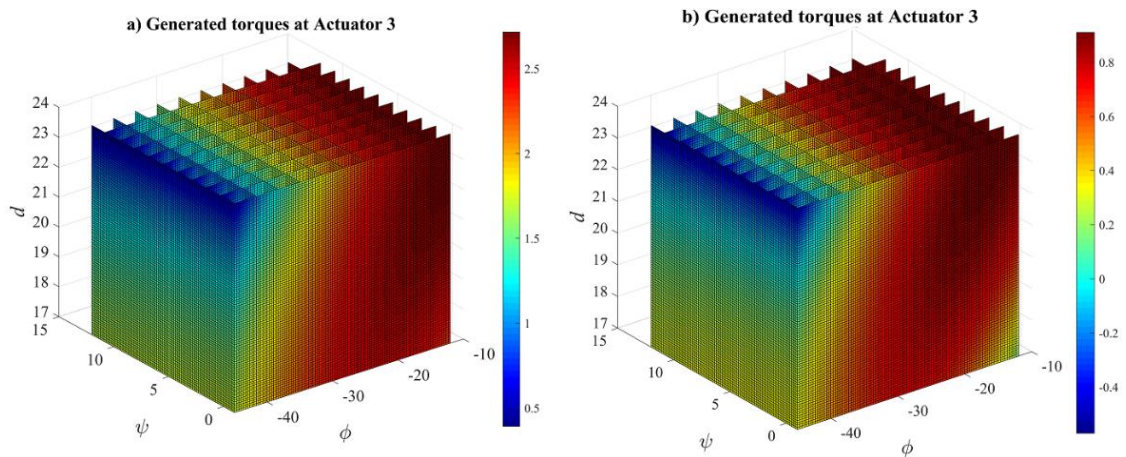


Figure 8.11. The generated torques inside the workspace at the third actuator a) without gravity compensation, b) with partial gravity compensation

8.6. Conclusions

Passive gravity balancing is useful for minimizing the power requirements of a robot's actuators. Hence, the actuators can be selected in small sizes and the use of high-speed reduction ratios in the actuation systems can be avoided. These are advantageous in two ways for the design of the NeuRoboScope system: (1) total mass on top of the patient is minimized (2) the actuator effort is minimized so that low reduction ratios are used which results in a backdrivable system configuration. The moving mass can be minimized if a spring-based solution is chosen over a counter-mass solution. This is important since the minimized mass of the parallel manipulator is required for enhancing the safety of the system. Nevertheless, the solution proposed is partial gravity balancing since the parallel manipulator has many moving links and counter-masses are not to be used to minimize the total mass. Also, the base platform of the parallel manipulator changes its orientation during the surgery which makes it impractical to use a linear spring with a fixed end to the inertial frame.

Partial gravity balancing is considered in this optimization as a convenient solution. PSO technique is used for the selection of spring parameters. In the optimization process, the objective function is selected to obtain the minimized sum for squares of actuators torques then another objective was applied to minimize the upper limit of the actuators' torques. The tilting angle of the base platform of the active parallel manipulator is considered in the selection of the design parameters. The results

in the tests raised the need for considering the pitch angle during the optimization process.

Additional tests are carried out to evaluate the possibility of using the same spring properties due to the symmetry of the parallel manipulator. In one scenario, for the first and second springs, the same spring constants and different initial angle values are used. In the other scenario, for the first and second springs, the same spring constants and initial angle values are used. In both cases, the results indicated that slightly higher actuator torques will be needed for these options. These slight tolerances can still be compensated by the actuators.

Finally, this partial gravity balancing design optimization of the active parallel manipulator is done via the use of the PSO method and comparative figures illustrated actuators' torques inside the workspace without/with the implementation of gravity compensation. In comparison to the first manufactured prototype of the parallel manipulator, a compact design is proposed which is shown to compensate most of the gravitational load.

CHAPTER 9

CONCLUSIONS

In this dissertation, the design of a robot assisted endoscope holder for pituitary tumor resection surgery named NeuRoboScope is studied based on safety features. The design of the system was initiated with the definition of pituitary tumor resection surgery and the description of the accompanied problems to be solved. Then, an extensive literature survey was carried out for studies that had similar problems and available solutions in the MIS. Many designs have been found for rigid laparoscope holder robotic arms designed for laparoscopic surgery and less for rigid ones for endoscope holders. Most of the robot assisted surgical systems for endonasal surgical techniques were designated for FESS in sinuses treatment. Such systems have a very similar surgical workspace for the endoscope in sphenoid sinus treatment to that of ESBS in pituitary tumor resection surgery.

The safety enhancement methodologies of specifically designed prototypes for endonasal endoscopic surgeries are investigated (FESS, ESBS, transsphenoidal endoscopic surgery, and paranasal). A list of 17 robot assisted endoscope holding systems is presented in Table 2.2. Then, a brief discussion on each is given. All of the listed systems are applied/applicable for endonasal endoscopic surgery. The systems (referenced with a (No.) as presented in Table 2.2) in (1, 2, 3, 5, 6, 9, and 11) utilized an industrial robot arm or a general function surgical robot applied for ESBS. These prototype systems are studied to verify some safety features and to validate the applicability in ESBS. There is just one commercial robot assisted endoscope holder (12) that is recently released for general endonasal endoscopic surgery. To the best of my knowledge, this robotic system is still at preclinical phase and no clinical surgery on patients was done for ESBS. Various other commercial systems were originally designed for other types of surgeries. An example is (15), where the manufacturer designed it for brain surgery but the applicability for endonasal endoscopic surgery has been stated in the product manual. The other example is (17), which is already designed for FESS but can also be tested for ESBS as has been case for (12). Other particularly designed prototypes for the FESS could also have similar potential preclinical tests for ESBS such as (7 and 14).

The common safety features in these systems were the implementation of the F/T sensors and redundant endoscope tracking/navigation system. However, for the commercial surgical systems in general applications of RAS, very limited information regarding some technical oriented safety details have been found. Most of the available studies in the literature are related to the preclinical and clinical tests conducted by surgical teams. It has been concluded that surgical teams are in general concern the most about user-robot interfacing simplicity and the time index of task completion. While safety details and the mechanical structure are less often assigned as a crucial index to measure. This does not mean the safety index being underestimated. The aim of the dissertation is built on the responsibility of designing a safe and optimized robot assisted endoscope holder system.

To set all design requirements, some measurements on both of surgeon's motion of the endoscope and the contact forces with nasal tissues were needed. To obtain this information, specific experimental setups are designed. Motion information is collected by mimicking a real surgery on a fresh cadaver. The angular motion ranges are obtained during different scenarios during this simulated real-like surgery. The extreme angles were useful and considered later for the structural synthesis of the active robot manipulator. However, it could be better to collect motion information by an accurate optical tracking/navigation system. By collecting a cloud of data along all surgery time and for various cadavers, statistical studies could be done to have accurate surgical workspace information. However, a statistical analysis on another work for the NeuRoboScope project was done on 28 patients to measure for some selective dimensions inside the nasal cavity.

The F/T sensors, in general, are very accurate when they are stationary, as well as the contact forces are close to the mounting side of the sensor. However, in the case scenario presented here, the contact force between the endoscope tip and the tissue inside the nasal cavity are to be tested. The F/T sensors have large dimensions to be fitted near the endoscope tip and no room at the commercial endoscopes between the telescope and endoscope camera to fit such sensors in series. For these reasons, by the use of a 3D printer, a special handle and fixing part were designed to fit the F/T sensor in between. By this configuration, the F/T sensor carries the endoscope and measures its weight in addition to the external forces. Bias reset option is a practical solution when the sensor has fixed orientation, but in the case presented here, the orientation is changing inside the nasal cavity. As a practical solution, to obtain higher accuracy in

measurements, the gravity cancellation was done by the engagement of the motion information, the endoscope's weight, and the center of mass position. An initial verification test was done to compare the forces with and without gravity cancellation and the weight effect was calculated. The contact force tests on a fresh cadaver were carried out in another study out of the scope of this dissertation.

After having a detailed procedure of the pituitary tumor resection surgery and the surgical workspace/environment analyzed experimentally, all design requirements with a full description of the NeuRoboScope system were clarified. The NeuRoboScope system is constituted mainly by two mechanisms: A passive arm that can carry and hold the second active robotic mechanism. The active robot arm can hold and direct the endoscope to a commanded position by performing two rotational and one transitional motion about an RCM to mimic the surgeon's manipulation inside the nasal cavity. In this dissertation, a novel serial active robot arm that can provide this motion is proposed and verified via kinematic analysis. As another option, a novel spatial active parallel manipulator was proposed in another thesis within the NeuRoboScope project. Consequently, the spatial active parallel manipulator was selected to be implemented in NeuRoboScope system due to its property of having a mechanically constrained RCM at pivot-point that gives an additional feature of safety for the system. The kinematic and dynamic analysis of the selected active parallel manipulator is carried out in this thesis to be used for verification and analysis of the model in the simulation. Since the calculated dynamic equation can be considered large and complex to be used in real-time control law, a simplified equation would be needed in the control. The exact dynamic solution can also be used to optimize the simplified dynamic solution to be used in the controller design task with optimum performance.

Adding various safety features can improve surgical robots adequately. In this dissertation, safety features were introduced in two categories: the mechanical safety features MSF and the control safety features CSF. Each safety feature is assigned with a number and listed in two tables in two different chapters. The mechanical safety features are introduced in Chapter 5. A brief discussion of the details and the characteristics of each MSF are presented. Then, optimization problems are stated for two MSFs which also have effects on other proposed SFs.

Regarding the MSFs, the implementation of mechanical limits on the passive arm's joints was trustworthy and can provide more safety for some joints while it was unfavorable for others being restricting the movability at the end-effector. The passive

joints that contribute to the change of the potential energy are the most dominant for implementing mechanical limits. For the passive arm proposed in this dissertation, the parallelogram loop has already a restricted in motion within a limited range. The joint that is responsible for the pitch angle is limited by the designed gravity compensation mechanism. It has been noticed that adding mechanical limits to the selected active parallel manipulator does not provide any safety to the patient, specifically for the insertion amount of the endoscope. This is because the third actuator, as noticed in the study of the workspace of the active parallel manipulator, has variable extremes in each different orientation/position of the endoscope. Adding to that, the surgical workspace differs from one patient to another.

The surgery zone was defined as a spherical volume and within this zone, the surgical workspace was included. The surgery zone should be within the workspace of the passive arm and the workspace of the active parallel manipulator during the surgery. The homing position of the active parallel manipulator can only be performed when the endoscope tip is out of the surgery zone. For this reason, the positioning of the system with respect to the patient and the surgeons is investigated. Best positioning for the base of the passive arm is selected to have maximum manipulability at the pivot-point with minimum impedance. This can be considered as a useful safety feature for the system in case of failure so the surgeon can push the tool/endoscope with minimum effort. In addition to that, the endoscope holder allows for fast switching between the robot and the surgeon for the endoscope holding task. To increase the reachability of the telescope within the surgery zone, some necessary modifications are included in the design of the passive arm to change its kinematic scheme. These modifications added advantages for gravity compensation and the stability of the system as well.

Gravity compensation with the methodologies to be followed for both of the passive arm and active robot are studied. Spring-based solution is selected for its advantages of resulting in a compact system and minimal added inertia. This also satisfies the safety feature of having a lightweight system. Compression spring was used in the passive arm inside the parallelogram loop and for the pitch angle in the wrist. Using compression spring can provide increased safety when compared with tension spring. This is because in compression spring, the acting force has a limited distance which is toward the spring in contrast to that of tension spring when it is acting away from the spring with no limits. Any failure in the spring due to excessive force can be totally unsafe in tension spring but for the compression spring, it is less likely to have a

failure, or the failure is harmless. This is also true for the spiral spring used in the active parallel manipulator for spring-based balancing. The flexibility in spiral spring is derived from the bending deflection of its plate. This deflection value is related to the angle of twisting and it will be restricted by the inner diameter of the shaft (in the center of the spiral) and the outer diameter of the packaging of the spiral. Selecting the stiffness value for the active robot is more complicated than to be calculated analytically. The first source of complication is due to the spatial motion of the internal linkages of the parallel mechanism which is dependent on the position of all actuators. This makes the position of the center of gravity as a function of three variables while each spiral spring has one DOF.

In the optimal design of the gravity compensation system for the active arm, the optimum design parameters, which are the stiffness values and the initial angles, are related to the desired objective of this optimization. Two objectives can be studied as: minimizing upper torque at the actuators; minimizing the energy consumption of the actuators. The procedure conducted here is (introduced in Chapter 8) the PSO method. An optimum solution for the objective of minimizing the upper torque at the actuators was obtained and tested for different pitch angles. The optional symmetric solution for the left and right-side nostrils workspace was also tested by selecting an identical spring and with/without identical initial angle as an additional design constraint in the optimization. The test was done on 10^6 points distributed equally inside the surgical workspace. The three actuators' torques were dropped by more than 66% by utilizing the proposed gravity compensation. This solution can provide the system with many sufficient advantages such as: having inherent safety features, minimizing the actuation load, and using capstan drives as transmission system allowing backdrivability. As a case scenario, any failure in capstan cables, especially for the actuated joint (in the middle) for the insertion motion of the endoscope, will drop the endoscope toward the patient. However, by the presence of the counter-spring balance system, the endoscope (if not designed to maintain its position or falling slowly) can move away from the patient upward with a suitable design of the balancing system. The impedance felt by the user will be at minimum since counter-masses are not used in the design of the balancing system. This was also considered in the optimization of the passive arm.

The passive arm is intended to be fixed at the operation table from behind the patient's head. In this way, the system can occupy less footage inside the OR layout. Maximizing the manipulability at the end-effector can add MSF to the system. This can

be done by changing the configuration and/or the structural properties of the passive arm. To change the configuration, the fixing point can be selected with respect to the manipulation point (at the wrist of the passive arm) position which is known with respect to the surgery zone relative to the patient. However, the manipulability index should have a restriction by adding another index which is the modified condition number. Another index was selected as a design constraint, which is the inertia matrix. These two indices are parts of the generalized inertia matrix. The structural synthesis is carried out by using these indices. To find an optimum solution of design parameters, a new novel optimization technique using redundancy resolution is proposed. In this new optimization, a redundancy resolution technique has been adopted by modifying an originally non-redundant robot arm to be a redundant arm via including virtual joints. These virtual joints can be any of the Denavit-Hartenberg parameter/s. Hence, the employment of redundancy resolution techniques is possible for this modified robot. In this passive arm, the first link length has been selected as a design parameter to be optimized with the fixing point location. Considering the design constraints, the passive arm was simplified to be a planner two-link arm RR. With the addition of the virtual joints, the modified arm was PRPR. Related to this specific case scenario, the design constraints are provided and the optimization procedure for this case scenario is explained along with the considered performance indices. Later, the structural synthesis optimization of the simplified passive arm is obtained by the newly proposed optimization technique. The results are compared and verified with the studies in the literature for the maximum manipulability and the properties in the condition number of a two-link arm. This new optimization technique can be used in various applications after defining each of the design parameters, the objective function as a function of the design parameters, and the necessary modifications in the problem. In this optimization technique, the real system should be tested according to the performance indices of the objective function while the modified virtual system is a part of the redundancy resolution and the control law.

Having only various mechanical safety features, which provide the system inherent safety, the system cannot be considered safe without the addition of CSFs. It should be noted that having a relatively high level of safety that increases the chance of acceptance of the surgical robot system. For example, surgical and other medical robots cannot be categorized as totally safe but instead, they can be considered as an important tool for treatment and they are still posing satisfactory safety standards. Since the initial

use of the RAS, many standards have been applied to enhance the performance and the safety of these surgical systems. However, researchers with the manufacturing engineers criticized the absence of a specific and clear standard for surgical robots. However, they followed many standards related to medical equipment which also listed in Chapter 6. In 2019, group of specialists have released new standards in RASE that can guide the researchers and engineers in producing robot assisted surgical systems with systematic tools to reduce any possible risks and failure. By adding safety features and eliminating potential system failures and errors, these systems will be more tolerable and authorized for many surgical treatments. However, such a system will be more expensive when it includes all add-on safety features. In any condition, these safety features should not be underestimated. Whenever the robot is active throughout the surgery, all safety features should be possibly activated. In the survey of complication reports and statistics for RAS, it has been reported that most of the complications are caused by the surgeons and not by the surgical robot systems. To minimize such complications the surgeons should be well trained on simulators and preclinical tests before being licensed for the use of the robot assisted surgical systems. A safety checklist can also be implemented in the system. Such implementations and improvements need usually a long-term studies and statistics. In this dissertation, the reviewed/proposed MSFs and CSFs are to be taken as a reference for the design of RASE in general and in the NeuRoboScope project for optimum safety. These safety features can be considered as promising to overcome possible limitations. However, most of these safety features need to be confirmed by extensive studies in preclinical and clinical tests before being implemented in a surgical system. In general, it has been noticed that most of the manufacturers of commercial surgical robots tend to have the second generation of their surgical system with a smaller size, light in weight, simple in structure. In general, the main criterion for the success of robot assisted endonasal endoscopic surgery and the design of the robot itself can be briefly discussed as follows:

- A lightweight and small size structure of the robot
- Easy implementation of control law
- Intuitive surgeon-robot interfacing
- A system that makes the surgery easier
- The surgeon can adopt robot assisted instead of assistant surgeon
- No unnecessary prolongation of the surgical time

- The implementation of reliable safety features
- Preclinical/clinical tests for evaluation and verification
- The availability of switching to manual endoscope holding at some very critical maneuvering as the surgeon prefers
- Being at reasonable price
- Having a degree of autonomy

As long as the listed points on the proposed safety features and related standards followed, the robot assistant endoscope holder will have an important role in the future of ESBS.

The possible future research avenues for the NeuRoboScope system are developing and testing the proposed safety features by an extensive study for each individual addition of the safety features. The outlook for the possible add-ons to this surgical system is through giving more important roles for the F/T sensor. These roles can be in implementing admittance control of the active robot manipulator and implementing various levels of virtual fixtures inside/outside the surgical workspace.

Finally, an expert's opinion on the medical robot field was presented as

Our experience has been that building a strong researcher/surgeon/industry team is one of the most challenging, but also one of the most rewarding aspects of medical robotics research. The only greater satisfaction is the knowledge that the results of such teamwork can have a very direct impact on patients' health. Medical robotics research is very hard work, but it is worth it (Taylor and Stoianovici, 2003).

REFERENCES

- Ab Wahab, Mohd Nadhir, Nefti-Meziani, Samia, and Atyabi, Adham. (2015). A comprehensive review of swarm optimization algorithms. *PLoS ONE*, 10(5), 1–36. DOI:10.1371/journal.pone.0122827
- Abedloo, Ebrahim, Molaei, Amir, and Taghirad, Hamid D. (2014). Closed-form dynamic formulation of spherical parallel manipulators by Gibbs-Appell method. *2014 Second RSI/ISM International Conference on Robotics and Mechatronics (ICRoM)*, 576–581. DOI:10.1109/ICRoM.2014.6990964
- AKTORmed. (2020). AKTORmed GmbH - ENDOFIX exo, accessed on 04-08-2020. <https://aktormed.info/en/products/endofix-exo-engl>
- Al Khudir, Khaled, Halvorsen, Gaute, Lanari, Leonardo, and De Luca, Alessandro. (2019). Stable Torque Optimization for Redundant Robots Using a Short Preview. *IEEE Robotics and Automation Letters*, 4(2), 2046–2053. DOI:10.1109/LRA.2019.2899667
- Altenburger, Ruprecht, Scherly, Daniel, and Stadler, Konrad S. (2016). Design of a passive, iso-elastic upper limb exoskeleton for gravity compensation. *ROBOMECH Journal*, 3(1). DOI:10.1186/s40648-016-0051-5
- Arakelian, Vigen. (2016). Gravity compensation in robotics. *Advanced Robotics*, 30(2), 79–96. DOI:10.1080/01691864.2015.1090334
- Asada, Haruhiko. (1983). A geometrical representation of manipulator dynamics and its application to arm design. *ASME. J. Dyn. Sys., Meas., Control.*, 105(3), 131–142. DOI:10.1115/1.3140644
- Ateş, Gizem. (2018). *Teleoperation system design of a robot assisted endoscopic pituitary surgery*. MSc Thesis, Izmir Institute of Technology, Izmir, Turkey.
- Ateş, Gizem, Majani, Ronny, and Dede, Mehmet İsmet Can. (2019). Design of a teleoperation scheme with a wearable master for minimally invasive surgery. In G. Carbone, M. Ceccarelli, and D. Pisla (Eds.), *New Trends in Medical and Service Robotics* (Vol. 65, pp. 45–53). Springer, Cham. DOI:10.1007/978-3-030-00329-6_6
- Ayit, Orhan, Yaşır, Abdullah, Vardarlı, Eren, Kiper, Gökhan, and Dede, Mehmet İsmet Can. (2018). Bir Ameliyat Robotunun Denetimi için Basitleştirilmiş Dinamik Modeli Simplified Dynamic Model for the Control of a Surgical Robot Fotonik Bölümü. *TOK2018 Otomatik Kontrol Ulusal Toplantısı?*, 12–14.
- Baillieul, John, Hollerbach, John, and Brockett, Roger. (1984). Programing and Control of Kinematically Redundant Manipulators. *The 23rd IEEE Conference on Decision and Control*, 768–774. DOI:10.1109/cdc.1984.272110

- Beitler, Jonathan J., Wadsworth, J. Trad, Hudgin, Patricia A., and Kian Ang, K. (2016). Sinonasal Cancer. In *OncoHEMA Key Fastest Oncology & Hematology Insight Engine*. <https://oncohemakey.com/sinonasal-cancer/>
- Birjandi, Seyed Ali Baradaran, Kühn, Johannes, and Haddadin, Sami. (2020). Observer-Extended Direct Method for Collision Monitoring in Robot Manipulators Using Proprioception and IMU Sensing. *IEEE Robotics and Automation Letters*, 5(2), 954–961. DOI:10.1109/LRA.2020.2967287
- Bolzoni Villaret, Andrea, Doglietto, Francesco, Carobbio, Andrea, Schreiber, Alberto, Panni, Camilla, Piantoni, Enrico, Guida, Giovanni, Fontanella, Marco Maria, Nicolai, Piero, and Cassinis, Riccardo. (2017). Robotic Transnasal Endoscopic Skull Base Surgery: Systematic Review of the Literature and Report of a Novel Prototype for a Hybrid System (Brescia Endoscope Assistant Robotic Holder). *World Neurosurgery*, 105, 875–883. DOI:10.1016/j.wneu.2017.06.089
- Brian Feroldi. (2017). Mazor Robotics Enters a New Era, accessed on 09-03-2020. <https://finance.yahoo.com/news/mazor-robotics-enters-era-160200173.html>
- Briner, Hans Rudolf, Simmen, Daniel, and Jones, Nick. (2005). Endoscopic Sinus Surgery: Advantages of the Bimanual Technique. *American Journal of Rhinology*, 19(3), 269–273. DOI:10.1177/194589240501900310
- Briot, Sébastien, and Goldsztejn, Alexandre. (2018). Topology optimization of industrial robots: Application to a five-bar mechanism. *Mechanism and Machine Theory*, 120, 30–56. DOI:10.1016/j.mechmachtheory.2017.09.011
- Çabuk, Burak, Ceylan, Savaş, Anik, İhsan, Tugasaygi, Mehtap, and Kizir, Selçuk. (2015). A haptic guided robotic system for endoscope positioning and holding. *Turkish Neurosurgery*, 25(4), 601–607. DOI:10.5137/1019-5149.JTN.13290-14.0
- Carricato, Marco, and Gosselin, Clément. (2009). A statically balanced Gough/Stewart-type platform: Conception, design, and simulation. *Journal of Mechanisms and Robotics*, 1(3), 1–16. DOI:10.1115/1.3147192
- Castelnuovo, Paolo, Dallan, Iacopo, Battaglia, Paolo, and Bignami, Maurizio. (2010). Endoscopic endonasal skull base surgery: Past, present and future. *European Archives of Oto-Rhino-Laryngology*, 267(5), 649–663. DOI:10.1007/s00405-009-1196-0
- Chalongwongse, Suwiphat, Chumnanvej, Sorayouth, and Suthakorn, Jackrit. (2019). Analysis of Endonasal Endoscopic Transsphenoidal (EET) surgery pathway and workspace for path guiding robot design. *Asian Journal of Surgery*, 42(8), 814–822. DOI:10.1016/j.asjsur.2018.12.016
- Chan, Jason Y. K., Leung, Iris, Navarro-Alarcon, David, Lin, Weiyang, Li, Peng, Lee, Dennis L. Y., Liu, Yun Hui, and Tong, Michael C. F. (2016). Foot-controlled robotic-enabled endoscope holder for endoscopic sinus surgery: A cadaveric feasibility study. *Laryngoscope*, 126(3), 566–569. DOI:10.1002/lary.25634

- Chavan, S. D., and Adgokar, Nisha P. (2015). An overview on particle swarm optimization: basic concepts and modified variants. *International Journal of Science and Research*, 4(5), 255–260. www.ijsr.net
- Chheta, Yogeshkumar R., Joshi, Rajesh M., Gotewal, Krishan Kumar, and Manoahstephen, M. (2017). A review on passive gravity compensation. *2017 International Conference of Electronics, Communication and Aerospace Technology (ICECA)*, 1, 184–189. DOI:10.1109/ICECA.2017.8203668
- Chiu, Stephen L. (1988). Task Compatibility of Manipulator Postures. *The International Journal of Robotics Research*, 7(5), 13–21. DOI:10.1177/027836498800700502
- Chumnanvej, Sorayouth, Chalongsongse, Suwiphath, Pillai, Branesh M., and Suthakorn, Jackrit. (2019). Pathway and workspace study of Endonasal Endoscopic Transsphenoidal (EET) approach in 80 cadavers. *International Journal of Surgery Open*, 16, 22–28. DOI:10.1016/j.ijso.2018.12.002
- Chung, Deok Gyoon, Hwang, Minho, Won, Jongseok, and Kwon, Dong-Soo. (2016). Gravity compensation mechanism for roll-pitch rotation of a robotic arm. *2016 IEEE/RSJ International Conference on Intelligent Robots and Systems (IROS)*, 338–343. DOI:10.1109/IROS.2016.7759076
- CMR Surgical. (2020). Press kit - CMR Surgical, accessed on 17-03-2020. <https://cmrsurgical.com/press-kit/>
- Colgate, J. Edward, and Brown, J. Michael. (1994). Factors affecting the Z-width of a haptic display. *Proceedings - IEEE International Conference on Robotics and Automation*, 4, 3205–3210. DOI:10.1109/robot.1994.351077
- Coloni, Alberto, Dorigo, Marco, and Maniezzo, Vittorio. (1992). Distributed optimization by ant colonies. In P. B. Francisco J. Varela (Ed.), *Toward a Practice of Autonomous Systems: Proceedings of the First European Conference on Artificial Life* (pp. 134–142). Elsevier. <https://re.public.polimi.it/handle/11311/508623>
- Cui, Huanqing, Shu, Minglei, Song, Min, and Wang, Yinglong. (2017). Parameter selection and performance comparison of particle swarm optimization in sensor networks localization. *Sensors*, 17(487), 1–18. DOI:10.3390/s17030487
- da Vinci Robot. (2019). Intuitive | Robotic Assisted Systems | da Vinci Robot, accessed on 09-03-2020. <https://www.intuitive.com/en-us/products-and-services/da-vinci/systems#%23>
- Dare A. Wells. (1967). *Theory and Problems of Lagrangian Dynamics*. McGraw-Hill, New York.
- De Luca, A., and Oriolo, G. (1990). The Reduced Gradient Method for Solving Redundancy in Robot Arms. *IFAC 11th Triennial World Congress*, 23(8), 133–138. DOI:10.1016/S1474-6670(17)51725-5

- Dede, Mehmet İsmet Can, Kiper, Gökhan, Ayav, Tolga, Tatlıcıoğlu, Enver, Özdemirel, Barbaros, Maarroof, Omar W., Ateş, Gizem, Berker, Mustafa, Işıkay, İlkey, and Hanalioğlu, Şahin. (2018). Cerrahin Anlık Yönlendirilebildiği Robot Yardımlı Endoskop Kontrol Sistemi Mimarisi - NeuRoboScope. *Türkiye Robotbilim Konferansı (ToRK 2018)*, 1–6. <http://hdl.handle.net/11147/6897>
- Dede, Mehmet İsmet Can, Maarroof, Omar W., Ateş, Gizem, Berker, Mustafa, Işıkay, İlkey, and Hanalioğlu, Şahin. (2018). Unilateral teleoperation design for a robotic endoscopic pituitary surgery system. In M. Husty and M. Hofbaur (Eds.), *New Trends in Medical and Service Robots. MESROB 2016. Mechanisms and Machine Science* (Vol. 48, pp. 101–115). Springer, Cham. DOI:10.1007/978-3-319-59972-4_8
- Dede, Mehmet İsmet Can, Maarroof, Omar W., and Ceccarelli, Marco. (2018). Analytical Dynamic Analysis of a Kinesthetic Haptic Device. *Dokuz Eylül University-Faculty of Engineering Journal of Science and Engineering*, 20(59), 492–508. DOI:10.21205/deufmd.2018205939
- Dede, Mehmet İsmet Can, Maarroof, Omar W., and Tatlıcıoğlu, Enver. (2016). A new objective function for obstacle avoidance by redundant service robot arms. *International Journal of Advanced Robotic Systems*, 13(2), 1–13. DOI:10.5772/62471
- Denavit, J., and Hartenberg, R. S. (1955). A kinematic notation for lower pair mechanisms based on matrices. *ASME Journal of Applied Mechanics*, 22, 215–221.
- Denso. (2020). Denso Design Operation Assisting Device iArmS, accessed on 09-03-2020. http://design.denso.com/en/works/works_020.html
- Dibekci, Aysan, and Bebek, Ozkan. (2018). Improving the Safety of Medical Robotic Systems. *2018 7th IEEE International Conference on Biomedical Robotics and Biomechatronics (Biorob)*, 73–78. DOI:10.1109/BIOROB.2018.8487914
- Dubeck, Deborah. (2014). Robotic-Assisted Surgery: Focus on Training and Credentialing. *Pennsylvania Patient Safety Advisory*, 11(3), 93–101.
- Dubey, Rajiv V., Euler, James A., and Babcock, Scott M. (1991). Real-Time Implementation of an Optimization Scheme for Seven-Degree-of-Freedom Redundant Manipulators. *IEEE Transactions on Robotics and Automation*, 7(5), 579–588. DOI:10.1109/70.97869
- Eichhorn, Klaus Wolfgang Georg, and Bootz, F. (2011). Clinical requirements and possible applications of robot assisted endoscopy in skull base and sinus surgery. In M. Pamir, V. Seifert, and T. Kiris (Eds.), *Intraoperative Imaging. Acta Neurochirurgica Supplementum* (Vol. 109, pp. 237–240). Springer, Vienna. DOI:10.1007/978-3-211-99651-5_37
- Eichhorn, Klaus Wolfgang Georg, Tingelhoff, K., Wagner, I., Westphal, R., Rilk, M., Kunkel, M. E., Wahl, F. M., and Bootz, F. (2008). Sensorbasierte messung

- mechanischer kräfte am endoskop während FESS: Schritte zur robotergestützten nasennebenhöhlenchirurgie. *Hno*, 8(56), 789–794. DOI:10.1007/s00106-007-1647-0
- Eichhorn, Klaus Wolfgang, Westphal, Ralf, Last, Carsten, Rilk, Markus, Bootz, Friedrich, Wahl, Friedrich M., and Jakob, Mark. (2015). Workspace and pivot point for robot-assisted endoscope guidance in functional endonasal sinus surgery (FESS). *International Journal of Medical Robotics and Computer Assisted Surgery*, 11(1), 30–37. DOI:10.1002/rcs.1599
- Elgolli, H., Houidi, A., Mlika, A., and Romdhane, L. (2019). Analytical analysis of the dynamic of a spherical parallel manipulator. *International Journal of Advanced Manufacturing Technology*, 101(1–4), 859–871. DOI:10.1007/s00170-018-2939-0
- Erten, H. Irem, Devenci, H. Arda, and Artem, H. Seçil. (2020). Stochastic Optimization Methods. In L. Aydin, H. S. Artem, and S. Oterkus (Eds.), *Designing Engineering Structures Using Stochastic Optimization Methods* (1st Editio, pp. 10–23). CRC Press. DOI:10.1201/9780429289576-2
- Fei, Baowei, Ng, Wan Sing, Chauhan, Sunita, and Kwoh, Chee Keong. (2001). The safety issues of medical robotics. *Reliability Engineering and System Safety*, 73, 183–192. DOI:10.1016/S0951-8320(01)00037-0
- Fischer, Miloš, Gröbner, Christina, Dietz, Andreas, Krinninger, Maximilian, Lüth, Tim C., and Strauß, Gero. (2011). A technique with manipulator-assisted endoscope guidance for functional endoscopic sinus surgery: Proof of concept. *Otolaryngology - Head and Neck Surgery*, 145(5), 833–839. DOI:10.1177/0194599811412726
- Freehand. (2015). *User Manual Version 2.2 Freehand 2010 Ltd* (Issue November).
- Freehand MIS Solutions. (2020). Home Page - Freehand MIS Solutions, accessed on 01-05-2020. <http://freehandsurgeon.com/Home>
- Friedrich, Daniel Thomas, Sommer, Fabian, Scheithauer, Marc O., Greve, Jens, Hoffmann, Thomas K., and Schuler, Patrick J. (2017). An Innovate Robotic Endoscope Guidance System for Transnasal Sinus and Skull Base Surgery: Proof of Concept. *Journal of Neurological Surgery, Part B: Skull Base*, 78(6), 466–472. DOI:10.1055/s-0037-1603974
- Funda, Janez, Gruben, Kreg, Eldridge, Ben, Gomory, S., and Taylor, R. (1995). Control and evaluation of a 7-axis surgical robot for laparoscopy. *Proceedings - IEEE International Conference on Robotics and Automation*, 2, 1477–1484. DOI:10.1109/robot.1995.525484
- Guiochet, Jérémie, Do Hoang, Quynh Anh, Kaâniche, Mohamed, and Powell, David. (2012). Applying Existing Standards to a Medical Rehabilitation Robot : Limits and Challenges. *IEEE/RSJ Int. Conf. on Intelligent Robots and Systems (IROS2012)*, 5.

- Gumbs, Andrew A., Crovari, Fernando, Vidal, Clement, Henri, Patrick, and Gayet, Brice. (2007). Modified robotic lightweight endoscope (ViKY) validation in vivo in a porcine model. *Surgical Innovation*, 14(4), 261–264. DOI:10.1177/1553350607310281
- Hagn, Ulrich, Konietschke, R., Tobergte, A., Nickl, M., Jörg, S., Kübler, B., Passig, G., Gröger, M., Fröhlich, F., Seibold, U., Le-Tien, L., Albu-Schäffer, A., Nothhelfer, A., Hacker, F., Grebenstein, M., and Hirzinger, G. (2010). DLR MiroSurge: A versatile system for research in endoscopic telesurgery. *International Journal of Computer Assisted Radiology and Surgery*, 5(2), 183–193. DOI:10.1007/s11548-009-0372-4
- He, Yucheng, Hu, Ying, Zhang, Peng, Zhao, Baoliang, Qi, Xiaozhi, and Zhang, Jianwei. (2019). Human–Robot Cooperative Control Based on Virtual Fixture in Robot-Assisted Endoscopic Sinus Surgery. *Applied Sciences*, 9(1659), 1–21. DOI:10.3390/app9081659
- He, Yucheng, Zhao, Baoliang, Hou, Xilong, Gao, Peng, Hu, Ying, and Zhang, Peng. (2016). An assistant robot system for sinus surgery. *Journal of Medical Devices*, 10(030925), 1–3. DOI:10.1115/1.4033801
- Herman, Benoît, Dehez, Bruno, Khanh, Tran Duy, Raucent, Benoît, Dombre, Etienne, and Krut, Sébastien. (2009). Design and preliminary in vivo validation of a robotic laparoscope holder for minimally invasive surgery. *International Journal of Medical Robotics and Computer Assisted Surgery*, 5(3), 319–326. DOI:10.1002/rcs.263
- Holland, John H. (1973). Genetic Algorithms and the Optimal Allocation of Trials. *SIAM Journal on Computing*, 2(2), 88–105. DOI:10.1137/0202009
- Hollerbach, John M., and Suh, Ki C. (1987). Redundancy Resolution of Manipulators through Torque Optimization. *IEEE Journal on Robotics and Automation*, 3(4), 308–316. DOI:10.1109/JRA.1987.1087111
- Hsieh, Michael, Saeidi, Hamed, Kam, Michael, Wei, Shuwen, Opfermann, Justin, Leonard, Simon, Kang, Jin, and Krieger, Axel. (2020). PD23-04: An Experimental Comparison Of Autonomous Robotic And Manual Laparoscopic Suturing. (Supplement) *The Journal of Urology*, 203(4S), e465. DOI:10.1097/JU.0000000000000873.04
- Iqbal, Hashim, and Aized, Tauseef. (2014). Workspace analysis and optimization of 4-links of an 8-DOF haptic master device. *Robotics and Autonomous Systems*, 62(8), 1220–1227. DOI:10.1016/j.robot.2014.03.006
- Isitman, Oğulcan. (2018). *Compliant control of a teleoperated endoscope robot*. MSc Thesis, Izmir Institute of Technology.
- ISO iec-80601-2-772019. (2019). ISO Standardization, accessed on 05-12-2019. <https://committee.iso.org/sites/tc299/home/projects/published/iec-80601-2-772019.html>

- ISO iec-80601-2-782019. (2019). ISO Standardization, accessed on 05-12-2019. <https://committee.iso.org/sites/tc299/home/projects/published/iec-80601-2-782019.html>
- Johns Hopkins. (2020). Surgery for Pituitary Tumors | Johns Hopkins Pituitary Tumor Center, accessed on 07-08-2020. https://www.hopkinsmedicine.org/neurology_neurosurgery/centers_clinics/pituitary_center/pituitary-tumor/treatment/surgery.html
- Jung, Min Yang, Taylor, Russell H., and Kazanzides, Peter. (2014). Safety Design View: A conceptual framework for systematic understanding of safety features of medical robot systems. *2014 IEEE International Conference on Robotics & Automation (ICRA)*, 1883–1888. DOI:10.1109/ICRA.2014.6907107
- Kane, Kevin J. (2018). The early history and development of endoscopic sinonasal surgery in Australia: 1985–2005. *Australian Journal of Otolaryngology*, 1, 7–7. DOI:10.21037/ajo.2018.01.08
- Kane, Thomas R., and Levinson, David A. (1983). The Use of Kane’s Dynamical Equations in Robotics. *The International Journal of Robotics Research*, 2(3), 3–21. DOI:10.1177/027836498300200301
- Kansas. (2020). Kansas City Health and Wellness Magazine, accessed on 05-03-2020. <http://kchealthandwellness.com/>
- Kazanzides, Peter. (2009). Safety Design for medical robots. *Proceedings of the 31st Annual International Conference of the IEEE Engineering in Medicine and Biology Society: Engineering the Future of Biomedicine, EMBC 2009*, 7208–7211. DOI:10.1109/IEMBS.2009.5335275
- Kennedy, James, and Eberhart, Russell. (1995). Particle swarm optimization (PSO). *Proc. IEEE International Conference on Neural Networks*, 1942–1948. DOI:10.1109/ICNN.1995.488968
- Kristin, Julia, Geiger, Robert, Kraus, Peter, and Klenzner, Thomas. (2015). Assessment of the endoscopic range of motion for head and neck surgery using the SOLOASSIST endoscope holder. *The International Journal of Medical Robotics and Computer Assisted Surgery*, 11(1), 418–423. DOI:10.1002/rcs.1643
- Lee, Kok Meng, and Shah, Dharman K. (1988). Kinematic Analysis of a Three-Degrees-of-Freedom In-Parallel Actuated Manipulator. *IEEE Journal on Robotics and Automation*, 4(3), 354–360. DOI:10.1109/56.796
- Lessard, Simon, Bigras, Pascal, and Bonev, Ilian A. (2007). A New Medical Parallel Robot and Its Static Balancing Optimization. *Journal of Medical Devices*, 1(4), 272–278. DOI:10.1115/1.2815329
- Li, Peng, Yip, Hiu Man, Navarro-Alarcon, David, Liu, Yunhui, Tong, Chi Fai Michael, and Leung, Iris. (2013). Development of a robotic endoscope holder for nasal surgery. *2013 IEEE International Conference on Information and Automation*,

ICIA 2013, 1194–1199. DOI:10.1109/ICInfA.2013.6720476

- Li, Yangmin, and Leong, Sio Hong. (2001). Kinematics Control of Redundant Manipulators Using CMAC Neural Network. *The 5th World Multiconference on Systemics, Cybernetics and Informatics(SCI2001)*, 274–279.
- Lian, Binbin, Sun, Tao, Song, Yimin, and Wang, Xiaoli. (2016). Passive and active gravity compensation of horizontally-mounted 3-RPS parallel kinematic machine. *Mechanism and Machine Theory*, 104, 190–201. DOI:10.1016/j.mechmachtheory.2016.05.021
- Lin, Weiyang, Navarro-Alarcon, David, Li, Peng, Wang, Zerui, Yip, Hiu Man, Liu, Yun Hui, and Tong, Michael C. F. (2015). Modeling, design and control of an endoscope manipulator for FESS. *IEEE International Conference on Intelligent Robots and Systems*, 811–816. DOI:10.1109/IROS.2015.7353465
- Luca, A. De, Oriolo, G., and Siciliano, B. (1992). Robot redundancy resolution at the acceleration level. *Laboratory Robotics and Automation*, 4, 97–97.
- Maarroof, Omar W. (2012). *Self-motion control of kinematically redundant robot manipulators*. MSc Thesis, Izmir Institute of Technology.
- Maarroof, Omar W., and Dede, Mehmet İsmet Can. (2016). Physical Human-Robot Interaction: Increasing Safety by Robot Arm's Posture Optimization. In S. W. Parenti-Castelli V. (Ed.), *ROMANSY 21 - Robot Design, Dynamics and Control. ROMANSY21 2016. CISM International Centre for Mechanical Sciences (Courses and Lectures)* (Vol. 569, pp. 329–337). Springer, Cham. DOI:10.1007/978-3-319-33714-2_37
- Maarroof, Omar W., Gezgin, Erkin, and Dede, Mehmet İsmet Can. (2012). General subtask controller for redundant robot manipulators. *2012 12th International Conference on Control, Automation and Systems*, 1352–1357.
- Madoglio, Alba, Zappa, Francesca, Mattavelli, Davide, Rampinelli, Vittorio, Ferrari, Marco, Tampalini, Fabio, Fontanella, Marco, Nicolai, Piero, Doglietto, Francesco, Agosti, Edoardo, Battaglia, Paolo, Biroli, Antonio, Bresson, Damien, Castelnuovo, Paolo, Fiorindi, Alessandro, Herman, Philippe, Karligkiotis, Apostolos, Locatelli, Davide, Pozzi, Fabio, ... Turri Zanoni, Mario. (2020). Hybrid Robotics for Endoscopic Skull Base Surgery: Preclinical Evaluation and Surgeon First Impression. *World Neurosurgery*, 134, e572–e580. DOI:10.1016/j.wneu.2019.10.142
- Mahalingam, Subbiah, and Sharan, Anand M. (1986). The optimal balancing of the robotic manipulators. *Proceedings. 1986 IEEE International Conference on Robotics and Automation*, 3, 828–835. DOI:10.1109/robot.1986.1087570
- Marcus, Hani J., Hughes-Hallett, Archie, Cundy, Thomas P., Yang, Guang Zhong, Darzi, Ara, and Nandi, Dipankar. (2015). da Vinci robot-assisted keyhole neurosurgery: a cadaver study on feasibility and safety. *Neurosurgical Review*, 38(2), 367–371. DOI:10.1007/s10143-014-0602-2

- Martin's Arm. (2020). Martin's Arm | Marina Medical Instruments, accessed on 09-03-2020. <https://marinamedical.com/product/martins-arm/>
- Martini, Alberto, Troncossi, Marco, and Rivola, Alessandro. (2019). Algorithm for the static balancing of serial and parallel mechanisms combining counterweights and springs: Generation, assessment and ranking of effective design variants. *Mechanism and Machine Theory*, 137, 336–354. DOI:10.1016/j.mechmachtheory.2019.03.031
- Mattheis, Stefan, Schlüter, Anke, Stähr, Kerstin, Holtmann, Laura, Höing, Benedikt, Hussain, Timon, Kanaan, Oliver, Eckstein, Anja, and Lang, Stephan. (2019). First Use of a New Robotic Endoscope Guiding System in Endoscopic Orbital Decompression. *Ear, Nose and Throat Journal*, 1–6. DOI:10.1177/0145561319885803
- MAZOR. (2020). Recovering Faster with Renaissance, accessed on 18-03-2020. https://www.youtube.com/watch?v=T7PaFN_Q7cQ
- Medrobotics. (2020). Flex® Robotic System: Expanding the reach of surgery, Medrobotics, accessed on 18-03-2020. <https://medrobotics.com/gateway/flex-robotic-system/>
- Medtech S.A. (2020). Rosa for Ventricular and Transnasal Neurosurgery. *Poster*, 459.
- Merlet, Jean-Pierre. (2006). *Parallel robots* (2nd ed.). Springer Science & Business Media.
- Miller, Karol. (2004). Optimal Design and Modeling of Spatial Parallel Manipulators. *The International Journal of Robotics Research*, 23(2), 127–140. DOI:10.1177/0278364904041322
- Mousavi, Said, Gagnol, Vincent, Bouzgarrou, Belhassen C., and Ray, Pascal. (2017). Control of a Multi Degrees Functional Redundancies Robotic Cell for Optimization of the Machining Stability. *16th CIRP Conference on Modelling of Machining Operations Control*, 58, 269–274. DOI:10.1016/j.procir.2017.04.004
- Müller, Andreas. (2020). Dynamics Modeling of Topologically Simple Parallel Kinematic Manipulators: A Geometric Approach. *Applied Mechanics Reviews*, 72(3), 1–34. DOI:10.1115/1.4045428
- Nakamura, Yoshihiko. (1990). *Advanced robotics: redundancy and optimization* (1st ed.). Addison-Wesley Longman Publishing Co., Inc.
- Nakamura, Yoshihiko, Hanafusa, Hideo, and Yoshikawa, Tsuneo. (1987). Task-Priority Based Redundancy Control of Robot Manipulators. *The International Journal of Robotics Research*, 6(2), 3–15. DOI:10.1177/027836498700600201
- Nakayama, Takayuki, Araki, Yousuke, and Fujimoto, Hideo. (2009). A new gravity compensation mechanism for lower limb rehabilitation. *2009 International Conference on Mechatronics and Automation*, 943–948.

DOI:10.1109/ICMA.2009.5246352

- Nathan, Cherie Ann O., Chakradeo, Vinaya, Malhotra, Kavita, D'Agostino, Horacio, and Patwardhan, Ravish. (2006). The voice-controlled robotic assist scope holder AESOP for the endoscopic approach to the sella. *Skull Base*, 16(3), 123–132. DOI:10.1055/s-2006-939679
- Ng, W. S., and Tan, C. K. (1996). On safety enhancements for medical robots. *Reliability Engineering and System Safety*, 54(1), 35–45. DOI:10.1016/S0951-8320(96)00091-9
- Nimsky, Christopher, Rachinger, J., Iro, H., and Fahlbusch, R. (2004). Adaptation of a Hexapod-Based Robotic System for Extended Endoscope-Assisted Transsphenoidal Skull Base Surgery. *Minimally Invasive Neurosurgery*, 47(1), 41–46. DOI:10.1055/s-2003-812465
- Ning, Lv, Wang, Xiaofei, and Jing, Zhang. (2017). Development of a safety design and evaluation research for minimally invasive surgery robot. *Proceedings of 2017 IEEE 2nd Advanced Information Technology, Electronic and Automation Control Conference, IAEAC 2017*, 1608–1612. DOI:10.1109/IAEAC.2017.8054285
- NIST/SEMATECH. (2013). *NIST/SEMATECH e-Handbook of Statistical Methods*. DOI:https://doi.org/10.18434/M32189
- O'Sullivan, Shane, Nevejans, Nathalie, Allen, Colin, Blyth, Andrew, Leonard, Simon, Pagallo, Ugo, Holzinger, Katharina, Holzinger, Andreas, Sajid, Mohammed Imran, and Ashrafian, Hutan. (2019). Legal, regulatory, and ethical frameworks for development of standards in artificial intelligence (AI) and autonomous robotic surgery. *International Journal of Medical Robotics and Computer Assisted Surgery*, 15(1), 1–12. DOI:10.1002/rcs.1968
- Ogiwara, Toshihiro, Goto, Tetsuya, Nagm, Alhusain, and Hongo, Kazuhiro. (2017). Endoscopic endonasal transsphenoidal surgery using the iArmS operation support robot: initial experience in 43 patients. *Neurosurgical Focus*, 42(5), 1–5. DOI:10.3171/2017.3.FOCUS16498.
- Okada, T., Uchida, H., and Uemura, N. (1999). *Spring balancer apparatus* (Patent No. EP0947296A2).
- Orekhov, Andrew L., Abah, Colette, and Simaan, Nabil. (2019). Snake-Like Robots for Minimally Invasive, Single Port, and Intraluminal Surgeries. *Encyclopedia of Medical Robotics*, 1–41.
- Özbay, Ufuk, Şahin, H. Türker, and Zergeroğlu, Erkan. (2008). Robust tracking control of kinematically redundant robot manipulators subject to multiple self-motion criteria. *Robotica*, 26(6), 711–728. DOI:10.1017/S0263574708004293
- Özgür, Erol, Andreff, Nicolas, and Martinet, Philippe. (2013). Linear dynamic modeling of parallel kinematic manipulators from observable kinematic elements. *Mechanism and Machine Theory*, 69, 73–89.

DOI:10.1016/j.mechmachtheory.2013.05.002

- Paul, Richard P., and Stevenson, Charles N. (1983). Kinematics of Robot Wrists. *The International Journal of Robotics Research*, 2(1), 31–38.
DOI:10.1177/027836498300200103
- Peng, Zhi Xin, and Adachi, Norihiko. (1993). Compliant Motion Control of Kinematically Redundant Manipulators. *IEEE Transactions on Robotics and Automation*, 9(6), 831–836. DOI:10.1109/70.265926
- Perret, Jérôme, and Vercruyssen, Pierre. (2014). Advantages of mechanical backdrivability for medical applications of force control. *Workshop on Computer/Robot Assisted Surgery (CRAS)*.
<https://www.researchgate.net/publication/273422833>
- Ramsay, G., Haynes, A. B., Lipsitz, S. R., Solsky, I., Leitch, J., Gawande, A. A., and Kumar, M. (2019). Reducing surgical mortality in Scotland by use of the WHO Surgical Safety Checklist. *British Journal of Surgery*, 106(8), 1005–1011.
DOI:10.1002/bjs.11151
- Rao, SS. (2019). *Engineering optimization: theory and practice*.
- RIVERFIELD. (2020). RIVERFIELD Inc. | Products, accessed on 10-03-2020.
<https://www.riverfieldinc.com/en/product/>
- Rojas-muñoz, Edgar, Cabrera, Maria Eugenia, and Lin, Chengyuan. (2020). Telementoring in Leg Fasciotomies via Mixed-Reality : Clinical Evaluation of the STAR Platform. *MILITARY MEDICINE*, 185(S1), 513–520.
DOI:10.1093/milmed/usz234
- ROSA. (2020). Rosa Knee System and Rosa ONE® Brain System, accessed on 10-03-2020. <https://www.zimmerbiomet.com/medical-professionals>
- Rosenberg, Louis B. (1993). Virtual fixtures: perceptual tools for telerobotic manipulation. *1993 IEEE Annual Virtual Reality International Symposium*, 76–82.
DOI:10.1109/vrais.1993.380795
- Ryu, Joel, Joo, Hyunggun, and Woo, Jongwoon. (2017). The safety design concept for surgical robot employing degree of autonomy. *2017 17th International Conference on Control, Automation and Systems (ICCAS 2017)*, 1918–1921.
DOI:10.23919/ICCAS.2017.8204272
- SAFROS. (2019). The SAFROS Project Patient Safety in Robotics Surgery, accessed on 18-06-2019. <http://157.27.254.120/safros/>
- Salcudean, Septimiu E., Bell, Gordon, Bachmann, Simon, Zhu, Wen-Hong, Abolmaesumi, Purang, and Lawrence, Peter D. (1999). Robot-assisted diagnostic ultrasound--design and feasibility experiments. *International Conference on Medical Image Computing and Computer-Assisted Intervention*, 1062–1071.
DOI:10.1007/10704282_115

- Salisbury, J. Kenneth, and Craig, John J. (1982). Articulated Hands: Force Control and Kinematic Issues. *The International Journal of Robotics Research*, 1(1), 4–17. DOI:10.1177/027836498200100102
- Sánchez, Alonso, Poignet, Philippe, Dombre, Etienne, Menciassi, Arianna, and Dario, Paolo. (2014). A design framework for surgical robots: Example of the Araknes robot controller. *Robotics and Autonomous Systems*, 62(9), 1342–1352. DOI:10.1016/j.robot.2014.03.020
- Schwartz, Theodore H., and Anand, Vijay K. (2014). *endoscopic skull base and pituitary approaches: a step-by-step guide for surgical instruction and cadaveric dissection*. Endo Press, Tuttlingen.
- Senhance Surgical. (2020). The First in Digital Laparoscopy | Senhance Surgical System, accessed on 09-03-2020. <https://www.senhance.com/us/digital-laparoscopy>
- Seraji, Homayoun. (1989). Configuration Control of Redundant Manipulators: Theory and Implementation. *IEEE Transactions on Robotics and Automation*, 5(4), 472–490. DOI:10.1109/70.88062
- Shi, Y., and Eberhart, R. C. (1998). Parameter selection in particle swarm optimization. *Proc. International Conference on Evolutionary Programming*, 591–600. DOI:10.1007/BFb0040810
- Stammberger, H., and Posawetz, W. (1990). Functional endoscopic sinus surgery - Concept, indications and results of the Messerklinger technique. *European Archives of Oto-Rhino-Laryngology*, 247(2), 63–76. DOI:10.1007/BF00183169
- Stienen, Arno H. A., Hekman, Edsko E. G., Van der Helm, Frans C. T., Prange, Gerdienke B., Jannink, Michiel J. A., Aalsma, Arthur M. M., and Van der Kooij, Herman. (2007). Freebal: dedicated gravity compensation for the upper extremities. *2007 IEEE 10th International Conference on Rehabilitation Robotics*, 804–808. DOI:10.1109/ICORR.2007.4428517
- STORZ, KARL. (2020). *Telescopes , Visualization and Documentation Systems: for Video-Assisted Cardiac Surgery and Open Heart Surgery with Minimal Access*. KARL STORZ.
- Strauß, Gero, Hofer, Mathias, Kehrt, S., Grunert, Ronny, Korb, Werner, Trantakis, C., Winkler, D., Meixensberger, Jürgen, Bootz, Friedrich, Dietz, Andreas, and Wahrburg, Jürgen. (2007). Ein konzept für eine automatisierte endoskopführung für die nasennebenhöhlenchirurgie. *HNO*, 55(3), 177–184. DOI:10.1007/s00106-006-1434-3
- Strauß, Gero, Mathias, Hofer, Kehrt, S., Grunert, Ronny, Korb, Werner, Trantakis, Ch., Winkler, D., Meixensberger, Jürgen, Bootz, Friedrich, Dietz, Andreas, and Wahrburg, Jürgen. (2007). [Manipulator assisted endoscope guidance in functional endoscopic sinus surgery: proof of concept]. *HNO*, 55 3(3), 177—184. DOI:10.1007/s00106-006-1434-3

- Stryker. (2020). Mako Technology Overview | Stryker, accessed on 09-03-2020. <https://www.stryker.com/us/en/joint-replacement/systems/mako-robotic-arm-assisted-surgery.html>
- Swaney, Philip J., Croom, Jordan M., Burgner, Jessica, Gilbert, Hunter B., Rucker, D. Caleb, Webster, Robert J., Weaver, Kyle D., and Russell, Paul T. (2012). Design of a quadramanual robot for single-nostril skull base surgery. *ASME 2012 5th Annual Dynamic Systems and Control Conference Joint with the JSME 2012 11th Motion and Vibration Conference, DSCC 2012-MOVIC 2012, 3*, 387–393. DOI:10.1115/DSCC2012-MOVIC2012-8536
- Swaney, Philip J., Gilbert, Hunter B., Webster, Robert J., Russell, Paul T., and Weaver, Kyle D. (2015). Endonasal Skull Base Tumor Removal Using Concentric Tube Continuum Robots : A Phantom Study. *Journal of Neurological Surgery, Part B*, 76(B2), 145–149. DOI:<http://dx.doi.org/10.1055/s-0034-1390401>.
- Taniguchi, Kazuhiro, Nishikawa, Atsushi, Sekimoto, Mitsugu, Kobayashi, Takeharu, Kazuhara, Kouhei, Ichihara, Takaharu, Kurashita, Naoto, Takiguchi, Shuji, Doki, Yuichiro, Mori, Masaki, and Miyazaki, Fumio. (2010). Classification, Design and Evaluation of Endoscope Robots. In S. H. Baik (Ed.), *Robot Surgery* (p. 172). InTech. DOI:10.5772/6893
- Tatlicioğlu, Enver, Braganza, David, Burg, Timothy C., and Dawson, Darren M. (2009). Adaptive control of redundant robot manipulators with sub-task objectives. *Robotica*, 27(6), 873–881. DOI:10.1017/S0263574708005274
- Taylor, Russell H. (2018). Russell H. Taylor - My Medical Robotics Research at IBM, accessed on 20-05-2020. [https://www.cs.jhu.edu/~rht/RHT Medical Robotics Research at IBM.html](https://www.cs.jhu.edu/~rht/RHT_Medical_Robotics_Research_at_IBM.html)
- Taylor, Russell H. (2006). A perspective on medical robotics. *Proceedings of the IEEE*, 94(9), 1652–1664. DOI:10.1109/JPROC.2006.880669
- Taylor, Russell H., Funda, Janez, Grossman, David D., Karidis, John P., and LaRose, David A. (1995). *Remote center of motion robot for surgery* (Patent No. 5,397,323). US.
- Taylor, Russell H., Menciassi, Arianna, Fichtinger, Gabor, Fiorini, Paolo, and Dario, Paolo. (2016). Medical robotics and computer-integrated surgery. In *Springer Handbook of Robotics* (pp. 1657–1683). Springer International Publishing. DOI:10.1007/978-3-319-32552-1_63
- Taylor, Russell H., and Stoianovici, Dan. (2003). Medical Robotics in Computer-Integrated Surgery. *IEEE Transactions on Robotics and Automation*, 19(5), 765–781. DOI:10.1109/TRA.2003.817058
- Think Surgical. (2020). Professionals – Think Surgical, Inc., accessed on 09-03-2020. <https://thinksurgical.com/professionals/#technology>
- Trelea, Ioan Cristian. (2003). The particle swarm optimization algorithm: Convergence

- analysis and parameter selection. *Information Processing Letters*, 85(6), 317–325. DOI:10.1016/S0020-0190(02)00447-7
- Trévilhot, Vincent, Garrel, R., Dombre, E., Poignet, P., Sobral, R., and Crampette, L. (2013). Robotic endoscopic sinus and skull base surgery: Review of the literature and future prospects. *European Annals of Otorhinolaryngology, Head and Neck Diseases*, 130(4), 201–207. DOI:10.1016/j.anorl.2012.03.010
- Trévilhot, Vincent, Sobral, Rafael, Dombre, Etienne, Poignet, Philippe, Herman, Benoît, and Crampette, Louis. (2013). Innovative endoscopic sino-nasal and anterior skull base robotics. *International Journal of Computer Assisted Radiology and Surgery*, 8(6), 977–987. DOI:10.1007/s11548-013-0839-1
- User Manual. (2010). Point setter, accessed on 03-06-2020.
https://www.karlstorz.com/cps/rde/xbcr/karlstorz_assets/ASSETS/3231031.pdf
- Uzun, Bengisu, Ayav, Tolga, Dede, Can, Berker, Mustafa, Isıkay, Ilkay, Hanalioğlu, Sahin, Özdemirel, Barbaros, Kiper, Gökhan, Tatlıcıoğlu, Enver, Maarroof, Omar W., Isitman, Oğulcan, Ateş, Gizem, and Yaşır, Abdullah. (2016). Neuroscope Sisteminin Model Tabanlı Sınaması Model Based Verification of Neuroscope System. *Otomatik Kontrol Ulusal Toplantısı, TOK'2016*, 347–352.
- Uzunoglu, Emre, Dede, Mehmet İsmet Can, and Kiper, Gökhan. (2016). Trajectory planning for a planar macro-micro manipulator of a laser-cutting machine. *Industrial Robot*, 43(5), 513–523. DOI:10.1108/IR-02-2016-0057
- Van Den Bergh, Frans. (2007). *An Analysis of Particle Swarm Optimizers* (Issue November). PhD Thesis, University of Pretoria.
- Vougioukas, Vassilios I., Hubbe, Ulrich, Hochmuth, Albrecht, Gellrich, Nils C., and van Velthoven, Vera. (2003). Perspectives and limitations of image-guided neurosurgery in pediatric patients. *Child's Nervous System*, 19(12), 783–791. DOI:10.1007/s00381-003-0836-8
- Vulliez, Margot, Zeghloul, Said, and Khatib, Oussama. (2018). Design strategy and issues of the Delthaptic, a new 6-DOF parallel haptic device. *Mechanism and Machine Theory*, 128, 395–411. DOI:10.1016/j.mechmachtheory.2018.06.015
- Wagner, Ingo, Tingelhoff, Kathrin, Westphal, Ralf, Kunkel, Maria Elizete, Wahl, Friedrich, Bootz, Friedrich, and Eichhorn, Klaus. (2008). Ex vivo evaluation of force data and tissue elasticity for robot-assisted FESS. *European Archives of Oto-Rhino-Laryngology*, 265(11), 1335–1339. DOI:10.1007/s00405-008-0644-6
- Wang, Jie, Yang, Xing, Li, Peng, Song, Shuang, Liu, Li, and Meng, Max Q. H. (2020). Design of a multi-arm concentric-tube robot system for transnasal surgery. *Medical and Biological Engineering and Computing*, 58(3), 497–508. DOI:10.1007/s11517-019-02093-9
- Wang, Jiegao, and Gosselin, Clément M. (1998). A new approach for the dynamic analysis of parallel manipulators. *Multibody System Dynamics*, 2, 317–334.

DOI:10.1023/A:1009740326195

- Wang, Jingguo, Li, Yangmin, and Zhao, Xinhua. (2010). Inverse Kinematics and Control of a 7-DOF Redundant Manipulator Based on the Closed-Loop Algorithm. *International Journal of Advanced Robotic Systems*, 7(4), 37. DOI:10.5772/10495
- Weede, Oliver, Mehrwald, Markus, and Wörn, Heinz. (2012). Knowledge-based system for port placement and robot setup optimization in minimally invasive surgery. *10th IFAC Symposium on Robot Control International Federation of Automatic Control*, 722–728. DOI:10.3182/20120905-3-HR-2030.00038
- Weill Cornell Brain and Spine Center. (2020). Pediatric Skull Base and Pituitary Surgery | Weill Cornell Brain and Spine Center. <https://weillcornellbrainandspine.org/pediatric-skullbase>
- WHO. (2019). WHO | About us, accessed on 28-06-2019. <https://www.who.int/patientsafety/about/en/>
- Wörn, Heinz, and Hoppe, Harald. (2001). Augmented reality in the operating theatre of the future. *Lecture Notes in Computer Science (Including Subseries Lecture Notes in Artificial Intelligence and Lecture Notes in Bioinformatics)*, 2208, 1195–1196. DOI:10.1007/3-540-45468-3_160
- Wurm, J., Dannenmann, T., Bohr, C., Iro, H., and Bumm, K. (2005). Increased safety in robotic paranasal sinus and skull base surgery with redundant navigation and automated registration. *International Journal of Medical Robotics and Computer Assisted Surgery*, 1(3), 42–48. DOI:10.1581/mrcas.2005.010310
- Xia, T., Baird, C., Jallo, G., Hayes, K., Nakajima, N., and Hata, N. (2008). An integrated system for planning, navigation and robotic assistance for skull base surgery. *Int J Med Robot*, 4, 321–330.
- Yaşır, Abdullah, and Kiper, Gökhan. (2018). Structural synthesis of 2R1T type mechanisms for minimally invasive surgery applications. *Mechanisms and Machine Science*, 52, 31–38. DOI:10.1007/978-3-319-60702-3_4
- Yaşır, Abdullah, Kiper, Gökhan, and Dede, Mehmet İsmet Can. (2020). Kinematic design of a non-parasitic 2R1T parallel mechanism with remote center of motion to be used in minimally invasive surgery applications. *Mechanism and Machine Theory*, 153, 17. DOI:10.1016/j.mechmachtheory.2020.104013
- Yaşır, Abdullah, Kiper, Gökhan, Dede, Mehmet İsmet Can, and der Wijk, Volkert. (2019). Static force balancing of a 2R1T parallel manipulator with remote center of motion. *IFTToMM World Congress on Mechanism and Machine Science*, 3219–3226. DOI:10.1007/978-3-030-20131-9_317
- Yip, Hiu Man, Wang, Zerui, Navarro-Alarcon, David, Li, Peng, Liu, Yun Hui, and Cheung, Tak Hong. (2015). A new robotic uterine positioner for laparoscopic hysterectomy with passive safety mechanisms: Design and experiments. *IEEE International Conference on Intelligent Robots and Systems*, 3188–3194.

DOI:10.1109/IROS.2015.7353819

- Yip, Michael, and Das, Nikhil. (2017). Robot Autonomy for Surgery. In *World Scientific Review* (pp. 281–313). DOI:10.1142/9789813232266_0010
- Yoon, Hyun Soo, Cha, Hyo Jeong, Chung, Jaeheon, and Yi, Byung Ju. (2013). Compact design of a dual master-slave system for maxillary sinus surgery. *IEEE International Conference on Intelligent Robots and Systems*, 5027–5032. DOI:10.1109/IROS.2013.6697083
- Yoshikawa, Tsuneo. (1985a). Dynamic Manipulability of Robot Manipulators. *Transactions of the Society of Instrument and Control Engineers*, 21(9), 970–975. DOI:10.9746/sicetr1965.21.970
- Yoshikawa, Tsuneo. (1990). *Foundations of robotics: analysis and control*.
- Yoshikawa, Tsuneo. (1985b). Manipulability and redundancy control of robotic mechanisms. *Proceedings - IEEE International Conference on Robotics and Automation*, 1004–1009. DOI:10.1109/ROBOT.1985.1087283
- ZEISS Medical Technolog. (2020). KINEVO 900 Neurosurgical Visualization Microscope - ZEISS Medical Technology. <https://www.zeiss.com/meditec/int/product-portfolio/surgical-microscopes/kinevo-900.html>
- Zeng, Bowei, Meng, Fanle, Ding, Hui, and Wang, Guangzhi. (2017). A surgical robot with augmented reality visualization for stereoelectroencephalography electrode implantation. *International Journal of Computer Assisted Radiology and Surgery*, 12(8), 1355–1368. DOI:10.1007/s11548-017-1634-1
- Zhong, Fangxun, Li, Peng, Shi, Jiadong, Wang, Zerui, Wu, Jiahao, Chan, Jason Y. K., Leung, Natalie, Leung, Iris, Tong, Michael C. F., and Liu, Yun-Hui. (2019). Foot-controlled Robot-Enabled EndoScope Manipulator (FREEDOM) For Sinus Surgery: Design, Control and Evaluation. *IEEE Transactions on Biomedical Engineering*, 1–12. DOI:10.1109/tbme.2019.2939557

VITA

Omar W. MaarooF

omarmaarooF@uomosul.edu.iq, Scopus Author ID: 55561100900

- **Experience:** (1) Assistant Engineer in the Mechanical Engineering Department at the University of Mosul (UOM) (2007-2008). (2) Engineer and research assistant in the Mechatronics Engineering Department at UOM (2008-2013). (3) Assistant Lecturer in the Mechatronics Engineering Department at UOM (2013-2019). (4) Project assistant in the Mechanical Engineering Department at İzmir Institute of Technology, Funded by The Scientific and Technological Research Council of Turkey (TUBITAK) via grant number 115E726 on the NeuRoboScope system project (2015-2017). (5) Lecturer (Assistant professor) in the Mechatronics Engineering Department at UOM (2019-present) giving lectures in Engineering Drawing (CAD) (MTE105), Mechanics of Materials (MTE204), Robotics Lab., Control Lab., and Automation Lab. Adding to that, supervising undergraduate projects and some office works.
- **Publications:**

Dede, M. İ. C., Kiper, G., Ayav, T., Tatlıcıoğlu, E., Özdemirel, B., MaarooF, O. W., Ateş, G., Berker, M., Işıkkay, İ., and Hanalioğlu, Ş. (2018). Cerrahın Anlık Yönlendirilebildiği Robot Yardımlı Endoskop Kontrol Sistemi Mimarisi - NeuRoboScope. *Türkiye Robotbilim Konferansı (ToRK 2018)*, 1–6.

Dede, M. İ. C., MaarooF, O. W., Ateş, G., Berker, M., Işıkkay, İ., and Hanalioğlu, Ş. (2018). Unilateral teleoperation design for a robotic endoscopic pituitary surgery system. In M. Husty and M. Hofbauer (Eds.), *New Trends in Medical and Service Robots. MESROB 2016. Mechanisms and Machine Science* (Vol. 48, pp. 101–115). Springer, Cham.

Dede, M. İ. C., MaarooF, O. W., and Ceccarelli, M. (2018). Analytical Dynamic Analysis of a Kinesthetic Haptic Device. *Dokuz Eylül University-Faculty of Engineering Journal of Science and Engineering*, 20(59), 492–508.

Dede, M. İ. C., MaarooF, O. W., and Tatlıcıoğlu, E. (2016). A new objective function for obstacle avoidance by redundant service robot arms. *International Journal of Advanced Robotic Systems*, 13(2), 1–13.

Görgülü, İ., MaarooF, O. W., Taner, B., and Dede, M. İ. C. (2017). Experimental Verification of Quasi-Static Equilibrium Analysis of a Haptic Device. *The International Symposium of Mechanism and Machine Science, 2017 AzCIFTtoMM*, 57–65.

Kanık, M., Berker, G., MaarooF, O. W., Uzunoğlu, E., and Dede, M. İ. C. (2017). Admitans Yapısında Kinematik Olarak Artıksıl Haptik Ana Sistem Tasarımı. *18. Ulusal Makina Teorisi Sempozyumu*, 5–7.

Kiper, G., Dede, M. İ. C., MaarooF, O. W., and Özkahya, M. (2017). Function generation with two loop mechanisms using decomposition and correction method. *Mechanism and Machine Theory*, 110, 16–26.

MaarooF, O. W. (2012). *Self-motion control of kinematically redundant robot manipulators*. MSc Thesis, İzmir Institute of Technology.

MaarooF, O. W., and Dede, M. İ. C. (2014a). A comparative study on application of decomposition method in function generation synthesis of over-constrained mechanisms. In V. Petuya, C. Pinto, and E. Lovasz (Eds.), *New Advances in Mechanisms, Transmissions and Applications. Mechanisms and Machine Science* (Vol. 17). Springer, Dordrecht.

MaarooF, O. W., and Dede, M. İ. C. (2014b). Kinematic synthesis of over-constrained double-spherical six-bar mechanism. *Mechanism and Machine Theory*, 73, 154–168.

MaarooF, O. W., and Dede, M. İ. C. (2016). Physical Human-Robot Interaction: Increasing Safety by Robot Arm's Posture Optimization. In S. W. Parenti-Castelli V. (Ed.), *ROMANSY 21 - Robot Design, Dynamics and Control. ROMANSY21 2016. CISM International Centre for Mechanical Sciences (Courses and Lectures)* (Vol. 569, pp. 329–337). Springer, Cham.

MaarooF, O. W., Dede, M. İ. C., and Kiper, G. (2017). Alternating error effects on decomposition method in function generation synthesis. In P. Wenger and P. Flores (Eds.), *New Trends in Mechanism and Machine Science. Mechanisms and Machine Science*, (Vol. 43, pp. 293–301). Springer, Cham.

MaarooF, O. W., Gezzin, E., and Dede, M. İ. C. (2012). General subtask controller for redundant robot manipulators. *2012 12th International Conference on Control, Automation and Systems*, 1352–1357.

Uzun, B., Ayav, T., Dede, C., Berker, M., Işıkkay, İ., Hanalioğlu, S., Özdemirel, B., Kiper, G., Tatlıcıoğlu, E., MaarooF, O. W., Isitman, O., Ateş, G., and Yaşır, A. (2016). Neuroboscope Sisteminin Model Tabanlı Sinaması Model Based Verification of Neuroboscope System. *Otomatik Kontrol Ulusal Toplantısı, TOK'2016*, 347–352.